COMPUTATIONAL HYPERSONIC BOUNDARY-LAYER STABILITY AND THE VALIDATION AND VERIFICATION OF EPIC

A Dissertation

by

TRAVIS SCOTT KOCIAN

Submitted to the Office of Graduate and Professional Studies of
Texas A&M University
in partial fulfillment of the requirements for the degree of

DOCTOR OF PHILOSOPHY

Chair of Committee,	Helen L. Reed
Committee Members,	Rodney Bowersox
	Edward White
	Prabir Daripa
Head of Department,	Rodney Bowersox

May 2018

Major Subject: Aerospace Engineering

ABSTRACT

Laminar-to-turbulent transition is a process that is critical in determining the system drag and surface heating of a flight vehicle, and the ability to predict, and possibly control, this process has become an essential component in vehicle design. The linear and nonlinear parabolized stability equations provide a method of analyzing different regions of the flowfield around a vehicle in a way that is both efficient and accurate. These methods have continued to evolve in terms of both capability and robustness. Coupled with data from wind tunnel experiments, they provide a powerful tool in understanding and addressing flow phenomena involved in the process of laminar-to-turbulent transition.

EPIC is a parabolized stability equations (PSE) solver developed within the Computational Stability and Transition laboratory at Texas A&M University that can address both the linear and nonlinear aspects of the stability problem. This capability provides a means to evaluate different instabilities and the underlying physics that drives them. PSE results are computed for several hypersonic geometries including the Langley 93-10 cone, Purdue compression cone, yawed straight cone, and HIFiRE-5 elliptic cone. Disturbances that are both two-dimensional and three-dimensional in nature are analyzed and compared with results obtained from direct numerical simulations, wind tunnel experiments, and alternate PSE codes. In addition, techniques for modeling stationary crossflow vortex paths and the evolution of spanwise wavenumber from the basic-state solution are formulated.

ACKNOWLEDGMENTS

I am extremely grateful to have had the opportunity to interact and work with the many individuals that have helped guide me during my studies at Texas A&M. I know that the present work was only made possible because of the contributions and support of those around me.

First and foremost, I would like thank my advisor, Dr. Helen Reed, for giving me the opportunity to pursue my graduate degree. I have gained far more than I can describe from her never-ending guidance, encouragement, and support. I could not imagine having a graduate experience with a better professor or person.

I am very appreciative for the discussions I have had with Dr. Rodney Bowersox, Dr. William Saric, and both of their experimental groups. I was able to draw from their vast knowledge and experience in order gain a perspective that I would not have achieved from solely a computational viewpoint. Ian Neel, Jerrod Hofferth, and Alex Craig deserve a special thanks for their direct contributions to this study. I would also like to acknowledge the other members of my committee, Dr. Edward White and Dr. Prabir Daripa, for their helpful advice and suggestions.

Thank you to my colleagues from the Computational Stability and Transition lab, Eduardo Perez, Matthew Tufts, Nicholas Oliviero, Alexander Moyes, Daniel Mullen, and Joseph Kuehl. I consider myself very fortunate to have been able to work with each of you on a daily basis and am grateful for both your support and friendship.

I would like to thank Rebecca Marianno and Colleen Leatherman for their tireless work. Their efforts have worked wonders towards providing an organized graduate experience, and our lab would not operate properly without them.

Finally, I would like to thank my family for their constant love and support. I would not be who I am today without you.

CONTRIBUTORS AND FUNDING SOURCES

Contributors

This work was supported by a dissertation committee consisting of my advisor Dr. Helen Reed and professors Dr. Rodney Bowersox, Dr. Edward White, and Dr. Prabir Daripa.

Funding Sources

This graduate study was supported by Program Manager Ivett Leyva under AFOSR grant FA9550-14-1-0365, Program Managers John Schmisseur and Rengasamy Ponnappan in the Air Force/NASA National Hypersonics Science Center in Laminar-Turbulent Transition under grant FA9550-08-0308, and by a dissertation research fellowship from the Texas Space Grant Consortium.

NOMENCLATURE

A	Disturbance Amplitude
$\mathcal{A}, \mathcal{B}, \mathcal{C}, \mathcal{D}, \mathcal{E}, \mathcal{F}$	Linear Stability Matrices
c	Disturbance Phase Speed
C_f	Skin-Friction Coefficient
c_p	Specific Heat Capacity at Constant Pressure
c_v	Specific Heat Capacity at Constant Volume
d	Straight Line Distance
F	Frequency (kHz)
h_1, h_2, h_3	Curvature Terms in (ξ, η, ζ) Directions, Respectively
i, j, k	Basic-State Indices
k_c	Wavenumber (Number of Waves)
m	Wavenumber Observed Locally (Number of Waves)
M	Mach Number
$\mathcal{NL}$	Vector of Nonlinear Terms
N_y	Number of Computational Normal Points
P	Absolute Static Pressure
Pr	Prandtl Number
r	Cylindrical Coordinate in Radial Direction
R	Radius of Revolution
R_g	Specific Gas Constant
Re	Reynolds Number
Re_θ	Momentum Thickness Reynolds Number

Re'	Unit Reynolds Number
s	Surface Distance
St	Stanton Number
t	Time
T	Absolute Static Temperature
u, v, w	Velocity Components in (ξ, η, ζ) Directions, Respectively
x, y, z	Orthogonal Cartesian Coordinates
α	Wavenumber in ξ Direction
β	Wavenumber in ζ Direction
γ	Ratio of Specific Heats
δ	Boundary Layer Length Scale
ζ	Spanwise Coordinate Tangent to Surface and Perpendicular to Marching Direction ξ
η	Wall-normal Coordinate and Perpendicular to Marching Direction ξ
θ	Cylindrical Coordinate in Azimuthal Direction
κ	Thermal Conductivity
λ	Wavelength
$\lambda_{\mathcal{L}}$	Lagrange Multiplier
λ_v	Second Viscosity Coefficient
μ	Dynamic Viscosity Coefficient
ξ	Coordinate Along Marching Direction
ρ	Density
ϕ	Primitive Variable Vector (u, v, w, T, ρ)
χ	Scale Factor
ψ	Wave Angle
ω	Angular Frequency (rad/sec)

ACRONYMS

ACE	Adjustable Contour Expansion
AoA	Angle of Attack
AFRL	Air Force Research Laboratory
BAM6QT	Boeing/AFOSR Mach-6 Quiet Tunnel
CFD	Computational Fluid Dynamics
CST	Computational Stability and Transition
DNS	Direct Numerical Simulation
DPLR	Data Parallel Line Relaxation
DRE	Discrete Roughness Element
DSTO	Defense Science and Technology Organization
EPIC	Euonymous Parabolized Instability Code
HIFiRE	Hypersonic International Flight Research Experimentation
LNS	Linearized Navier-Stokes
LPSE	Linear Parabolized Stability Equations
LST	Linear Stability Theory
M6QT	Mach 6 Quiet Tunnel
NPSE	Nonlinear Parabolized Stability Equations
PSE	Parabolized Stability Equations
RMS	Root Mean Square

SUBSCRIPTS

art	Artificial Value
e	Quantity Evaluated at Edge of Boundary Layer
i	Imaginary Value
r	Real Value

ref	Reference Value
w	Quantity Evaluated at Wall
0	Initial Value
∞	Quantity Evaluated at Infinity
$\perp$	Perpendicular
ACCENTS	
T	Transpose
$\wedge$	Shape Function Quantity
$\dagger$	Complex Conjugate
$-$	Basic State Quantity
$\circ$	Degrees
$'$	Disturbance Quantity
$\sim$	Slowly Varying
$\rightarrow$	Vector

TABLE OF CONTENTS

Page

LIST OF FIGURES

FIGURE Page

LIST OF TABLES

TABLE Page

1. INTRODUCTION AND BACKGROUND

1.1 Motivation

Modern research and development continues to focus on new and efficient ways to reduce system drag for aircraft designs. For example, the International Air Transport Association reported that commercial-class aircraft used 18.8% of the operating budget on fuel in 2017 [2]. This is a value that is on the order of billions of dollars, and improvements in vehicle performance can result in substantial savings.

System drag can be decomposed into separate components based on the source of the effect. For a high speed civil transport aircraft, Bushnell [3] states that the drag is approximately on the order of $\frac{1}{3}$ skin-friction drag, $\frac{1}{3}$ wave drag, and $\frac{1}{3}$ vortex drag due to lift. When flow separation occurs, another component deemed pressure drag also becomes a significant contributor. The process of boundary-layer transition heavily impacts drag and produces many other effects on the performance of an aircraft. In addition to reducing skin-friction drag, laminar flow also yields benefits in reducing the heating that occurs at the surface of a vehicle. This becomes even more important when one enters the hypersonic flow regime as turbulent flow can produce heating rates that are higher than those of laminar flow by a factor of six or more. In other instances, turbulent flow can be used as a beneficial tool in the design of an aircraft. One such example occurs at the inlet of a jet engine. Turbulent flow at this location will improve the mixing of the fuel and the oxidizer resulting in a higher efficiency. It can also prevent flow separation in areas that are susceptible under laminar flow conditions and help to maintain control authority for control surfaces. Additionally, preventing flow separation can reduce the penalties incurred by pressure drag in the aft region of a body. Pressure drag from separation often carries a larger penalty than the increase in skin-friction drag due to turbulent flow.

The focus of this dissertation is on the hypersonic flight regime. Recent advancement and

progress in the field of hypersonics has led to the development and testing of investigative and flight capable vehicles. One such program was the DARPA/Air Force Falcon program [4]. The objectives of the program were to create a reusable vehicle that can take-off and land on modern runways, achieve hypersonic cruise velocities, and reach any location in the world in two hours or less. The test flight of the Hypersonic Technology Vehicle #2 (HTV-2) required a unique combination of integrated technologies. These included the development of lightweight high-temperature materials, optimization of aerodynamic design for high lift to drag ratio, and a sustained propulsion system. Two flights were conducted with the HTV-2 achieving speeds of Mach 20 for both. However, each was only able to sustain flight for approximately 9 minutes out of the 30 minutes designated for the mission before being terminated. It was reported that damage to the outer aeroshell due to the combination of aerodynamic force and heating contributed to this result.

Another program labeled the Hypersonic International Flight Research Experimentation (HIFiRE) program was a joint hypersonic flight test program by the Air Force Research Laboratory (AFRL) and the Australian Defense Science and Technology Organization (DSTO) [5]. The main objective was to obtain aerothermodynamic data including the heating created by a transitional boundary layer. HIFiRE-1 was the first of the flight test series and consisted of an axisymmetric circular cone geometry with a 7° half angle. The flight test launched in March 2010 and successfully provided transition measurements in a flight environment. Later flight tests were organized in order to study boundary layer stability and transition on a non-axisymmetric configuration. This geometry was a 2:1 elliptic cone and focused on leading edge transition and three-dimensional (3-D) instabilities. The first flight, HIFiRE-5a, was tested in April 2012, but did not obtain the intended trajectory or Mach number because the second stage of the sounding rocket failed to ignite. Despite this, useful supersonic data was still obtained. A second flight was completed in May 2016 and designated HIFiRE-5b. This second flight successfully achieved hypersonic speeds and provided extensive data in regions associated with various disturbances including near the centerline,

on the leading edges, and in the highly 3-D region between them [6].

The results of these recent flight tests have spawned a number of studies showing that the development of instabilities in the boundary layer leading to transition to turbulence can create extreme levels of heating which could have devastating effects on a hypersonic vehicle. For this reason, it is vital to understand and predict the behavior of such mechanisms and any influence they might have on the vehicle flight capabilities.

1.2 Objective

This work uses the Euonymous Parabolized Instability Code (EPIC [7]) in combination with a basic-state data processing and extraction code, both developed within the Computational Stability and Transition (CST) laboratory at Texas A&M University. The primary objective of the present work is to develop methods to accurately model the physics of various mechanisms and, by extension, the transition process for a variety of general hypersonic vehicles. As transition studies are known to be very sensitive, a very important aspect of this work is a close collaboration with high quality experiments providing both crucial validation and a different perspective in the identification of relevant mechanisms.

1.3 Background on Instability Mechanisms

The behavior of a laminar boundary layer exposed to freestream disturbances or surface imperfections is often determined by the growth of an assortment of different instability mechanisms. Much of the foundation and most extensive descriptions of the stability problem are provided by Mack [8] and Federov [9] including an in depth analysis of supersonic boundary layers for speeds up to Mach 10, key differences between disturbances in the supersonic and subsonic regimes, laminar flow control, and receptivity.

Receptivity in particular is an elusive aspect that heavily influences the onset of transition [10, 11, 12, 13] and is the beginning stage for any stability analysis. Receptivity determines how freestream vorticity, freestream noise, and surface roughness affect the initial amplitude of a disturbance as it enters the boundary layer. A close collaboration between computations

and experiments is necessary in order to investigate this multivariable process. Computations will require validation of receptivity models provided from experimental measurements. However, the measurements will have undergone a stage of receptivity as the disturbances enter the boundary layers of the measurement devices themselves, further adding to the complexity of the problem.

A combination of efforts from experiments, computations, and theory have revealed that hypersonic boundary layers are especially vulnerable to the following mechanisms:

1. Attachment-Line Instability
2. Leading-Edge Contamination
3. First Mode
4. Second Mode
5. Görtler Instability
6. Traveling Crossflow
7. Stationary Crossflow
8. Transient Growth

While the focus of this study will involve the development of these mechanisms within hypersonic flowfields, a majority of the existing fundamental research has occurred within the low speed regime. As such, the aforementioned mechanisms will be described using findings acquired from research in both high speed and low speed flow.

The attachment-line instability is one that forms from a perturbation along the leading edge of a vehicle. The flow along this line is entirely spanwise, and if the perturbation causes the attachment-line boundary layer to become turbulent, the boundary layer on all portions aft of this location will also be turbulent [14, 15]. Larger leading edge radii are more

susceptible to this mechanism, and Pfenninger [16] and Poll [17, 18] have developed criteria dictating the maximum allowable radius that will maintain laminar flow. Other means of control consist of reducing the wing sweep of the vehicle or applying suction to the leading edge.

If a wing root is contaminated with turbulent flow from a structure such as a fuselage or other body, this turbulence will travel along the attachment line of the leading edge of the wing. The entire boundary layer over the wing surface will become turbulent as a result. This process is known as leading-edge contamination. Modern hypersonic vehicle design tends to favor vehicles that have a blended wing body or flying wing shape which erases the possibility of having a turbulent wing root. However, this mechanism is still present for systems that have a series of control surfaces impinging on a main body, such as the fins on a missile or rocket. If this mechanism is present, one way to address it is through the use of a Gaster bump [19]. A Gaster bump will create a stagnation region which allows a fresh boundary layer to be formed. A design criterion based on momentum thickness Reynolds number can also be used to help determine whether turbulent structures along the leading edge will be self-sustaining or become dampened [20].

In the presence of a subsonic boundary layer, an inflection point in the flow profile can lead to the first-mode instability. For supersonic flow, this mechanism is instead associated with a generalized inflection point. In contrast to incompressible flow, the most unstable first-mode disturbance in supersonic flow is always oblique. It was found that by cooling the vehicle or model wall, one could stabilize the first-mode mechanism.

Once the freestream velocity for an adiabatic flat plate increases to a point where the Mach number is greater than approximately 4, the two-dimensional (2-D) second mode, or Mack mode, begins to surpass the three-dimensional first mode. The second mode is an acoustic wave that requires an embedded region of flow to be locally supersonic relative to the phase speed of the disturbance. The frequency and growth of this mechanism are highly tuned to the height of the local boundary layer and the maximum of this instability wave is

believed to occur between the vehicle wall and the relative sonic line. These acoustic waves can be stabilized by heating the vehicle wall, which results in a decrease in local relative Mach number coupled with an increase in viscosity, thickening of the boundary layer, decrease in frequency, and decrease in growth rate. Recent investigations, however, have shown Mack modes that travel at supersonic speeds relative to the freestream velocity and radiate out of the boundary layer and into the freestream [21, 22, 23]. The supersonic modes have been seen in flows with highly cooled walls and possess unique features including instabilities over a wider frequency range than their subsonic counterparts and a "slanted" wave pattern outside of the boundary layer [24].

The Görtler instability has a highly dependent and integrated relationship with the geometric shape of the surface itself. In most cases, this instability is destabilized by concave wall curvature and generates streamwise-oriented counter-rotating vortices [25], although it has also been shown to exist in the presence of a wall jet over a convex surface [26]. These vortices create a considerable distortion to the mean flow and an identifiable mushroom-shaped distribution.

When the flowfield is predominantly 3-D, the instability mechanisms most important in the transition process also tend to be 3-D. In this case, the streamlines are curved under the action of pressure gradients and wing sweep, and the resulting boundary-layer profile is twisted. This situation may lead to the development of traveling crossflow, which is a moving wave with both a frequency and a spanwise wavelength component. Additionally, the twisted boundary layer may contribute to the growth of the stationary crossflow instability. An imbalance between the centripetal acceleration and the pressure gradient within the boundary layer results in a flow component that is perpendicular to the direction of the local inviscid streamline. For incompressible flow, the combination of this flow component with the streamwise velocity results in the creation of an inflection point, which is highly unstable and a driving force in the growth of co-rotating vortices known as stationary crossflow. In compressible flows, this combination instead leads to the unstable behavior associated with

a generalized inflection point of the mass-flux profiles (figure 1.1). These co-rotating vortices are highly nonlinear in nature and may begin to distort the mean flow as they increase in amplitude. Effective ways of reducing the development of stationary crossflow involve polishing the physical surface, reducing the extent of favorable pressure gradient near the attachment line, and, to a lesser extent, utilizing suction. An additional method that has shown promising results in influencing the growth of crossflow is the use of discrete roughness elements (DREs) [27, 28]. The philosophy behind DREs is that they can be spaced in order to excite the naturally occurring most unstable wavelength or, opposingly, motivate the growth of a smaller non-optimal wavelength which can take energy away from what would have been the most amplified.

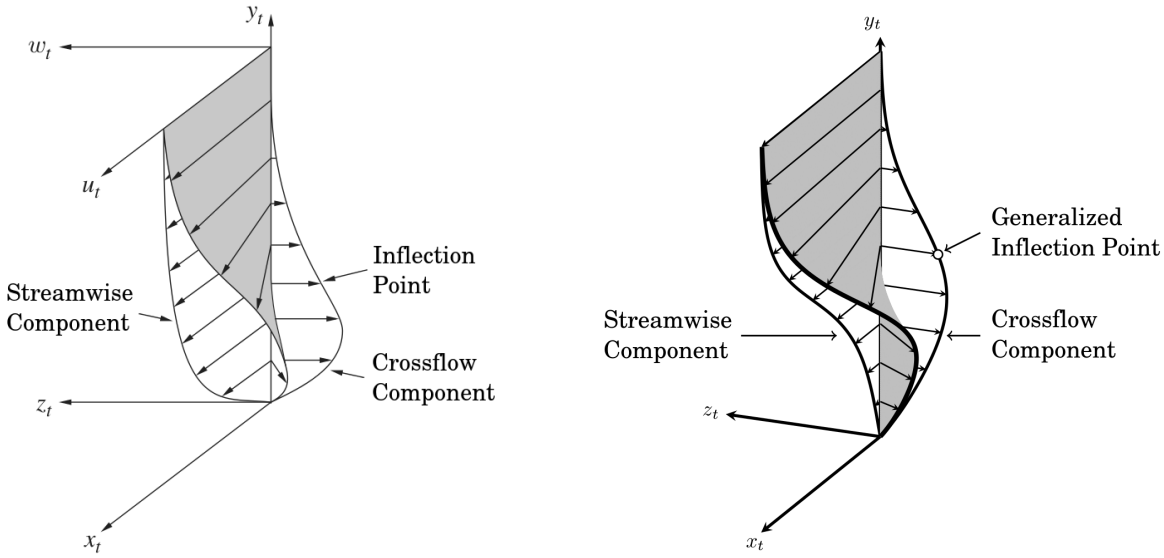

(a) Incompressible flow [29] (b) Compressible flow [1]

Figure 1.1: Diagrams of typical crossflow profiles

Unlike most of the mechanisms discussed in this section, transient growth is an instability that is non-modal in nature and grows algebraically as opposed to exponentially. This behavior tends to occur in the presence of large surface roughness or freestream turbulence.

When two non-orthogonal, stable modes interact, they may create a resultant disturbance that is unstable. The study of transient growth has become a very important aspect in the analysis of blunt bodies, such as reentry vehicles, which are inherently stable to alternative mechanisms such as streamwise instabilities and stationary crossflow [30, 31, 32].

1.4 Advancement of Stability Methods

Many of the first analysis techniques for boundary-layer stability used empirical data or formulated metrics in order to predict the behavior of various flows. The downfall of these methods is that they do not represent any physical processes. A good example of this is the transition location predicted using the parameter of $\frac{Re_\theta}{M_e}$. Reshotko [33, 34] has determined the strong influence that density, and by extension altitude, has for this quantity which might be successfully used in correlating the altitude at which a given reentry vehicle will transition. However, $\frac{Re_\theta}{M_e}$ does not provide accurate trends involving Mach number and it ignores important effects such as surface roughness, pressure gradients, and surface temperature. For cruise vehicles flying at constant altitude, this quantity is not relevant in helping to determine the x location of transition. A second example of a parameter that uses only the basic-state flowfield around a geometry to predict transition is the crossflow Reynolds number. This quantity is used for 3-D flows that are dominated by the stationary crossflow disturbance, such as on conical shapes. Reed & Haynes [35] emphasize caution when using this parameter to develop a correlation beyond the database involved in its formulation as the crossflow Reynolds number is limited in applicability on general geometries.

The advent of high speed computing allowed the stability community to find direct solutions to the formulated linear stability theories based on varying assumptions and numerical techniques. Lees & Reshotko [36] and Zaat [37] developed methods for numerical integration of the inviscid stability equations. Finite-difference methods were initially developed by Thomas [38] for use on plane Poiseuille flow who was followed shortly by Kurtz [39]. Orszag [40] used Chebyshev polynomials in order to improve upon spectral methods initially implemented by Gallagher & Mercer [41] for Couette flow. In addition, Brown and Sayre [42]

were the first to use shooting methods in their solutions. Many of the solutions computed by Mack [21] at this time compared well to the available experimental data. Mack also used his solutions to compare with the asymptotic theory developed by Lees & Lin [43] and Dunn & Lin [44]. The asymptotic theory attempted to reduce the eighth order system of equations to a sixth order system by an order of magnitude argument. Although early work provided accurate solutions for incompressible flat plate boundary layers, this was not the case above low supersonic Mach numbers, and Mack [8] concluded that the Dunn-Linn equations were not adequate for flow above M = 1.6. It wasn't until many years later that the methodologies continued to evolve, and as computing power increased, so did the capabilities of these solution methods.

Malik & Orszag [45] began the development of a code capable of computing the stability of three-dimensional compressible boundary layers. The code used matrix finite-differencing in addition to a boundary value method, differing from the initial value method utilized by Mack. Whereas the initial value approach operated using a shooting method with Runge-Kutta integration on a relatively stiff system [46], the boundary value method instead reduced the system of ordinary differential equations into a set of linear algebraic equations. Early forms of shooting methods were susceptible to the growth of parasitic error which would eventually contaminate the solution and worsened with increasing Reynolds number. To address this, Radbill and Van Driest [47] applied the method of Gram-Schmidt orthonormalization to stability problems involving boundary-layer flows. Gram-Schmidt orthonormalization purifies each integration step by creating two linearly independent solution vectors that can be combined to construct a solution that is fully free of one of the generating vectors and filters the error when the linear independence of these solutions has been destroyed [48]. The new boundary value method proved to be significantly more computationally efficient than the commonly used initial value technique, and Malik [49] gave a thorough description of the numerical schemes and procedures used to address solution accuracy and numerical stability.

Efforts were then furthered to accurately formulate and model the disturbances for com-

plex geometries. Many of the existing methods relied on empirical correlations, required extensive effort to tune specific stability parameters, ignored nonlinear effects, or consumed immense amounts of memory and processing time in order to accurately model a complex design. It also became evident that the upstream history of the instability mechanisms needed to be accounted for in order to track the growth of specific modes. Two of the assumptions that were addressed were the linearization of terms in the disturbance equations and the parallel flow approximation, both of which were initially implemented because of the practicality of solving the system of equations with limited computational resources. Linearization consisted of using a method of multiple scales argument to drop nonlinear terms with the assumption that they were small compared to other terms in the equation set while parallel flow assumed a boundary layer was locally parallel to the surface and neglected the velocity in the wall-normal direction. To this end, Herbert and Bertolotti [50, 51, 52] developed the modern parabolized stability equations, both linear (LPSE) and nonlinear (NPSE). This method takes advantage of simplifying assumptions about the flowfield in order to reduce the complexity of the equation set and solve for the growth of a disturbance along a marching path.

Linear stability theory (LST) and LPSE are extremely useful in obtaining growth rates and relative amplification as long as the instabilities remain small and behave in a linear manner. However, attempting to accurately predict boundary-layer transition using linear analysis or by creating extrapolations between tunnel experiments and flight will produce large margins of error that tend to become case dependent. Rather, the underlying physics that dominates the transition process must be understood. For computations, the goal is to be able to model the flow such that, given the same initial conditions as a flight or wind tunnel experiment, the predicted behavior will match that seen in an identical physical setting. It has become obvious that to achieve this goal, the nonlinear interactions between different modes coupled with receptivity must be examined in great detail. Nonlinear effects and modal interaction play an important, and sometimes early, role in transition and necessitate

an approach that can capture these effects. The nonlinear parabolized stability equations were formulated to address these requirements and are capable of accurately producing the evolution of different mechanisms with only a fraction of the run time and computational cost of direct numerical simulation (DNS). For hypersonic applications, EPIC and LASTRAC [53] are two of the primary codes in use that are capable of performing linear and nonlinear analysis for 2-D and 3-D flowfields, and Roache [54] provides an excellent description of the modern processes involved in validating and verifying computational solutions. New modifications continue to be added to the PSE methods allowing them to become more robust and proficient. This has led to a wide array of knowledge on a variety of variables in the stability problem including chemistry effects, curvature, nose bluntness, wavepackets, and shock effects [55, 56, 57, 58, 59, 22].

1.5 Outline

In this dissertation, sections $2-4$ will introduce the details of stability methods applied in the present research. Sections $5-6$ will then provide results centered around the second-mode instability for axisymmetric geometries in a 2-D flowfield. The final set of results is provided in sections $7-8$. Here, an analysis is performed for the multiple modes found in 3-D boundary layers, including crossflow and second mode.

2. STABILITY METHOD

Different methods may be applied to model disturbance growth within the boundary layer. This work utilizes linear stability theory and both the linear and nonlinear parabolized stability equations. Furthermore, only the spatial stability of the disturbance mechanisms will be considered.

Under a spatial stability analysis, the wavenumber components α and β are defined as complex while ω is strictly real. This signifies that the growth and amplification of disturbances can only change as they move through space rather than in time.

2.1 Governing Equations

Assuming a calorically perfect gas, the governing equations of fluid flow in a Cartesian coordinate system are comprised of the Navier-Stokes equations, conservation of energy, mass continuity, and equation of state (equations 2.1−2.4). The Navier-Stokes equations define the conservation of momentum in the x, y, and z directions.

$$\rho\left[\frac{\partial\vec{V}}{\partial t}+\left(\vec{V}\bullet\nabla\right)\vec{V}\right]=-\nabla P+\nabla\left[\lambda\left(\nabla\bullet\vec{V}\right)\right]+\nabla\bullet\left[\mu\left(\left(\nabla\vec{V}\right)+\left(\nabla\vec{V}\right)^{T}\right)\right] \tag{2.1}$$

$$\begin{aligned}\rho c_p\left[\frac{\partial T}{\partial t}+\left(\vec{V}\bullet\nabla\right)T\right]=&\nabla\bullet(\kappa\nabla T)+\frac{\partial P}{\partial t}+\left(\vec{V}\bullet\nabla\right)P+\lambda\left(\nabla\bullet\vec{V}\right)^{2}\\&+\frac{\mu}{2}\left[\left(\nabla\vec{V}\right)+\left(\nabla\vec{V}\right)^{T}\right]^{2}\end{aligned} \tag{2.2}$$

$$\frac{\partial\rho}{\partial t}+\nabla\bullet\left(\rho\vec{V}\right)=0 \tag{2.3}$$

$$P=\rho R_g T \tag{2.4}$$

2.1.1 Viscosity

All computations in the present study will assume air as a calorically perfect gas and use Sutherland's law to calculate the values for dynamic viscosity (μ). Since it is important that variables in a basic-state flowfield match those in the corresponding stability calculations, this formulation is applied in both the steady-state flow solver and EPIC stability code. Equation 2.5 shows Sutherland's law and defines the associated constants.

$$\mu = \frac{C_1 T^{3/2}}{T + S_\mu}$$

$$C_1 = \frac{\mu_{ref}}{{T_{ref}}^{3/2}} \left(T_{ref} + S_\mu\right) \tag{2.5}$$

$$S_\mu = 110.556 \text{ K}, \qquad T_{ref} = 273.111 \text{ K}, \qquad \mu_{ref} = 1.716 \times 10^{-5} \left(\frac{\text{kg}}{\text{m} \cdot \text{s}}\right)$$

2.2 Curvature

Since a PSE solution is found along a specified path, stability calculations are performed in a local coordinate system that is aligned with the direction of marching. Additionally, most flight vehicle or model surfaces will not be perfectly flat. To account for surface curvature effects, the coordinate system is transformed into curvilinear coordinates where the metrics h_1, h_2, and h_3 represent the curvature in the ξ, η, and ζ directions, respectively [7]. Curvature terms are defined in equation 2.6

$$h_{1,3} = \frac{\partial\xi + \frac{y \cdot \partial\xi}{R}}{2R \cdot \sin\left(\frac{\partial\xi}{2R}\right)} \tag{2.6}$$

where y is the wall-normal distance of each grid point away from the surface, R is the local radius, and $\partial\xi$ is the constant streamwise step size along a path. Physically, these metrics represent a ratio of the surface distance between two points along a curved geometry versus the straight-line distance. If the surface is flat, then these distances are equal and the metric

coefficient reduces down to a value of 1. The h_2 metric corresponds to the wall-normal grid and thus does not have curvature. In the present formulation, this means that $h_2 = 1$ everywhere in the equation set. Note that the current derivation breaks down as $R \to 0$. This is not a significant concern, however, as this will only occur if the surface approaches a singularity.

2.3 Disturbance Equations

Once the governing equations have been transformed into a curvilinear coordinate system, the full set of disturbance equations can be formulated. To begin, a generic disturbance is considered by decomposing the flow variables into a steady basic-state quantity, which represents the flow that exists in the absence of any environmental disturbances or forcing, plus a disturbance. This formulation is shown in equation 2.7. In addition, it is assumed that the basic state is a solution to the governing equations of motion. Substituting equation 2.7 into the governing equations and subtracting terms defined solely by basic-state quantities yields the disturbance equations. Each stability method considers a different solution form of the disturbance.

$$\begin{aligned} \phi\left(\xi,\eta,\zeta,t\right) &= \underbrace{\bar{\phi}\left(\tilde{\xi},\eta\right)}_{\text{basic state}} + \underbrace{\phi'\left(\xi,\eta,\zeta,t\right)}_{\text{disturbance}} \\ \phi &= \left[u,v,w,T,\rho\right]^T \end{aligned} \tag{2.7}$$

Finally, a single matrix representation can be assembled by combining the aforementioned system of individual disturbance equations. This final form is presented as

$$\begin{aligned} \mathcal{B}_0\frac{\partial\phi'}{\partial t} + \mathcal{B}_1\frac{\partial\phi'}{\partial\xi} + \mathcal{B}_2\frac{\partial\phi'}{\partial\eta} + \mathcal{B}_3\frac{\partial\phi'}{\partial\zeta} + \mathcal{C}_1\frac{\partial^2\phi'}{\partial\xi^2} + \mathcal{C}_2\frac{\partial^2\phi'}{\partial\eta^2} + \mathcal{C}_3\frac{\partial^2\phi'}{\partial\zeta^2} \\ + \mathcal{D}_1\frac{\partial^2\phi'}{\partial\xi\partial\eta} + \mathcal{D}_2\frac{\partial^2\phi'}{\partial\xi\partial\zeta} + \mathcal{D}_3\frac{\partial^2\phi'}{\partial\eta\partial\zeta} + \mathcal{F}_0\phi' = \mathcal{N}\mathcal{L} \end{aligned} \tag{2.8}$$

where $\mathcal{B}_0$, $\mathcal{B}_1$, $\ldots\mathcal{F}_0$ are (5×5) matrices filled strictly with basic-state values. All linear

terms reside on the left side of the equation while nonlinear terms form a (5×1) vector and are represented as $\mathcal{NL}$.

Solving equation 2.8 for external fluid flows requires the specification of boundary conditions at the geometry surface and in the freestream. Conceptually, we expect the no-slip condition at the wall to drive all velocity components to zero, including the disturbance quantities. Additionally, a perturbation should asymptotically decay as it approaches the freestream, except in very specific situations. The applied homogeneous boundary conditions are shown in equation 2.9.

$$\begin{aligned} \eta = 0: \quad & \begin{cases} u' = v' = w' = T' = 0 \\ u' = v' = w' = \frac{\partial T'}{\partial \eta} = 0 \end{cases} \\ \eta \to \infty: \quad & \begin{cases} u' = v' = w' = T' = \rho' = 0 \\ \frac{\partial u'}{\partial \eta} = \frac{\partial v'}{\partial \eta} = \frac{\partial w'}{\partial \eta} = \frac{\partial T'}{\partial \eta} = \frac{\partial \rho'}{\partial \eta} = 0 \end{cases} \end{aligned} \tag{2.9}$$

Any perturbation with a frequency component must remain at the mean wall temperature at the surface and hold $T' = 0$. For stationary disturbances, such as stationary crossflow, this temperature condition can be replaced with $\frac{\partial T'}{\partial \eta} = 0$ [8]. Either of the two sets of freestream boundary conditions are a valid option for stability calculations. The current work applies the freestream conditions based on disturbance derivative as this tends to provide a smoother and clearer mode shape when analyzing hypersonic flow.

2.3.1 Linear Stability Theory

LST has been the most widely used approximate method for stability analysis in the aerospace community. In this approach, the basic state is assumed "locally parallel" so that the wall-normal velocity is set to zero, the flow quantities are functions of the wall-normal direction only, $\bar{\phi}(\eta)$, and disturbance amplitude is small so that nonlinear terms may be neglected. A separable solution may be sought which results in a disturbance of the normal-mode form

$$\phi'(\xi,\eta,\zeta,t) = \hat{\phi}(\eta)\, e^{i(\alpha\xi+\beta\zeta-\omega t)} + c.c. \tag{2.10}$$

whose stability is described by a local generalized eigenvalue problem. Values for ω, β_r, and β_i are specified in order to solve for α_r and α_i. The entire growth of each disturbance is assigned to the imaginary part of α, and it is assumed that no growth occurs in the spanwise direction ($\beta_i = 0$). Different components of the wave equation also describe physical attributes of the disturbance such as phase speed and wave angle (equation 2.11).

$$\psi = \tan^{-1}\left(\frac{\beta_r}{\alpha_r}\right) \quad \text{and} \quad c = \frac{\omega}{\sqrt{\alpha_r^2+\beta_r^2}} \tag{2.11}$$

Equation 2.10 is the result of utilizing a Fourier transform in the ξ and ζ directions and a Laplace transform in time. The presence of a complex disturbance shape function requires the addition of the complex conjugate ($c.c.$) to create a disturbance ϕ' that is real. After substituting equation 2.10 into equation 2.8 and implementing all LST assumptions, the stability equation is reduced to equation 2.12.

$$\mathcal{A}\frac{\partial^2\hat{\phi}}{\partial\eta^2} + \mathcal{B}\frac{\partial\hat{\phi}}{\partial\eta} + \mathcal{C}\hat{\phi} = 0 \tag{2.12}$$

At this stage, $\mathcal{A}$, $\mathcal{B}$, and $\mathcal{C}$ are a set of (5×5) matrices containing only linear terms for each wall-normal point. In the case of cones and other highly curved bodies, the surface curvature terms play a significant role and will therefore be retained in the LST analysis. Appendix B fully describes the components of these linear matrices.

Each LST solution will provide the local growth rate of a disturbance at a single axial location. For linear calculations along a path, the size of a disturbance is generally provided in terms of the natural logarithm of the amplitude ratio with respect to the neutral stability point or initialization point. This relation is commonly referred to as the N-factor. When first introduced for LST, only growth rates were accounted for as shown in equation 2.13. The current work, instead, uses LST to initialize all PSE calculations by providing the solution

at the first marching step.

$$N = \ln\left(\frac{A}{A_0}\right) = \int_{\xi_0}^{\xi} -\alpha_i \partial\xi \tag{2.13}$$

2.3.1.1 Eigenvalue Solution

By applying finite difference methods, the governing system of coupled partial differential equations can be simplified to a system of algebraic equations. Boundary conditions are applied to the first and last wall-normal grid points, setting up a system that can be solved for the unknown complex eigenvalue α. The corresponding eigenvector $\hat{\phi}$ is comprised of five variables for each wall-normal location. Since the system contains nonlinear terms with respect to α, the eigenvector is expanded to the form seen in equation 2.14.

$$\hat{\Phi}_j = \begin{bmatrix} \hat{u}_j \\ \hat{v}_j \\ \hat{w}_j \\ \hat{T}_j \\ \hat{\rho}_j \\ \alpha\hat{u}_j \\ \alpha\hat{v}_j \\ \alpha\hat{w}_j \\ \alpha\hat{T}_j \end{bmatrix} \tag{2.14}$$

The generalized eigenvalue problem can now be solved as

$$\mathbf{A}\hat{\Phi} = \alpha\mathbf{B}\hat{\Phi} \tag{2.15}$$

where $\mathbf{A}$ and $\mathbf{B}$ are $(9N_y \times 9N_y)$ matrices and $\hat{\Phi}$ is a $(9N_y \times 1)$ vector. All α terms are set to zero in the development of matrix $\mathbf{A}$ while matrix $\mathbf{B}$ contains only terms with α and α^2 coefficients. This eigenvalue problem is typically solved by either using the direct QZ

algorithm, which will provide the complete spectrum of $9N_y$ results, or the iterative Arnoldi method, which provides a reduced set of results centered around an initial guess. Regardless of which method is used, many of the resulting solutions will be spurious and must be removed in order to select the desired mode. Filtering the unwanted modes is performed by cycling through a series of increasingly strict criteria based on physical attributes of the disturbance mechanisms. Examples of these filters include the use of phase speed (c), wave angle (ψ), and number of zero crossings, among others. A high number of zero crossings produces sources of shear that typically remove energy from the disturbance, and the objective of the current study is to analyze the unstable instabilities.

2.3.2 Linear Parabolized Stability Equations

Excellent introductions to the PSE method and summary of its initial development were provided by Herbert [60]. During the early stages of both LPSE and NPSE, much was established related to basic marching procedures, curvature, normalization conditions, and numerical stability of the method itself [51, 52, 61, 62, 63, 64]. In a relatively short time, the field rapidly expanded to include complex geometries, compressible flow, and finite-rate thermodynamics [22, 53, 64, 65, 66, 67, 68, 69, 70, 71, 72, 73].

Similar to LST, the evolution of disturbances in the boundary layer is described using the disturbance equations that are obtained by decomposing the total flow into a basic state plus a disturbance and assuming that the basic state is a solution to the original equations of motion. LPSE, however, removes the parallel flow assumption and becomes a marching solution that incorporates the upstream history of the disturbance. Simplifying assumptions are imposed to take advantage of the properties of the basic-state flowfield. First, the basic state quantities are assumed to vary slowly in the marching direction, $\bar{\phi}\left(\tilde{\xi}, \eta\right)$, with slow variable $\tilde{\xi} = \frac{\xi}{Re}$. In addition, the flowfield is assumed to be spanwise invariant. This enables the disturbance to be separated into the product of a slowly varying shape function and a rapidly varying wave function. Each disturbance quantity is transformed spectrally in the ζ direction and in time such that it is periodic in these dimensions. Equation 2.16

shows the disturbance form for LPSE where $\alpha\left(\tilde{\xi}\right)$ is the slowly varying complex streamwise wavenumber.

$$\phi'\left(\xi,\eta,\zeta,t\right) = \underbrace{\hat{\phi}\left(\tilde{\xi},\eta\right)}_{shape}\underbrace{e^{i\left(\int\alpha\left(\tilde{\xi}\right)\partial\xi+\beta\zeta-\omega t\right)}}_{wave}+c.c. \tag{2.16}$$

The presence of a streamwise viscous term allows disturbances to be diffused upstream while, more importantly, the inviscid convection term in the streamwise direction allows acoustic waves to potentially propagate upstream [61]. In order to address the elliptic behavior of the disturbance equation, the ellipticity is retained for the wave part while a parabolization is applied to the shape function through a scaling analysis that truncates second derivatives of the shape functions with respect to ξ, which are $\mathcal{O}\left(\frac{1}{Re^2}\right)$. Additionally, the remaining ellipticity can be accounted for through the use of a minimum step size criteria [63] which allows the marching solution to essentially "step over" this upstream influence.

The above decomposition results in an ambiguity in growth between the shape and amplitude functions. A condition is imposed which absorbs the exponential growth into the fast varying wave function, resulting in a shape function $\hat{\phi}$ which varies slowly in the ξ direction. To ensure that the shape function is progressing properly in the streamwise direction, a normalization condition is applied. The current work applies equation 2.17 as the normalization condition for LPSE and NPSE. Once the magnitude of the complex error is less than a specified tolerance, the solution at the current step is considered converged, and a marching step is taken.

$$\frac{\int_0^\infty\left(\hat{u}^\dagger\frac{\partial\hat{u}}{\partial\xi}+\hat{v}^\dagger\frac{\partial\hat{v}}{\partial\xi}+\hat{w}^\dagger\frac{\partial\hat{w}}{\partial\xi}+\hat{T}^\dagger\frac{\partial\hat{T}}{\partial\xi}+\hat{\rho}^\dagger\frac{\partial\hat{\rho}}{\partial\xi}\right)d\eta}{max\left(\hat{\phi}\cdot\hat{\phi}^\dagger\right)} = err_r + ierr_i \tag{2.17}$$

It is important to note that $\hat{\phi}_{(n,k)}$ represents five distinct variables $\Big[\hat{u}_{(n,k)}, \hat{v}_{(n,k)}, \hat{w}_{(n,k)}, \hat{T}_{(n,k)}, \hat{\rho}_{(n,k)}\Big]$, whereas $\alpha_{(n,k)}$ can only be refined by one single quantity. Instead of trying to isolate and select the most crucial term, all five terms are combined. This ensures that all aspects of

the flow are evolving downstream as they should. A Pythagorean normalization parameter [7] is applied to the solution condition so that modes comprised of very small magnitudes do not bypass the tolerance.

Substituting the LPSE disturbance from equation 2.16 into equation 2.8 and removing all $\frac{\partial^2}{\partial \xi^2}$ terms results in the LPSE stability equations.

$$\mathcal{A}\frac{\partial^2 \hat{\phi}}{\partial \eta^2} + \mathcal{B}\frac{\partial^2 \hat{\phi}}{\partial \xi \partial \eta} + \mathcal{C}\frac{\partial \hat{\phi}}{\partial \eta} + \mathcal{D}\frac{\partial \hat{\phi}}{\partial \xi} + \mathcal{E}\hat{\phi} = 0 \tag{2.18}$$

The (5×5) matrices $\mathcal{A}$, $\mathcal{B}$, $\mathcal{C}$, $\mathcal{D}$, and $\mathcal{E}$ are linear, and the evolution of $\alpha\left(\tilde{\xi}\right)$ is determined iteratively for the LPSE solution at each marching step. Details of the matrices are provided in appendix C.

First-mode, Mack-mode, and crossflow instabilities in a 3-D boundary layer are analyzed by marching along a predetermined path. For LPSE, a single mode is marched and nonlinear interactions are neglected. Unlike LST, LPSE calculations require the inclusion of the disturbance shape function in the evaluation of disturbance amplification. Additionally, experiments performed in supersonic and hypersonic flow typically measure and provide disturbance amplitudes with respect to mass flux. N-factors based on variables associated with mass flux are of the form seen in equation 2.19.

$$N = max\left[e^{i\int \alpha_i \partial \xi}\sqrt{\left(\bar{\rho}\hat{u}_r + \bar{u}\hat{\rho}_r\right)^2 + \left(\bar{\rho}\hat{u}_i + \bar{u}\hat{\rho}_i\right)^2}\right] \tag{2.19}$$

A point of emphasis of the current work will be the validation of EPIC with multiple hypersonic wind tunnels. Therefore, all N-factors will be provided using the derivation presented in equation 2.19.

2.3.3 Nonlinear Parabolized Stability Equations

The NPSE formulation is an efficient and powerful tool for studying the stability and transition of advection-dominated laminar flows in that it includes curvature, nonparallel, and nonlinear effects at a fraction of the resources required for DNS. This is important

when analyzing disturbances such as stationary crossflow which is an inviscid instability that experiences early nonlinear effects.

Numerous efforts in the community have validated and verified NPSE over a range of operating conditions and geometries. Reed et al. [74] provides a list of articles. With appropriate modeling of the operating and disturbance input conditions, remarkable agreement has been obtained among theory, computations, and experiments.

Like LPSE, the disturbances in the NPSE formulation consists of a slowly varying shape function and rapidly varying wave component. However, multiple modes can now be solved simultaneously. The representation of NPSE disturbances is provided in equation 2.20

$$\phi'(\xi,\eta,\zeta,t) = \sum_{n=-\infty}^{\infty}\sum_{k=-\infty}^{\infty} \frac{A_{0_{(n,k)}}}{2} \underbrace{\hat{\phi}_{(n,k)}\left(\tilde{\xi},\eta\right)}_{shape} \underbrace{e^{i\left(\int \alpha_{(n,k)}\left(\tilde{\xi}\right)\partial\xi + k\beta\zeta - n\omega t\right)}}_{wave} \tag{2.20}$$

where each element of the series represents a distinct mode and $A_{0_{(n,k)}}$ is the total initial amplitude of an individual disturbance. The subscripts n and k correspond to integer multiples of the primary disturbance frequency and spanwise wavenumber, respectively, with each mode having its own unique combination. Note that in practice, this infinite sum is truncated at the specified number of harmonics. In order for the disturbances to have a physical meaning, the resulting quantities must also be real. This is done by combining a mode (n,k) with its complex conjugate $(-n,-k)$. Half of the initial amplitude $A_{0_{(n,k)}}$ is applied to both a mode and its complex conjugate so that the resulting sum is equal to the total amplitude of the disturbance. Mean flow distortion, designated as $(0,0)$, has no complex conjugate and thus must be treated uniquely. Due to the statute that all disturbances must be real, a corollary is established that the shape function $\hat{\phi}_{(0,0)}$ must be completely real while $\alpha_{(0,0)}$ must be completely imaginary.

Applying harmonic balancing to identify nonlinear modal interactions and inserting equation 2.20 into equation 2.8 produces the system of NPSE stability equations

$$\sum_{n=-\infty}^{\infty}\sum_{k=-\infty}^{\infty}\left[\mathcal{A}\frac{\partial^2\hat{\phi}}{\partial\eta^2}+\mathcal{B}\frac{\partial^2\hat{\phi}}{\partial\xi\partial\eta}+\mathcal{C}\frac{\partial\hat{\phi}}{\partial\eta}+\mathcal{D}\frac{\partial\hat{\phi}}{\partial\xi}+\mathcal{E}\hat{\phi}\right]_{(n,k)} \\ \frac{A_{0_{(n,k)}}}{2}e^{i\left(\int\alpha_{(n,k)}\left(\tilde{\xi}\right)\partial\xi+k\beta\zeta-n\omega t\right)}=\mathcal{NL}_{(n,k)} \tag{2.21}$$

where the matrix operators on the left side of the equation are the same as those used for LPSE. Through this formulation, each mode is provided its own set of equations. The $\mathcal{NL}$ terms are of the form shown in equation 2.22

$$\begin{aligned}\mathcal{NL}_{(n,k)}=&\sum_{n_1}\sum_{n_2}\sum_{k_1}\sum_{k_2}\frac{1}{4}A_{0_{(n_1,k_1)}}A_{0_{(n_2,k_2)}}NL^{quad}_{(n,k)} \\ &e^{i\int\left[\alpha_{(n_1,k_1)}\left(\tilde{\xi}\right)+\alpha_{(n_2,k_2)}\left(\tilde{\xi}\right)\right]\partial\xi}e^{i[(k_1+k_2)\beta\zeta-(n_1+n_2)\omega t]} \\ &+\sum_{n_1}\sum_{n_2}\sum_{n_3}\sum_{k_1}\sum_{k_2}\sum_{k_3}\frac{1}{8}A_{0_{(n_1,k_1)}}A_{0_{(n_2,k_2)}}A_{0_{(n_3,k_3)}}NL^{cubic}_{(n,k)} \\ &e^{i\int\left[\alpha_{(n_1,k_1)}\left(\tilde{\xi}\right)+\alpha_{(n_2,k_2)}\left(\tilde{\xi}\right)+\alpha_{(n_3,k_3)}\left(\tilde{\xi}\right)\right]\partial\xi}e^{i[(k_1+k_2+k_3)\beta\zeta-(n_1+n_2+n_3)\omega t]}\end{aligned} \tag{2.22}$$

where integer values n_1, n_2, n_3 and k_1, k_2, k_3 span from $-\infty$ to ∞. Harmonic balancing also ensures that the integer sum of modes defining the quadratic and cubic terms produces a phase speed that matches the linear terms on the left-hand side of equation 2.21. Numerically, this is represented as $n_1+n_2+(n_3)=n$ and $k_1+k_2+(k_3)=k$ where the values in parentheses are only included for cubic terms. For example, modes defined by an (n,k) combination of $(1,-1)$ and $(0,1)$ can interact with a $(1,0)$ mode. As a result, the system of equations for each individual mode gets coupled with the other specified modes through the nonlinear terms. A full description of nonlinear matrix inputs is detailed by Oliviero [7].

Unlike the previously described linear methods which assume infinitesimally small amplitudes, NPSE yields finite-amplitude disturbances. These amplitude quantities can be provided using any combination of the primitive variables. Equation 2.23 shows the method used to calculate the maximum u-amplitude of a single mode.

$$u'_{max}(\xi) = max\left[\frac{A_0}{2}\hat{u}\left(\tilde{\xi},\eta\right)e^{i\int\alpha(\tilde{\xi})\partial\xi} + \frac{A_0^{\dagger}}{2}\hat{u}^{\dagger}\left(\tilde{\xi},\eta\right)e^{-i\int\alpha^{\dagger}(\tilde{\xi})\partial\xi}\right] \tag{2.23}$$

2.4 EPIC

EPIC [7], developed within the CST laboratory at Texas A&M, upholds the "spanwise uniform" or "quasi 3-D" assumption. That is, a fully 3-D boundary layer along an arbitrary path may be considered, but the flow is assumed to be uniform in the direction perpendicular to the marching path at each location. The stability code is written in a general orthogonal curvilinear coordinate system and accounts for the curvatures of a generic 3-D geometry. LPSE considers only a single monochromatic wave. For NPSE, harmonic balancing is used to identify nonlinear modal interactions, which are iteratively converged, and $\alpha_{(n,k)}$ for each mode is independently refined with the above method. The present work holds Prandtl number (Pr) and $\gamma = \frac{c_p}{c_v}$ constant (c_p and c_v are constant). Additionally, a linear relationship between the second viscosity coefficient $\left(\bar{\lambda}_v\right)$ and dynamic viscosity ($\bar{\mu}$) is assumed, while perturbations of the thermodynamic quantities are formed by applying a Taylor expansion.

Studying the evolution of instabilities by way of either LST or PSE requires a path along which to march as well as a model of the evolution of the spanwise wavenumber along that path. Section 3 talks about the process of determining the appropriate marching path and then acquiring the basic-state data along that path for the stability analysis. Section 4 then discusses the treatment of spanwise wavenumber and how to properly model its evolution along a geometry.

3. BASIC-STATE DATA EXTRACTION*

As mentioned previously, the PSE methods are marching schemes and thus require a path to march along. In the past, obtaining data along this path was a very cumbersome and time consuming procedure. An external grid was first generated with a Fortran script and imported into Tecplot 360, which is a computational fluid dynamics (CFD) visualization and analysis software used for post-processing flow solver data. The Fortran script contained many variables that defined the geometry, number of axial and wall-normal points, axial grid spacing, growth parameters for the spacing of wall-normal points, and potentially path direction. Additionally, the wall-normal distance between the geometry surface and shock typically varied in an irregular fashion so the mesh was often separated into multiple segments where variables were assigned unique values for each segment. Constants for all of these variables were manually iterated upon until a satisfactory mesh was finally created.

Data was then acquired along the generated mesh by using the interpolation schemes internal to Tecplot. An issue emerged from this practice at the geometry surface if the first point of each wall-normal line was seen to be slightly off of the wall or if off-wall points were used in the interpolation of values. In this instance, the newly interpolated velocity components at the wall would be non-zero. A manual adjustment was applied to these velocity values after the interpolation to ensure that the no-slip condition was satisfied at the wall.

The above procedure had to be repeated for each path and became extremely tedious when acquiring paths from geometries of different sizes, geometries with vastly different flowfields, and especially when obtaining paths that turned as they progressed through a 3-D flowfield. In order to improve the method of data collection, a code has been developed

*Portions of this section are reprinted from "EPIC: NPSE Analysis of Hypersonic Crossflow Instability on Yawed Straight Circular Cone" by Nicholas B. Oliviero, Travis S. Kocian, Alexander J. Moyes, Helen L. Reed, 2015. *AIAA 2015-2772*, Copyright 2015 by Nicholas Oliviero, Travis Kocian, Alexander Moyes, Helen Reed.

that extracts from the basic state all of the necessary information required for EPIC to perform a stability analysis. For a standard PSE computation, this includes a combination of flow variables and geometric features. The global downstream spatial coordinate x, wall-normal distance of points from the surface, relative distance from the downstream oriented x-axis, and radii of curvature in the marching and spanwise directions represent the geometric components of the extracted data. These terms are used to define the mapping of data to a wall clustered computational normal grid. Additionally, a combination of the procured variables generates the required curvature terms for the stability equations. The remaining components necessary for an EPIC stability calculation include the primitive flow variables $\bar{u}$, $\bar{v}$, $\bar{w}$, $\bar{\rho}$, and $\bar{T}$.

The data extraction code requires a structured dataset with indices oriented such that the i-coordinate is downstream, j-coordinate is off-wall, and k-coordinate is in the spanwise direction. This orientation allows the algorithm to take advantage of the structure of the dataset and search through large volumes of data in an efficient and optimal manner.

3.1 Data Preparation

Once the basic-state solver, in this case the Data Parallel Line Relaxation (DPLR) NASA CFD code [75], has finished producing a flowfield solution, the necessary variables need to be exported to one or more data files. These variables include the global coordinates (x, y, z), structured grid indices (i, j, k), velocity components ($\bar{u}$, $\bar{v}$, $\bar{w}$), density, and temperature. Grids are commonly generated using multiple zones, and each zone to be used in the eventual stability analysis will need to be included. The preparation code is capable of handling zones that divide the geometry in both the i-coordinate and k-coordinate directions.

Separate azimuthal or spanwise zones within each i-coordinate tier are joined, and duplicate points at the zone intersections are identified and removed. The k-index is also adjusted to span from $k = 1$ to $k = k_{max}$ for the full geometry, rather than each zone having its own maximum value. After this process is completed, the remaining axial tiers are joined, and an identical adjustment is applied to the i-coordinate to accommodate for the presence of zone

intersections. All zones are now in the form of a single matrix with dimensions of $(n \times 11)$ where n is the total number of points in the flowfield. The reconstruction process is outlined in figure 3.1.

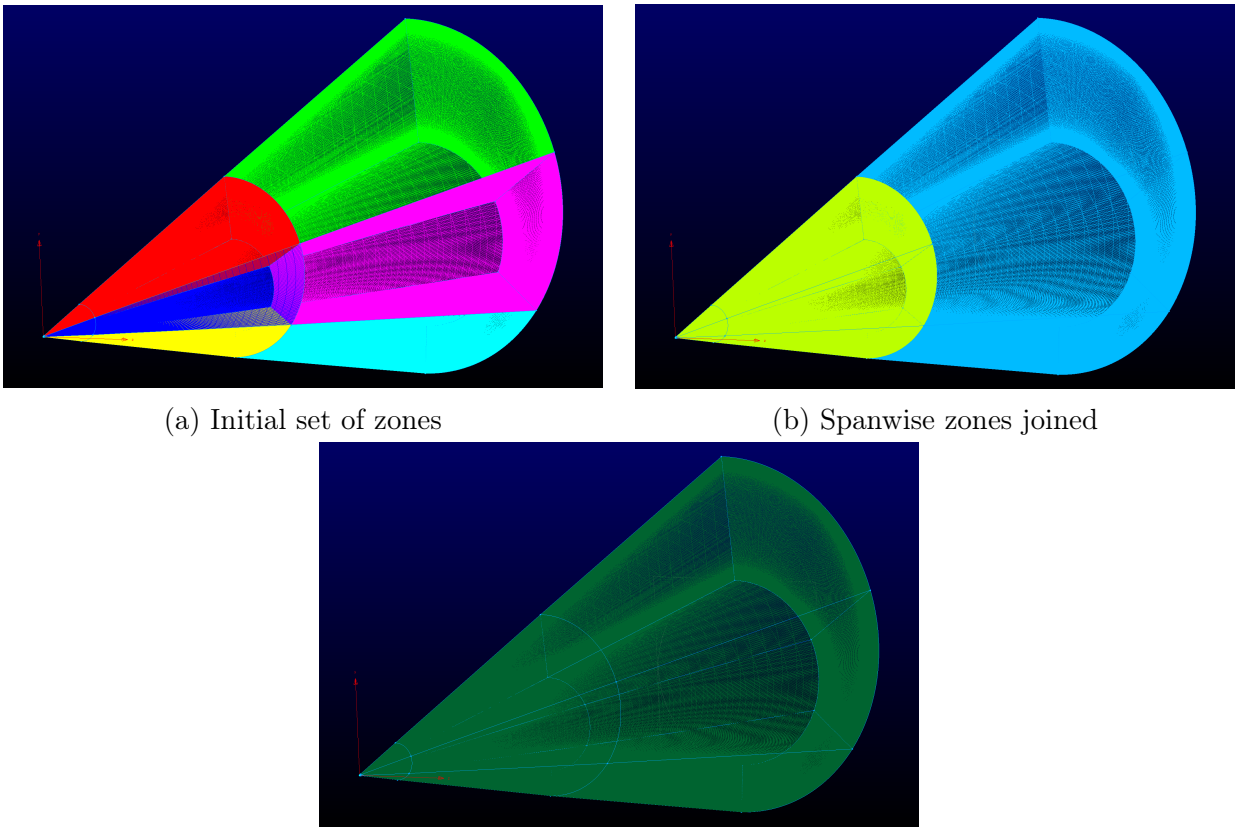

(a) Initial set of zones

(b) Spanwise zones joined

(c) All zones joined

Figure 3.1: Order for combination of basic-state datasets

It is important to arrange the data into a structure that enables paths to be obtained in a practical time frame. Many fully resolved 3-D flowfields, including those utilized in the present work, can have $\mathcal{O}(10^8)$ cells. To address this, a pattern is created that organizes the combined dataset matrix so that, as one progresses through the rows of the matrix, the points move along the k-coordinate, then the j-coordinate, and finally the i-coordinate. The resulting row location for each point in the final flowfield matrix is provided in equation 3.1.

$$Row = (i-1) \cdot j_{max} \cdot k_{max} + (j-1) \cdot k_{max} + k \tag{3.1}$$

Using this structure allows any point to be instantly selected simply by using its uniquely assigned set of grid indices. The preparation procedure only needs to be executed once for each basic state. Afterwards, any number of paths can be extracted for an ensuing stability analysis.

3.2 Surface Proximity

The data extraction process marches along the surface of a geometry with constant step size and can follow a variety of different disturbance paths types. To begin, a local cloud of surface points very near the current surface location is defined. A combination of index and physical distance is used in order to guarantee that, regardless of whether the local grid spacing is very small or very large with respect to the chosen step size, there are always a sufficient number of surrounding points to define the local environment. Operations are performed on this reduced area of data in order to further accelerate computational run time.

In order to obtain values from neighbors with defined quantities, one first needs to know which cell the current location resides in and which points surround it. Retrieving this information is achieved by finding the closest basic-state point and all points that were directly connected. This means that if the closest point has indices (i, 1, k), then the current surface marching location must exist within the cells defined by ($i \pm 1$, 1, $k \pm 1$). Opposite corners of the group of cells representing all possible locations are then connected by straight lines. These lines are projected onto a common plane in addition to the current marching location. Figure 3.2 shows an example of this procedure. With all points now defined by the same plane, the winding number (A.1) for each potential cell is computed until the surrounding surface points are identified. If the situation arises that the marching location lies directly between two surface points, then only these two points need to be identified. This holds true for all cases for which a point of interest is directly in line with

two points in the flowfield. Operations involving the interpolation of quantities from four points of a surrounding cell are reduced to a straightforward linear interpolation of the two in-line points, greatly simplifying the acquisition of data for that location.

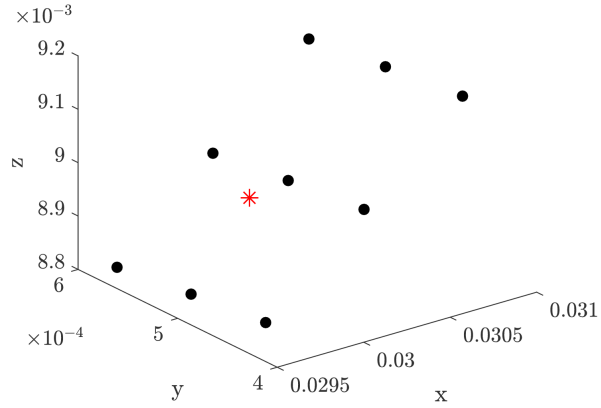

(a) Initial set of points and current location (∗)

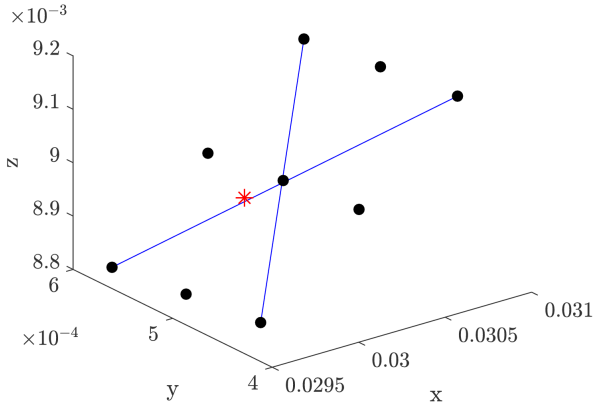

(b) Lines used to created projected plane

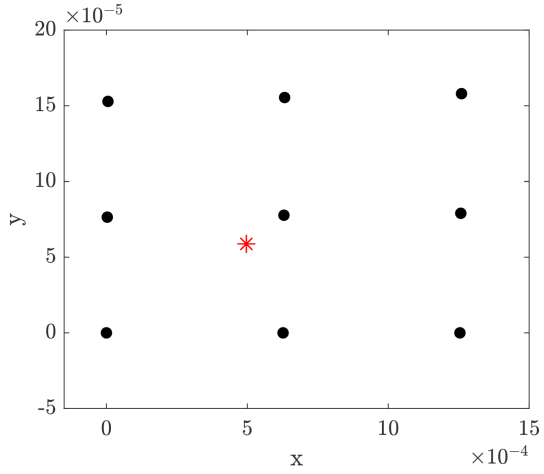

(c) All points after projection

Figure 3.2: Projecting data points to common plane

3.2.1 Flow Variable Acquisition

EPIC requires off-wall data at each step to populate a line that is normal to the geometry surface. As such, information about the flowfield is provided in a matching format. A wall-

normal line is generated using information gathered from the points defining the cell around the marching location. Line segments are created from neighboring points along constant i-coordinates and constant k-coordinates for each point of the cell. Three-point sets defining the line segments are rotated to lie on the $x - y$ plane, and a quadratic function is fit to the sets along each constant coordinate. An analytical derivative of the quadratic function provides slopes at each point, forming wall tangents in the i and k directions (equation 3.2). Performing a cross product of the tangent lines results in wall-normal lines for each point of the surrounding cell.

$$
\begin{gathered}
y = ax^2 + bx + c \\
\frac{dy}{dx} = 2ax + b \\
\begin{bmatrix} {x_1}^2 & x_1 & 1 \\ {x_2}^2 & x_2 & 1 \\ {x_3}^2 & x_3 & 1 \end{bmatrix} \begin{bmatrix} a \\ b \\ c \end{bmatrix} = \begin{bmatrix} y_1 \\ y_2 \\ y_3 \end{bmatrix} \qquad \text{and} \qquad slope = \begin{bmatrix} 1 & \frac{dy}{dx} & 0 \end{bmatrix}
\end{gathered}
\tag{3.2}
$$

Acquiring data at the point of interest on the surface requires an interpolation of nearby quantities. The interpolation scheme needed to be sufficiently robust to operate on skewed cell shapes while maintaining a high level of accuracy. To this end, a general 2-D linear interpolation technique (A.2), based on bilinear interpolation, is implemented on the 3-D slopes of the four cell wall-normal lines, providing the necessary normal line at the marching location.

From here, obtaining data along the wall-normal line is done by simply combining the aforementioned methods of winding number and 2-D interpolation. In an effort to reduce the user input required to operate the extraction code, the resolution and point distribution along a wall-normal line is determined automatically by the architecture of the original grid used in the basic-state computation. By looping through all of the grid j-coordinates, "levels" or "surfaces" of data with identical j-index are isolated in the off-wall direction. Winding numbers are once again computed for each local selection of cells in order to de-

termine which cell the wall-normal line passes through. Each normal line is ended at the location which intersects the plane of cells associated with j_{max} so that the interpolation of values will always be confined to within the basic-state flowfield. Distributing the points in this manner produces a spacing that mimics the resolution and accuracy of the original basic state. The final wall-normal profile is completed by interpolating flow values to each of these j-coordinate locations and rotating the velocity components such that $\bar{u}$ aligns with the direction of marching, $\bar{v}$ is wall normal, and $\bar{w}$ is perpendicular to the other two components. Since each plane of data is its own entity and does not rely on information from the j-coordinate above or below it, the process of locating the wall-normal intersection and interpolating values at each j-index plane is performed in parallel.

3.2.2 Vortex Paths

A variety of marching paths, based on different properties of the flow, can be extracted for use in a stability analysis. Most commonly, inviscid streamlines are used as representative disturbance paths for Mack modes, stationary and traveling crossflow, and so forth. For the stationary crossflow instability, a method has been devised which uses the mass flux of the basic-state quantities. Originally inspired by Kuehl et al. [71], the current method physically aligns the crossflow vortex paths such that the generalized inflection point, $\frac{\partial}{\partial \eta}\left(\bar{\rho}\frac{\partial \bar{w}}{\partial \eta}\right) = 0$, occurs at $\bar{\rho}\bar{w} = 0$. Here, $\bar{w}$ is the velocity component in the direction tangent to the surface and perpendicular to the marching direction. This will be referred to as the inflection-point method. The exciting part of this method is that the direction of marching is predicted solely from the undisturbed basic-state profiles of a 3-D geometry prior to doing a stability analysis. Figure 3.3 shows the result of using the inflection-point method, with $\bar{u}$ being the velocity component along the marching direction. Shown also are the $\bar{w}$ distributions perpendicular to the direction of marching and the mass flux $\bar{\rho}\bar{w}$ distributions with the generalized inflection point indicated by a dot.

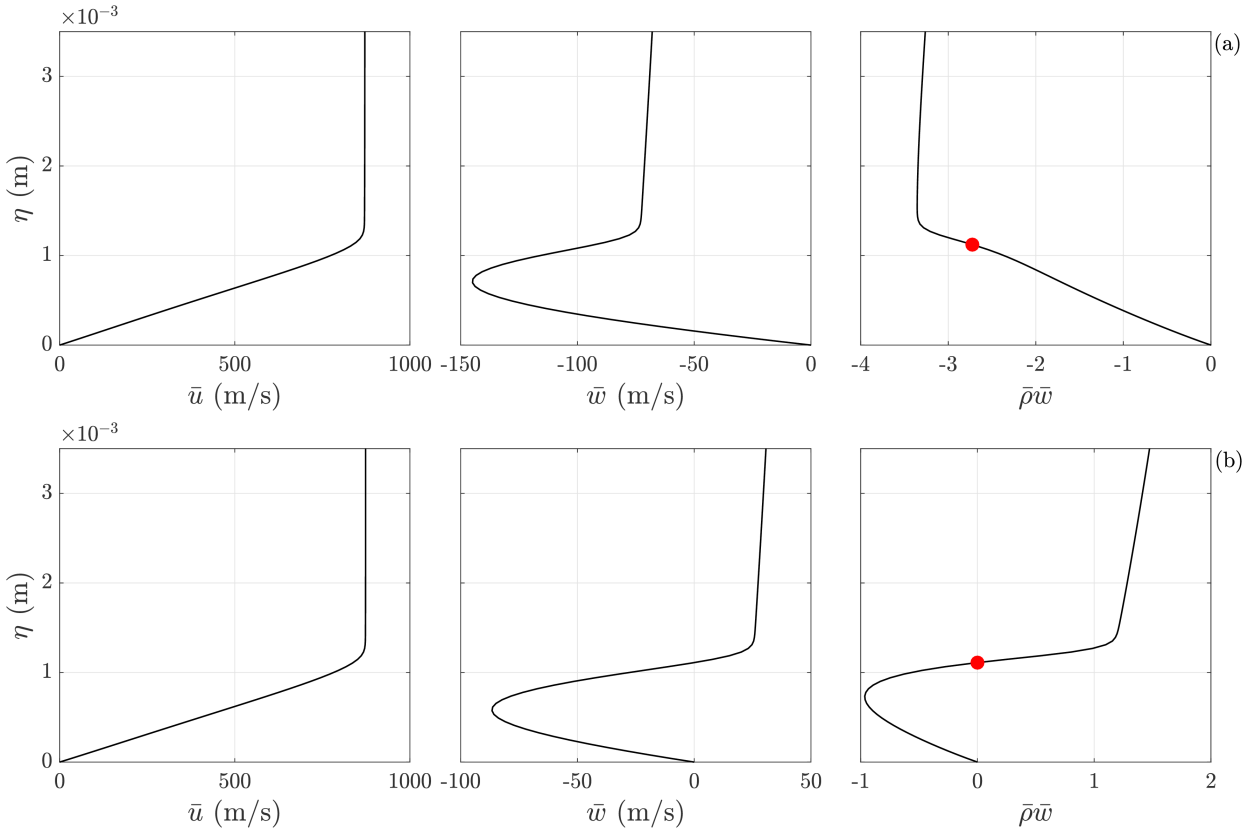

Figure 3.3: Basic-state u, w, and ρw profiles (a) in the down-geometry direction and (b) oriented in the direction of marching along a stationary crossflow vortex path

3.2.3 Surface Curvature

Curvature effects are accounted for in EPIC for all stages of the stability methodology. The radius of curvature in the spanwise direction is also important in the definition and treatment of the spanwise wavenumber presented in the current work. EPIC's framework is set in a coordinate system that is perpendicular to the wall and tangent the geometry surface, and radii for the h_1 and h_3 curvature terms are locally calculated to be in matching coordinates.

The spanwise radius is calculated by performing a search through a local proximity of surface points in order to find locations based on i-coordinate that are immediately in front of or behind the current location, with respect to the marching direction. This process is

repeated for the streamwise curvature term using the k-coordinate, but with respect to the spanwise direction. Pairs of points now define the bounds of the surface location in the local path frame. Each pair is linearly interpolated to the plane parallel and perpendicular to the marching direction for the radii in the streamwise and spanwise directions, respectively. Figure 3.4 shows the procedure for defining the in-plane lines.

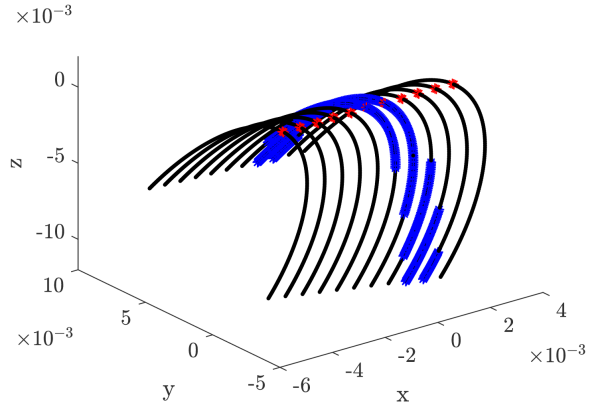

(a) Local surface with closest indices

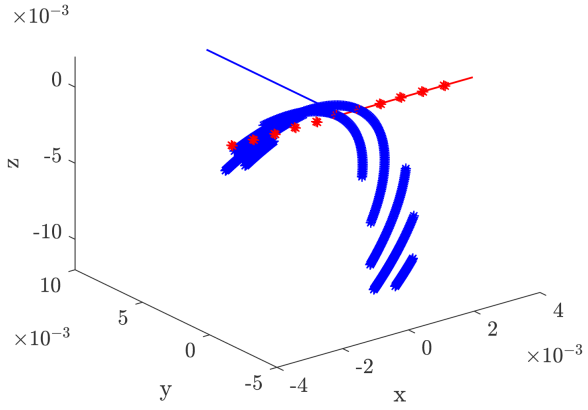

(b) Closest i (blue) and k (red) indices to planes

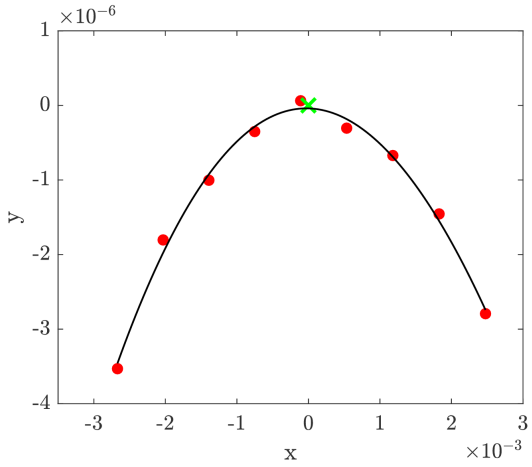

(c) Least-squares solution (black line) for streamwise radius. The × marks the current surface location.

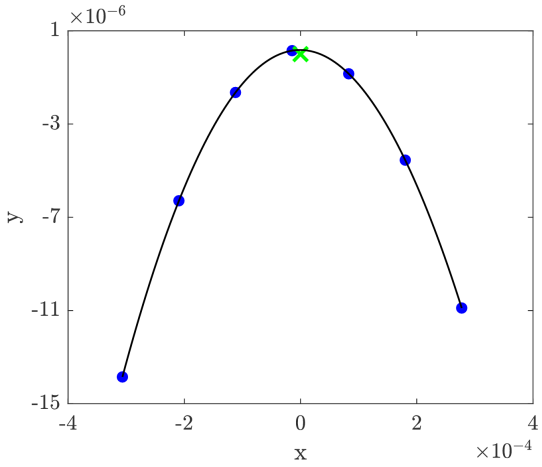

(d) Least-squares solution (black line) for spanwise radius. The × marks the current surface location.

Figure 3.4: Method for finding surface curvature

With points defined on a plane oriented in the proper frame of reference, an equation is generated using points closest to the current surface location and solved using 2-D linear least squares (A.3). An analytical derivative of the system provides terms that generate the local radii of curvature as defined in equation 3.3.

$$R = \frac{\left(1 + \frac{dy}{dx}^2\right)^{3/2}}{\left|\frac{d^2y}{dx^2}\right|} \tag{3.3}$$

3.2.4 Stepping

Once all of the data has been successfully acquired at the current marching location, the extraction code has to take a step forward and ensure that the new location is in fact on the geometry surface. To maintain a constant step size over any physical topology, the geometry is first flattened. It can be very challenging to devise a universal numerical method that flattens out generic 3-D shapes. Fundamental complications exist, especially since many geometries cannot be flattened onto a plane without "overlapping" or "folding" the shape.

The extraction code addresses this dilemma through a series of sequential rotations. To begin, the nearby surface is flattened along a line of constant k-index. Rather than having all points rotate about a common axis, each subsequent level of points that share an i-index rotate about the previously flattened set of points. Flattening the remaining points uses an identical procedure, albeit rotations now occur about lines perpendicular to the previous operation. Straight line distances on the new flattened surface are now representative of the surface distance between points on the original shape. Stepping is completed by moving a distance defined by the step size along the flattened shape, rotating the step direction by an angle determined by the marching path type, and using an interpolation of the original geometry grid points to find the step location in 3-D space. Examples of how a geometry is flattened with this method are shown in figure 3.5.

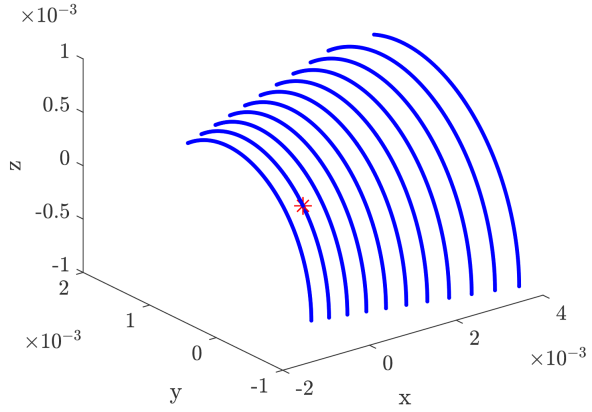

(a) Circular geometry with current location (∗)

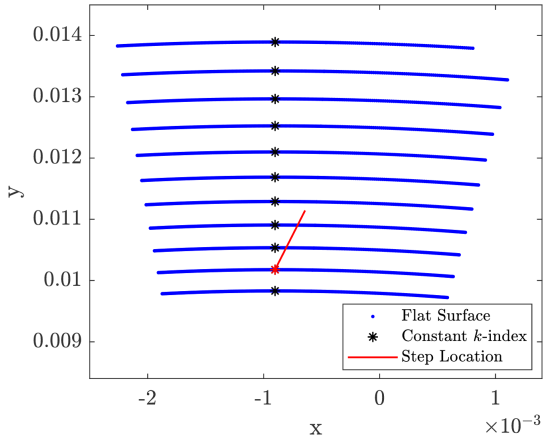

(b) Flattened circular geometry

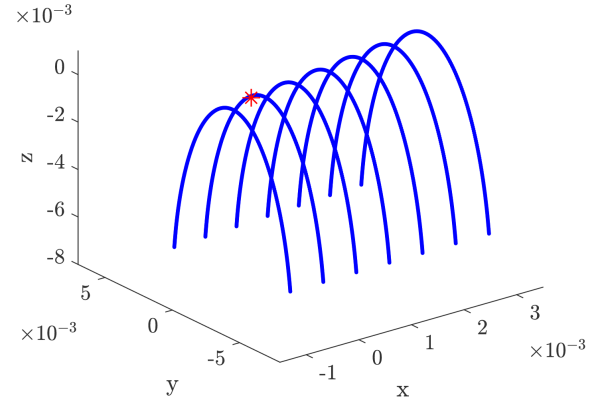

(c) Elliptic geometry with current location (∗)

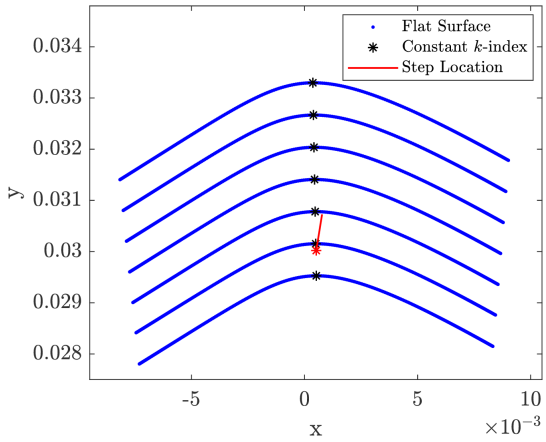

(d) Flattened elliptic geometry

Figure 3.5: Flattened geometries for surface marching

4. VARIATION OF SPANWISE WAVENUMBER*

For the stationary crossflow instability, it was mentioned in Balakumar & Owens [76] that it appeared as though the wavelength of vortices varied locally along a vortex path (see their figure 20b). A new method was formulated in Oliviero et al. [77], again based solely upon the undisturbed basic state, to model the evolution of the wavenumber in the direction perpendicular to the marching path for stationary crossflow. Physically, it was assumed that the number of azimuthal waves remained constant between two vortex paths. The concept is expanded to include traveling crossflow by considering the waves at instantaneous moments in time with respect to each other. As two paths moved down along the cone geometry, the azimuthal angle between the two would either grow, shrink, or remain the same. This change in angle was used to determine what the local effective wavenumber would be as seen here:

$$\begin{aligned} m_{local} &= m_0 \frac{\Delta\theta_0}{\Delta\theta_{local}} \\ m_{_\perp} &= \frac{R_{_\perp} \Delta\theta_{local}}{d} m_{local} \end{aligned} \tag{4.1}$$

For a cone, two stations are defined along a given marching path identified from the basic state. Stations defined as "local" indicate different locations along that path whereas stations defined with subscript "0" refer to the first point of that path. The trajectories of neighboring paths are also monitored. The following procedure describes the formulation of terms in equation 4.1.

*Portions of this section are reprinted from "EPIC: NPSE Analysis of Hypersonic Crossflow Instability on Yawed Straight Circular Cone" by Nicholas B. Oliviero, Travis S. Kocian, Alexander J. Moyes, Helen L. Reed, 2015. *AIAA 2015-2772*, Copyright 2015 by Nicholas Oliviero, Travis Kocian, Alexander Moyes, Helen Reed.

*Portions of this section are reprinted from "Hypersonic Crossflow Instability" by Travis S. Kocian, Alexander J. Moyes, Helen L. Reed, Stuart A. Craig, William S. Saric, Steven P. Schneider, and Joshua B. Edelman, 2018. *AIAA 2018-0061*, Copyright 2018 by Travis Kocian, Alexander Moyes, Helen Reed, Stuart Craig, William Saric, Steven Schneider, Josh Edelman.

- At the initial point of the marching path, $\Delta\theta_0$ is the difference in geometric azimuthal angle between the current path and a neighboring path, and m_0 is the initial number of waves specified with respect to the azimuthal direction

- Then, at a point further down the marching path, $\Delta\theta_{local}$ is the local difference in azimuthal angle between the current path and the neighboring path, and m_{local} is the local number of waves predicted with respect to the azimuthal direction

- The stability formulation requires a wavenumber perpendicular to the marching path so that locally $R_{\perp}$ is the radius of revolution perpendicular to the marching path, d is the straight line distance between one's current location on the path and a point on the neighboring path that intersects the plane perpendicular to the current path, and $m_{\perp}$ is the predicted local number of waves perpendicular to the marching path

The quantities for θ are in radians for this definition. A physical representation of this method is depicted for a circular cone in figure 4.1. Neighboring paths on both sides of the marching path of interest are used, and the result is averaged in order to alleviate single-sided biasing of the wavenumber variation.

This method appears to violate the irrotationality condition when considering the total number of waves around the cone. The irrotationality condition states that $\frac{\partial\beta}{\partial\xi} = \frac{\partial\alpha}{\partial\zeta}$ which, for a conical geometry, is equivalent to stating that the total number of waves around the defined surface remains constant [8]. This condition is expressed in equation 4.2.

$$k_c = \beta R = constant \tag{4.2}$$

In order to satisfy equation 4.2, a supplementary adjustment is made which artificially modifies the local radius of curvature in the path-perpendicular, or spanwise, direction by the inverse scale applied to the number of waves. Equation 4.3 shows the relationship between different components of the wavenumber. The variable χ_1 is the scale factor that is applied

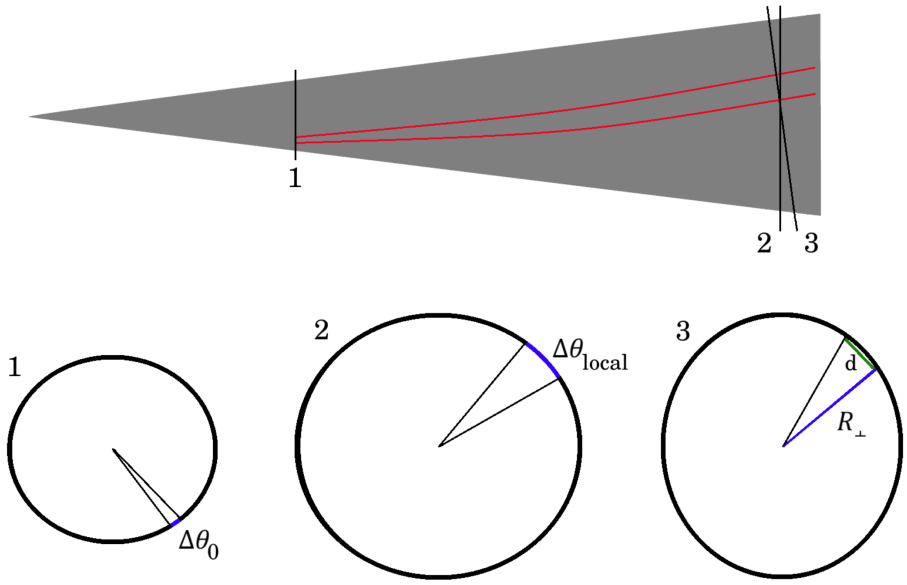

Figure 4.1: Visual portrayal of the formulation for the variation of wavenumber perpendicular to the marching path

to the number of waves seen locally and R_{art} is the artificial radius of curvature created to account for this scale.

$$\begin{aligned} k_c &= \beta R_{art} \\ \beta &= \frac{2\pi\chi_1}{\lambda} \\ R_{art} &= \frac{R_\perp}{\chi_1} \\ \chi_1 &= \frac{m_\perp}{m_0} = \frac{R_\perp \Delta\theta_0}{d} \end{aligned} \tag{4.3}$$

R_{art} is used in order to generate the spanwise curvature terms for the stability equations while the scale factor χ_1 is applied in the wave component shown in equation 2.16. The spanwise wavelength, λ, of the disturbance is thus allowed to vary through the adjustment made to the number of waves depending on both the vehicle geometry and the divergence or convergence of paths. This occurs while also satisfying the irrotationality condition through the combination of β and R_{art}.

The above formulation originates from the basis of an axisymmetric circular cone. In an effort to generalize the concept, the underlying idea behind mapping the variation of azimuthal wavenumber was expanded in order to accommodate more general and arbitrary shapes. To accomplish this, an adjustment is applied directly to the spanwise wavelength of the disturbance mechanism. The assumption is made that if two crossflow waves are propagating downstream along two neighboring paths, then the change in surface distance between the paths is indicative of the behavior of the wavelength. This value will change with each axial station as the two paths either approach each other or separate. By utilizing the ratio of the local distance with respect to that of the original position, a scale can be applied to the spanwise wavelength of any disturbance input into the PSE stability calculations. When the spanwise radius of curvature approaches infinity, as is the case for flat plate or swept wing geometries, it is recommended to continue to apply the scale factor on the wavelength. Pressure gradients may still affect the flow such that the wavelengths of crossflow vortices grow or shrink, and the spanwise wavelength appears to be a more important aspect of the disturbance growth than spanwise curvature. Analogous to the aforementioned procedure, the distances between neighboring paths on both sides of the path of interest are averaged to reduce single-sided biasing of the wavenumber variation. Equation 4.4 shows the relationship between components of the wavenumber. These components also satisfy the irrotationality condition outlined in the previous method.

$$\begin{aligned} k_c &= \beta R_{art} \\ \beta &= \frac{2\pi}{\lambda_0 \chi_2} \\ R_{art} &= R_{\perp_0} \chi_2 \\ \chi_2 &= \frac{s_\perp}{s_{\perp_0}} \end{aligned} \tag{4.4}$$

The scale factor χ_2 is taken from the ratio of spanwise surface distances between neighboring paths and is applied directly to the spanwise wavelength of the disturbance. It is

important to note that the adjustment to the radius of curvature is opposite that of the aforementioned method. This is a byproduct of applying the scale factor to the wavelength as opposed to the number of waves since they hold an inverse relationship with each other. Additionally, the artificial local radius is based solely on the radius of curvature at the initial location. The creation of this scale factor from surface distances already incorporates any changes in surface size in addition to the convergence or divergence of paths.

5. PURDUE COMPRESSION CONE

The second-mode instability has been widely studied on representative geometries such as flat plates and cones. Transition to turbulence may not be observed on straight cones under quiet wind tunnel conditions [78], the issue being experimental size restrictions which limit the length over which disturbances can grow. To address this, flared cones (compression cones) have been considered for study. Relative to the straight cone, a flare creates an adverse pressure gradient which destabilizes disturbances causing them to grow faster and shifts the laminar-turbulent transition point forward on the geometry body. In addition, a flare with concave curvature may possibly induce centrifugal Görtler instabilities in the form of counter-rotating vortices [25].

5.1 Geometry and Grid Topology

The considered geometry is the constant-flare radius Purdue compression cone [79]. This particular cone is an ideal model for studying the second-mode instability. The cone is specifically designed to maintain a relatively constant boundary-layer height along the length of the geometry and, given that the second-mode frequency tends to tune to the boundary-layer height, this isolates specific second-mode disturbances and enables them to grow over a long stretch of the cone surface. The model used has a nose bluntness of 0.001 m and a radius of curvature of 3 m for the flare. The total length of the model is 0.49 m, with a base diameter of 0.117 m. Figure 5.1 shows the cone geometry.

A structured mesh provides an inherent advantage over unstructured in terms of accuracy of the solution. This is particularly important in the boundary layer which is a region associated with high gradients and the focal point of this study. It is also required in order to obtain flow data using the aforementioned extraction code. Since the only configuration considered in the present study is at 0° yaw and the flow is axisymmetric, a 2-D grid is sufficient. The generated mesh contains 800 off-wall points and 1250 streamwise points.

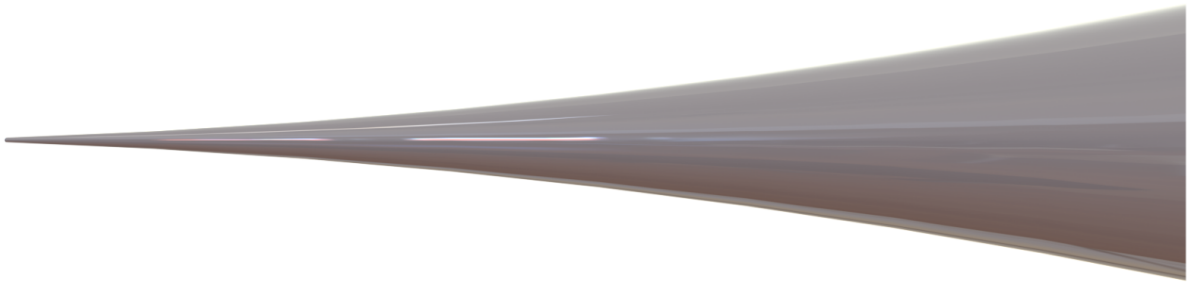

Figure 5.1: Purdue compression cone

5.1.1 Flow Conditions

The basic state is a highly resolved, verified solution to the full Navier-Stokes equations and represents the flow that exists in the absence of any environmental disturbances or forcing. The steady laminar flow over the considered geometry is computed using DPLR, as are all configurations and flowfields in the present text. A compression cone Mach contour can be seen in figure 5.2. The cone will only be analyzed at one condition: 0° AoA, freestream Mach number $M = 6$, freestream temperature $T_\infty = 52.8$ K, and freestream pressure $P_\infty = 611.1$ Pa abs, which results in a unit Reynolds number $Re' = 10.3 \times 10^6$/m. A wall boundary condition of $T_{wall} = 300$ K is also imposed, and the thermodynamic properties assume air as an ideal gas and apply a constant $Pr = 0.72$.

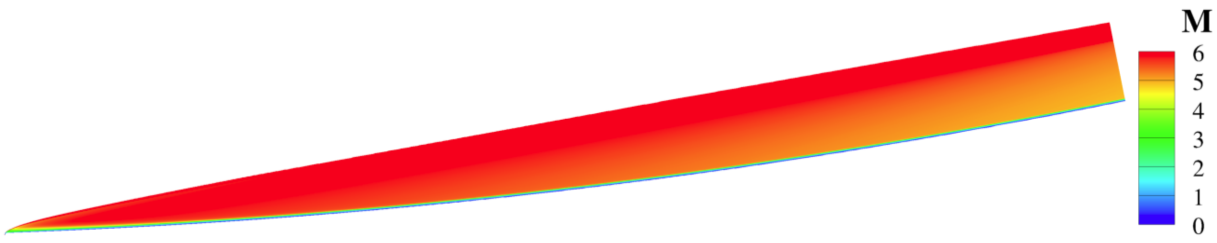

Figure 5.2: Purdue compression cone laminar basic-state solution

5.2 LPSE

As previously mentioned, the second-mode instability is of high interest in the study of the Purdue compression cone. LPSE calculations were performed over a range of frequencies and are shown in figure 5.3. A higher fidelity frequency band with an interval of 1 kHz was computed in addition to those presented in the figure, and it is found that the most amplified second mode at the end of the cone model has a frequency of 287 kHz and reaches an N-factor of 19.46. The most amplified frequency is in excellent agreement with existing results from both computations and experiments. Huang & Zhong [80] performed a DNS of transient flow resulting from the interaction between a freestream hot spot perturbation and bow-shock under the same flow conditions as the current computations. They found that the hot spot excites the second-mode instability and witnessed a most amplified frequency of 286 kHz at $x = 0.394$ m. Wheaton et al. [79] similarly reported PSE results that gave a most amplified frequency of 285 kHz at $x = 0.4$ m while coinciding experimental measurements detected a maximum frequency of 295 kHz at $x = 0.4$ m. Balakumar & Kegerise [81] performed both LST and LPSE calculations on the cone and found peak frequencies of 279 kHz and 286 kHz, respectively, at an axial location of $x = 0.4$ m. Additional PSE computations were performed by Li et al. [82] who found a maximum N-factor of approximately 19 for frequencies in the vicinity of 290 kHz.

A special note is to be made with regards to the amplification of the second mode. While LPSE N-factors are reaching very large values, the disturbances are only being modeled linearly. This allows the LPSE N-factor to continue to increase through the end of the geometry and reach levels that are unobtainable in a true physical setting. Examples including a DNS of the Purdue cone [83] and NPSE calculations in the present work show that the second-mode disturbance would have reached saturation before this point. This would be accompanied by mean flow distortion effects and the rapid growth of 3-D instabilities. Fedorov & Tumin [84] also estimated that kinetic fluctuations in a hypersonic flow would lead to transition once values of $N \approx 17$ were reached. However, it is still beneficial to provide

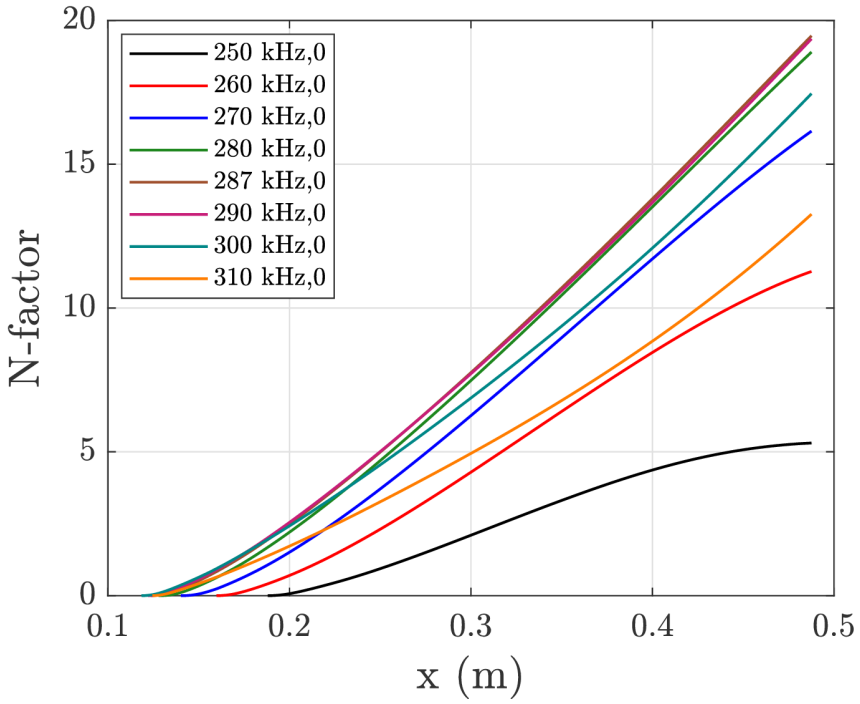

Figure 5.3: Second-mode N-factors on Purdue compression cone

the downstream development of LPSE N-factors for verification purposes with other linear calculations.

The effects of concave curvature also led to the development of strong Görtler instabilities. Figure 5.4 shows N-factors for disturbances with various constant azimuthal wavenumbers. In addition to analyzing the second mode, Li et al. [82] completed LPSE calculations for Görtler instabilities over a range of different azimuthal wavenumbers. A wavenumber of 50 resulted in the largest N-factor from their computations, in agreement with the results in figure 5.4. The N-factors for each of the wavenumbers and relative amplification of the disturbances with respect to each other compares favorably with their figure 10a.

5.2.1 Convergence Study

The very first step of any PSE analysis is to generate a converged and accurate base flow. Structured grids tend to be favored due to the accuracy advantage over an equally

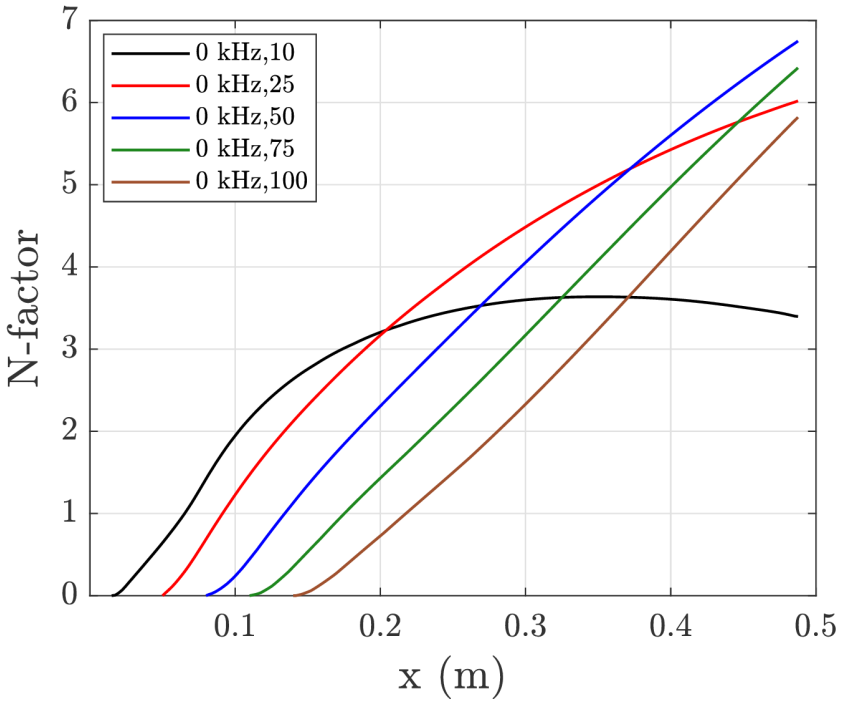

Figure 5.4: Görtler N-factors on Purdue compression cone

dense unstructured grid. It is also important to place a sufficient number of grid points in regions associated with high gradients such as near the shock and boundary layer. Stability calculations have been shown to be very sensitive to variances in basic-state flow profiles. In the hypersonic flow regime, the boundary layers undergo very large changes within a height that is typically very small, and one needs to be sure that these values are highly resolved.

A convergence study was performed for the Purdue compression cone at Mach 6 with the same freestream flow conditions used in the LPSE analysis. Stability characteristics appear to be more sensitive to changes in grid density and architecture than flow values such as pressure. For this reason, the basic state is assumed to be converged once LPSE N-factors converge for different grids. Second-mode disturbances at the peak frequency of 287 kHz are compared for three different meshes of the Purdue compression cone as seen in figure 5.5. The three grids consist of approximately 250 thousand, 500 thousand, and 1 million cells. The lower resolution grids maintain the same ratio of cells in the axial and off-wall

directions and were generated by applying an equal scale to the number of grid points in both directions.

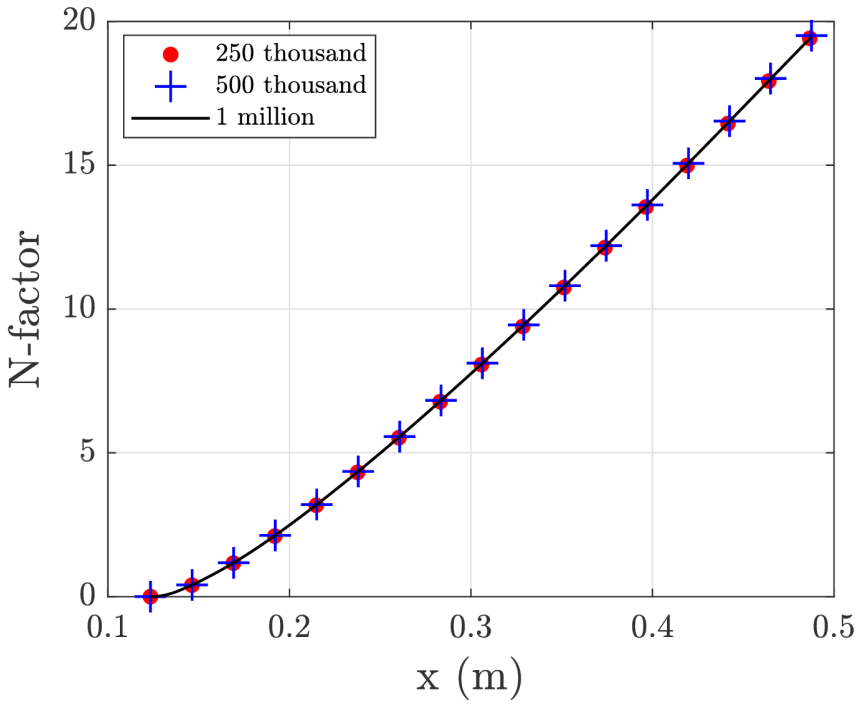

Figure 5.5: Second-mode N-factors for three grid densities

Differences in N-factor among all three cases are on the order of 0.5% or smaller. The flow conditions and geometry size are comparable to those tested in the quiet tunnel experiments at both Purdue University and Texas A&M University. Placing $70-100$ off-wall grid points within the boundary layer proved sufficient in obtaining the displayed level of convergence and may be a sufficient standard when studying comparable 2-D geometries under similar flow conditions. All presented computations for this cone geometry will hereby use the grid generated using 1 million cells.

5.2.2 Influence of Boundary-Layer Height on Second Mode

It is widely known that the growth rates of the second-mode instability are highly tuned to the height of the local boundary layer. This relationship is further investigated using the Purdue compression cone. Figure 5.6 shows the LPSE growth rates of the most unstable frequencies at different axial locations on the geometry. Alongside the growth rates is the local boundary-layer height along the length of the cone. The edge of the boundary layer is defined as the location for which the local total enthalpy is equal to 99.5% of the freestream total enthalpy.

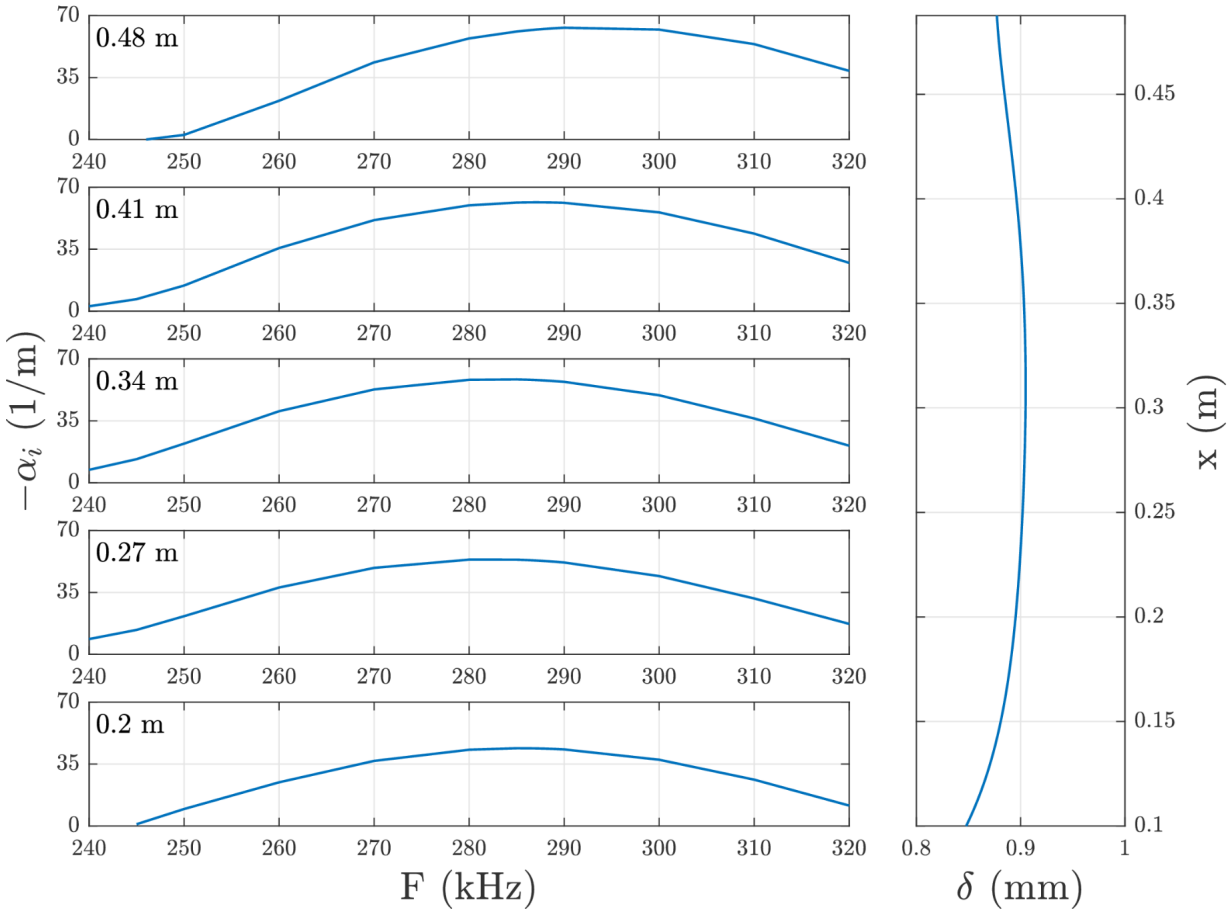

Figure 5.6: Local growth rates for LPSE second-mode instabilities and boundary-layer thickness of the Purdue compression cone

For a majority of the model length, the boundary-layer height remains nearly constant which causes the most unstable frequency to remain relatively constant as well. The most unstable frequency has a very subtle shift near the end of the model, in accordance with the small decrease in boundary-layer height. Rather than amplify for a period and then decay as the boundary layer begins to grow, a single frequency can persist until the end of the model. Controlling the behavior of the boundary layer in this manner enables a large amplification of the second mode in comparison to cones of similar size and under similar flow conditions. This result further reinforces the effectiveness of creating a geometry with constant boundary-layer height in order to study second-mode dominated flows and breakdown that occurs due to a nonlinear interaction with the second-mode instability.

5.3 K-type Breakdown

Klebanoff et al. [85] originally discovered the process known as fundamental resonance, or K-type breakdown, when performing experiments involving incompressible flat plate boundary layers. This process occurs when a high amplitude 2-D primary wave phase locks with a pair of lower amplitude secondary oblique waves, allowing energy to be transferred through to them. These secondary oblique waves will have opposite wave angles from each other and the same frequency as the primary wave. The resulting nonlinear interactions will cause a rapid amplification of the secondary waves. Experiments saw this effect through the formation of aligned Λ vortices as the flow approached breakdown. The source of the fundamental 2-D wave from the experiments, which were performed in a wind tunnel with a freestream velocity of approximately 50 ft/s, was the Tollmien-Schlichting instability. At the significantly higher speeds of the current study, the 2-D second mode is most amplified and will be used as the fundamental wave. Fasel et al. [86] describe the approach and application of K-type breakdown in the hypersonic flow regime.

Experiments were performed at Purdue University in the Boeing/AFOSR Mach-6 Quiet Tunnel (BAM6QT) facility using the compression cone model with a nominally smooth wall for unit Reynolds numbers between $7.3 - 10 \times 10^6$/m [83]. Under quiet conditions,

temperature-sensitive paint revealed a series of streamwise streaks due to heating on the model surface. The nonlinear growth and breakdown of second-mode waves was also detected through pressure fluctuation measurements with the maximum value reaching 30% of the mean surface pressure before breakdown occurred. Ward et al. [87] observed the heat streaks appear, disappear, and then reappear along the surface. McKiernan et al. [88] were able to alter the heat streak patterns by applying small roughness elements to the model surface, but noticed that the trends of pressure fluctuation data remained unchanged.

Hader & Fasel [89] performed DNS in order to investigate the source and behavior of the streaks. Computations were carried out by using a "controlled" set of disturbances which were introduced into the computational domain through the use of a blowing and suction slot at the wall. The first set of tests was to determine whether the subharmonic or fundamental resonance produced stronger secondary mechanisms. Li et al. [82] had shown that both the subharmonic and fundamental instability can lead to large amplification. Hader & Fasel [89] proceeded to identify the azimuthal wavenumber which produced the largest secondary growth rate for both situations, and it was found that the fundamental resonance was dominant. In order to determine which disturbance quantities would be initialized in the DNS, a parameter study was performed of the fundamental resonance onset. The study revealed that an azimuthal wavenumber of $k_c = 80$ produced the strongest secondary growth, and wavenumbers of $k_c = 40$ and $k_c = 120$ would be computed in addition to the most unstable case. For all cases, streamwise streaks of high skin friction and heat transfer were seen at the cone surface, matching what was observed in the experiments.

A direct link between the development of the heat streaks and the steady vortical modes was shown by Hader & Fasel [89]. When these steady streamwise modes entered the strongly nonlinear region, they would create heat streaks on the cone surface. As these disturbances continued to grow, they would lift away from the wall for some extent before being pushed back down. This behavior aligned with the streak patterns seen by Ward et al.

The current effort is focused on using EPIC and the NPSE method in order to replicate the

nonlinear evolution of K-type breakdown seen in both the experiments and with DNS. Mayer et al. [90] showed the feasibility of using NPSE in order to model the oblique breakdown process, which is of a similar nature to fundamental resonance, at Mach 3. A comparison with DNS found good agreement ranging from the initial receptivity stage all the way to the initial breakdown process where the mean wall shear nearly doubled that of its laminar value.

Although the DNS of Hader & Fasel was at a slightly larger Re', an identical frequency value of 300 kHz will be used as input for NPSE in order to make a direct comparison. Despite not being deemed the most amplified wavenumber from the DNS parameter study, the 3-D modes will be initialized with $k_c = 40$. Linear oblique modes with higher azimuthal wavenumbers were significantly more stable than the 2-D second mode, as seen in figure 5.7. This made initializing the $(1, 1)$ and $(1, -1)$ oblique pair difficult at the earlier axial locations of the geometry. Defining a wavenumber of $k_c = 40$ allowed the nonlinear system to evolve over a larger region of the cone and enabled the NPSE solution to progress to the end of the geometry.

In order to define the initial conditions for NPSE, maximum temperature disturbance amplitudes were extracted from figure 12a of the Hader & Fasel [89] DNS computations. Amplitudes were then converted to u-amplitudes by running LST at a specified axial location and using the ratio of $\hat{T}$ and $\hat{u}$ mode shapes to scale the values. Initial conditions for the corresponding NPSE calculation are provided in table 5.1. Disturbance amplitudes are based on U_e at the initialization point and computations also included 4 superharmonics of each (n, k) combination. Harmonics are, by default, given amplitudes that are powers of the initialized mode. For example, the first superharmonic $A_{0_{(2n,2k)}}$ will have an amplitude $A_{0_{(n,k)}}^2$.

Figure 5.8 shows NPSE maximum u-amplitudes for each of the individual modes. The fundamental $(1, 0)$ disturbance appears to begin to saturate at around $x = 0.35$ m before obtaining a peak amplitude of 17% and stabilizing at $x = 0.38$ m. Shortly thereafter, the

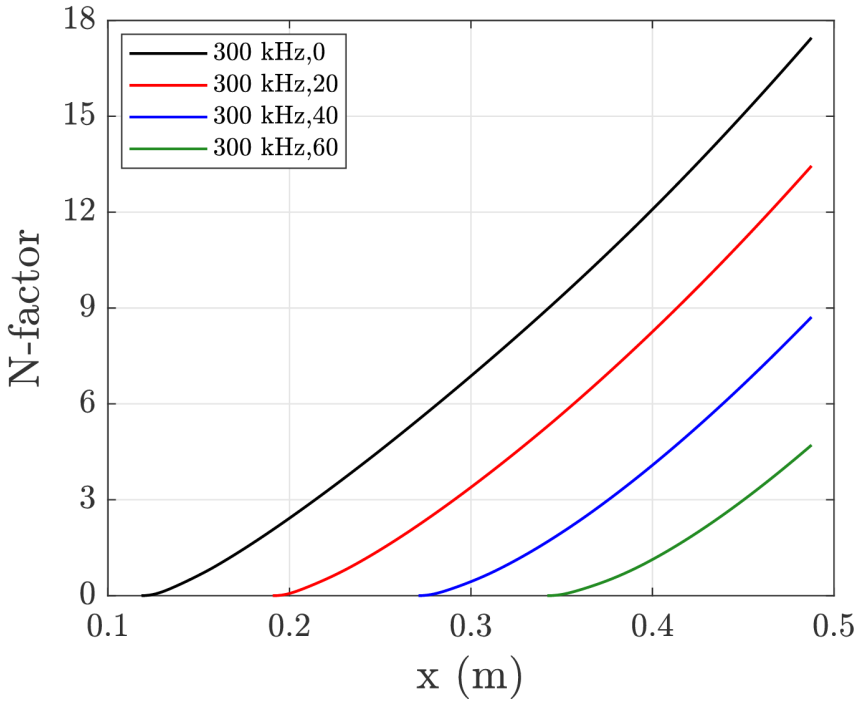

Figure 5.7: N-factors for 2-D and oblique second-mode instabilities

x_0 (m)	F (kHz)	k_c	$u'_{(1,0)}$	$u'_{(1,\pm1)}$	$u'_{(0,1)}$
0.25	300	40	1.5×10^{-3}	3.1×10^{-5}	2.0×10^{-6}

Table 5.1: Inputs for K-type NPSE

$(0, 1)$ surpasses it and becomes the most amplified disturbance for an extent. These two modes cross each other two more times at $x = 0.425$ and 0.44 m before the $(0, 1)$ finally maintains the largest amplitude and reaches a maximum value of 37% near the end of the cone.

To directly compare with amplitudes from the DNS simulation, figure 5.9 provides disturbance amplitudes in the form of T'. Both the NPSE calculations and DNS results from figure 12a of Hader & Fasel [89] see the primary 2-D second mode saturate around an axial location of $x = 0.34$ m after achieving an amplitude on the order of 100%. This NPSE value is based on T_e at the initialization point of the computation. Mean flow distortion decreases

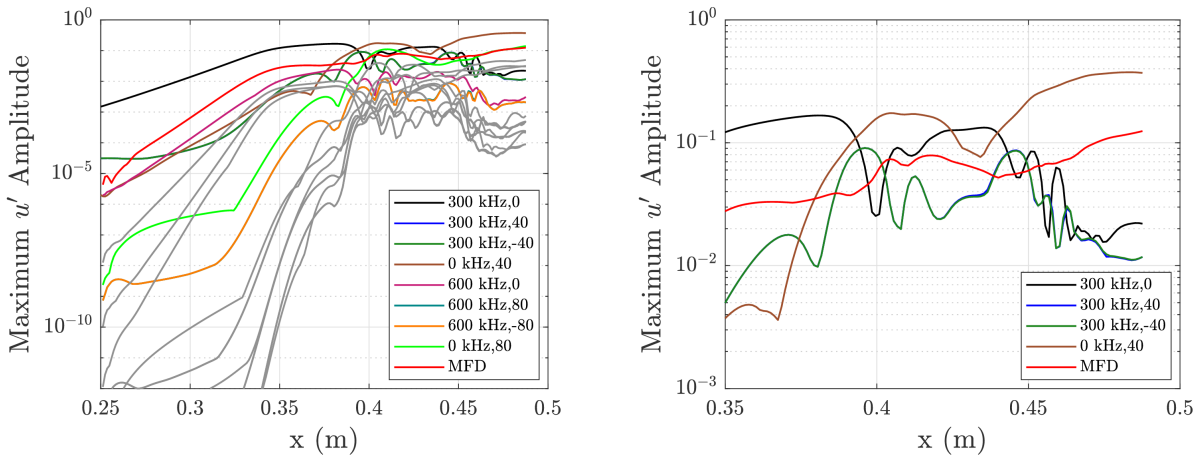

(a) All modes

(b) Initialized modes

Figure 5.8: Maximum u-amplitudes from NPSE for K-type simulation

in a region very close to the first decrease of the $(1, 0)$ mode before increasing again and obtaining substantial amplification at the end of the cone. Amplitudes between the NPSE and DNS results are very similar for a majority of the modes, however, some discrepancies do exist. In particular, the zero frequency steady modes behave differently towards the end of the cone. For the NPSE calculation, the $(0, 1)$ continues to grow and remains the most amplified while the $(0, 2)$ achieves an amplitude just below that of the mean flow distortion. In comparison, the DNS shows the $(0, 2)$ surpass all modes for a stretch between $x = 0.38$ and 0.41 m while the $(0, 1)$ is noticeably more stable. One possible explanation is that the $(0, 2)$ mode is initialized at a much smaller amplitude in the NPSE calculation that what is shown in the DNS.

Perturbations were averaged in time and combined with the basic state in order to create a time averaged Stanton number. The distribution of time averaged Stanton number is shown in figure 5.10. For visual purposes, the half-cone surface has been numerically flattened to represent surface distance measured from the symmetry line of the geometry.

Streaks first appear at an axial location of $x = 0.36$ m. At this point 20 individual streaks are visible. Since figure 5.10 depicts only half of the cone model, this would be equivalent to

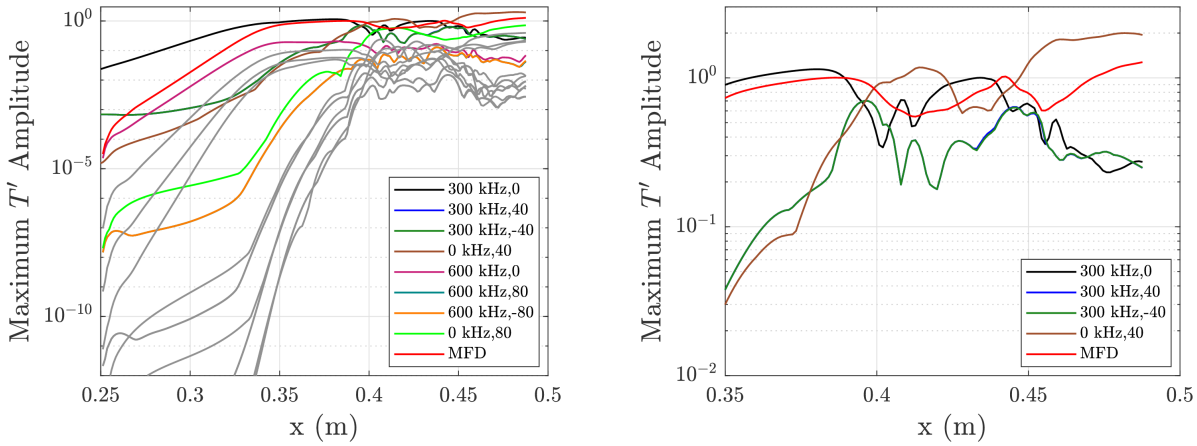

(a) All modes (b) Initialized modes

Figure 5.9: Maximum T-amplitudes from NPSE for K-type simulation

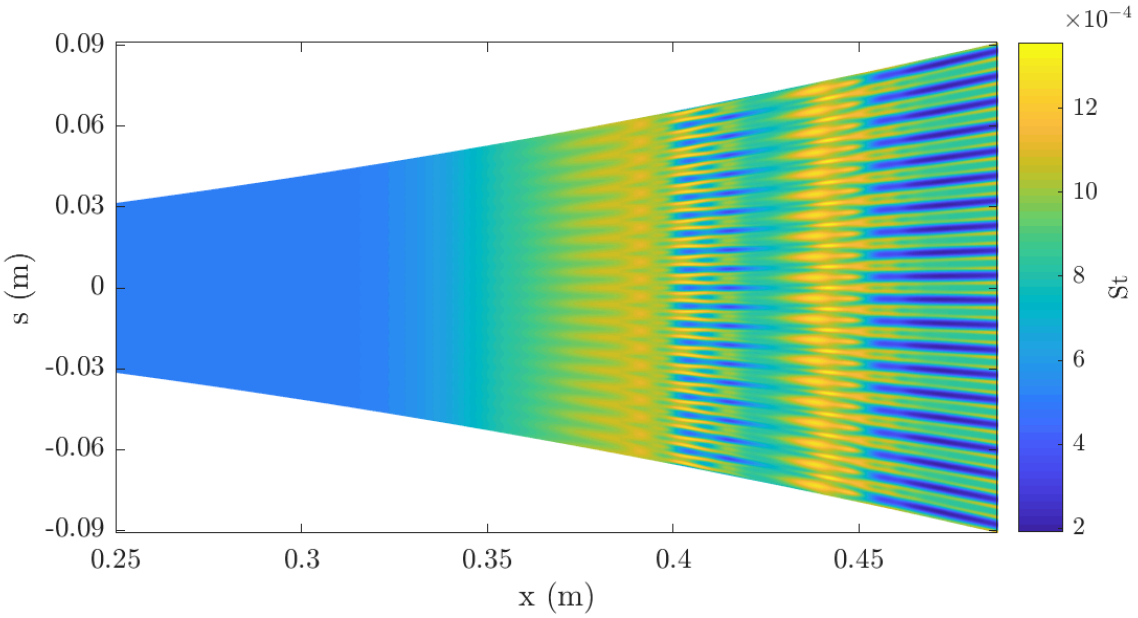

Figure 5.10: Stanton number distribution on the surface of the Purdue compression cone

seeing 40 streaks around the full circumference. Moving down the cone, the streaks appear to split, vanish, and then reappear again. Some axial locations also show the streaks take on a staggered front. After $x = 0.45$ m, the amount of visible streaks has doubled such that there are 80 around the cone azimuth. This behavior is consistent with what was observed

during wind tunnel tests in the BAM6QT at Purdue University. Figure 9 from Chynoweth et al. [83], while at a slightly smaller Re', shows that applying 40 evenly spaced roughness elements caused 80 streaks to form, and that the streaks appeared in a staggered pattern. In a similar manner, 30 brass rods were used to produce figure 8 from McKiernan et al. [88] which shows a similar splitting of the streaks.

In order to gauge the intensity of the hot streaks, skin-friction coefficients are extracted from EPIC at 4 axial locations. These values are also time averaged and are shown in figure 5.11. From these axial slices, it is much easier to determine the streak locations and how they evolve along the cone. Progressing from figure 5.11a to figure 5.11d also demonstrates the transformation from 40 to 80 azimuthal streaks created by peaks in C_f.

Since the azimuthal position of streaks varies along the cone, there is no straight line path that passes through the "hot" streak portion for the full cone length. However, it is still insightful to see how C_f deviates from the steady-state laminar flow values. Figure 5.12 shows the skin-friction coefficient for a slice that passes through $s = 0$ in figure 5.10.

Nonlinear effects begin to become significant and cause the skin-friction coefficient to deviate from the laminar basic-state value at around $x = 0.3$ m. There also appears to be an initial peak, followed by a portion that falls below the laminar value, and then a second peak. The descent from the first peak occurs at the same location that the primary 2-D fundamental mode begins to decrease in amplitude. The behavior of the skin-friction coefficient displays remarkable similarity with results from the DNS simulation of Hader & Fasel [89], as seen in their figures 6a and 7a. Peaks occur in similar axial locations, and their figure 7a also sees a span where the skin-friction coefficient drops below that of the basic state value.

The EPIC results matched very well with those of the experiments and DNS. NPSE was able to reproduce the heat streaks seen in both the experiments and DNS computations. Individual modes also experienced nonlinear interactions and amplifications similar to that of the DNS.

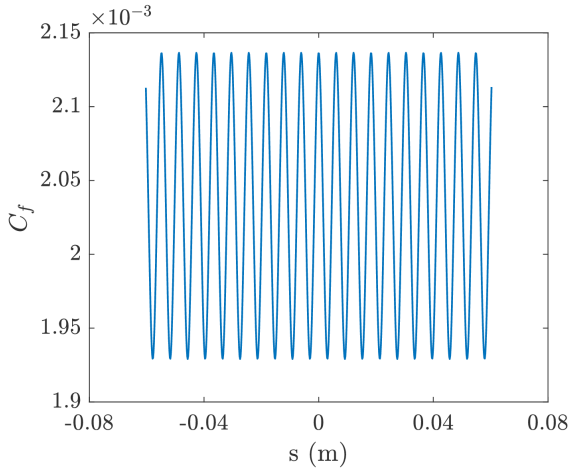

(a) $x = 0.38$ m

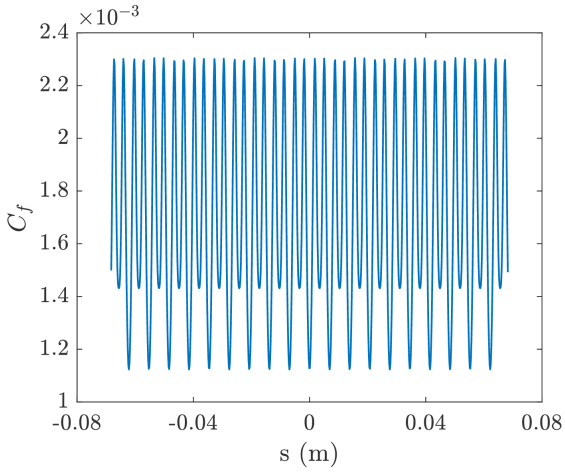

(b) $x = 0.41$ m

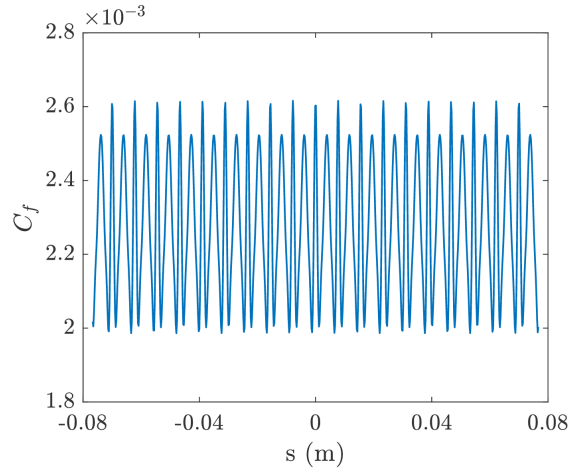

(c) $x = 0.44$ m

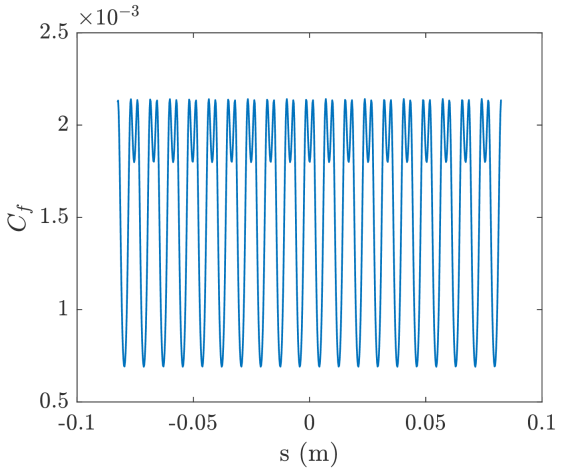

(d) $x = 0.46$ m

Figure 5.11: Time averaged skin-friction coefficients along axial slices of the Purdue compression cone

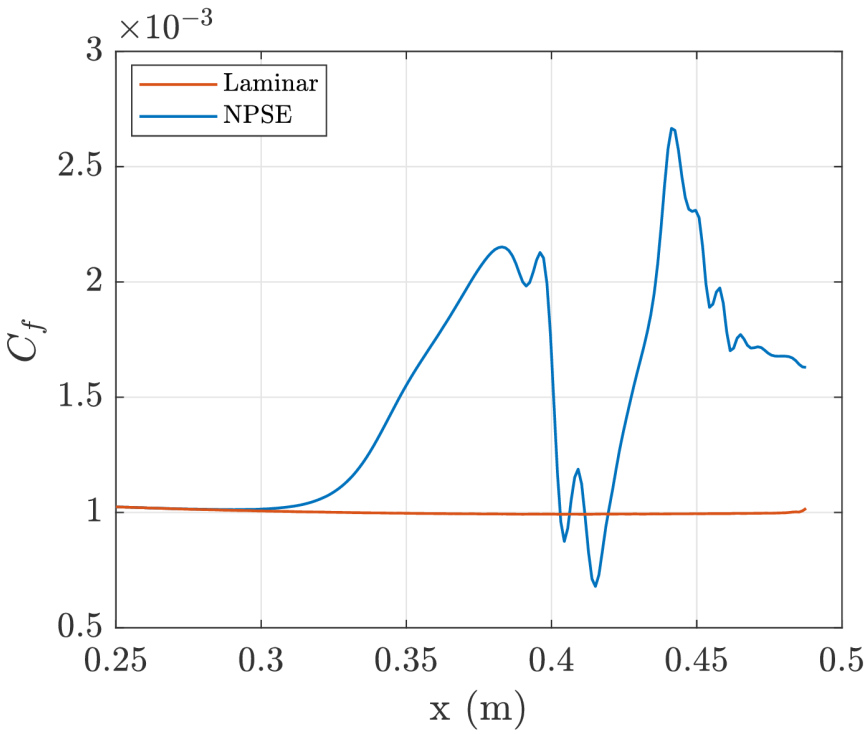

Figure 5.12: Time averaged skin-friction coefficient along the length of the cone at $s = 0$

6. LANGLEY 93-10 FLARED CONE*

6.1 Geometry and Grid Topology

Another flared cone geometry widely studied for the second-mode instability is the Langley 93-10. The model under consideration is 0.508 m in length and consists of a nose tip with a radius of 38 microns. The nose was modeled using the modified-super-ellipse equation in order to eliminate discontinuities in slope and curvature at the juncture [91]. This method is shown in equation 6.1

$$\left(\frac{a-x}{a}\right)^{m(x)} + \left(\frac{y}{b}\right)^2 = 1 \tag{6.1}$$

where $m(x) = 2 + \left(\frac{x}{a}\right)^2$, a is the major axis, and b is the minor axis. For modeling the Langley 93-10 flared cone, a and b are set to be equal to more closely resemble a circular nose tip. The geometry transitions from a 5° half-angle cone to a flare at 0.254 m. The flare has a radius of curvature of 2.364 m and extends to the base of the cone, which is 0.117 m in diameter. A model of the geometry is shown in figure 6.1.

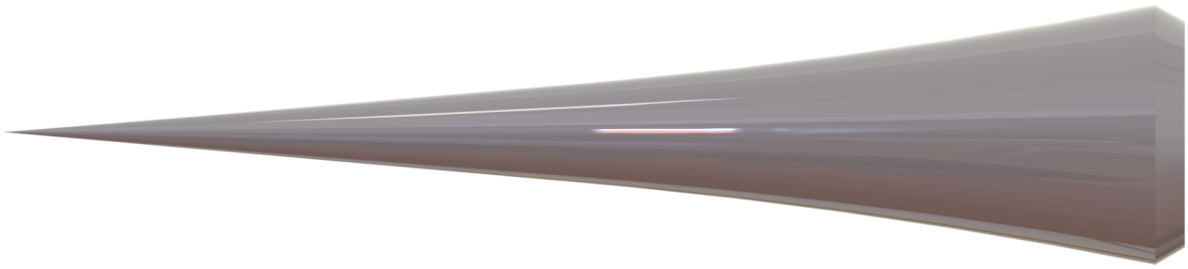

Figure 6.1: Langley 93-10 flared cone

*Portions of this section are reprinted from "Hypersonic Stability Analysis of a Flared Cone" by Travis S. Kocian, Eduardo Perez, Nicholas B. Oliviero, Joseph J. Kuehl, Helen L. Reed, 2013. *AIAA 2013-0667*, Copyright 2013 by Travis Kocian, Eduardo Perez, Nicholas Oliviero, Joseph Kuehl, Helen Reed.

For the case at 0° AoA, a 2-D grid is used with the same resolution as that used in the Purdue compression cone analysis. This grid contains 800 points in the off-wall direction and 1250 in the streamwise direction. Cases at slight angle of attack will also be considered which require a 3-D grid. For these cases, a single topology was created which models half of the cone geometry due to the symmetric nature of the flow. This mesh consisted of 750 points in the axial direction, 475 in the off-wall direction, and 181 azimuthally. Since the yaw angles being studied are very small, the resulting azimuthal gradients are expected to be small, and emphasis was placed on the axial and wall-normal resolution of the basic state.

6.1.1 Flow Conditions

Run conditions for the computations were matched to test conditions in the Texas A&M Mach 6 Quiet Tunnel. These consisted of a freestream Mach number $M = 5.91$, unit Reynolds number $Re' = 10.1 \times 10^6$/m, freestream static pressure $P_\infty = 629.6$ Pa abs, and freestream temperature $T_\infty = 53.85$ K. Runtimes for the M6QT are not long enough to establish adiabatic-wall conditions. Over the course of a wind tunnel experiment with the 93-10 cone, temperatures vary between 386 K and 403 K for a variety of locations along the cone and throughout the run. While the actual wind tunnel model had a small temperature variation on the body as time passed, the primary set of computational analyses uses a wall temperature $T_w = 398$ K to represent an average value. All computations assumed air as an ideal gas and a constant $Pr = 0.72$.

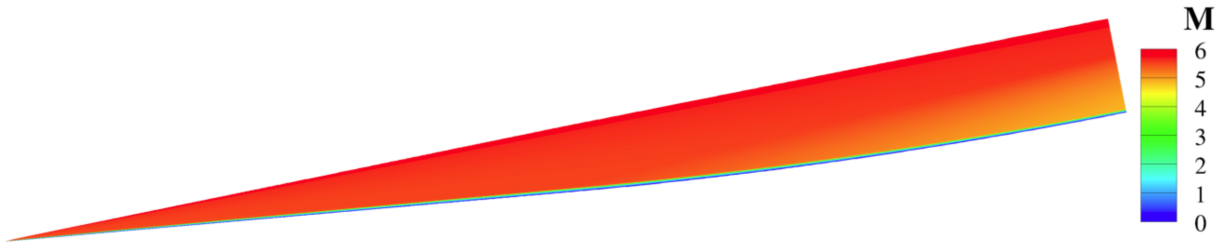

Figure 6.2: Langley 93-10 laminar basic-state solution

Moreover, Hofferth et al. [92] noted the difficulty in obtaining an exactly 0° AoA during a typical experiment and its significant effect on second-mode frequency. Therefore cases of 0°, 0.16°, and 0.32° AoA were considered as part of the computational study as representative of the experimental setup.

6.2 LPSE

LPSE was calculated for the Langley 93-10 flared cone using a constant wall temperature of 398 K. Mass-flux mode shapes from the LPSE calculations are compared to experimental profiles of fluctuating voltage for different axial locations on the cone. The computational mode shapes represent the locally most amplified second-mode frequency at each location and have been normalized. These disturbance profiles are presented in figure 6.3. A $230-330$ kHz passband was used to filter the experimental data in order to produce the RMS profiles and compare to the single frequency LPSE modes. Comparison of the computational mode shapes and experimental profiles reveals excellent agreement, and Hofferth et al. [92] attributes the slight differences at the latter axial locations to the likely onset of the early stages of transition.

The most amplified second-mode frequency from LPSE computations was found to be 241 kHz which reached an N-factor of 14.7 at the end of the cone geometry, as shown in figure 6.4. One can see that, when progressing down the axial length of the cone, the N-factors of different frequencies cross multiple times as they surpass and overtake each other. This can be attributed to the varying boundary-layer height along the cone, especially on the front half before the flaring of the vehicle surface occurs.

A comparison of experimental and computational results for most amplified frequency at $x = 0.50$ m is provided in figure 6.5. Hot-wire data from the experiment was uncalibrated so a proportionate scaling can not be made between the data and LPSE N-factors. However, it is still beneficial to compare frequencies that have experienced the largest amplification and how they progress downstream.

There is an evident disagreement in most amplified frequency in the validation effort.

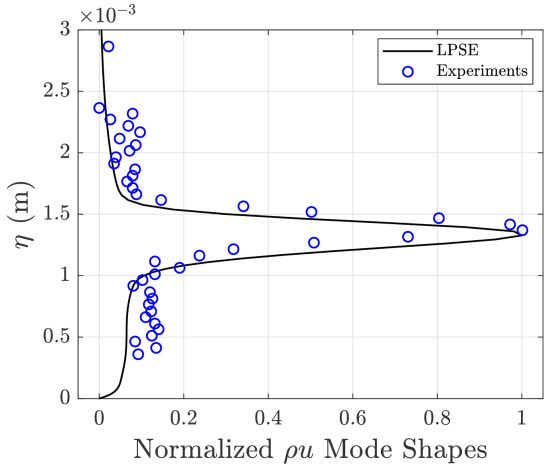

(a) $x = 0.41$ meters, $Re' = 9.7 \times 10^6$/m for experiment

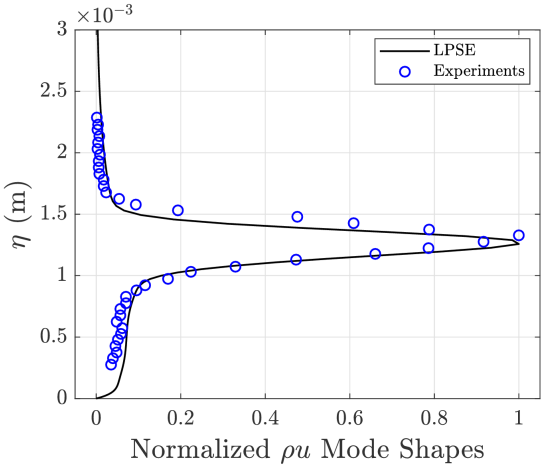

(b) $x = 0.46$ meters, $Re' = 10.3 \times 10^6$/m for experiment

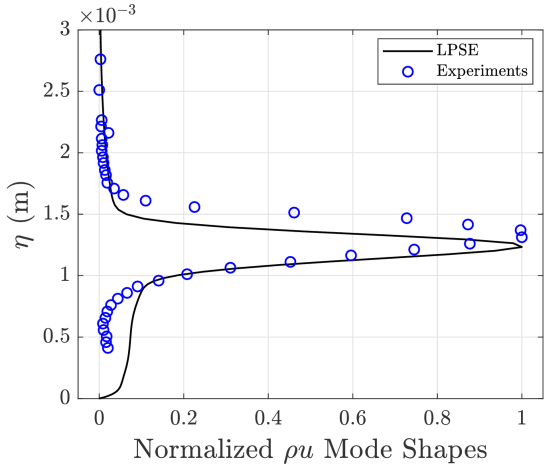

(c) $x = 0.48$ meters, $Re' = 10.3 \times 10^6$/m for experiment

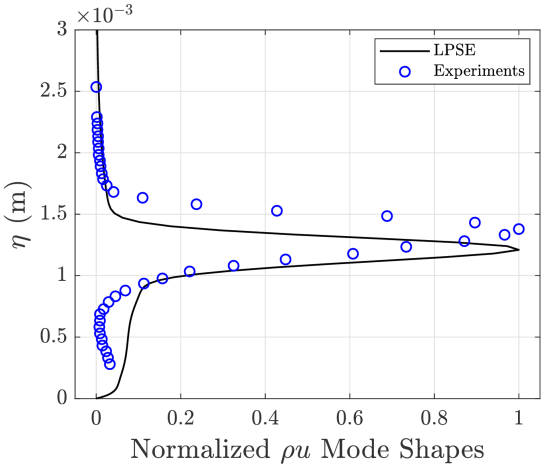

(d) $x = 0.50$ meters, $Re' = 10.3 \times 10^6$/m for experiment

Figure 6.3: Comparison of ρu mass-flux mode shapes for locally most amplified LPSE frequencies and experimental fluctuating voltage profiles

While LPSE computations are finding a most amplified frequency of $F = 240$ kHz, the experiments are finding the energy to instead center around $F = 280$ kHz. Following sections will attempt to deduce the cause of this discrepancy.

6.2.1 Influence of Boundary-Layer Height on Second Mode

Copying the practice used in the evaluation of the Purdue compression cone, the influence of boundary-layer height on the most unstable second-mode frequency is evaluated. LPSE

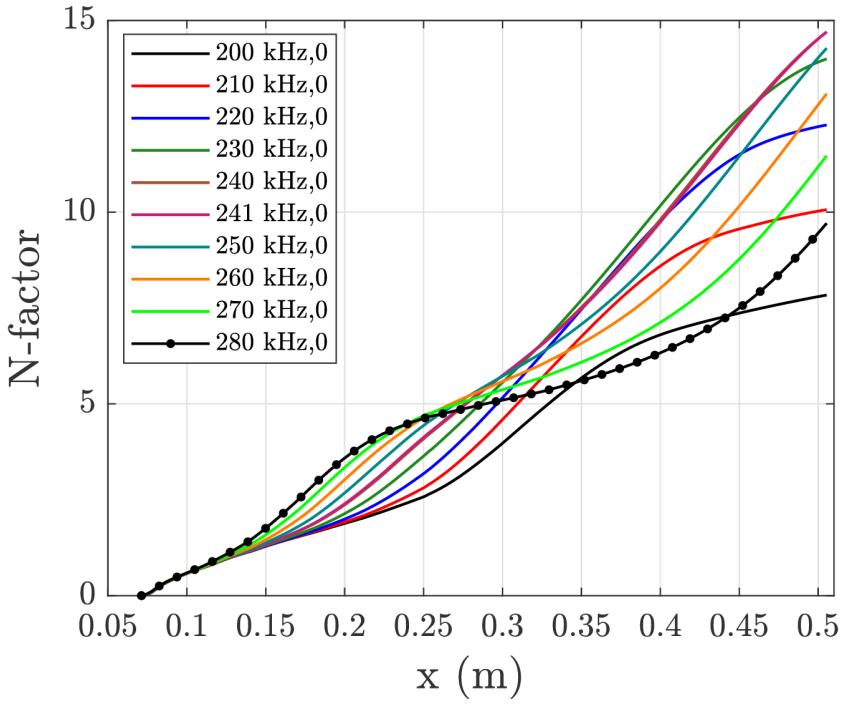

Figure 6.4: Second-mode N-factors with $T_w = 398$ K

growth rates of the most unstable frequencies are shown in figure 6.6 for different axial stations in combination with the local boundary-layer height along the cone length. The edge of the boundary layer is again defined as the location for which the local total enthalpy is equal to 99.5% of the freestream total enthalpy.

Unlike the Purdue compression cone, the first half of the Langley 93-10 geometry is simply a straight cone, and the boundary-layer height varies on a more substantial scale. This, in turn, causes the locally most unstable frequency to shift as one progresses down the cone length. The variation in most unstable second-mode frequency likely has a heavy influence in the findings that second-mode N-factors for the Langley 93-10 are lower than those of the Purdue cone.

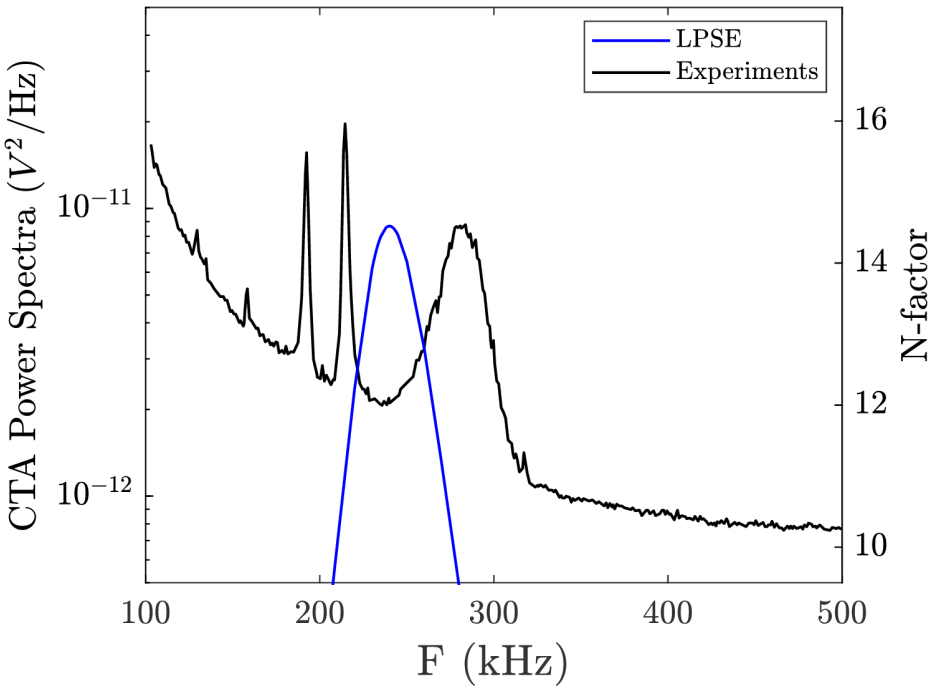

Figure 6.5: Peak frequencies of LPSE N-factor compared with RMS of experimental spectra at $x = 0.5$ m

6.2.2 Effect of Wall Temperature

In order to address the sensitivity between most amplified frequency and the wall temperature, an investigative case was tested using a constant wall temperature of $T_w = 386$ K. This was the lowest wall temperature measured at any point along the cone geometry during the experimental run. Figure 6.7 shows that computations originally performed using a constant wall temperature of 398 K acted as a sort of average that was bounded by the experimentally measured values along most of the cone geometry. It also shows that the wall temperature of the flared cone varied axially and temporally during the wind tunnel test.

A lower wall temperature decreases the boundary-layer thickness, which in turn increases the most amplified frequency. The effect on LPSE N-factor is shown in figure 6.8.

The most amplified frequency for the $T_w = 386$ K case was 246 kHz at the end of the geometry. However, the lower wall temperature is an exaggerated cooler wall than what

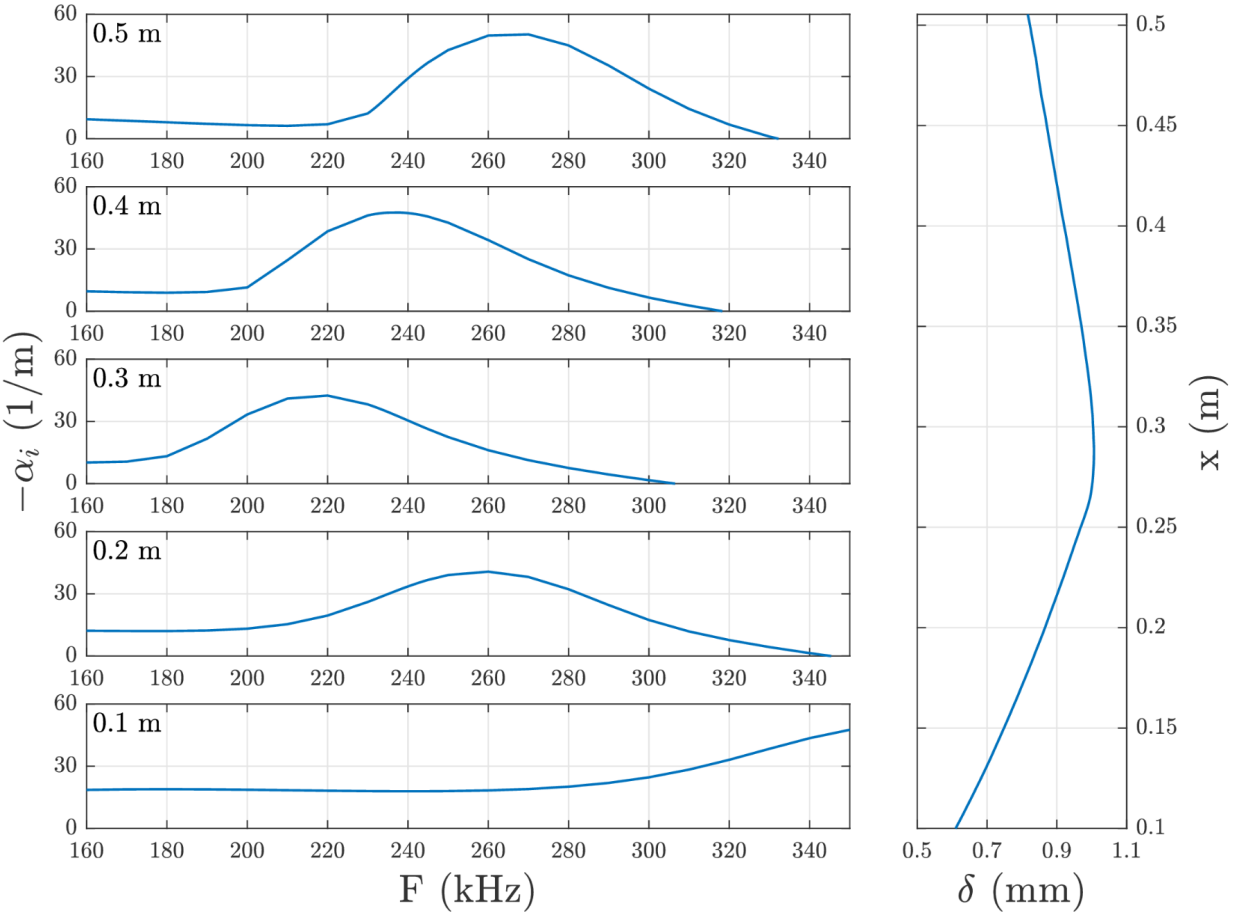

Figure 6.6: Local growth rates for LPSE second-mode instabilities and boundary-layer thickness of the Langley 93-10 cone

would be seen experimentally along the full extent of the cone model. Rather, this acts a a bound in order to see the maximum frequency shift attributed to the wall temperature difference. Despite this, the most amplified second-mode frequency only shifted from 241 kHz to 246 kHz. Experimental peak frequencies were near 280 kHz leaving a sizable difference to be accounted for still. It is concluded that the wall temperature effect alone is not enough to compensate for the difference between the computational and experimental observations.

6.2.3 Effect of Small Angle of Attack on Second Mode

One of the variables that must be closely monitored is the angle of attack of the model when mounted in the wind tunnel [93, 69]. For example, the simple act of tightening the

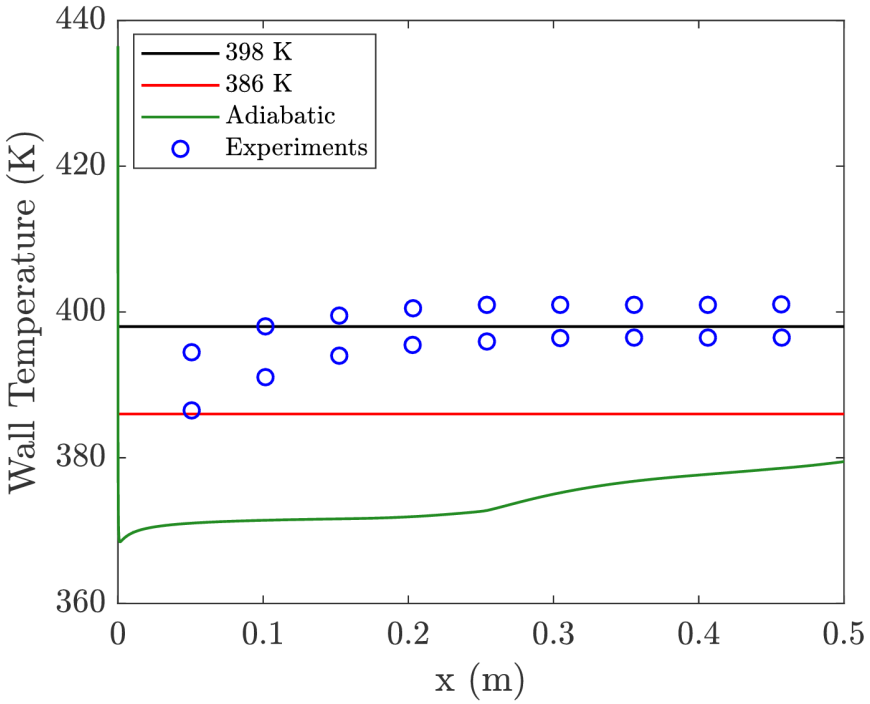

Figure 6.7: Wall temperature distributions for the Langley 93-10 flared cone. Shown are the experimental conditions in the M6QT, the adiabatic distribution, and two computational values with constant T_w.

mounting bolts can result in several tenths of a degree offset in geometric-aerodynamic alignment. Also, some studies have shown that disproportional heating of the nozzle will create a variation in boundary-layer thickness around the nozzle wall and thus create an asymmetric flow. Even a small AoA offset provides a modification to the basic state that influences these highly sensitive stability mechanisms. To investigate this effect, figure 6.9 shows a comparison of the most amplified frequency found for both the computational and experimental setups at an axial location of 0.495 m.

It can be easily seen that there is still a small difference in the most amplified frequencies between the computational simulation and wind tunnel results, even after the geometric alignment and aerodynamic effects are taken into account. A separate capability, known as the focused schlieren technique, was developed to replace the constant-temperature hot-wire anemometry technique [94].

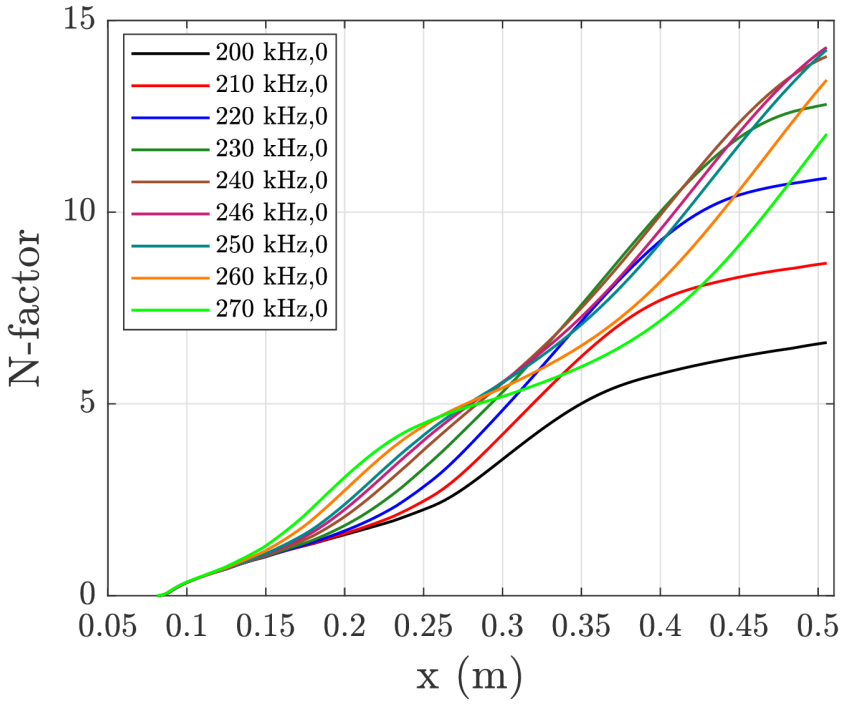

Figure 6.8: Second-mode N-factors with $T_w = 386$ K

- By measuring the top and bottom of the cone separately with a newly implemented focused schlieren technique, and comparing the frequency difference to a sensitivity estimate, there was an approximate 0.05° AoA aerodynamic offset in pitch in the freestream direction of the tunnel [94]. The effects of an unequal temperature distribution for the tunnel nozzle are shown in the translation of experimental data points in figure 6.9 from the empty circles to the red diamonds.

- Hofferth et al. also mention a possible offset in yaw in the direction along which the profiles were measured that would shift the experimental results even closer to the computational results. This effect is factored in as error bars in figure 6.9.

- Additionally, it is important to factor in the small disagreements that arise from the assumption of constant wall temperature on the computational model. Wall temperature effects could account for a shift on the order of a few kHz.

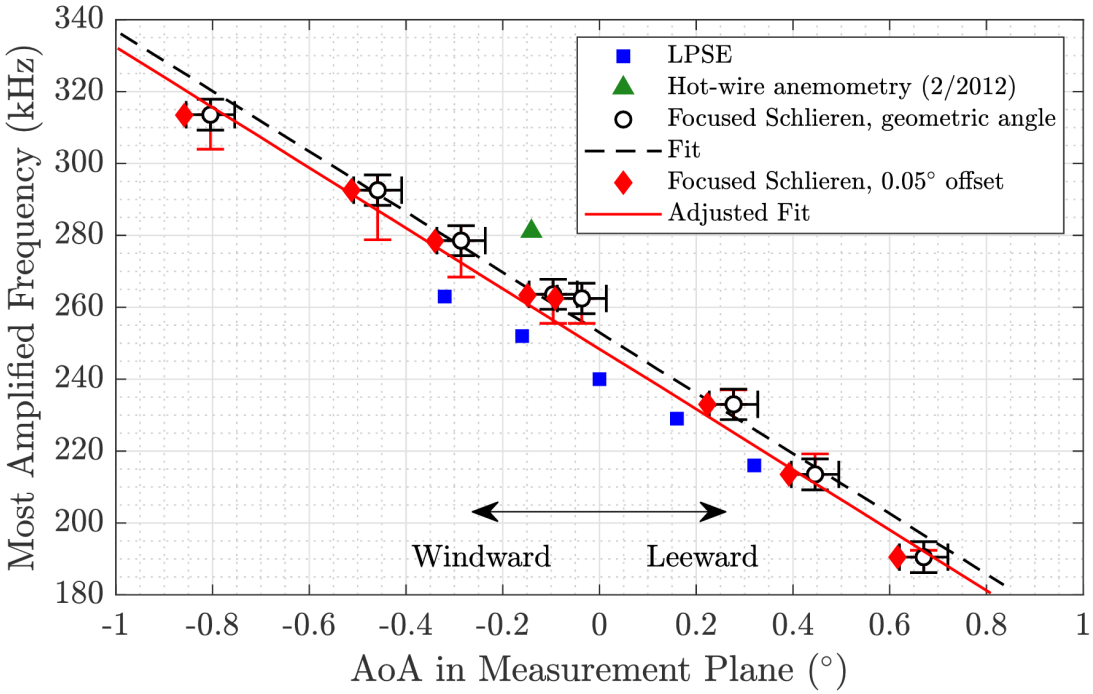

Figure 6.9: Most amplified second-mode frequencies from computations and experiments. Black error bars indicate uncertainty in the laser-scan alignment technique. Red error bars provide a notional estimate of the effect of residual out-of-plane misalignment.

After accounting for the additional potential sources of error, the difference in peak frequencies between the LPSE computations and experiments becomes greatly reduced. Another important takeaway of the present analysis is that the second mode has an extremely high sensitivity to small variations in AoA. Applying a data fit to the experimental measurements resulted in a $\Delta F \approx 8.4$ kHz for a change in AoA of only 0.1° while the LPSE results produced a slightly smaller relationship of $\Delta F \approx 7.3$ kHz per 0.1°.

With a possible offset in yaw with respect to the direction along which the profiles were measured, a focused schlieren measurement taken along the top of the flared cone no longer lies along the symmetry plane of the model with respect to the freestream flow direction. To this effort, an exploratory case was computed for an angle of attack of 0.32°. LPSE calculations were performed along the windward plane as well as multiple azimuthal locations up to 90° off of the windward plane. This would represent the off symmetry plane

measurements potentially occurring in the experiments. Figure 6.10 shows that the most amplified frequency varies slowly up to 30° away from the windward plane. An estimation of the azimuthal angle offset in the wind tunnel was predicted to be approximately 20°. This effectively falls within the range of azimuthal angles that computations found to have a very small effect on most amplified frequency and results in a shift of only 2 kHz.

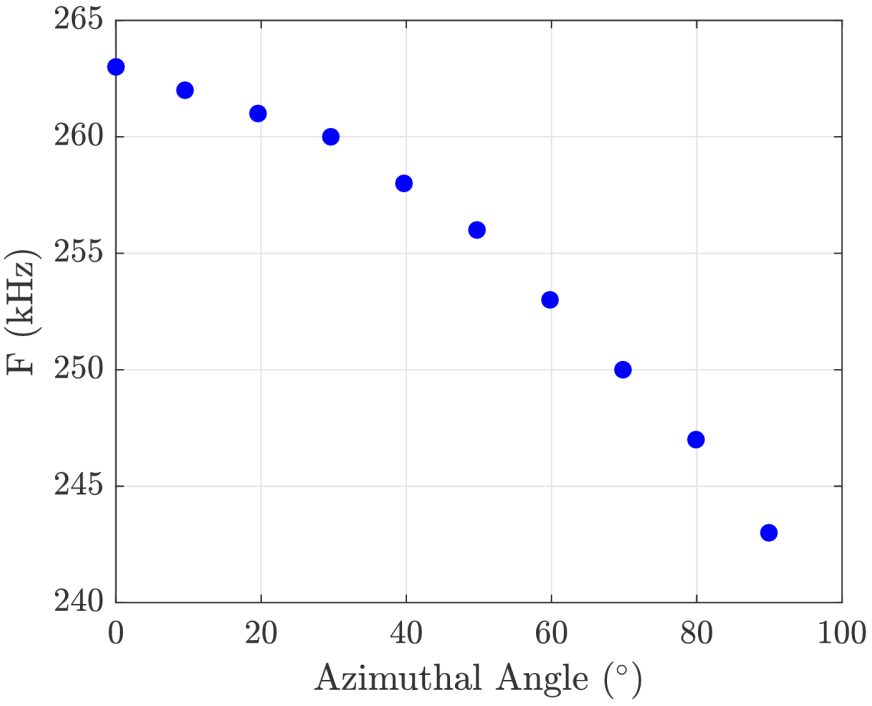

Figure 6.10: LPSE results for most unstable second-mode frequency for the Langley 93-10 cone at 0.32° AoA along the windward plane and azimuthally off windward

Working closely with the experiments of Hofferth et al. has led to the quantification of the extreme sensitivity of the second mode to changes in AoA. Special care must be taken when placing a model in a wind tunnel as even a small misalignment with the freestream flow can significantly alter the stability results. The sensitivity of second-mode disturbances can be used as an accurate alignment indicator, however, by measuring opposite sides of a symmetric model to make sure that peak second-mode frequencies match.

7. YAWED STRAIGHT CONE*

The crossflow instability has been widely studied at hypersonic speeds on generic configurations such as the yawed straight circular cone. Variations of this geometry have been analyzed using both experiments and computations producing a widespread range of literature on the subject [95, 96, 97, 98, 99]. Balakumar & Owens [76] and Gronvall et al. [100] considered DNS solutions of roughness induced stability on a 7° half-angle straight cone yawed to 6° AoA at Mach 6. In the Texas A&M M6QT, Craig & Saric [1] conducted detailed measurements within the boundary layer of the crossflow instability. Additionally, Muñoz et al. [101] used surface-mounted pressure sensors to measure the frequency and wave content of both low and high frequency instabilities in the regions associated with crossflow.

7.1 Geometry and Grid Topology

The yawed straight cone being used for this analysis has a nose radius of 0.05 mm, length of 0.508 meters (20 inches), and half-angle of 7°. Figure 7.1 shows the structured grid used in the calculation of the basic state and contains 369 points along the axial direction, 425 in the off-wall direction, and 399 azimuthally. Only half of the cone was modeled in order to take advantage of the symmetry of the flow and reduce computational cost. The grid underwent a manual iteration process in order to capture and resolve the shock. An area of difficulty exists at the nose of conical geometries for which a four-sided structured mesh must be fitted to a spherical or hemispherical nose. This problem was resolved by creating a rectangular domain on the nosetip and blending three connected domains to this section. This method produces two singularities at the intersection of these domains which are smoothed so as to minimize their effect before reaching the nose-body juncture. This grid topology, as well as the two singularities, can be seen in figure 7.2.

*Portions of this section are reprinted from "EPIC: NPSE Analysis of Hypersonic Crossflow Instability on Yawed Straight Circular Cone" by Nicholas B. Oliviero, Travis S. Kocian, Alexander J. Moyes, Helen L. Reed, 2015. *AIAA 2015-2772*, Copyright 2015 by Nicholas Oliviero, Travis Kocian, Alexander Moyes, Helen Reed.

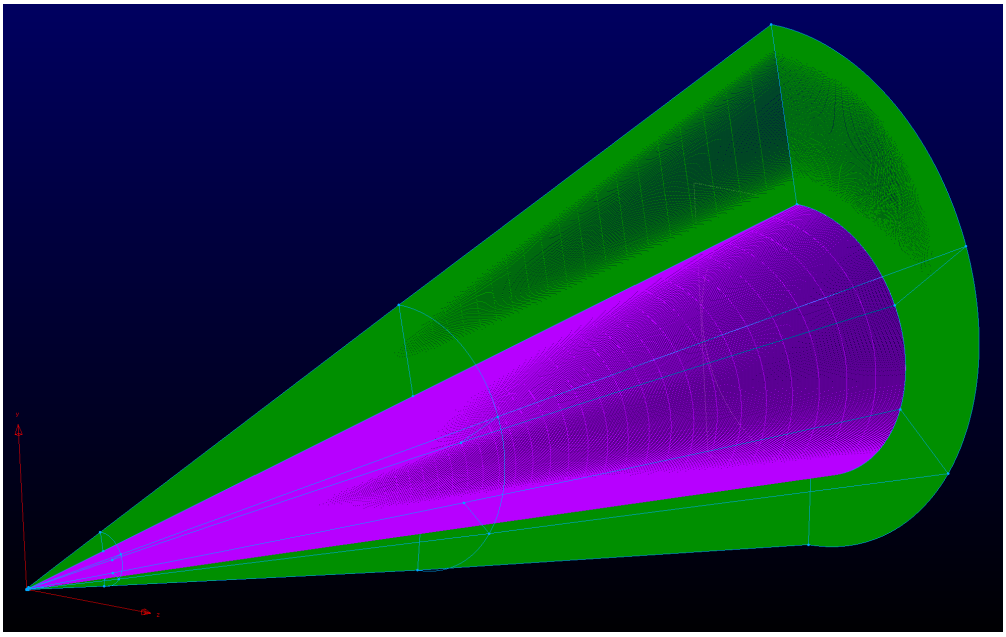

Figure 7.1: Structured grid for the yawed straight cone

7.1.1 Flow Conditions

The present yawed cone calculations are performed with the cone geometry having an AoA of 6°. A comparison of the conditions used in the basic-state calculation are shown in table 7.1 in conjunction with those used in the previously mentioned literature.

Quantity	Current	Balakumar & Owens	Gronvall et al.	Muñoz et al.	Craig & Saric	Edelman & Schneider
Re' (10^6/m)	10.1	10.4	9.5	$5.9 - 11.8$	10.0	9.8
M	6	6	6	6	5.91	6
AoA (°)	6	6	6	6	5.6	6
T_∞ (K)	53.42	53.42	52.85	57.32 ± 0.61	53.85	$50.0 - 51.83$
P_∞ (Pa abs.)	611.4	611.4	587.1	$443.4 - 886.7$	622.6	524.0
T_w (K)	300	300	300	298 ± 2	400	300

Table 7.1: Comparison of various computational and experimental flow variables used in the present analysis of the yawed straight cone

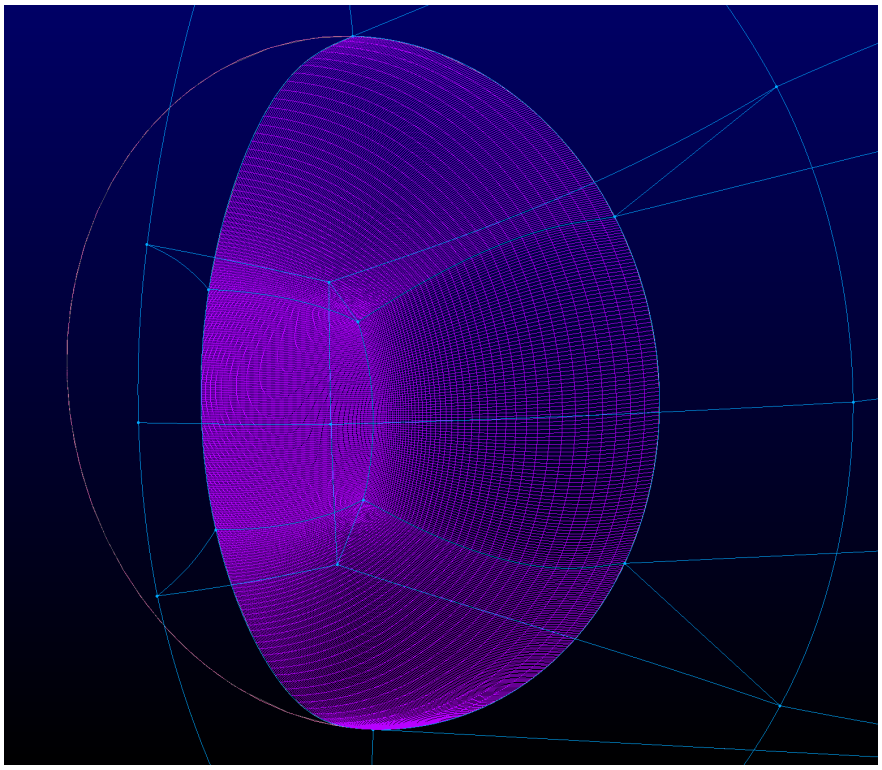

Figure 7.2: Grid topology on nose of yawed straight cone

A no-slip, constant $T_w = 300$ K wall boundary condition was applied on the cone surface. All computations were performed assuming air as an ideal gas and a constant $Pr = 0.72$. A Mach contour of the undisturbed basic-state solution is shown in figure 7.3.

7.2 Windward and Leeward LPSE

In regions where the flow is 2-D, such as along the planes of symmetry, both 2-D and 3-D mechanisms may be present and of interest to the stability problem. N-factors based on ρu for the 2-D disturbance along the leeward plane are shown in figure 7.4. The N-factors along this plane reach a value of 12.4 for a frequency of 80 kHz. It is to be noted that the area near the leeward plane has large spanwise gradients which may have an effect on the results in this region.

N-factors for the 2-D second-mode instability along the windward plane are shown in figure 7.5a. The boundary-layer height along this plane grows with increasing axial location

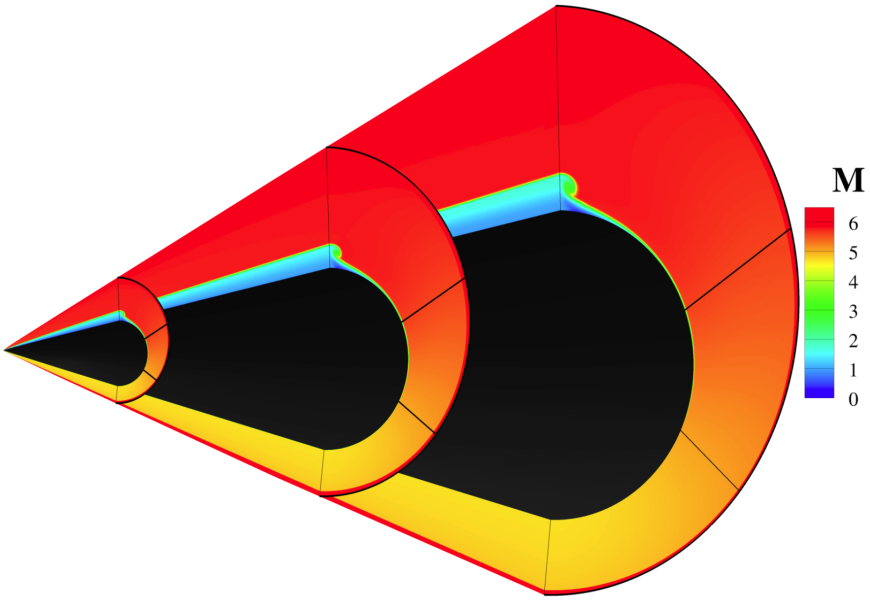

Figure 7.3: Yawed straight cone laminar basic-state solution

in a more standard sense than the leeward plane due to the lack of a "mushroom" structure. This, in turn, causes different second-mode frequencies to tune to the local flowfield and become unstable at different locations along the cone length. The maximum N-factor reaches a value of approximately 4 at the end of the cone for a frequency near 450 kHz. N-factors for the first-mode instability are shown in figure 7.5b. The most amplified first-mode disturbances along the windward plane are found to be oblique, and a maximum N-factor of 5.6 is achieved for a first mode with a frequency of 50 kHz and wavenumber of 100. At the last axial location, this most amplified disturbance has a wave angle $\psi = 53°$.

7.3 Vortex Paths and Spanwise Wavenumber Evolution

Balakumar & Owens [76] performed DNS calculations on a similar yawed cone. Figure 7.6 shows a comparison between crossflow vortex trajectories derived from the DNS solution and those predicted by the inflection-point method, keeping the designation specified in the DNS. Here, θ is the azimuthal angle around the cone with $\theta = 0°$ being windward and $\theta = 180°$ being leeward. The streamwise distance is along the axis of the cone. As Balakumar

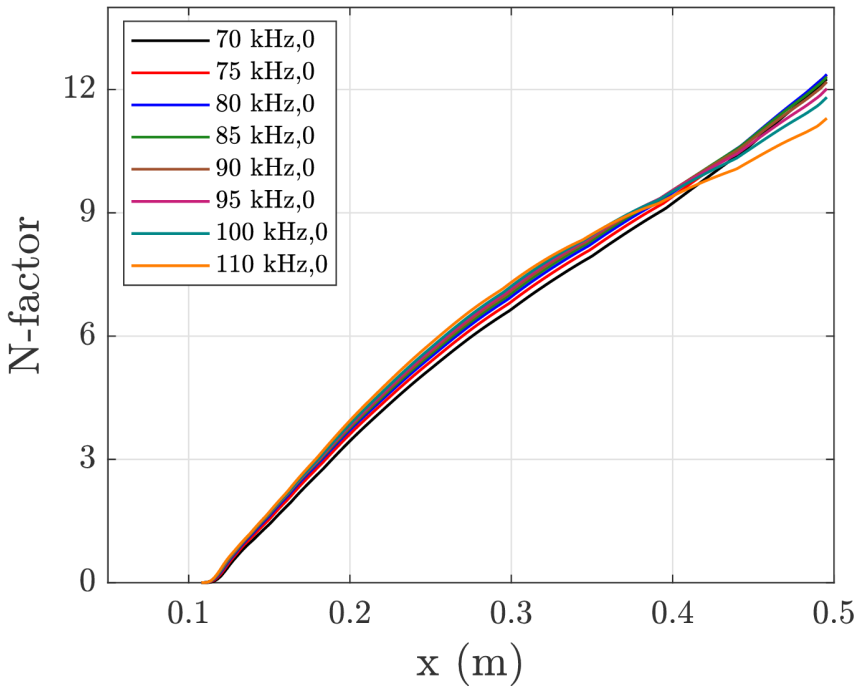

Figure 7.4: 2-D disturbance N-factors along the leeward plane

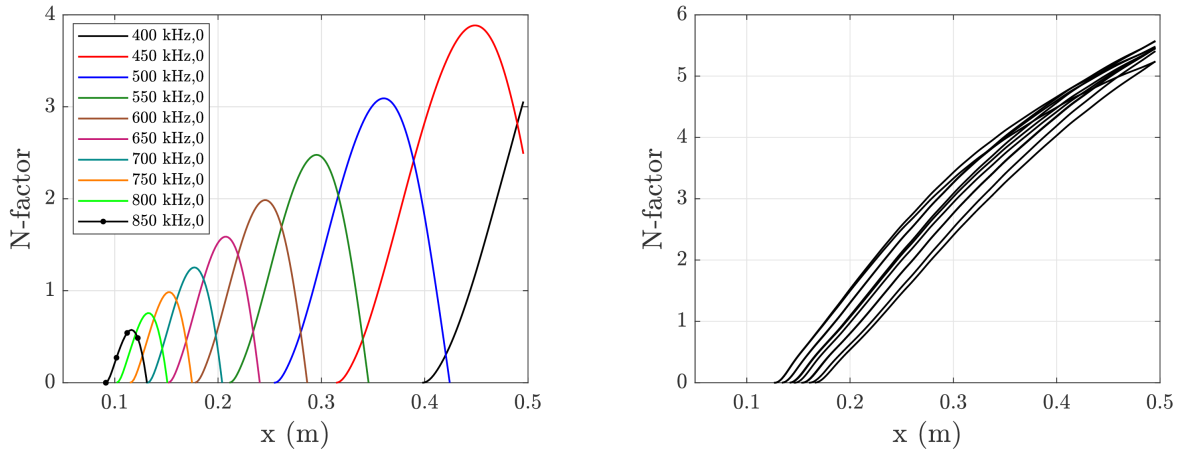

(a) Second-mode N-factors

(b) First-mode N-factors

Figure 7.5: Disturbance N-factors along the windward plane

& Owens [76] were modeling the flow with a necklace of rather large, periodically spaced roughness elements at an axial location of $x = 0.05$ m, their full disturbed simulation ended

approximately 0.2 meters down the cone. Alternatively, the present predictions are from a smooth (no roughness) undisturbed DPLR basic state prior to any stability calculations.

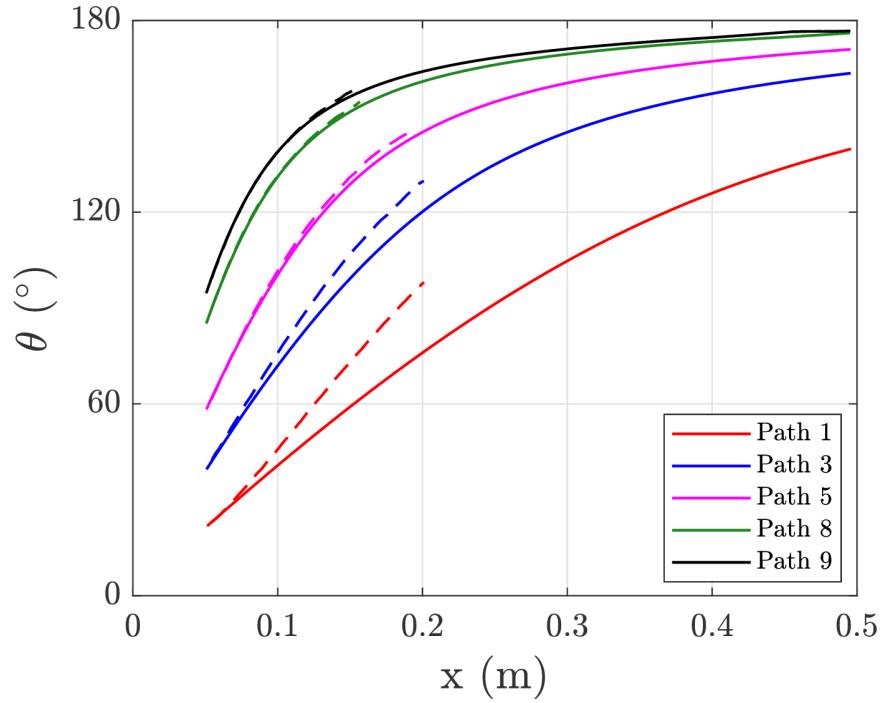

Figure 7.6: Comparison of inflection-point method (solid lines) vs. DNS vortex trajectories (dashed lines) for 5 paths

A separate DNS was produced by Gronvall et al. [100] on the yawed cone geometry. The conditions for that simulation are displayed in table 7.1. A patch of roughness was generated near the windward portion of the cone model between 0.05 m and 0.2 m. This created a series of heat flux streaks which stemmed from the roughness source. These streaks were extracted from their figure 15b and are shown alongside paths from the DNS of Balakumar & Owens [76] as well as paths extracted using the inflection-point method. This is shown in figure 7.7.

The predicted inflection-point paths are in qualitatively good agreement with the paths from Balakumar & Owens in regions closer to the leeward plane. However, as the inflection-

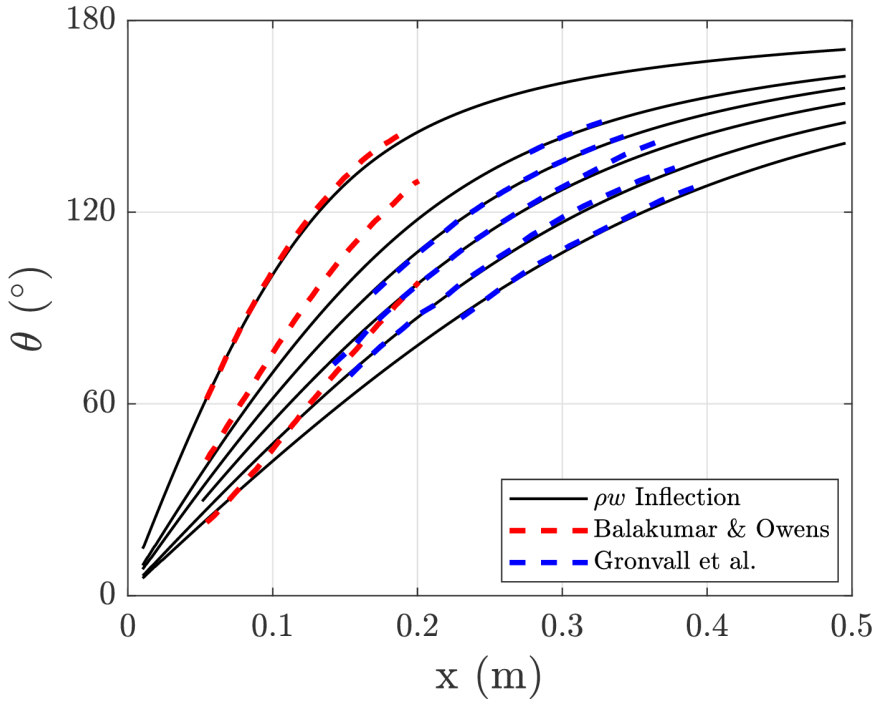

Figure 7.7: Comparison of inflection-point method paths, DNS trajectories from Balakumar & Owens, and DNS trajectories from Gronvall et al.

point paths move towards the windward plane they begin to deviate from the behavior of their DNS path trajectories. In this region, and in areas further downstream, the inflection-point method instead aligns with the paths from Gronvall et al. Short of having the exact details of the DNS solutions, there are a few possibilities that may account for the differences between the two DNS solutions themselves and the predicted vortex paths. These include a slight variation in flow conditions, a potential difference in the viscosity model, and the method used to introduce the stationary crossflow disturbance. The PSE method superposes the disturbance onto a clean basic state while the two DNS solutions generate the crossflow vortices with different roughness patterns. The Balakumar & Owens roughness was in a discrete pattern periodically spaced around the azimuth with a maximum height of 0.01 mm, resulting in estimated initial u-amplitudes between $0.1\% - 0.5\%$, while the roughness pattern of Gronvall et al. was a randomly distributed pattern near the windward plane with

an RMS height of 0.02 mm. It is possible that these roughness patterns are locally and uniquely modifying the flowfield in the simulations and that this variation may influence the disturbance trajectories.

In order to give a more thorough depiction of the various disturbance trajectory types, multiple sets of paths were extracted around the azimuth emanating from a single axial location and followed inviscid streamlines, the inflection point associated with the spanwise velocity component ($\bar{w}$) as discussed in Kuehl et al. [71], and the present inflection-point method. These path types are compared with the Balakumar DNS paths in figure 7.8.

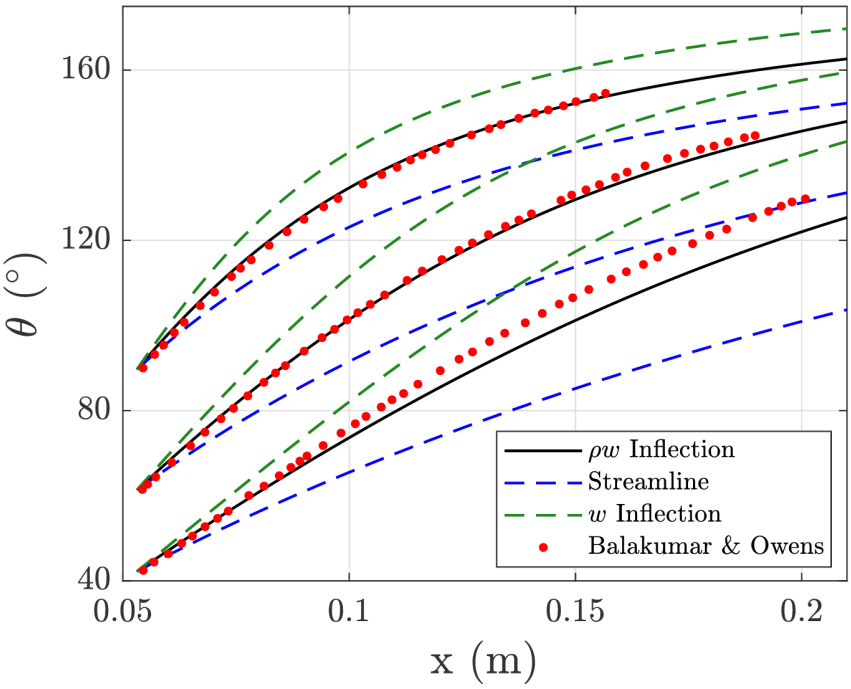

Figure 7.8: Comparison of DNS vortex trajectories (red dots), mass-flux inflection-point paths (black lines), spanwise velocity inflection-point paths (green dashed lines), and inviscid streamlines (blue dashed lines)

It is apparent that the vortex paths found from the inflection-point method differ rather significantly from those that would be found by following either an inviscid streamline or

the $\bar{w}$ inflection point. The vortex paths appear to be closer to the paths extracted from the DNS solution, especially as they move farther from the windward plane and into the region associated with strong crossflow. Reed et al. [74] showed that it is important to use a proper marching path as growth rates and N-factors vary depending on which direction one marches. This is further demonstrated in the following sections.

Streaks from stationary crossflow were observed using IR thermography on an identical geometry in the BAM6QT, and data corresponding to the disturbance trajectories were provided from Edelman & Schneider [102]. The range of experimental data was limited to the portion of the model visible through the viewing window. Crossflow vortices for the experiment were generated using 12 individual roughness elements spaced 9° apart. If extrapolated, this distribution would be equivalent to 40 elements around the full cone circumference. Figure 7.9 shows a comparison of paths calculated with the inflection-point method and those extracted from the IR images of the experiments.

The paths show excellent agreement with one another in the region available from the experiments. While one would not expect the data extracted from a wind tunnel experiment to be as smooth as data obtained numerically, the paths appear to have comparable slopes and trends with those predicted using the inflection-point method. In addition to providing an accurate path for modeling the evolution of the instability, the ability to predict the paths of the crossflow vortex can also be used to help define the optimal location for sensors in future experiments.

Based on this proposed method and utilizing vortex paths shown in figure 7.6, the evolution of wavenumber downstream is predicted and shown in figure 7.10a for the various vortex paths as designated in the DNS of Balakumar & Owens [76]. This calculation uses the inflection-point method coupled with the wavenumber adjustment as outlined in equation 4.4. The comparison is made with respect to a cylindrical frame to match the values provided from the DNS. In their DNS, Balakumar & Owens simulated a uniform necklace of periodically spaced roughness elements applied azimuthally around the cone at $x = 0.05$ me-

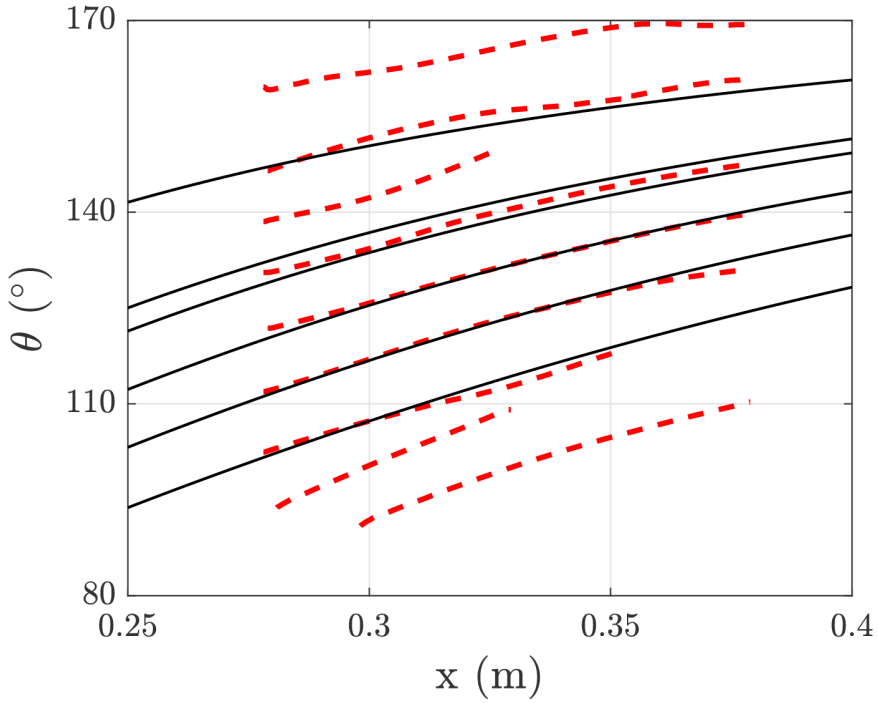

Figure 7.9: Comparison of inflection-point paths (black lines) and paths extracted from the Purdue experiment (red dashed lines)

ters from the nose to induce crossflow vortex formation. The element spacing corresponded to an initial azimuthal number of waves of 40 which was used as the initial value for the evolution of wavenumber downstream for all of the inflection-point paths.

For EPIC, the spanwise wavenumber is required to be oriented perpendicular to the marching direction. This distribution of wavenumbers is then input into EPIC and used as it marches down the body. The two methods described previously in equations 4.3 and 4.4 are compared in figure 7.10b.

Comparison with the wavenumbers extracted from figure 20b in the DNS of Balakumar & Owens [76] shows agreement in both the behavior of how the wavenumber varies for each path as well as the magnitude of the wavenumber at each axial location. Similar to the vortex paths, agreement with Balakumar & Owens is better when further away from the windward plane. However, recall that the present vortex paths are in the region near

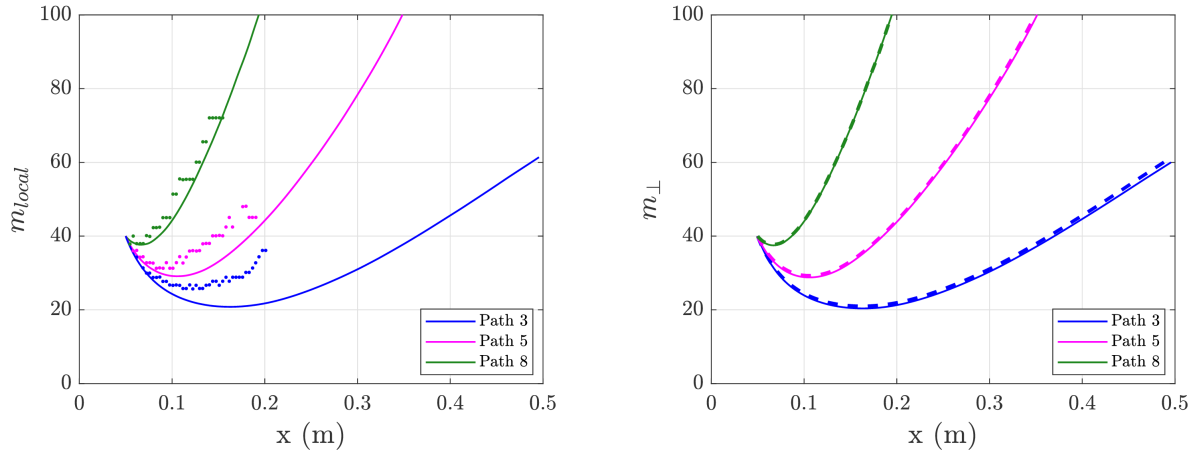

(a) Predicted number of waves in azimuthal direction vs. DNS

(b) Predicted number of waves perpendicular to marching path for χ_1 (solid) vs. χ_2 (dashed)

Figure 7.10: Varying azimuthal wavenumber for each path

the windward plane and are consistent with those of Gronvall et al. Unfortunately, the wavenumber variation is unavailable from their results. The differences in wavenumber may once again be attributed to the method used in generating the stationary crossflow vortices. If roughness is modifying the local flowfield and altering the disturbance trajectories, then the corresponding influence on the disturbance wavelengths due to the crowding of neighboring trajectories will also be affected. As with the calculation of the vortex paths, being able to obtain the variation of spanwise wavenumber from the basic state provides a means to more accurately model the physics of the stability problem.

7.4 3-D LPSE

The inviscid streamlines and inflection-point method paths were used for LPSE calculations to determine the growth of both stationary and traveling crossflow. Multiple paths for each method were run that span different azimuthal locations around the yawed cone geometry. Values shown represent the largest ρu N-factors for all azimuthal wavenumbers and frequency-wavenumber combinations for the stationary and traveling crossflow disturbances, respectively. Figure 7.11 shows the N-factors for stationary crossflow for both path types.

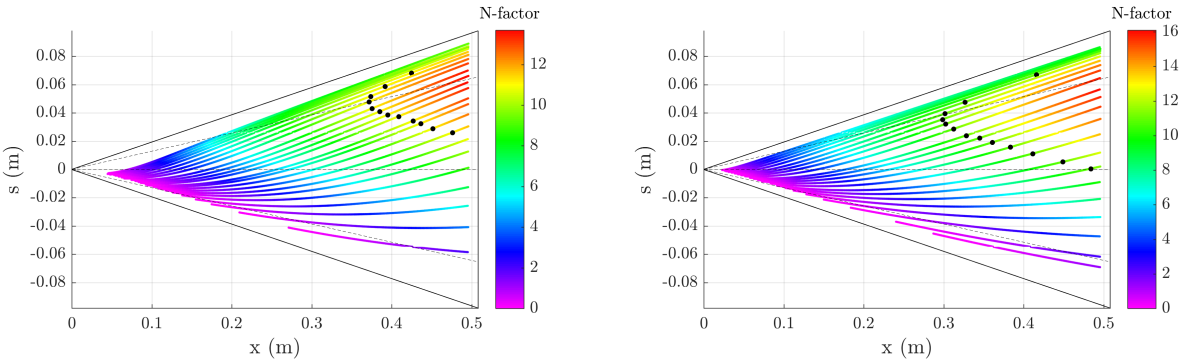

(a) (b)

Figure 7.11: N-factors for stationary crossflow using (a) inflection-point paths and (b) inviscid streamlines. The "dot" marks an N-factor of 11. The lower, center, and upper dashed lines on the flattened cone represent 30°, 90°, and 150° from windward, respectively.

It can be seen that calculations on the inviscid streamlines typically produce larger N-factors than those performed on the paths from the inflection-point method. The inflection-point paths and inviscid streamlines produce maximum N-factors of 13.7 and 16.1, respectively. Results for the inviscid streamlines match very well with the LPSE streamline results of Balakumar & Owens (see their figure 10b) on the same geometry. Dots have been placed at the locations for which N = 11. This allows for an easier visualization of the front created at a stage of constant amplification.

Figure 7.12 shows N-factors for the traveling crossflow case which obtained a maximum N-factor of 19.3. The frequency band for the most amplified disturbances for all of the paths was between $15 - 50$ kHz. Inviscid streamlines are used for the marching paths again as a verification with the LPSE results provided by Balakumar & Owens (see their figure 10a). It is important to note that the stationary crossflow path formulation does not apply in this case, and rather the group velocity direction should be modeled.

Traveling crossflow reaches a higher N-factor than the stationary crossflow instability for each respective path. This agrees with the LPSE results found in Balakumar & Owens [76] in which the traveling crossflow case generally reaches a larger N-factor at a smaller axial distance than the stationary case does. Both cases also show that the amplification front

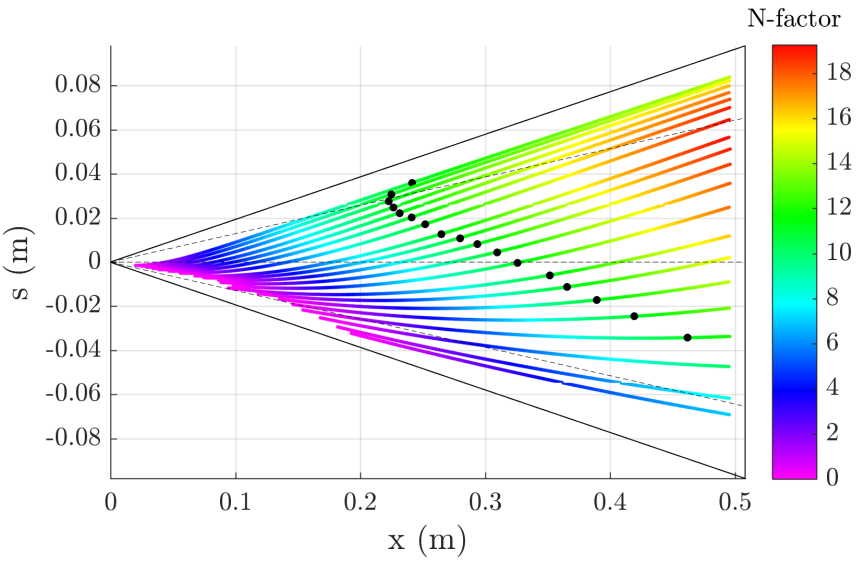

Figure 7.12: N-factors for traveling crossflow using inviscid streamlines. The "dot" marks an N-factor of 11. The lower, center, and upper dashed lines on the flattened cone represent 30°, 90°, and 150° from windward, respectively.

for the crossflow instability takes on an arc shape where the front is farther forward in the regions above the shoulder where significant 3-D boundary-layer effects occur and farther downstream near the windward and leeward planes.

The presented results use the wavelength scale factor introduced previously in equation 4.4. It is argued that the resulting effects of the correction on the spanwise curvature of the vehicle are small in comparison to the need for modeling the variation of local wavelength and that the wavelength scale factor adjustment more accurately emulates the actual physics of the problem. In an effort to investigate this, LPSE calculations were run for three paths coinciding to figure 7.10a. Each of the stationary crossflow calculations were initialized at an axial location of $x = 0.05$ meters with an azimuthal wavenumber of 40. This corresponds to the number and location of roughness elements used in the Balakumar & Owens DNS solution. N-factor results were compared for various combinations of spanwise curvature and wavelength scale factor adjustments. 1) As a baseline, each path was initially run without using any additional scale factor and by including all curvature terms. In other

words, the spanwise wavenumber $m_\perp$ was held constant and the disturbance wavelength was dependent only on the radius of revolution. This is the most common procedure utilized in PSE calculations for a conical geometry. 2) Then, the h_3 spanwise curvature term was turned off in order to determine the effect the term has on the growth of the disturbance. 3) Each path was then run using the scale factor described in equation 4.4 in addition to including all curvature terms. This is the method used for the stability calculations present in this paper. 4) Finally, the scale factor is included without the h_3 curvature term. This calculation is marked with an asterisk since removing the spanwise curvature term eliminates the ability to satisfy the irrotationality condition from equation 4.2. The purpose of this calculation is rather to provide the influence of spanwise curvature when the scale factor is applied to the wavelength. The maximum ρu N-factor for each of the four computations is provided in table 7.2.

Run #	χ_2	h_3	Path 3 N_{max}	Path 5 N_{max}	Path 8 N_{max}
1	OFF	ON	12.48	11.36	8.68
2	OFF	OFF	12.87	11.63	8.75
3	ON	ON	9.81	9.14	3.94
4	ON	OFF*	10.17	9.54	4.57

Table 7.2: Effects of spanwise curvature (h_3) and wavelength scale factor (χ_2) on maximum N-factor. The case marked with an asterisk ($*$) does not satisfy the irrotationality condition.

While the spanwise curvature term does have an effect on maximum N-factor, the largest change between a traditional run with and without that curvature term (run 1 & run 2) is only $\Delta N = 0.39$. Conversely, the difference between a traditional run and one with the wavelength scale factor (run 1 & run 3) is noticeably larger. A difference of up to $\Delta N = 4.74$ can be seen in table 7.2. This result helps reinforce and justify the use of the scale factor to more accurately model the spanwise wavelength of a disturbance as it develops downstream as well as the adjustment to the spanwise curvature term to satisfy irrotationality.

7.5 3-D NPSE

N-factors obtained from an LPSE evaluation can be very useful and insightful as to the behavior of an instability and remain so as long as laminar flow is maintained and the disturbances remain linear. The LPSE formulation itself does not take initial disturbance amplitude into account. However, the very nature of the stationary crossflow instability creates structures that tend to distort the mean flow and can display nonlinear effects early on. Thus, it is prudent to model this mechanism using NPSE.

To verify EPIC, a comparison was made with the DNS of Balakumar & Owens. They simulated 40 uniformly spaced roughness elements applied azimuthally around the cone at an axial distance of 0.05 meters from the nose to induce crossflow vortex formation. Initializing downstream of the roughness with the initial amplitudes and wavenumbers estimated from their figures 19b and 20b, respectively, EPIC was marched along the predicted vortex paths numerically corresponding to those from the DNS. Inputs for these calculations are provided in table 7.3 where $u'_{(0,1)}$ represents the primary mode amplitude with respect to U_e.

Path	x_0 (m)	$u'_{(0,1)}$ (%)
Path 3	0.062	0.33
Path 5	0.059	0.35
Path 8	0.059	0.24

Table 7.3: Inputs for stationary crossflow NPSE

The downstream wavenumbers were designated to be those predicted from the basic state (figure 7.10a) to account for the vortex paths locally diverging or converging together. In the EPIC NPSE calculation, it was found sufficient to include the mean-flow distortion term, the primary mode, and five superharmonics such that the impact of additional harmonics became negligible.

Figure 7.13 shows NPSE maximum u-amplitudes for three different paths and compares

them to DNS results derived from figure 19 found in Balakumar & Owens [76]. The path numbers correspond to the same paths as seen in figure 7.6 of this paper and figure 19a from the DNS. Here, u is assumed to be in the direction of the stationary crossflow vortex along the cone surface for the NPSE solution.

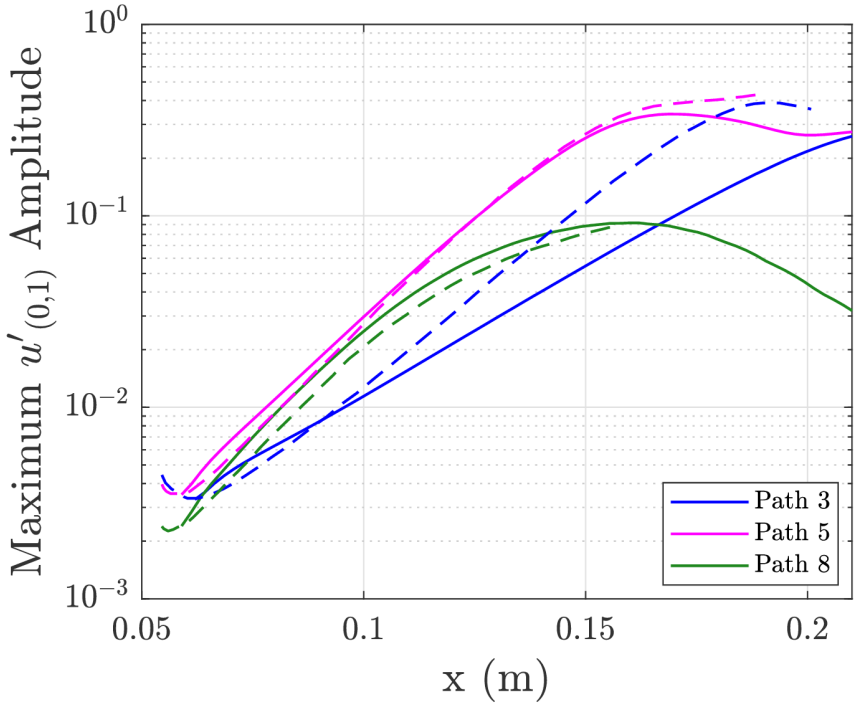

Figure 7.13: Maximum u-amplitudes from NPSE (solid lines) compared with u-amplitudes calculated from DNS (dashed lines)

The NPSE calculations were started at axial locations corresponding to positive growth in the DNS, and the results compare favorably with the DNS amplitudes. Some of the variance stems from the slight differences in disturbance trajectory described prior and the evolution of downstream wavenumber. It is also worth noting that path 8 approaches the leeward plane of the model where the flowfield varies more rapidly in span. This is an area that is challenging to the PSE methodology as it assumes spanwise invariance in the basic state.

The disturbance modes can be reconstructed into a wave and added to the basic-state values in order to recreate the full flowfield. Figure 7.14 shows the development of the stationary crossflow vortices at different axial and azimuthal locations. The development compares well locally with the DNS results in figure 13 from Balakumar & Owens [76]. Crossflow wavelengths, amplitudes, and the physical height of the vortices are well predicted.

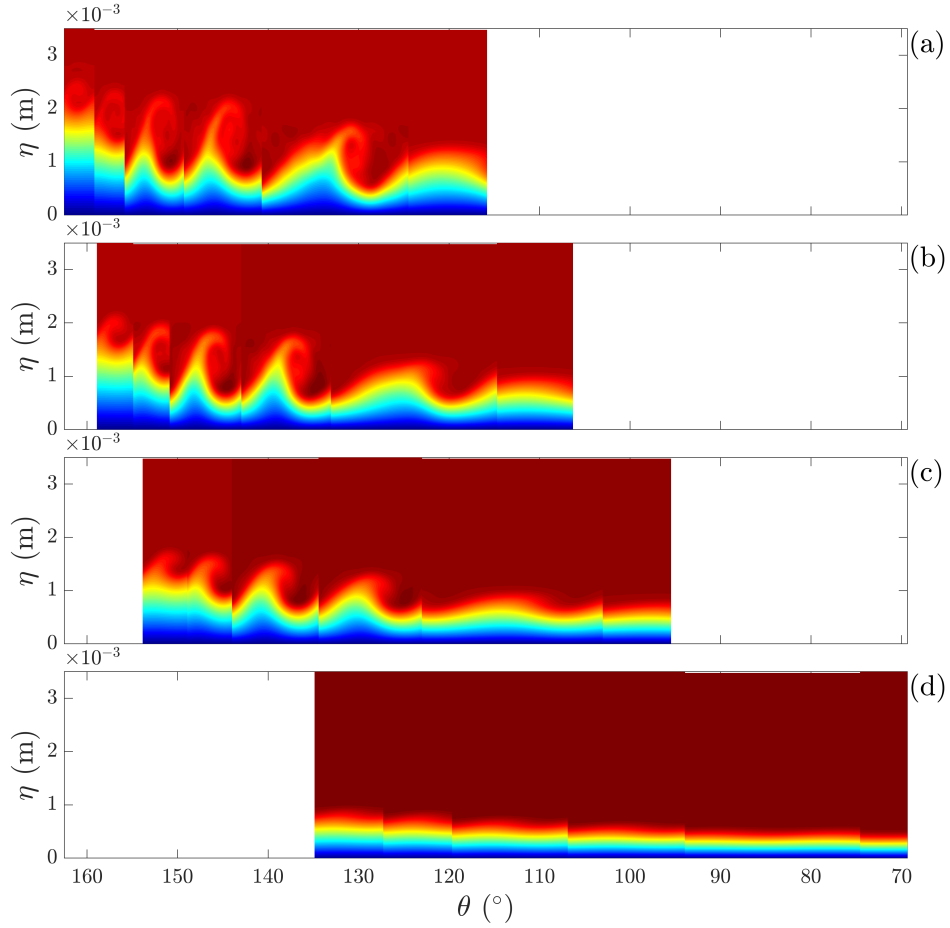

Figure 7.14: Total flow of u-velocity (basic state combined with perturbation values) showing the development of stationary crossflow vortices at axial locations of (a) 200 mm, (b) 175 mm, (c) 150 mm, and (d) 100 mm

Of note is that the rebuilt flowfield is not continuous. In order to produce figure 7.14, NPSE was used for the inflection-point paths along the cone. Each path was given a differ-

ent initial u-amplitude in order to reflect the disturbance amplitude that would be seen as a product of the ring of roughness elements used by Balakumar & Owens [76] (their figure 19b). The evolved disturbances from each path were then combined with the basic state at the designated locations and assumed to span an azimuthal interval θ until boundaries of individual runs intersected. Axial distances of 100 mm, 150 mm, and 200 mm compare directly with axial locations from the DNS. The 175 mm axial distance shows the intermediate growth between the 150 mm and 200 mm stages.

The development of the vortices becomes more distinct as axial distance increases and the amplitudes of the disturbances grow. It can also be seen that the physical presence of the crossflow vortices is most prominent above an azimuthal angle of 100 degrees from the windward plane where the flowfield is significantly 3-D.

7.5.1 Instability Mechanisms Observed at Braunschweig

Experiments were conducted by Muñoz et al. [101] on a 0.4-meter long 7° half-angle cone at 6° AoA in the Hypersonic Ludwieg Tube at Braunschweig in Germany at conventional tunnel conditions. Both low and high frequency instabilities were seen in regions usually associated with crossflow. The cone was instrumented with surface-mounted pressure sensors in order to measure the spatial extension, frequency content, and wave content of these instabilities at axial locations of $x = 0.209$, 0.234, 0.26, and 0.36 m.

Muñoz et al. [101] took measurements at $x = 0.36$ m at an angle $\theta = 70°$ from the windward plane and found an instability with a frequency between $20 - 50$ kHz and wave angle ψ (based on the local inviscid direction) of $65.4° \pm 3.5°$. The local wave angle led them to believe that the disturbance was a first-mode instability.

Figure 7.15a shows LPSE N-factors along an inviscid streamline that intersects the measurement location for frequencies ranging from $10 - 70$ kHz. Each frequency was run with a wide range of azimuthal wavenumbers and the combination that resulted in the largest N-factor for each frequency at $x = 0.36$ m is shown in figure 7.15b. From this evaluation, the locally most amplified frequency observed is 33 kHz with an N-factor of 11.25.

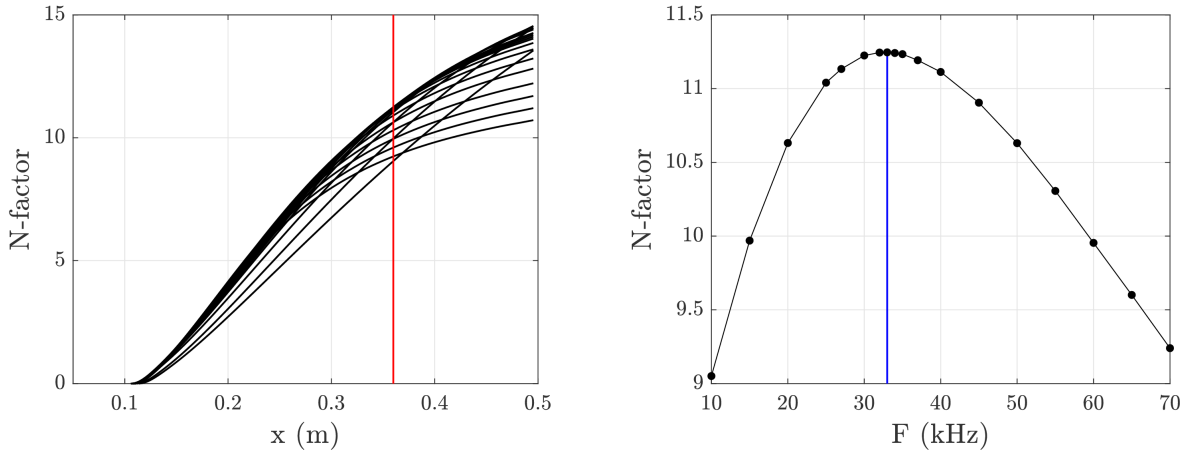

Figure 7.15: (a) LPSE N-factors for frequencies between $10-70$ kHz with a red line marking $x = 0.36$ m and (b) N-factors at an axial location of 0.36 m with azimuthal angle $\theta = 70°$ from windward (maximum N-factor corresponds to 33 kHz and is shown with the vertical blue line)

The local wave angles were then calculated at the sensor location for the frequency-beta combinations shown in figure 7.15. The 33 kHz disturbance has $\psi = 66.9°$ at the measurement location and is marked in figure 7.16 with a vertical line. The frequency of this disturbance is within the range of frequencies seen in the experiments and the wave angle is in excellent agreement with the measured value.

Additional calculations were performed in an effort to distinguish which type of instability mechanism was being measured. First, stationary crossflow was run on the same path using the same global spanwise wavenumber, k_c, as the 33 kHz disturbance that produced the largest N-factor at $x = 0.36$ m. This wavenumber was held constant as the frequency was slowly increased up to 33 kHz. Figure 7.17 shows the u, v, and w modes, normalized by the u component, for each of these incremental frequency-beta combinations. These modes show a gradual progression and change as the frequency is increased rather than a rapid and sudden switch. Growth rates were also obtained from LPSE calculations for a range of frequencies at the $x = 0.36$ m measurement location. These growth rates correspond to

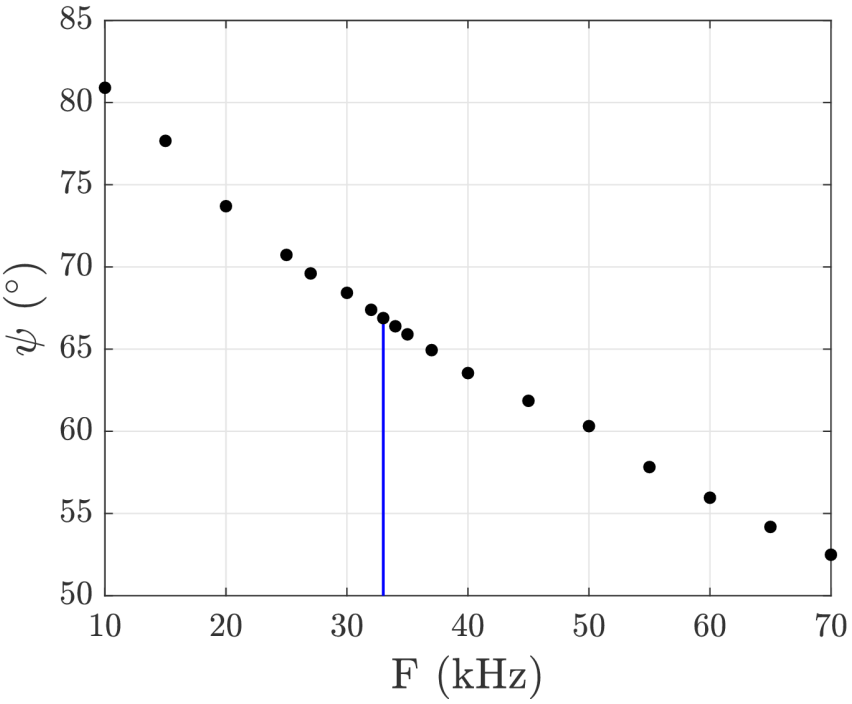

Figure 7.16: Wave angle based on local inviscid direction vs. frequency. The vertical blue line marks the 33 kHz disturbance.

disturbances with the same constant global wavenumber as previously mentioned and are shown in figure 7.18. The 33 kHz disturbance is shown to align with the curve originating at stationary crossflow. The combined behavior of the modes and local growth rates lead to the belief that the instability is traveling crossflow.

7.5.2 M6QT Experimental Comparison

Experiments on a yawed straight cone were performed in the Mach 6 Quiet Tunnel (M6QT) at Texas A&M University by Craig & Saric [1]. The model length and dimensions were identical to the model used in all of the stability calculations presented thus far. However, the experiment was run at slightly different conditions than those of existing basic-state computations used for the comparison. These conditions are listed in table 7.1.

The experiment provided detailed azimuthal distributions for off-wall hot-wire measurements of boundary-layer mass-flux profiles at different axial locations from the nose tip.

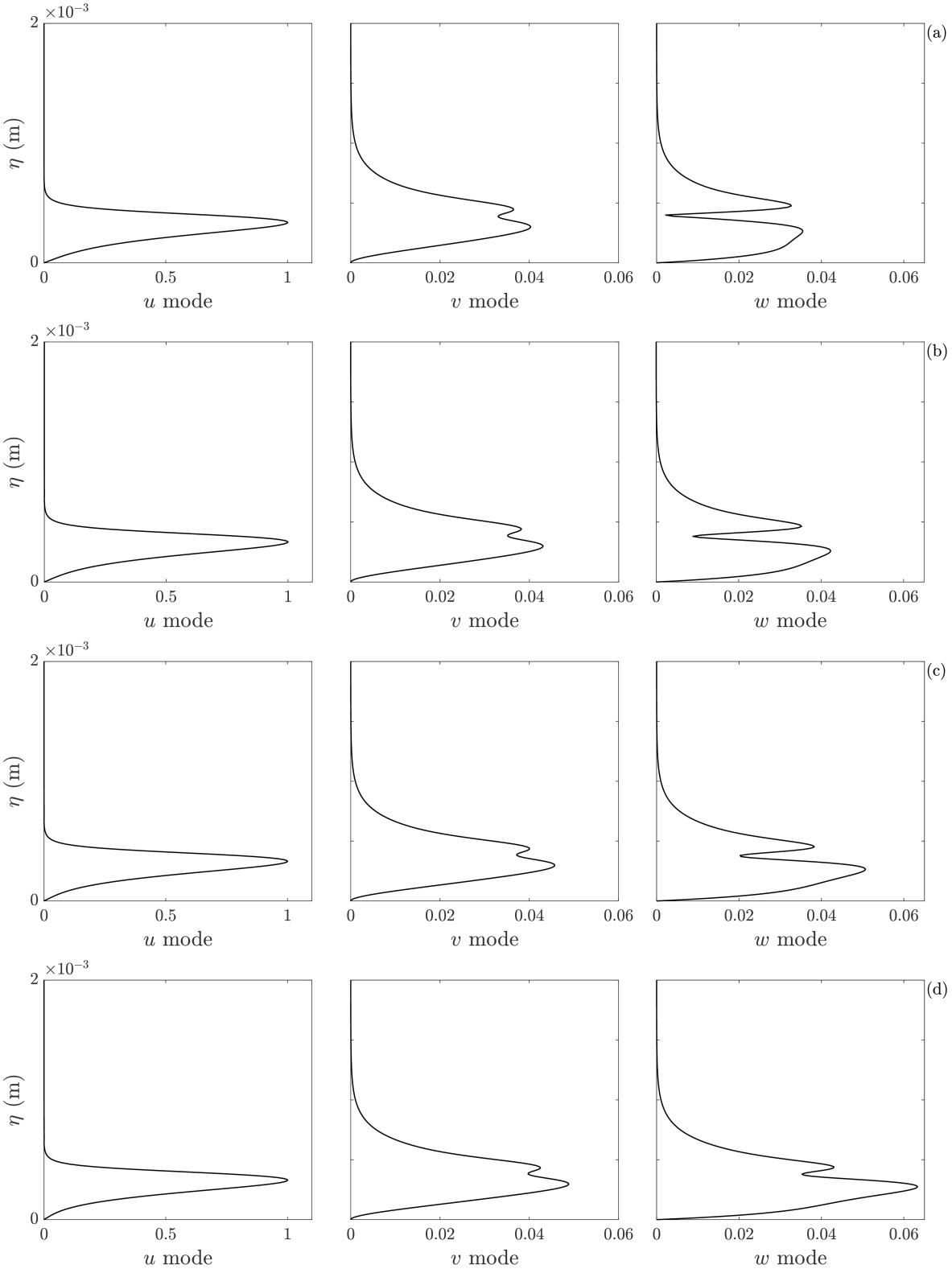

Figure 7.17: u, v, and w mode shapes of disturbances at neutral points for (a) 0 kHz, (b) 10 kHz, (c) 20 kHz, and (d) 33 kHz

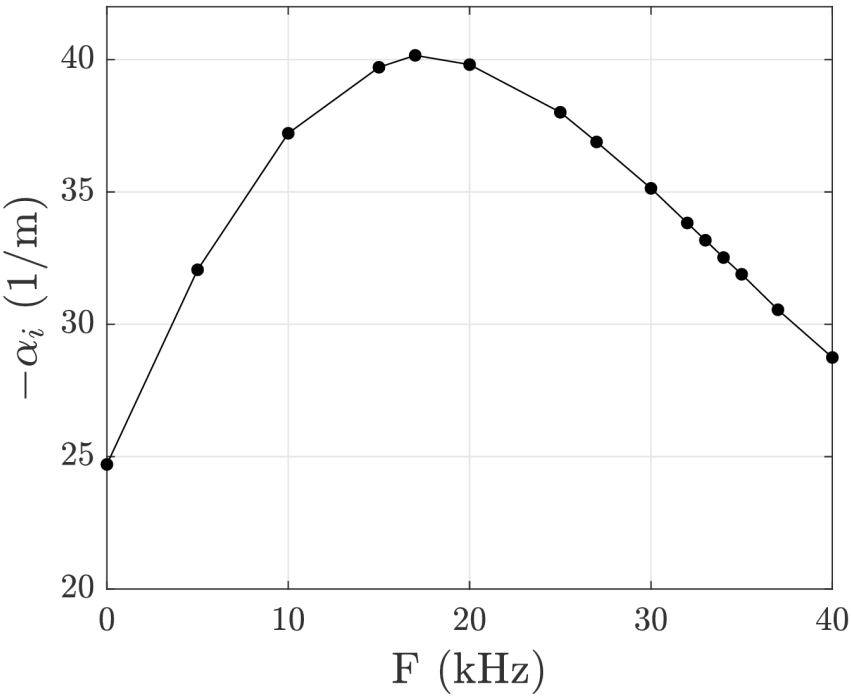

Figure 7.18: Growth rates for disturbances with constant wavenumber k_c at $x = 0.36$ m

Three stationary crossflow vortex paths corresponding to these measurement locations were predicted using the inflection-point method. These paths intersect locations with an azimuthal angle of 118° from windward at 0.36, 0.37, and 0.38 meters axially and are shown in figure 7.19a. Based on an estimation of the wavelengths found in the experiment, the stationary crossflow disturbance formed with an azimuthal wavenumber of 60 at these locations. Using this observed value, the variations in azimuthal wavenumber along each path were calculated as described previously. These variations are shown in figure 7.19b.

Since the surface of the model used in the experiments was polished to an RMS roughness height of 2.15 μm with no artificially added roughness elements, one would expect that the wavelengths of the crossflow vortices which formed would directly correlate to the naturally most amplified wavenumber under the given flow conditions. To investigate this, an LPSE calculation was performed on the path which intersected the center measurement location at $x = 0.37$ meters. Results for a span of different wavenumbers are shown in figure 7.20.

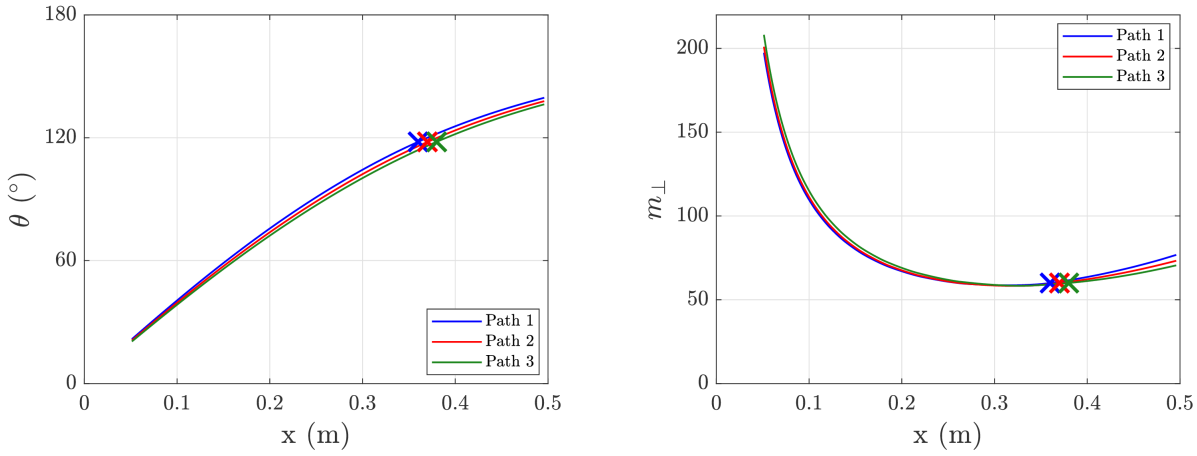

(a) (b)

Figure 7.19: (a) Inflection-point paths and (b) their varying azimuthal wavenumbers are provided. Each × marks a location of comparison with experimental results.

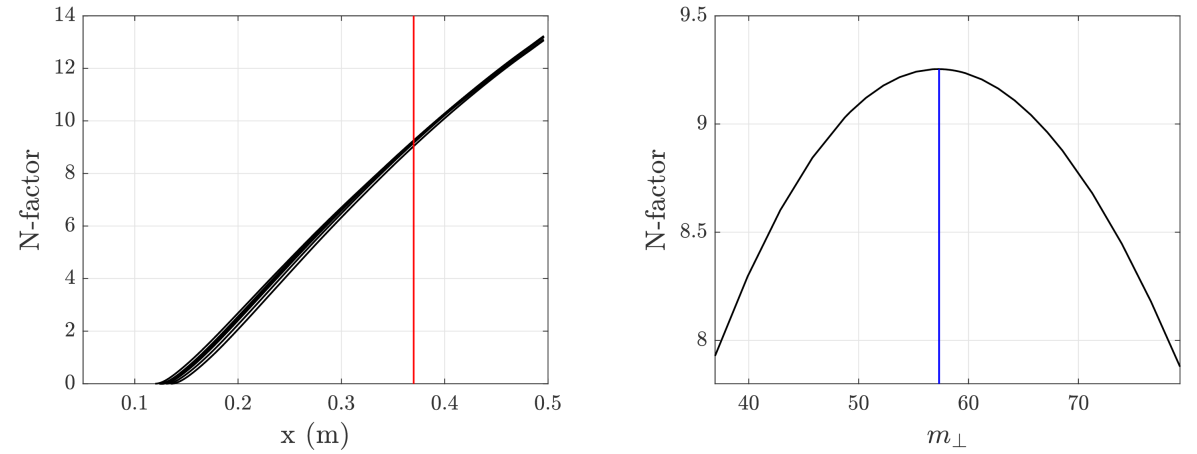

(a) (b)

Figure 7.20: (a) N-factors along a vortex path intersecting the experiment measurement location at $x = 0.37$ m and (b) N-factor vs. number of waves predicted by equation 4.4 at the measurement location

The wavenumbers for the stationary crossflow disturbances in figure 7.20a are initialized at an axial location of $x = 0.051$ m. This is the same starting location as that shown in figure 7.19a. From this analysis and by applying equation 4.4, the most amplified disturbance at $x = 0.37$ m and $\theta = 118°$ had an initial azimuthal wavenumber of 193 upstream (corre-

sponding to an initial crossflow disturbance wavelength of approximately 0.21 mm). This instability produced a downstream wavenumber of 57 that was very near the observed value of 60 from the experiments and is marked with a vertical line in figure 7.20b. In comparison, it was predicted that 201 initial azimuthal waves would produce a local wavenumber of 60 at the measurement location based on figure 7.19b. This result exhibits remarkable agreement between the predicted value from the computations and the estimated value from the experiments. Additionally, these findings support the claim that the most amplified wavenumber from LPSE would match that seen in the experiment while further validating the method used in predicting the evolution of spanwise wavenumber.

NPSE calculations were performed for stationary crossflow such that the local azimuthal wavenumber was 60 at the three locations of comparison. Disturbances were initialized at an axial location of $x = 0.2$ meters with u-amplitudes of 3×10^{-4} based on U_e. As the upstream condition from the experiments was unknown, this value was iterated to best match the resulting computational flowfield with the experimental flowfield and could be used by other stability modelers as a guideline for initial conditions on a smooth surface. The flowfield was then reconstructed by combining the velocity and density disturbances with the basic state and conducting a series of coordinate transformations to be consistent with the experimental measurements. Contours of axial mass flux are shown in figure 7.21 alongside experimental measurements.

The structures of the vortices agree well with those measured in the M6QT using hot-wires [1], and both experimental and computational results show the crossflow vortices become more developed and pronounced as axial location increases. The experiments were also able to measure a mass-flux RMS at the three locations and show a representative mode shape of the stationary crossflow disturbance. Corresponding computational RMS profiles were produced from the axial ρu mass flux of the basic state and the disturbances and are shown in figure 7.22 alongside the results from the experiment. The maximums of the mass-flux RMS mode shapes for both the computations and experiments achieve values of approximately

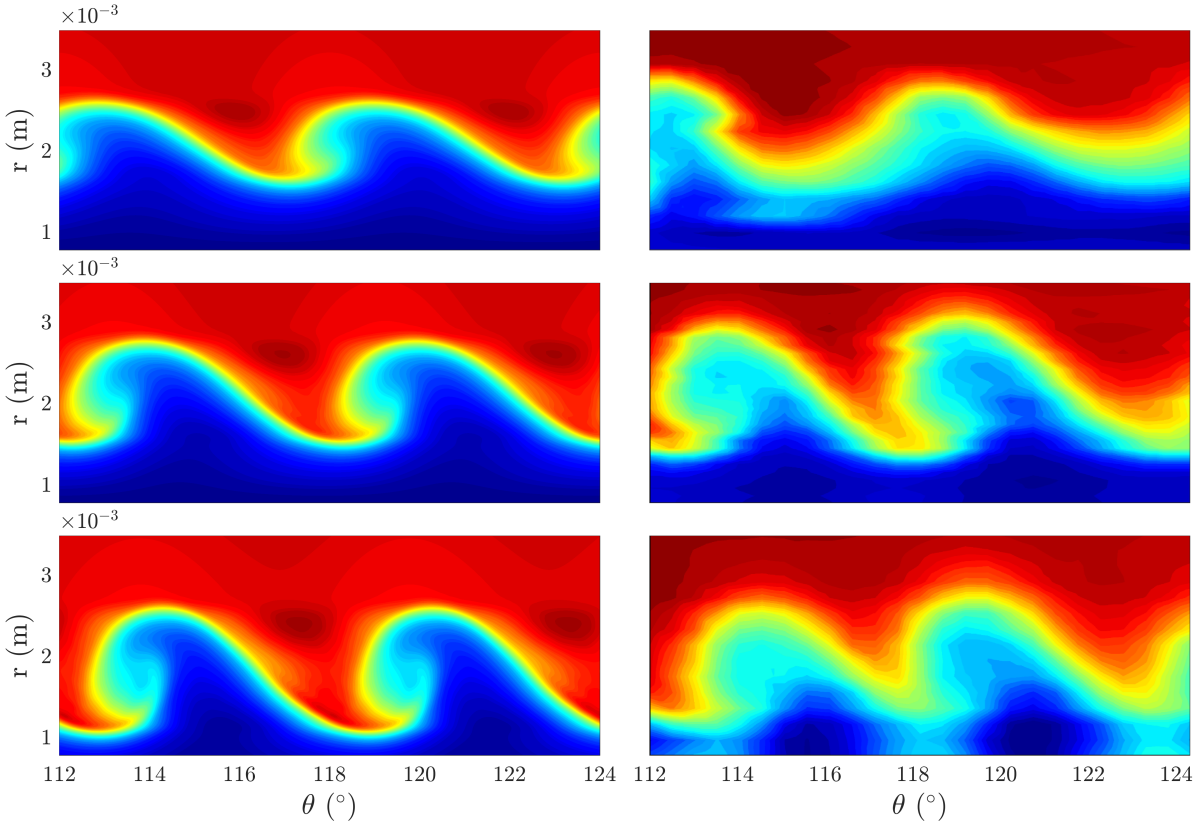

Figure 7.21: Development of stationary crossflow vortices at an azimuthal angle of 118° at $x = 360$ mm (top), 370 mm (center), and 380 mm (bottom) for NPSE computations (left) and the M6QT experiment (right). Contours are created using normalized ρu mass flux. (Experiment image attributed to Craig & Saric [1])

0.2, although it is difficult to obtain a quantitative comparison with the experiments without knowing the initial amplitudes for the disturbances upstream. Qualitatively, the RMS mode shapes for both the computations and experiments appear to develop into a double-lobed structure with similar cross-over heights. Since the experiments did not know the exact location of the wall with respect to the hot-wire, the computations were translated vertically in order to match the estimated location of the experimental measurements.

EPIC has demonstrated the ability to capture the nonlinear development of stationary crossflow and validated results with the quiet tunnel experiments of Craig & Saric. Matching the downstream spanwise wavelength of the experimentally witnessed vortices also further supports the use of the χ_2 scale factor when using PSE to model crossflow.

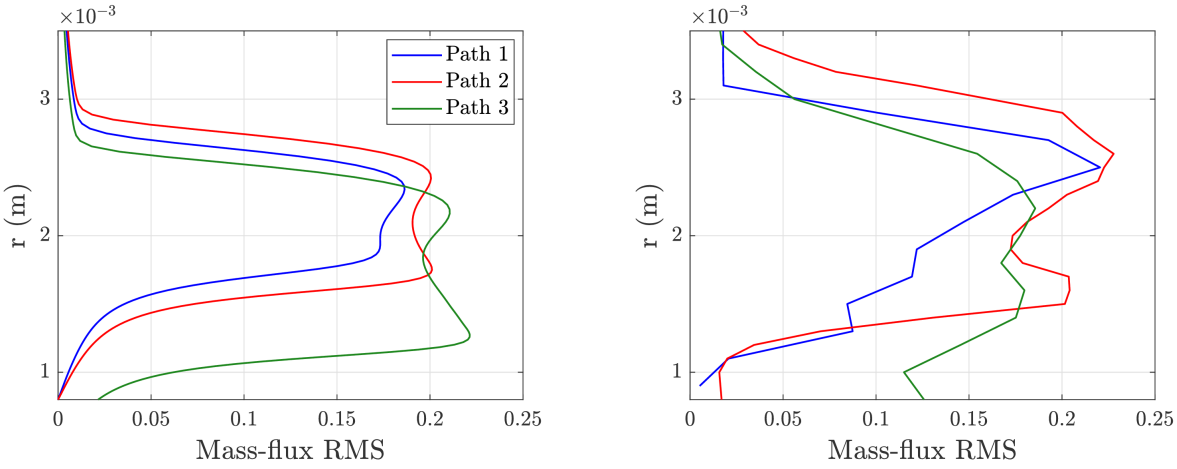

(a) NPSE

(b) Experiments

Figure 7.22: Comparison of computational and experimental RMS representing the mode shape of the disturbance. The lines correspond to locations at 118° from windward and axial distances of 360 mm (blue), 370 mm (red), and 380 mm (green). (Experiment image attributed to Craig & Saric [1])

8. HIFiRE-5 ELLIPTIC CONE*

The HIFiRE-5 geometry is of great importance to the study of hypersonic boundary-layer stability due to the invaluable data acquired during the vehicle flight test. Numerous advanced studies were performed in anticipation of the flight from both a computational and experimental standpoint in an effort to predict the development of 2-D and 3-D instabilities in the boundary layer. Efforts were focused on the improvement of existing transition prediction techniques as well as the development and use of new methodologies.

8.1 Geometry and Grid Topology

The geometry considered in the present study is the 38.1% scale HIFiRE-5 elliptic cone, which matches the dimensions primarily used in the wind tunnel analyses. Nosetip dimensions include a nose radius of 0.95 mm along the semi-minor axis and 1.9 mm along the semi-major axis. The total length of the model is 0.328 m, and the base radius is 0.041 m and 0.082 m along the semi-minor and semi-major axis, respectively. A 2:1 relationship is maintained along the entire length of the cone.

The steady, laminar, basic-state solution is computed using the DPLR CFD code. The mesh is a multi-domain structured grid and consists of 700 points in the axial direction, 569 in the off-wall direction, and 505 around the azimuth. Symmetry allows the basic state to be calculated as a half-cone solution.

8.1.1 Flow Conditions

The selected flow conditions are based on values from wind tunnel experiments and DNS calculations. Flow quantities consisted of freestream Mach number $M = 6$, 0° AoA, freestream temperature $T_\infty = 52.3$ K, and freestream pressure $P_\infty = 690.6$ Pa abs., resulting

*Portions of this section are reprinted from "PSE and Spatial Biglobal Instability Analysis of Reduced Scale and Flight HIFiRE-5 Geometry" by Travis S. Kocian, Alexander J. Moyes, Daniel Mullen, Helen L. Reed, 2017. *AIAA 2017-0768*, Copyright 2017 by Travis Kocian, Alexander Moyes, Daniel Mullen, Helen Reed.

in a unit Reynolds number $Re' = 11.8 \times 10^6/\text{m}$. A no slip wall boundary condition of $T_w = 300$ K is imposed on the cone surface, and all computations were performed assuming air as an ideal gas and applying a constant Prandtl number $Pr = 0.72$.

The fully developed flowfield for the steady-state solution at various axial locations is shown in figure 8.1. Development of distinct mushroom structures and neighboring features can be seen due to the strong azimuthal velocity created by the geometry. The formation of these complex flow structures are all a product of the steady, undisturbed, laminar flow basic-state solution, and no intentional disturbances or excitations are input to cause their manifestation. For the purpose of geometric reference, the symmetry plane near the formation of these mushroom structures will be referred to as the leeward plane.

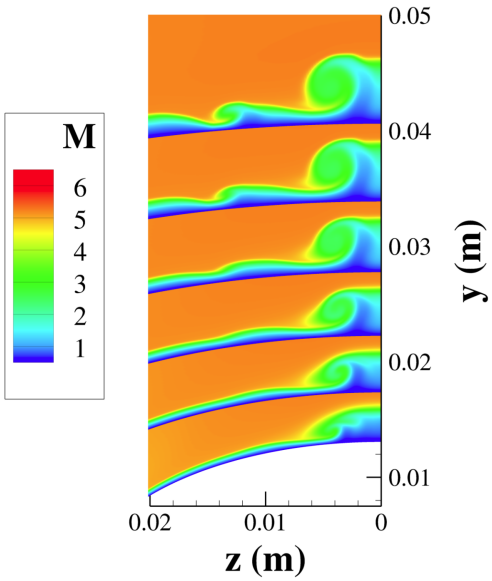

(a) Six slices are shown at axial locations of 0.1, 0.135, 0.175, 0.22, 0.27, and 0.325 meters

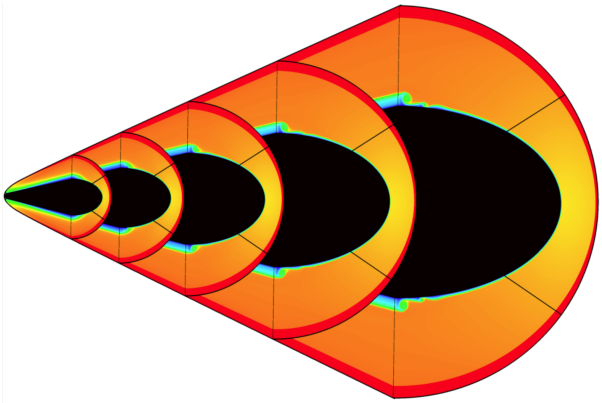

(b) Full basic-state flowfield of the 38.1% model

Figure 8.1: Mach contours of the HIFiRE-5 geometry

8.2 Linear Primary Instability Analysis

8.2.1 2-D LPSE

While stationary crossflow is prominent in regions with a strong 3-D velocity component, alternate instabilities are of more interest in regions where the flow itself is predominantly 2-D, such as the planes of symmetry. N-factors for 2-D disturbances at $Re' = 11.8 \times 10^6$/m are shown along the attachment line and leeward plane in figure 8.2 and figure 8.3, respectively.

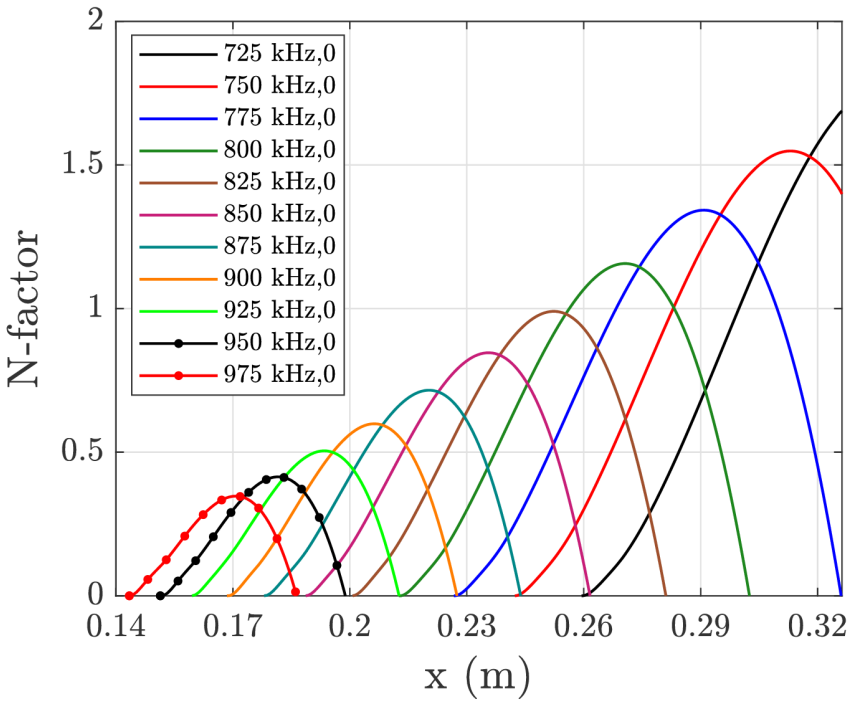

Figure 8.2: 2-D N-factors at different frequencies along the attachment line

The 2-D disturbances along the attachment line never grow to substantial levels. In contrast, N-factors along the leeward plane reach values up to 10.16 at 108 kHz. It is to be noted that the leeward plane has large spanwise gradients which may have an effect on the results in this region given the spanwise invariance assumption applied to the PSE methodology.

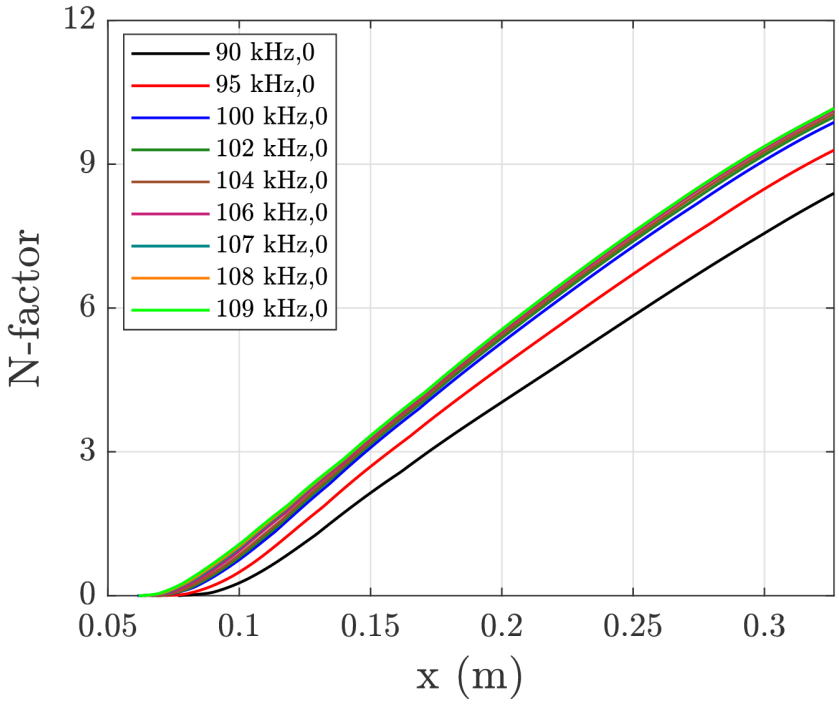

Figure 8.3: 2-D N-factors at different frequencies along the leeward plane

8.2.2 Stationary Crossflow

8.2.2.1 Variation of Spanwise Wavenumber

A spanwise pressure gradient is created by the elliptic nature of the HIFiRE-5 geometry. This, in turn, creates a crossflow component in the basic-state flowfield and inflectional velocity profiles that are particularly unstable for the stationary crossflow instability. A disturbance propagation path is provided for PSE analysis in the form of the inflection-point method discussed previously in order to march the solution downstream. Table 8.1 shows information for the vortex paths used in the LPSE and NPSE analysis of the 38.1% scale configuration. Details are provided for a select distribution of the paths in order to show the trend around the vehicle azimuth.

It has been seen from experiments and DNS that the wavelengths of stationary crossflow vortices vary as they move downstream. Using the method proposed in equation 4.4 and

Path #	x_0	x_{end}	s_0	s_{end}	$m_{\perp 0}$	$m_{\perp end}$
1	0.03	0.326	0.0103	0.0289	60	295
2	0.03	0.326	0.0104	0.0305	70	303
3	0.03	0.326	0.0106	0.0323	75	272
4	0.03	0.326	0.0107	0.0345	100	287
5	0.03	0.326	0.0108	0.0373	130	283
6	0.03	0.326	0.0109	0.0410	170	274
7	0.03	0.326	0.0110	0.0437	260	265
8	0.03	0.326	0.0110	0.0475	400	245
9	0.05	0.326	0.0168	0.0508	190	233
10	0.05	0.326	0.0169	0.0533	230	210

Table 8.1: Path designations, axial x locations (in meters), their arc length locations (in meters) measured from the leeward plane, and the spanwise wavenumbers resulting in the largest LPSE N-factors for stationary crossflow

utilizing the calculation of disturbance paths mentioned previously, the evolution of local wavenumber downstream is predicted and shown in figure 8.4 for the vortex paths of the HIFiRE-5 geometry.

8.2.2.2 3-D LPSE

LPSE calculations were performed on the inflection-point method paths in order to determine the growth of stationary crossflow. Multiple paths, including those listed in table 8.1, were run for a large range of initial spanwise wavenumbers, and figure 8.5 shows the resulting N-factors on the HIFiRE-5 model. Values shown in the contour represent the largest N-factor at each location for all spanwise wavenumbers of the stationary crossflow disturbance. Both inflection-point paths and inviscid streamlines were used in this analysis in order to show the influence of path type.

The peak N-factor along inflection-point paths is 8.75 while inviscid streamlines produce a higher value of 9.65, agreeing with the findings from the analysis of the yawed straight cone. Visually, the N-factor distributions show that the amplification front appears to take on an arc shape where the front is farther forward in the crossflow region and farther downstream near the geometric planes of symmetry. Borg & Kimmel [103] display a very similar pattern

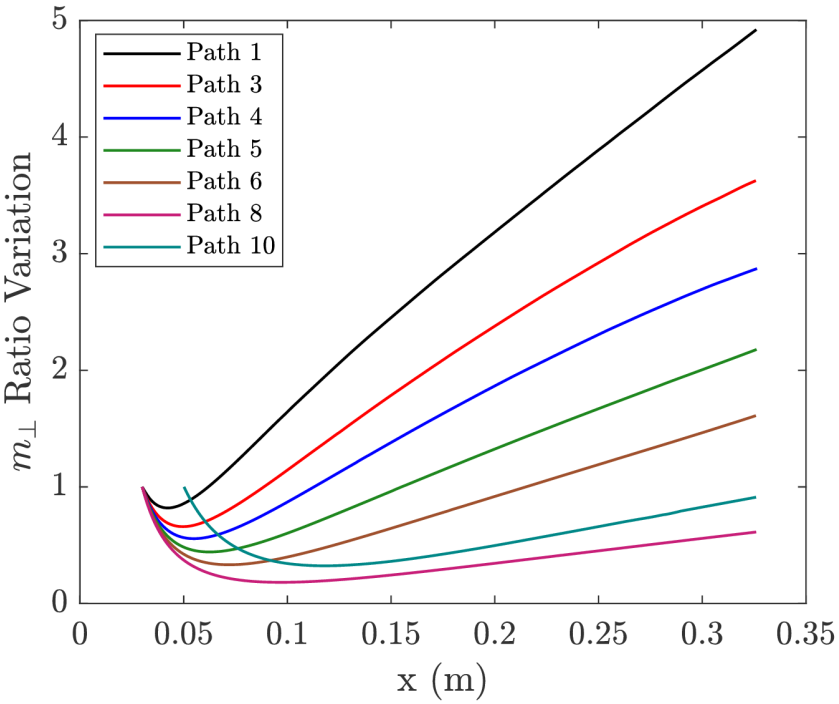

Figure 8.4: Ratio variation of local azimuthal wavenumber along HIFiRE-5 geometry

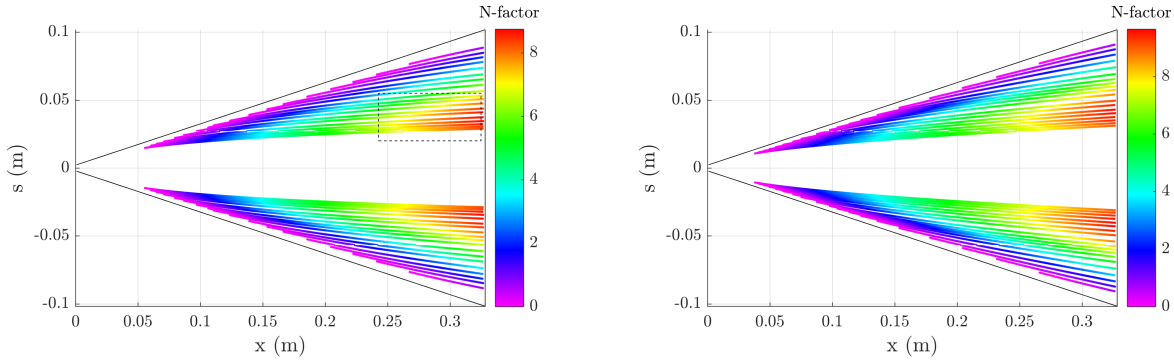

(a) (b)

Figure 8.5: N-factors for stationary crossflow using (a) inflection-point paths and (b) inviscid streamlines. The $s = 0$ location on the flattened cone represents the leeward plane.

under identical flow conditions in both heat flux (their figure 4e) and transition front (their figure 5a). The dashed box in figure 8.5a represents the region Dinzl & Candler [104] focused on in DNS calculations for a similar flowfield. NPSE analyses will focus on this area as well.

8.2.3 Traveling Crossflow

LPSE was also used in the investigation of traveling crossflow. Whereas stationary crossflow calculations use vortex paths, traveling crossflow instead is calculated on inviscid streamlines. Figure 8.6 shows the N-factors for traveling crossflow for the HIFiRE-5 geometry. Values shown represent the largest N-factor at each location for all combinations of frequencies and azimuthal wavenumbers of the disturbances. The traveling crossflow instability shows a behavior that is similar to that of stationary crossflow in that the amplification front once again takes on an arc shape where the front is farther forward in the crossflow region and farther downstream near the planes of symmetry. Traveling crossflow reaches noticeably larger N-factors than stationary crossflow with a peak of 15.06, reinforcing the pattern seen in other similar geometries.

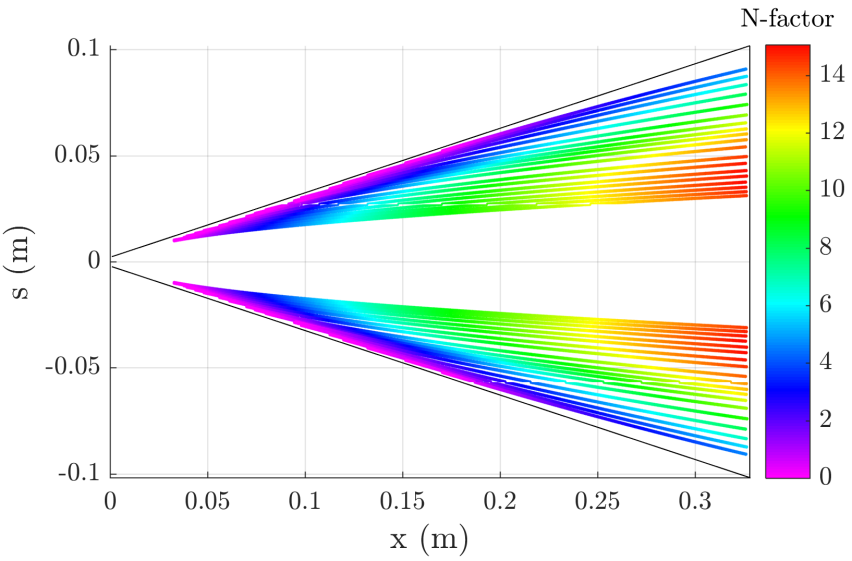

Figure 8.6: N-factors for traveling crossflow using inviscid streamlines. The $s = 0$ location on the flattened cone represents the leeward plane.

8.2.4 Spanwise Wavelength

Due to the collaborative nature of the research on this particular geometry, an opportunity exists to further validate and verify the effects of the χ_2 scale factor described in equation 4.4. Corresponding wind tunnel tests and DNS have analyzed the same 38.1% scale geometry and described the variation of crossflow wavelength as it progresses along the vehicle surface.

Borg & Kimmel [105] performed a unit Reynolds number sweep in the BAM6QT at Purdue University with the 38.1% model in the tunnel. IR data was collected during the experiments and, in each image, streaks oriented in approximately the streamwise direction were visible. These streaks were created by stationary crossflow vortices across the cone. A spanwise cut was taken for each Reynolds number in order to determine the present spanwise wavelengths from the IR data. For each spanwise cut, the mean was subtracted, and discrete Fourier transforms were calculated on the top and bottom sides of the model. Visualization of the streaks was obtained using both oil flow and IR for $Re' = 12.1$ and $Re' = 12.3 \times 10^6$/m, respectively, in order to confirm their results. At a spanwise cut of $x = 305.1$ mm, distinct peak wavelengths of 3.0 and 4.2 mm were seen.

Dinzl & Candler [104] also examined the evolution of crossflow wavelength on the HIFiRE-5 model at $Re' = 11.8 \times 10^6$/m. Local wavelengths were found by overlaying extracted paths onto the disturbance heat flux and finding the distance to the neighboring streaks. Multiple traces were analyzed through this process, and results were shown individually as well as through a calculated average. A common behavior was seen in which all of the initial crossflow wavelengths would start at small sizes of less than 1 mm and grow to an average of approximately 3 mm by the end of the cone model. Similar to the findings of the current study, it was concluded that one could not predict the evolution of disturbance wavelength as a function of axial distance alone.

The current method is tested to see if the combination of inflection-point paths and χ_2 scale factor will produce similar wavelengths as those seen in the experiments and DNS.

Crossflow trajectories are first extracted that pass through the shoulder region of the geometry where higher stationary crossflow N-factors are seen. Next, the wavenumbers which produce the largest amplification at the end of the geometry are identified. Local wavelengths at every axial location for each of the extracted paths are shown in figure 8.7.

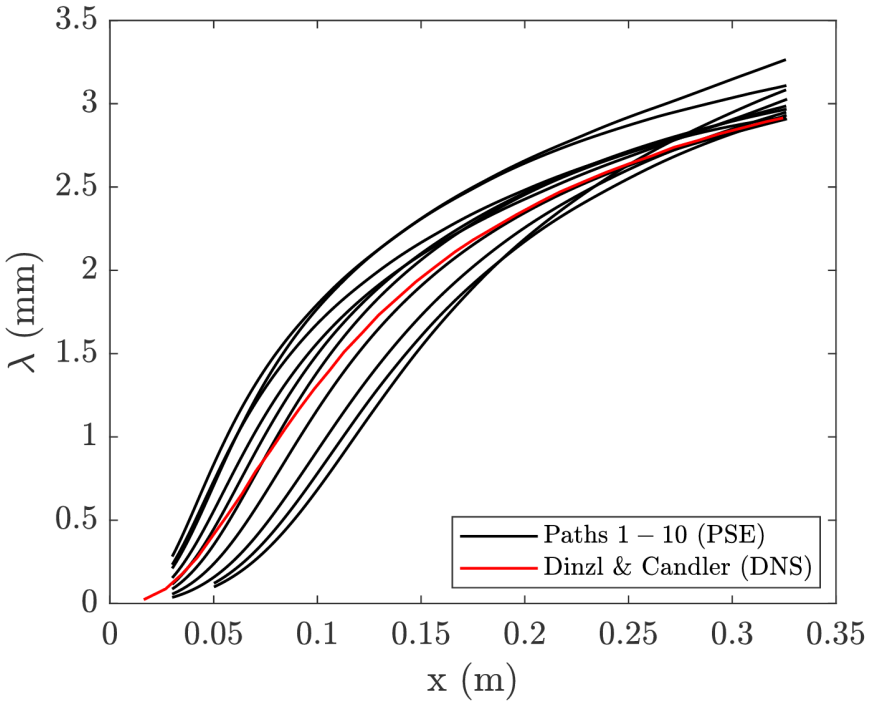

Figure 8.7: Spanwise wavelengths for stationary crossflow disturbances along inflection-point paths using the global wavenumber k_c which produced the largest N-factor for each. Paths pass through the region of highest amplification on the geometry and are compared with the average DNS wavelength.

Wavelengths at axial locations of 0.305 m, matching the experimental measurement location, and at the end of the geometry are around 3 mm. This compares extremely well with wavelengths seen in the experiments and DNS. The DNS value from Dinzl & Candler [104] was found by averaging the wavelengths around the azimuth and is shown in their figure 13d. Present findings further support the notion that the scale factor can be applied to the study of crossflow and help predict the behavior of vortices as they progress downstream.

8.2.5 Convergence Study

Calculations on the Purdue compression cone showed the grid resolution and topology that produced a converged 2-D basic state. Using the same ideology that LPSE N-factors provide a reliable means of quantifying convergence, the 3-D flowfield of the HIFiRE-5 is analyzed using a set of three grids with different resolutions. Grid densities used in this study contain 49 million, 96 million, and 193 million cells. An additional level of analysis is included when investigating this 3-D topology in the form of disturbance propagation path. An inflection-point method vortex path is extracted from each of the iteratively converged flowfields at an identical initial location. This means that each dataset will undergo a series of computations within the previously described data extraction code. Computations involved in determining the vortex paths are very sensitive to details of the flow profiles, and differences in trajectory would indicate differences in the basic states themselves. A comparison of paths between the three resolutions is shown in figure 8.8.

Divergence in trajectory stays relatively small throughout the length of the model with a maximum difference of only 1.1° between the 49 and 193 million cell grids at the last axial station. An LPSE analysis was then performed on each of the three paths using a wavenumber of $k_c = 100$, which was found to be the most amplified at the end of the cone from the LPSE analysis. Scale factors from the highest resolution path were applied to the other two in order to isolate the influence of basic-state flow variables. Differences in N-factor were less than 0.9% between all cases as shown in figure 8.9. From this analysis, it was deemed that a resolution of 49 million cells is satisfactory for 3-D geometries of similar size and under similar flow conditions. While the lower resolution grid would be sufficient, all presented computations for this cone geometry will source from the grid generated using 193 million cells.

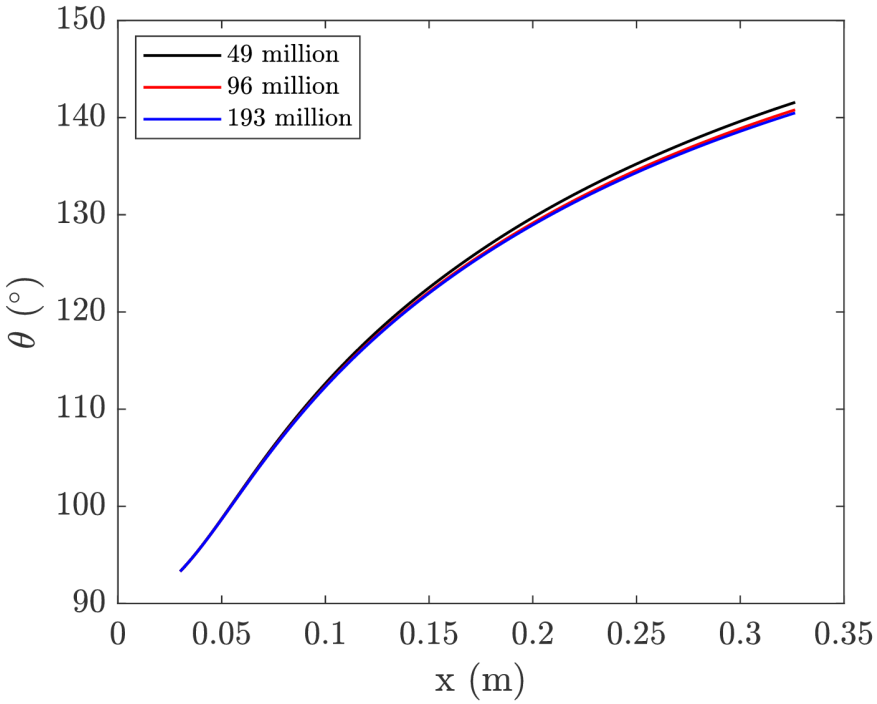

Figure 8.8: Inflection-point paths for three grid resolutions of the HIFiRE-5 geometry. Global (y, z) coordinates were converted to θ for comparison where 90° represents the attachment line along the semi-major axis.

8.3 Nonlinear Primary Instability Analysis

The stationary crossflow instability can display nonlinear effects early on. Therefore, it is necessary to provide an initial disturbance amplitude and model the instability with NPSE as the very nature of the vortex structures significantly distorts the mean flow. The following calculations are performed using the NPSE capabilities of EPIC to analyze the stationary crossflow instability in particular.

8.3.1 Amplitude Evaluation

The same flow conditions were investigated using DNS by Dinzl & Candler [106]. Randomly distributed roughness elements were applied near the nose of the cone in the DNS calculations to induce crossflow vortex formation. The maximum roughness height for the comparative case was 2 μm, and the amplitudes of their figure 16a were used in an effort to

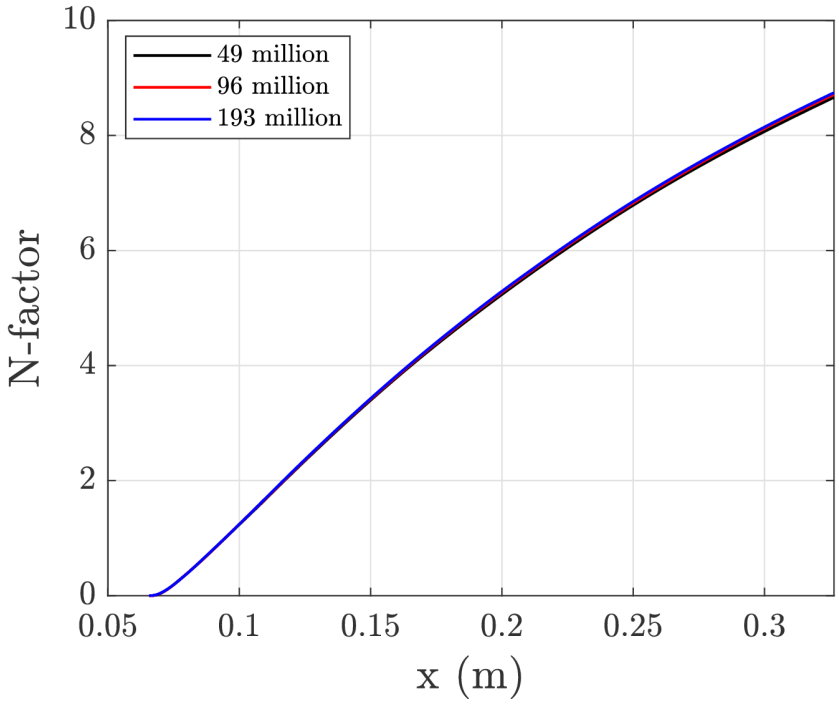

Figure 8.9: Stationary crossflow N-factors for grid resolutions of 49, 96, and 193 million cells

provide initial conditions for the NPSE calculations. The figure provided axial locations and corresponding u-amplitudes for three paths from the DNS. Since only three disturbances, and thus only three disturbance paths, are depicted, an assumption was made in order to estimate what initial amplitude, and at what axial location, the paths in table 8.1 would need to be initialized at for NPSE. Extrapolating the DNS amplitudes to an axial location of $x = 0.13$ m produced values between 0.1 and 0.75%. Using these quantities as a bound, it was decided to use an initial u-amplitude of $u'_{(0,1)} = 4 \times 10^{-3}$ for all paths at this axial location. This amplitude is based on the edge u-velocity at each path's initialization point.

EPIC was marched along the predicted vortex paths corresponding to those shown in the dashed box of figure 8.5a. Wavenumbers that produced the largest N-factors from the LPSE calculations were chosen for the corresponding NPSE analysis. Based on nonlinear calculations performed on the yawed straight cone, it was found to be sufficient to include the mean-flow distortion term, the primary harmonic, and 5 superharmonics. Figure 8.10 shows

NPSE results for maximum u-amplitude fluctuation of the primary mode for 5 different paths, similar to DNS results derived from figure 16a found in Dinzl & Candler [106].

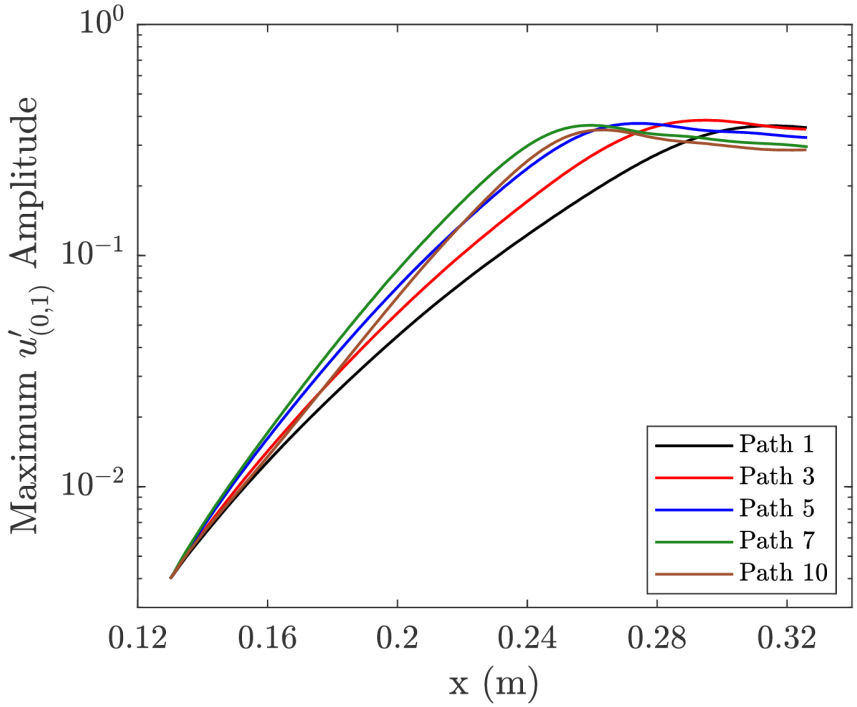

Figure 8.10: Maximum u-amplitudes from NPSE

The path numbers correspond to the same paths designated in table 8.1. Presented NPSE calculations assume u to be in the direction of the stationary crossflow vortex path along the cone surface. Maximum amplitudes reach values equal to approximately 38.5% before the primary mode begins to saturate.

8.3.2 Flow Visualization and Reconstruction

A full flowfield can be recreated by reconstructing the disturbance modes into a wave and adding them to the basic-state values. Figure 8.11 shows the development of the stationary crossflow vortices at different axial and arc length locations. The region portrayed in figure 8.11 is identical to the dashed box region in figure 8.5a.

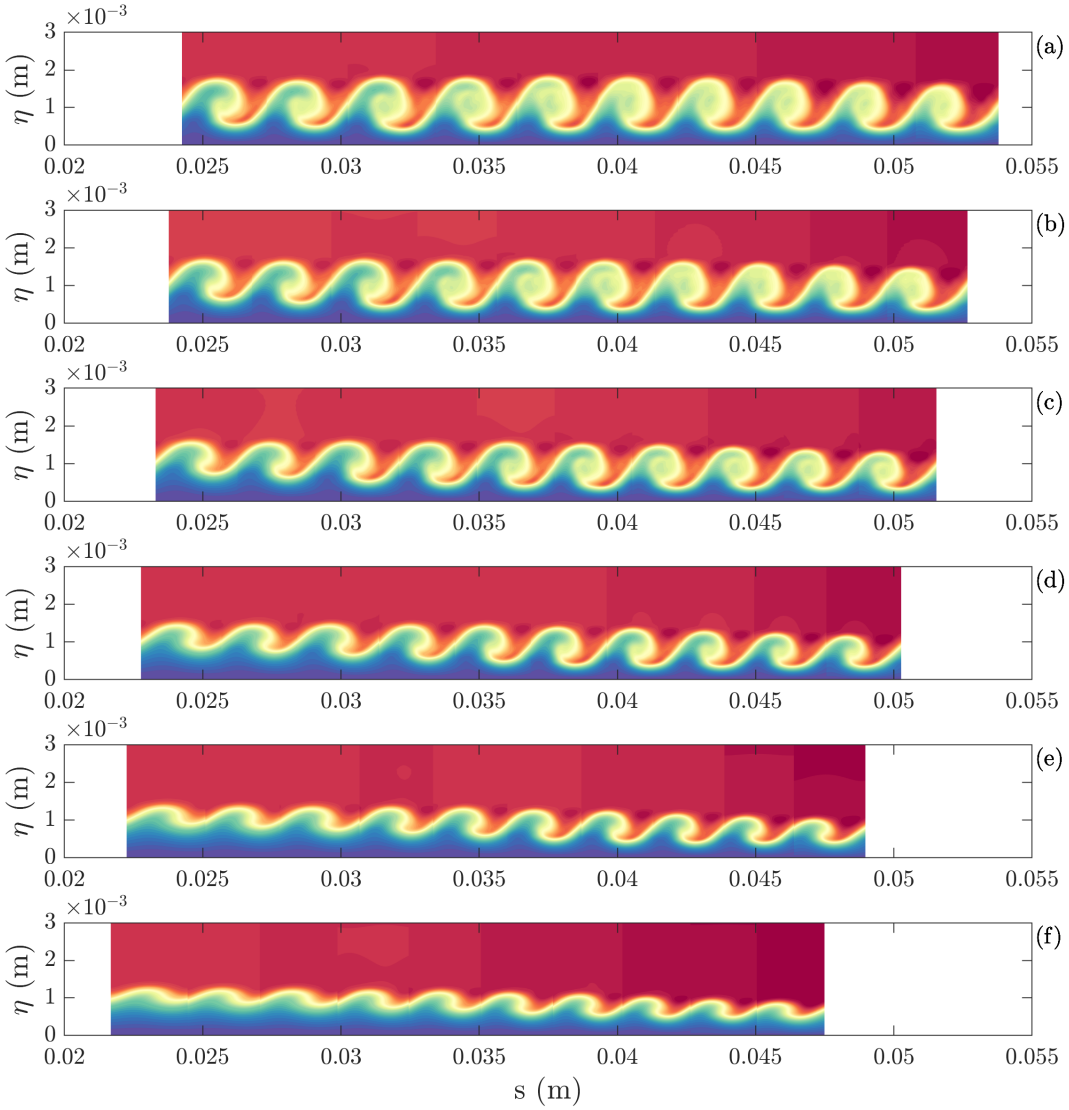

Figure 8.11: Total flow of ρu mass flux showing the development of stationary crossflow vortices at different axial locations and arc lengths (measured from leeward) of the cone. The axial locations in terms of x/L are (a) 0.95, (b) 0.9, (c) 0.85, (d) 0.8, (e) 0.75, and (f) 0.7. The flow is from bottom to top.

Development of the stationary vortex compares well locally with the DNS results in figure 11 from Dinzl & Candler [106]. Physical features such as crossflow wavelength and evolution are well predicted. Note that the rebuilt flowfield is not completely continuous. NPSE was

calculated for the inflection-point paths along the cone in order to produce figure 8.11. Each path was given an initial u-amplitude of $u'_{(0,1)} = 4 \times 10^{-3}$ at an axial location of $x = 0.13$ m in order to reflect the disturbance amplitude that would be seen as a product of the roughness elements used by Dinzl & Candler. The axial distances shown range from an x/L of 0.7 to 0.95 and increase by a uniform step size of 0.05. Evolved disturbances from each path were then combined with the basic state at the designated locations and assumed to span an azimuthal interval of one wavelength. The development of the vortices becomes more pronounced as axial distance increases and the amplitudes of the disturbances grow. It can also be seen that the physical presence of the crossflow vortices is most prominent where the flowfield is significantly 3-D, and the development front matches the shape of the N-factor front from LPSE. Stationary crossflow vortices at the latter axial stations show a strong rollover effect where the disturbances have become highly nonlinear.

As previously mentioned, the maximum amplitudes of the crossflow disturbances are reaching values of approximately 38.5% of the edge u-velocity. Amplitudes of this level create large distortions to the mean flow and produce the clear formation of vortices. More importantly, this becomes a state which is known to be very susceptible to the immediate and rapid growth of high-frequency secondary disturbances. If the secondary instabilities are in fact very unstable, then they will become the driving force on the transition process of the flowfield.

9. NOTABLE ADVANCEMENTS

While the present work discusses a wide array of topics ranging from the formulation of key concepts to results on hypersonic geometries, I have introduced a few select aspects that have played an especially integral role in the progression of the EPIC stability code. These contributions have advanced the approach of PSE for 3-D instabilities and improved the standard procedure for a stability analysis within the CST laboratory at Texas A&M University.

I first developed an in-house data extraction code that provides all of the necessary data in a format compatible with EPIC. Doing so alleviated the hassle and time commitment of having to iteratively generate grids that could provide paths for LST and PSE computations. Features intrinsic to the code also automatically adapt to the provided basic-state grid architecture and remove unknown variables that were previously dependent on the user.

A new technique was devised for determining the proper trajectory of the stationary crossflow disturbance. By tracking the generalized inflection point of the mass-flux profile, this path now conceptually follows a physical attribute of the flow that is directly associated with the generation of the mechanism itself. Of significance, this also enables a path to be obtained purely from the basic state before any stability calculations are performed. Inflection-point paths have been validated and verified with trajectories from a quiet tunnel experiment and two DNS computations. Differences in LPSE N-factors for stationary crossflow on inflection-point paths versus inviscid streamlines have been seen to be significant.

I have formulated a method that models the downstream evolution of spanwise wavelength for the crossflow instabilities. Unlike previous methods, which held wavelength constant or scaled it directly with the radius of curvature, the χ_2 scale factor provides a means to accurately account for the wavelength variation on general geometries at any location in the flowfield. This capability captures a physical behavior of crossflow that was previously unavailable for PSE calculations, and the scale factor has been integrated into the

EPIC stability solver, making it the only stability code at present that can model the wavelength in this manner. Scale factors, like the inflection-point paths, are acquired from the basic-state flowfield without the need of additional stability calculations. Furthermore, this technique has been validated with measurements from a quiet wind tunnel and verified with two different DNS calculations.

Through multiple validation and verification efforts, details on stability sensitivities and mechanism identification were revealed.

- The extreme sensitivity between second mode and AoA was shown using EPIC in conjunction with the quiet tunnel experiments of Hofferth et al. This has directly led to a new practice for properly aligning a model in a wind tunnel by matching the peak second-mode frequencies on opposite sides of a symmetric geometry.

- A question also existed as to what mechanism was being measured in the experiments of Muñoz et al. Mode shapes and LPSE N-factors were used to identify the disturbance as traveling crossflow.

In addition, EPIC demonstrated the capability to analyze stability problems to an extent beyond that of existing PSE calculations.

- NPSE successfully modeled the growth and nonlinear interactions of disturbances in a K-type breakdown. The behavior of individual modes and the resulting heating effects were verified with existing DNS.

- A set of experiments by Craig & Saric at Texas A&M University provided the first extensive measurements of crossflow waves in a hypersonic boundary layer, and the provided data validated the development of the χ_2 scale factor through the excellent agreement of crossflow wavelength and amplification. This also further reinforces the capability of EPIC to capture the nonlinear evolution of the crossflow instability.

10. CONCLUSIONS AND FUTURE WORK

10.1 Conclusions

The next generation of flight vehicles will be greatly dependent on the ability to create designs that achieve optimal levels of both mission performance and efficiency. These will likely delve into the realm of hypersonic flow which can be both a harsh and sensitive environment. A key determining factor involved in the operation of every vehicle will be the ability to predict, and possibly even control, the onset of laminar to turbulent transition.

A system has been developed to analyze the stability of boundary layers for steady-state hypersonic flight configurations. In this sense, criteria have been established for producing basic-state flowfields for both 2-D and 3-D geometries. In addition, a unique and efficient data extraction code has been created which acts as a link between the DPLR flow solver and EPIC stability code. EPIC itself has seen improvements in efficiency, linear and nonlinear capability, and the implementation of additional flow physics. Simultaneously, the framework has been modified to grant stricter control of the numerics and applied assumptions. The CST laboratory at Texas A&M University has continued to use the provided methods in the evaluation of boundary-layer stability, even beyond the scope of the present work.

Stationary crossflow has been identified as a critical mechanism due to the likelihood that hypersonic vehicles, such as waveriders, will experience a 3-D flowfield with inflectional flow profiles. The early onset of nonlinear effects and distortion of the mean flow make it vital to reduce the uncertainty associated with the disturbance amplification, and it is known that the marching path used in a PSE calculation has a significant effect on the resulting growth. A method was developed to model the trajectory of stationary crossflow by aligning the propagation direction such that the generalized inflection point $\frac{\partial}{\partial \eta}\left(\bar{\rho}\frac{\partial \bar{w}}{\partial \eta}\right) = 0$ occurs at $\bar{\rho}\bar{w} = 0$. Quiet tunnel experiments and DNS computations have helped to validate and verify the spatial progression of these paths, which are predicted solely from the basic state.

The evolution of spanwise wavelength for crossflow instabilities has been modeled in a new way that introduces the ability to capture additional flow physics in a PSE calculation. Existing assumptions have been shown to be case dependent or incorrect when applied to more complex geometries. A scale factor, χ_2, can be applied to accurately model the evolution of spanwise wavelength by capturing properties of both the vehicle surface and flowfield in a way that still satisfies the irrotationality condition of the wave. Notably, this scale factor is obtained strictly from the basic-state. The resulting impact on disturbance growth was shown to be significant and produced excellent agreement with parallel computations and experiments.

NPSE was used in order to investigate the streaking pattern seen on the Purdue compression cone in both experiments and companion DNS computations. Highly nonlinear interactions between multiple modes were creating a K-type breakdown and producing heat streaks along the cone surface. Using values obtained from DNS, EPIC was able to recreate the streak pattern and showed that the streaks doubled in number as the 3-D modes became more amplified. Results helped to confirm the viability of using NPSE in order to compute the effects of K-type breakdown.

Validation with quiet tunnel experiments helped reinforce the methodologies and capabilities described in this work. Stationary crossflow paths agreed with those generated using DREs on the yawed cone at Purdue. Additionally, the χ_2 scale factor was used in conjunction with EPIC NPSE to reproduce the stationary crossflow vortices seen at Texas A&M on the same geometry. Experiments at Texas A&M also identified the high sensitivity of the second-mode instability to model alignment on the Langley 93-10 flared cone.

EPIC has been extensively validated and verified over a range of multiple geometries, each of which has provided further knowledge to the understanding of the stability of hypersonic boundary layers and the transition process. Use of the EPIC stability code and additional capabilities available within the CST laboratory will continue to provide keen insight into the unknowns still associated with laminar-to-turbulent transition.

10.2 Future Considerations

An extensive analysis has displayed the capabilities of the PSE code EPIC and shown its potential for application to a wide variety of general hypersonic vehicles. Validation and verification efforts revealed excellent agreement with both experiments and DNS, however, more targeted comparisons would be greatly beneficial to future development. Additionally, aspects of the transition process still need to be addressed in order to accomplish the ultimate goal of transforming EPIC from a code used for analysis to one used for prediction.

10.2.1 Additional DNS for Yawed Straight Cone

Following the generalized inflection point of the mass flux profile appears to align with the stationary crossflow trajectories extracted from various computational [76, 100] and experimental [1, 92] sources. Nevertheless, some discrepancies still exist in the case of the Balakumar & Owens DNS near the windward plane of their yawed cone computations. Differences in the paths in this region are believed to carry over to the ensuing NPSE calculations and produce differences in disturbance amplitudes. A uniquely directed DNS may provide insight into the source of the disparity.

First, it would be beneficial to determine if the forcing of a particular wavenumber is influencing the downstream progression of the stationary vortices. DNS could investigate this by creating a distribution of random roughness on the cone surface to replicate the natural roughness of the Craig & Saric experiment, as opposed to using a patch or ring of roughness. This should allow the naturally most amplified wavelengths to grow and generate the largest crossflow disturbances.

The remaining unknown would then be whether the physical generation of the roughness itself was locally modifying the flowfield and affecting the crossflow trajectories. In order to compare with the prior suggestion of random roughness, a specific pattern of DREs would need to be implemented. This pattern would need to lie along the branch-I neutral point while having a spacing that would excite the naturally most amplified wavenumber.

Knowledge of the crossflow stability behavior would need to be known in advance since axial locations for the neutral points would vary azimuthally around the cone. Either EPIC or the random roughness DNS could provide these neutral point locations and initial wavenumbers.

10.2.2 Extended NPSE Validation

While it was extremely useful to compare crossflow vortices from NPSE calculations with the developed vortices from the Craig & Saric experiment, even more can be gained by monitoring the full evolution of the disturbance from its initialization location. Multiple upstream measurements of disturbance amplitude would allow the full linear and nonlinear growth of the disturbance to be validated.

Careful collaboration would be required between computations and experiments to successfully obtain the desired data. Not only would an experiment need to track and follow a single disturbance path, but NPSE calculations need to be sure to follow along that same path. This becomes more complicated when studying an instability in a 3-D flowfield where the path gradually turns. Experiments would also be limited with regards to the upstream extent of the measurements as, eventually, the disturbance becomes too small to isolate from the tunnel noise floor.

At opportunity exists for the CST laboratory and National Aerothermochemistry and Hypersonics Laboratory at Texas A&M to perform this comparison. Both groups have access to geometries that produce 3-D flowfields, such as the yawed straight cone and HIFiRE-5 elliptic cone. Computations can help determine the trajectory of a stationary crossflow disturbance and help guide measurement locations or sensor placement on the experiment model. While more measurement locations would produce a more detailed comparison, obtaining the largest possible measurement span would be more important in detailing crossflow growth and validating EPIC NPSE.

10.2.3 Receptivity Model

A set of initial conditions is required as input before any NPSE calculation can begin modeling the nonlinear interactions and growth of various disturbances. Currently, initial amplitudes are extracted from existing experiments or DNS computations. A receptivity model could determine how disturbances from the freestream enter the boundary layer and would establish the relevant disturbance amplitudes, spectra, and length scales.

The linearized Navier-Stokes (LNS) equations have been used with success in modeling the receptivity process for both 2-D and 3-D instabilities in low-speed flows. An LNS capability could potentially be used in conjunction with EPIC to model all of the phases of transition ranging from freestream fluctuations through the highly nonlinear stages associated with the presence of strong secondary growth. Doing so would remove the dependence of NPSE initial conditions on existing DNS and experiments. This would be a key step in progressing EPIC towards the end goal of transition prediction.

10.2.4 Low-Speed Flows

The present study focuses predominantly on the stability of boundary layers in hypersonic flowfields. However, EPIC was developed in a framework that should apply across multiple flow regimes including subsonic flows. Oliviero [7] performed a subsonic verification of EPIC LPSE with LASTRAC on the SWIFTER wing glove for the stationary crossflow disturbance, but this is the only instance involving an official comparison for low-speed flows. Validation and verification efforts on additional geometries in low-speed flowfields would reinforce the use of EPIC for a wide range of general stability calculations. Additionally, some instability mechanisms, such as Tollmien-Schlichting waves, are not present in hypersonic flows. Expanding the application of EPIC in this manner would further display the robustness of the stability solver.

REFERENCES

[1] A. Craig and W. Saric, "Crossflow instability in a hypersonic boundary layer," *Journal of Fluid Mechanics*, vol. 808, pp. 224–244, 2016.

[2] International Air Transport Association, "Economic performance of the airline industry," December 2017. http://www.iata.org/publications/economics/Reports/Industry-Econ-Performance/IATA-Economic-Performance-of-the-Industry-end-year-2017-report.pdf, Tech. Rep., Accessed April 2018.

[3] D. Bushnell, "Supersonic laminar flow control," *R. Barnwell and M. Hussaini (eds) Natural Laminar Flow and Laminar Flow Control, Springer*, pp. 233–245, 1992.

[4] S. Walker, J. Sherk, D. Shell, R. Schena, J. Bergmann, and J. Gladbach, "The DARPA/AF Falcon program: The hypersonic technology vehicle #2 (HTV-2) flight demonstration phase," *AIAA 2008-2539*, 2008.

[5] R. Kimmel and D. Adamczak, "HIFiRE-1 background and lessons learned," *AIAA 2012-1088*, 2012.

[6] T. Juliano, J. Poggie, K. Porter, R. Kimmel, J. Jewell, and D. Adamczak, "HIFiRE-5b heat flux and boundary-layer transition," *AIAA 2017-3134*, 2017.

[7] N. Oliviero, "EPIC: A new and advanced nonlinear parabolized stability equation solver," *Masters thesis, Texas A&M University*, 2015.

[8] L. Mack, "Boundary-layer linear stability theory," *AGARD Report 709: Special Course on Stability and Transition of Laminar Flow*, pp. 3.1–3.81, 1984.

[9] A. Fedorov, "Transition and stability of high-speed boundary layers," *Annual Review of Fluid Mechanics*, vol. 43, pp. 79–95, 2011.

[10] M. Morkovin, "Critical evaluation of transition from laminar to turbulent shear layers with emphasis on hypersonically traveling bodies," *AFFDL-TR-68-149, Air Force Flight Dynamics Lab*, 1969.

[11] M. Morkovin, "On the many faces of transition," *Viscous Drag Reduction, CS Wells (ed.), New York: Plenum*, pp. 1–31, 1969.

[12] E. Reshotko, "Boundary layer stability and transition," *Annual Review of Fluid Mechanics*, vol. 8, pp. 311–350, 1976.

[13] M. Morkovin, "Instability, transition to turbulence and predictability," *AGARD No. 236, presented at the AGARD Fluid Dynamics Panel Symposium on "Laminar-Turbulent Transition"*, 1978.

[14] D. Arnal, J. Perraud, and A. Séraudie, "Attachment line and surface imperfection problems," *RTO-EN-AVT-151*, 2008.

[15] H. Reed and W. Saric, "Attachment-line heating in a compressible flow," *Journal of Engineering Mathematics*, vol. 84, pp. 99–110, 2014.

[16] W. Pfenninger, "Flow phenomena at the leading edge of swept wings," *AGARDograph*, vol. 97 Part IV, 1965.

[17] D. I. A. Poll, "Some observations of the transition process on the windward face of a long yawed cylinder," *Journal of Fluid Mechanics*, vol. 150, pp. 329–356, 1984.

[18] D. I. A. Poll, "Boundary layer transition on the windward face of space shuttle during re-entry," *AIAA 85-0899*, 1985.

[19] M. Gaster, "A simple device for preventing turbulent contamination on swept leading edges," *Journal of the Royal Aeronautical Society*, vol. 69, pp. 788–789, 1965.

[20] D. Arnal and J. C. Juillen, "The experimental study of transition and leading edge contamination on swept wings," *AGARD CP-438 Paper 6*, 1988.

[21] L. Mack, "Boundary-layer stability theory," *Jet Propulsion Laboratory Technical Report 900-277 Rev. A*, 1969.

[22] C.-L. Chang, H. Vinh, and M. Malik, "Hypersonic boundary-layer stability with chemical reactions using PSE," *AIAA 97-2012*, 1997.

[23] N. Bitter and J. Shepherd, "Stability of highly cooled hypervelocity boundary layers," *Journal of Fluid Mechanics*, vol. 778, pp. 586–620, 2015.

[24] C. Knisely and X. Zhong, "An investigation of sound radiation by supersonic unstable modes in hypersonic boundary layers," *AIAA 2017-4516*, 2017.

[25] W. Saric, "Görtler vortices," *Annual Review of Fluid Mechanics*, vol. 26, pp. 379–409, 1994.

[26] J. Floryan, "Görtler instability of boundary layers over concave and convex walls," *Physics of Fluids*, vol. 29, pp. 2380–2387, 1986.

[27] W. Saric, A. Carpenter, and H. Reed, "Passive control of transition in three-dimensional boundary layers, with emphasis on discrete roughness elements," *Philosophical Transactions of the Royal Society A*, vol. 369, pp. 1352–1364, 2011.

[28] C. Schuele, T. Corke, and E. Matlis, "Control of stationary cross-flow modes in a Mach 3.5 boundary layer using patterned passive and active roughness," *Journal of Fluid Mechanics*, vol. 718, pp. 5–38, 2013.

[29] E. White and W. Saric, "Secondary instability of crossflow vortices," *Journal of Fluid Mechanics*, vol. 525, pp. 275–308, 2005.

[30] E. Reshotko, "Transient growth: A factor in bypass transition," *Physics of Fluids*, vol. 13, pp. 1067–1075, 2001.

[31] A. Tumin and E. Reshotko, "Spatial theory of optimal disturbances in boundary layers," *Physics of Fluids*, vol. 13, pp. 2097–2104, 2001.

[32] A. Leidy, E. Reshotko, F. Siddiqui, and R. Bowersox, "Characterizing the transient growth mechanism on a hypersonic blunt body at a high angle of attack," *AIAA 2016-3951*, 2016.

[33] E. Reshotko, "Is Re_θ/M_e a meaningful transition criterion?," *AIAA Journal*, vol. 45 No. 7, pp. 1441–1443, 2007.

[34] E. Reshotko, "Transition issues for atmospheric entry," *Journal of Spacecraft and Rockets*, vol. 45 No. 2, pp. 161–164, 2008.

[35] H. Reed and T. Haynes, "Transition correlations in three-dimensional boundary layers," *AIAA Journal*, vol. 32 No. 5, pp. 923–929, 1994.

[36] L. Lees and E. Reshotko, "Stability of the compressible laminar boundary layer," *Journal of Fluid Mechanics*, vol. 12, pp. 555–590, 1962.

[37] J. A. Zaat, "Numerische beiträge zur stabilitätstheorie der grenzschichten," *Grenzschichtforschung Symp., IUTAM*, pp. 127–138, 1958.

[38] L. Thomas, "The stability of plane Poiseuille flow," *Physical Review*, vol. 91 No. 4, pp. 780–783, 1953.

[39] E. Kurtz, "Study of the stability of parallel flows," *PhD dissertation, Massachusetts Institute of Technology*, 1961.

[40] S. Orszag, "Accurate solution of the Orr-Sommerfeld stability equation," *Journal of Fluid Mechanics*, vol. 50, pp. 689–703, 1971.

[41] A. Gallagher and A. Mercer, "On the behavior of small disturbances in plane Couette flow," *Journal of Fluid Mechanics*, vol. 13, pp. 91–100, 1962.

[42] W. Brown and P. Sayer, "An exact solution of the Orr-Sommerfeld stability equation for low Reynolds numbers," *Report No. BLC-43, Northrop Aircraft Inc.*, 1954.

[43] L. Lees and C. Lin, "Investigation of the stability of the laminar boundary layer in a compressible fluid," *NACA Tech. Note No. 1115*, 1946.

[44] D. Dunn and C. Lin, "On the stability of the laminar boundary layer in a compressible fluid," *Journal of the Aeronautical Sciences*, vol. 22, pp. 455–477, 1955.

[45] M. Malik and S. Orszag, "Efficient computation of the stability of three-dimensional compressible boundary layers," *AIAA 81-1277*, 1981.

[46] O. Asfar, J. Masad, and A. Nayfeh, "A method for calculating the stability of boundary layers," *Computers and Fluids*, vol. 18 No. 3, pp. 305–315, 1990.

[47] J. Radbill and E. Van Driest, "A new method for prediction of stability of laminar boundary layers," *AFOSR Report No. 66-0702*, 1966.

[48] A. Wazzan, T. Okamura, and A. Smith, "Stability of laminar boundary layers at separation," *Physics of Fluids*, vol. 10, pp. 2540–2545, 1967.

[49] M. Malik, "Numerical methods for hypersonic boundary layer stability," *Journal of Computational Physics*, vol. 86, pp. 376–413, 1990.

[50] T. Herbert, "Boundary-layer transition analysis and prediction revisited," *AIAA 91-0737*, 1991.

[51] F. Bertolotti, "Linear and nonlinear stability of boundary layers with streamwise varying properties," *PhD dissertation, Ohio State University*, 1991.

[52] F. Bertolotti, T. Herbert, and P. Spalart, "Linear and nonlinear stability of the Blasius boundary layer," *Journal of Fluid Mechanics*, vol. 242, pp. 441–474, 1992.

[53] C.-L. Chang, "LASTRAC.3d: Transition prediction in 3D boundary layers," *AIAA 2004-2542*, 2004.

[54] P. Roache, "Verification of codes and calculations," *AIAA Journal*, vol. 36 No. 5, pp. 696–702, 1998.

[55] A. Nayfeh, "Stability of three-dimensional boundary layers," *AIAA Journal*, vol. 18 No. 4, pp. 406–416, 1980.

[56] M. Malik and D. Poll, "Effect of curvature on three-dimensional boundary-layer stability," *AIAA Journal*, vol. 23 No. 9, pp. 1362–1369, 1985.

[57] M. Malik, R. Spall, and C.-L. Chang, "Effect of nose bluntness on boundary layer stability and transition," *AIAA 90-0112*, 1990.

[58] C.-L. Chang and M. Malik, "Effects of shock on the stability of hypersonic boundary layers," *AIAA 90-1448*, 1990.

[59] G. Stuckert and H. Reed, "Linear disturbances in hypersonic, chemically reacting shock layers," *AIAA Journal*, vol. 32 No. 7, pp. 1384–1393, 1994.

[60] T. Herbert, "Parabolized stability equations," *Annual Review of Fluid Mechanics*, vol. 29, pp. 245–283, 1997.

[61] C.-L. Chang, M. Malik, G. Erlebacher, and M. Hussaini, "Compressible stability of growing boundary layers using parabolized stability equations," *AIAA 91-1636*, 1991.

[62] R. Joslin, C. Streett, and C.-L. Chang, "3-D incompressible spatial direct numerical simulation code validation study: A comparison with linear stability and parabolic stability equation theories in boundary-layer transition on a flat plate," *NASA TP-3205*, 1992.

[63] F. Li and M. Malik, "On the nature of PSE approximation," *Theoretical and Computational Fluid Dynamics*, vol. 8, pp. 253–273, 1996.

[64] T. Haynes and H. Reed, "Simulation of swept-wing vortices using nonlinear parabolized stability equations," *Journal of Fluid Mechanics*, vol. 405, pp. 325–349, 2000.

[65] H. Johnson, T. Seipp, and G. Candler, "Numerical study of hypersonic reacting boundary layer transition on cones," *Physics of Fluids*, vol. 10 No. 10, pp. 2676–2685, 1998.

[66] M. Malik, "Hypersonic flight transition data analysis using parabolized stability equations with chemistry effects," *Journal of Spacecraft and Rockets*, vol. 40 No. 3, pp. 332–344, 2003.

[67] H. Johnson and G. Candler, "Hypersonic boundary layer stability analysis using PSE-Chem," *AIAA 2005-5023*, 2005.

[68] H. Johnson and G. Candler, "Analysis of laminar-turbulent transition in hypersonic flight using PSE-Chem," *AIAA 2006-3057*, 2006.

[69] F. Li, M. Choudhari, C.-L. Chang, and J. White, "Analysis of instabilities in non-axisymmetric hypersonic boundary layers over cones," *AIAA 2010-4643*, 2010.

[70] P. Paredes, V. Theofilis, D. Rodríguez, and J. Tendero, "The PSE-3D instability analysis methodology for flows depending strongly on two and weakly on the third spatial dimension," *AIAA 2011-3752*, 2011.

[71] J. Kuehl, E. Perez, and H. Reed, "JoKHeR: NPSE simulations of hypersonic crossflow instability," *AIAA 2012-0921*, 2012.

[72] T. Kocian, E. Perez, N. Oliviero, J. Kuehl, and H. Reed, "Hypersonic stability analysis of a flared cone," *AIAA 2013-0667*, 2013.

[73] E. Perez, H. Reed, and J. Kuehl, "Instabilities on a hypersonic yawed straight cone," *AIAA 2013-2879*, 2013.

[74] H. Reed, E. Perez, J. Kuehl, T. Kocian, and N. Oliviero, "Verification and validation issues in hypersonic stability and transition prediction," *Journal of Spacecraft and Rockets*, vol. 52, pp. 29–37, 2015.

[75] M. Wright, "Data parallel line relaxation (DPLR) code user manual acadia," *NASA-TM-2009-215388*, 2009.

[76] P. Balakumar and L. Owens, "Stability of hypersonic boundary layers on a cone at angle of attack," *AIAA 2010-4718*, 2010.

[77] N. Oliviero, T. Kocian, A. Moyes, and H. Reed, "EPIC: NPSE analysis of hypersonic crossflow instability on yawed straight circular cone," *AIAA 2015-2772*, 2015.

[78] K. Casper, S. Beresh, J. Henfling, R. Spillers, B. Pruett, and S. Schneider, "Hypersonic wind-tunnel measurements of boundary-layer pressure fluctuations," *AIAA 2009-4054*, 2009.

[79] B. Wheaton, T. Juliano, D. Berridge, A. Chou, P. Gilbert, K. Casper, L. Steen, S. Schneider, and H. Johnson, "Instability and transition measurements in the Mach-6 quiet tunnel," *AIAA 2009-3559*, 2009.

[80] Y. Huang and X. Zhong, "Numerical study of boundary-layer receptivity on blunt compression-cones in Mach-6 flow with localized freestream hot-spot perturbations," *RTO-MP-AVT-200*, 2012.

[81] P. Balakumar and M. Kegerise, "Receptivity of hypersonic boundary layers over straight and flared cones," *AIAA Journal*, vol. 53 No. 8, pp. 2097–2109, 2010.

[82] F. Li, M. Choudhari, C.-L. Chang, M. Wu, and P. Greene, "Development and breakdown of Görtler vortices in high speed boundary layers," *AIAA 2010-705*, 2010.

[83] B. Chynoweth, S. Schneider, C. Hader, H. Fasel, A. Batista, J. Kuehl, T. Juliano, and B. Wheaton, "A history and progress of research on boundary-layer transition on a Mach 6 flared cone," *AIAA 2018-0060*, 2018.

[84] A. Fedorov and A. Tumin, "Receptivity of high-speed boundary layers to kinetic fluctuations," *AIAA 2016-3191*, 2016.

[85] P. Klebanoff, K. Tidstrom, and L. Sargent, "The three-dimensional nature of boundary-layer instability," *Journal of Fluid Mechanics*, vol. 12, pp. 1–34, 1962.

[86] H. Fasel, J. Sivasubramanian, and A. Laible, "Numerical investigation of transition in a flared cone boundary layer at Mach 6," *8th IUTAM-ABCM Symposium on Laminar Turbulent Transition*, vol. 14, pp. 26–35, 2015.

[87] C. Ward, B. Wheaton, A. Chou, C. Berridge, L. Letterman, R. Luersen, and S. Schneider, "Hypersonic boundary-layer transition experiments in the Boeing/AFOSR Mach-6 quiet tunnel," *AIAA 2012-0282*, 2012.

[88] G. McKiernan, B. Chynoweth, and S. Schneider, "Instability and transition experiments in the Boeing/AFOSR Mach 6 quiet tunnel," *AIAA 2015-1735*, 2015.

[89] C. Hader and H. Fasel, "Fundamental resonance breakdown for a flared cone at Mach 6," *AIAA 2017-0765*, 2017.

[90] C. Mayer and H. Fasel, "Detailed comparison of DNS with PSE for oblique breakdown at Mach 3," *AIAA 2010-4596*, 2010.

[91] N. Lin, H. Reed, and W. Saric, "Leading-edge receptivity: Navier-Stokes computations," *Royal Aeronautical Society Conference on Boundary-Layer Transition and Control*, 1991.

[92] J. Hofferth, W. Saric, J. Kuehl, E. Perez, T. Kocian, and H. Reed, "Boundary-layer instability and transition on a flared cone in a Mach 6 quiet wind tunnel," *International Journal of Engineering Systems Modelling and Simulation*, vol. 5, pp. 109–124, 2013.

[93] J. Lachowicz, N. Chokani, and S. Wilkinson, "Hypersonic boundary layer stability over a flared cone in a quiet tunnel," *AIAA 96-0782*, 1996.

[94] J. Hofferth, D. Floryan, R. Humble, and W. Saric, "High-bandwidth optical measurements of the second-mode instability in a Mach 6 quiet tunnel," *AIAA 2013-0378*, 2013.

[95] J. Kendall, "Wind tunnel experiments relating to supersonic and hypersonic boundary-layer transition," *AIAA Journal*, vol. 13 No. 3, pp. 290–299, 1975.

[96] K. Stetson, "Mach 6 experiments of transition on a cone at angle of attack," *Journal of Spacecraft and Rockets*, vol. 19 No. 5, pp. 397–403, 1982.

[97] G. Stuckert and H. Reed, "Linear stability of supersonic cone boundary layers," *AIAA Journal*, vol. 30 No. 10, pp. 2402–2410, 1992.

[98] E. Swanson and S. Schneider, "Boundary-layer transition on cones at angle of attack in a Mach-6 quiet tunnel," *AIAA 2010-1062*, 2010.

[99] T. Kocian, A. Moyes, H. Reed, S. Craig, W. Saric, S. Schneider, and J. Edelman, "Hypersonic crossflow instability," *AIAA 2018-0061*, 2018.

[100] J. Gronvall, H. Johnson, and G. Candler, "Hypersonic three-dimensional boundary layer transition on a cone at angle of attack," *AIAA 2012-2822*, 2012.

[101] F. Muñoz, D. Heitmann, and R. Radespiel, "Instability modes in boundary layers of an inclined cone at Mach 6," *Journal of Spacecraft and Rockets*, vol. 51, pp. 442–454, 2014.

[102] J. Edelman and S. Schneider, "Secondary instabilities of hypersonic stationary crossflow waves," *AIAA Journal*, vol. 56 No. 1, pp. 182–192, 2018.

[103] M. Borg and R. Kimmel, "Measurements of crossflow instability modes for HIFiRE-5 at angle of attack," *AIAA 2017-1681*, 2017.

[104] D. Dinzl and G. Candler, "Direct simulation of hypersonic crossflow instability on an elliptic cone," *AIAA Journal*, vol. 55 No. 6, pp. 1769–1782, 2017.

[105] M. Borg and R. Kimmel, "Simultaneous infrared and pressure measurements of cross-flow instability modes for HIFiRE-5," *AIAA 2016-0354*, 2016.

[106] D. Dinzl and G. Candler, "Direct numerical simulation of crossflow instability excited by microscale roughness on HIFiRE-5," *AIAA 2016-0353*, 2016.

APPENDIX A

MATHEMATICAL FORMULAS

A.1 Winding Number

The winding number of a closed curve is an integer value representing the number of times that the defined curve travels around a point in space. The curve itself must lie within the same plane as the point of interest, and by moving along the curve, a polar angle θ can be measured with respect to the origin. Starting and ending at the same position along a closed curve ensures that the total encompassing angle must result in an integer multiple of 2π. Winding number is then defined as

$$wn = \frac{\theta_{end} - \theta_0}{2\pi} \tag{A.1}$$

for any curve around the origin, and applying a translation to the system allows a winding number to be defined for any point. Moving counterclockwise or clockwise along this curve will produce an integer that is either positive or negative, respectively. In the sense of the present work, the closed curve is defined as the set of points which create a structured cell, and the total angle is found by summing the individual rotations from point to point. Examples of winding number are shown in figure A.1.

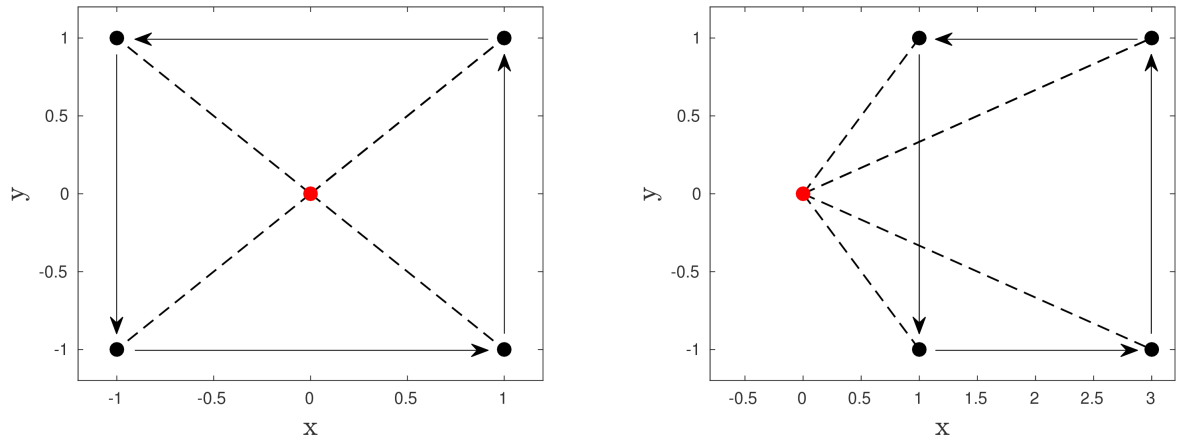

(a) $wn = 1$ (b) $wn = 0$

Figure A.1: Examples of winding number

A.2 General 2-D Interpolation

Obtaining data at an arbitrary location in space requires interpolating values from nearby data points. Datasets are provided to the extraction code in a structured format with (i,j,k) indices in order to ensure that the surrounding cell can be identified. If a point of interest resides within the domain of a cell, only the four points creating that cell are used in the interpolation.

Bilinear interpolation typically operates by first performing a linear interpolation in one direction and then again in a second direction. A limitation of this method is that the four points defining a cell would need to create a quadrilateral with four right angles. This is rarely the case when involving the point distribution on the surface or in the flowfield of most geometries. Instead, a general interpolation scheme is applied which recovers the bilinear interpolation scheme when the points form a rectangle. A general quadratic function is first created as seen in equation A.2.

$$f(x, y) = a_1x^2 + a_2xy + a_3y^2 + b_1x + b_2y + c \tag{A.2}$$

Points forming the cell produce a linear system of four equations that the general quadratic must satisfy. This system can also be represented as $Xa = q$ where x and y are the cell coordinates and q is a vector containing the quantity being interpolated from the surrounding cell.

$$\begin{bmatrix} x_1^2 & x_1y_1 & y_1^2 & x_1 & y_1 & 1 \\ x_2^2 & x_2y_2 & y_2^2 & x_2 & y_2 & 1 \\ x_3^2 & x_3y_3 & y_3^3 & x_3 & y_3 & 1 \\ x_4^2 & x_4y_4 & y_4^2 & x_4 & y_4 & 1 \end{bmatrix} \begin{bmatrix} a_1 \\ a_2 \\ a_3 \\ b_1 \\ b_2 \\ c \end{bmatrix} = \begin{bmatrix} q_1 \\ q_2 \\ q_3 \\ q_4 \end{bmatrix} \tag{A.3}$$

At this stage, the system of equations is underdetermined and cannot be solved. However, if attempting to recover a bilinear interpolation for the rectangular case, the quadratic coefficients need to be minimized. Logically, a purely linear model should be selected if it is capable of fitting the data. A solution is then found by minimizing

$$e = a_1^2 + a_2^2 + a_3^2 = a^T E a \tag{A.4}$$

where E is a diagonal matrix with inputs of $[1, 1, 1, 0, 0, 0]$. Applying the method of Lagrange multipliers to minimize the terms in equation A.4 allows the system to be solved alongside the original underdetermined system as seen in equation A.5.

$$\begin{matrix} Ea + X^T\lambda_{\mathcal{L}} = 0 \\ Xa = q \end{matrix} \quad \Longrightarrow \quad \begin{bmatrix} E & X^T \\ X & 0 \end{bmatrix} \begin{bmatrix} a \\ \lambda_{\mathcal{L}} \end{bmatrix} = \begin{bmatrix} 0 \\ q \end{bmatrix} \tag{A.5}$$

The variable $\lambda_{\mathcal{L}}$ represents a four element vector of Lagrange multipliers, and the combined equations can now be treated as a single linear system that can be solved through a simple matrix inversion. Ultimately, a (6×1) coefficient matrix is produced that minimizes the quadratic terms in equation A.2.

A.3 Linear Least Squares

One strategy for determining a continuous function for a set of scattered data in order to obtain a best fit is through the use of linear least squares. Linear least squares is an approach that fits a mathematical model to a set of data which often times produces an overdefined system of equations and, subsequently, has no exact solution. The model is defined as linear as long as the provided data is expressed linearly in terms of the unknown parameters of the model. An advantage of this method is that good results can be obtained even with small sets of available data.

The definition of best fit in this sense is calculated by minimizing the sum of the squares of residual errors. Using this particular criterion, the unique linear least-squares solution produces a regression line that is better than all other data fits.

The least-squares procedure for a linear regression can be extended to instead represent a polynomial regression. Computations in the present work apply a fourth order polynomial of the general form shown in A.6.

$$y = b_0 + b_1 x + b_2 x^2 + ... \; b_n x^n \tag{A.6}$$

As mentioned previously, the objective is to find a polynomial that minimizes the energy of the residual. Equation A.7 shows the sum of the squares of the residuals.

$$E = \sum_{i=1}^{k} \left[y_i - \left(b_0 + b_1 x_i + b_2 x_i^2 + ... \; b_n x_i^n \right) \right]^2 \tag{A.7}$$

To minimize this quantity, we take the derivative of the residual values with respect to each of the unknown coefficients of the polynomial, as seen in equation A.8.

$$\frac{\partial (E)}{\partial b_n} = -2 \sum_{i=1}^{k} \left[y_i - \left(b_0 + b_1 x_i + b_2 x_i^2 + ... \; b_n x_i^n \right) \right] x^n = 0 \tag{A.8}$$

The unknown coefficients can be solved directly from the observed data. In the general

case, finding a least-squares polynomial is equivalent to simultaneously solving a system of linear equations.

$$\begin{bmatrix} k & \sum_{i=1}^{k} x_i & \cdots & \sum_{i=1}^{k} x_i^n \\ \sum_{i=1}^{k} x_i & \sum_{i=1}^{k} x_i^2 & \cdots & \sum_{i=1}^{k} x_i^{n+1} \\ \vdots & \vdots & \ddots & \vdots \\ \sum_{i=1}^{k} x_i^n & \sum_{i=1}^{k} x_i^{n+1} & \cdots & \sum_{i=1}^{k} x_i^{2n} \end{bmatrix} \begin{bmatrix} b_0 \\ b_1 \\ \vdots \\ b_n \end{bmatrix} = \begin{bmatrix} \sum_{i=1}^{k} y_i \\ \sum_{i=1}^{k} x_i y_i \\ \vdots \\ \sum_{i=1}^{k} x_i^n y_i \end{bmatrix} \tag{A.9}$$

APPENDIX B

LST MATRIX FORMULATION

After applying all of the LST assumptions, the stability problem takes the form seen in equation B.1.

$$\mathcal{A}\frac{\partial^2\hat{\phi}}{\partial\eta^2} + \mathcal{B}\frac{\partial\hat{\phi}}{\partial\eta} + \mathcal{C}\hat{\phi} = 0 \tag{B.1}$$

The solution vector is comprised of five flow variables $\hat{\phi} = \left[\hat{u},\ \hat{v},\ \hat{w},\ \hat{T},\ \hat{\rho}\right]$, and $\mathcal{A}$, $\mathcal{B}$, and $\mathcal{C}$ are (5×5) matrices that exist for each wall-normal location. Components of each matrix are provided where each term represents a basic-state quantity. In addition, all matrices are formatted such that columns $1-5$ represent terms associated with $\hat{u}$, $\hat{v}$, $\hat{w}$, $\hat{T}$, and $\hat{\rho}$, respectively. The first through last rows then account for ξ-momentum, η-momentum, ζ-momentum, energy, and continuity, accordingly.

B.1 A-Matrix

$$\mathcal{A} = \begin{bmatrix} -\frac{\mu}{Reh_2^2} & 0 & 0 & 0 & 0 \\ 0 & -\frac{1}{Reh_2^2}\left(\lambda + 2\mu\right) & 0 & 0 & 0 \\ 0 & 0 & -\frac{\mu}{Reh_2^2} & 0 & 0 \\ 0 & 0 & 0 & -\frac{\kappa}{PrReh_2^2} & 0 \\ 0 & 0 & 0 & 0 & 0 \end{bmatrix}$$

B.2 B-Matrix

$$\mathcal{B}_{1,1} = \frac{\mu}{Reh_2^3}\frac{\partial h_2}{\partial \eta} - \frac{1}{Reh_1h_2^2h_3}\left(h_1h_3\frac{\partial \mu}{\partial T}\frac{\partial T}{\partial \eta} + h_1\mu\frac{\partial h_3}{\partial \eta} + h_3\mu\frac{\partial h_1}{\partial \eta}\right)$$

$$\mathcal{B}_{1,2} = \frac{\lambda h_3}{Re}\left(\frac{1}{h_1^2h_2h_3}\frac{\partial h_1}{\partial \xi} + \frac{1}{h_1h_2^2h_3}\frac{\partial h_2}{\partial \xi} + \frac{1}{h_1h_2h_3^2}\frac{\partial h_3}{\partial \xi}\right) - \frac{\lambda}{Reh_1^2h_2h_3}\left(h_1\frac{\partial h_3}{\partial \xi} + h_3\frac{\partial h_1}{\partial \xi} + i\alpha h_1h_3\right) + \frac{3\mu}{Reh_1h_2^2}\frac{\partial h_2}{\partial \xi} - \frac{i\alpha\mu}{Reh_2h_1}$$

$$\mathcal{B}_{1,3} = 0$$

$$\mathcal{B}_{1,4} = -\frac{1}{Reh_2^2}\frac{\partial \mu}{\partial T}\left(\frac{\partial u}{\partial \eta} - \frac{u}{h_1}\frac{\partial h_1}{\partial \eta}\right)$$

$$\mathcal{B}_{1,5} = 0$$

$$\mathcal{B}_{2,1} = -\frac{\lambda}{Reh_1h_2^2h_3}\left(i\alpha h_2h_3 + h_2\frac{\partial h_3}{\partial \xi} + h_3\frac{\partial h_2}{\partial \xi}\right) - \frac{\mu}{Reh_1h_2h_3}\left(i\alpha h_3 + \frac{\partial h_3}{\partial \xi}\right) - \frac{3\mu}{Reh_1h_2^2}\frac{\partial h_2}{\partial \xi}$$

$$\mathcal{B}_{2,2} = \left[\frac{\lambda}{Reh_2}\left(\frac{1}{h_1^2h_2h_3}\frac{\partial h_1}{\partial \eta} + \frac{1}{h_1h_2^2h_3}\frac{\partial h_2}{\partial \eta} + \frac{1}{h_1h_2h_3^2}\frac{\partial h_3}{\partial \eta}\right) - \frac{1}{Reh_1h_2^2h_3}\frac{\lambda}{\mu}\frac{\partial \mu}{\partial T}\frac{\partial T}{\partial \eta}\right]h_1h_3 - \frac{2\lambda}{Reh_1h_2^2h_3}\left(h_1\frac{\partial h_3}{\partial \eta} + h_3\frac{\partial h_1}{\partial \eta}\right) - \frac{2}{Reh_2^2}\frac{\partial \mu}{\partial T}\frac{\partial T}{\partial \eta} - \frac{2\mu}{Reh_1h_2^2h_3}\left(h_1\frac{\partial h_3}{\partial \eta} + h_3\frac{\partial h_1}{\partial \eta} - \frac{h_1h_3}{h_2}\frac{\partial h_2}{\partial \eta}\right)$$

$$\mathcal{B}_{2,3} = -\frac{\lambda}{Reh_1h_2^2h_3}\left(i\beta h_1h_2 + h_1\frac{\partial h_2}{\partial \zeta} + h_2\frac{\partial h_1}{\partial \zeta}\right) - \frac{\mu}{Reh_1h_2h_3}\left(i\beta h_1 + \frac{\partial h_1}{\partial \zeta}\right) - \frac{3\mu}{Reh_2^2h_3}\frac{\partial h_2}{\partial \zeta}$$

$$\mathcal{B}_{2,4} = \frac{\rho}{h_2\gamma M^2} - \frac{1}{Reh_1h_2^2h_3}\frac{\lambda}{\mu}\frac{\partial \mu}{\partial T}\left(uh_2\frac{\partial h_3}{\partial \xi} + uh_3\frac{\partial h_2}{\partial \xi} + wh_1\frac{\partial h_2}{\partial \zeta} + wh_2\frac{\partial h_1}{\partial \zeta}\right) - \frac{2}{Reh_1h_2^2h_3}\frac{\partial \mu}{\partial T}\left(wh_1\frac{\partial h_2}{\partial \zeta} + uh_3\frac{\partial h_2}{\partial \xi}\right)$$

$$\mathcal{B}_{2,5} = \frac{T}{h_2\gamma M^2}$$

$$\mathcal{B}_{3,1} = 0$$

$$\mathcal{B}_{3,2} = -\frac{\lambda}{Reh_1h_2h_3^2}\left(i\beta h_1h_3 + h_1\frac{\partial h_3}{\partial \zeta} + h_3\frac{\partial h_1}{\partial \zeta}\right) + \frac{\lambda h_1}{Re}\left(\frac{1}{h_1^2h_2h_3}\frac{\partial h_1}{\partial \zeta} + \frac{1}{h_1h_2^2h_3}\frac{\partial h_2}{\partial \zeta} + \frac{1}{h_1h_2h_3^2}\frac{\partial h_3}{\partial \zeta}\right) + \frac{3\mu}{Reh_2^2h_3}\frac{\partial h_2}{\partial \zeta} - \frac{i\beta\mu}{Reh_2h_3}$$

$$\mathcal{B}_{3,3} = -\frac{1}{Reh_2^2}\frac{\partial \mu}{\partial T}\frac{\partial T}{\partial \eta} - \frac{\mu}{Reh_1h_2h_3}\left(\frac{h_1}{h_2}\frac{\partial h_3}{\partial \eta} + \frac{h_3}{h_2}\frac{\partial h_1}{\partial \eta} - \frac{h_1h_3}{h_2^2}\frac{\partial h_2}{\partial \eta}\right)$$

$$\mathcal{B}_{3,4} = -\frac{1}{Reh_2^2h_3}\frac{\partial \mu}{\partial T}\left(h_3\frac{\partial w}{\partial \eta} - w\frac{\partial h_3}{\partial \eta}\right)$$

$$\mathcal{B}_{3,5} = 0$$

$$\mathcal{B}_{4,1} = -\frac{2\mu\left(\gamma-1\right)M^2}{Reh_2}\left(\frac{1}{h_2}\frac{\partial u}{\partial \eta} - \frac{u}{h_1h_2}\frac{\partial h_1}{\partial \eta}\right)$$

$$\mathcal{B}_{4,2} = -\frac{2\left(\gamma-1\right)M^2}{Reh_2}\left[\left(2\mu+\lambda\right)\left(\frac{w}{h_2h_3}\frac{\partial h_2}{\partial \zeta} + \frac{u}{h_1h_2}\frac{\partial h_2}{\partial \xi}\right) + \lambda\left(\frac{w}{h_1h_3}\frac{\partial h_1}{\partial \zeta} + \frac{u}{h_1h_3}\frac{\partial h_3}{\partial \xi}\right)\right]$$

$$\mathcal{B}_{4,3} = -\frac{2\mu\left(\gamma-1\right)M^2}{Reh_2}\left(\frac{1}{h_2}\frac{\partial w}{\partial \eta} - \frac{w}{h_2h_3}\frac{\partial h_3}{\partial \eta}\right)$$

$$\mathcal{B}_{4,4} = -\frac{1}{PrReh_1h_2^2h_3}\left[\kappa\left(h_1\frac{\partial h_3}{\partial \eta} + h_3\frac{\partial h_1}{\partial \eta} - \frac{h_1h_3}{h_2}\frac{\partial h_2}{\partial \eta}\right) + 2h_1h_3\frac{\partial \kappa}{\partial T}\frac{\partial T}{\partial \eta}\right]$$

$$\mathcal{B}_{4,5} = 0$$

$$\mathcal{B}_{5,1} = 0$$

$$\mathcal{B}_{5,2} = \frac{\rho}{h_2}$$

$$\mathcal{B}_{5,3} = 0$$

$$\mathcal{B}_{5,4} = 0$$

$$\mathcal{B}_{5,5} = 0$$

B.3 C-Matrix

$$
\begin{aligned}
\mathcal{C}_{1,1} = &\rho\left(-i\omega + \frac{u}{h_1}i\alpha + \frac{w}{h_3}i\beta + \frac{w}{h_1h_3}\frac{\partial h_1}{\partial \zeta}\right)\\
&- \frac{\lambda}{Reh_1^2h_2h_3}\left(-\alpha^2h_2h_3 + i2\alpha h_2\frac{\partial h_3}{\partial \xi} + i2\alpha h_3\frac{\partial h_2}{\partial \xi} + 2\frac{\partial h_2}{\partial \xi}\frac{\partial h_3}{\partial \xi} + h_2\frac{\partial^2 h_3}{\partial \xi^2} + h_3\frac{\partial^2 h_2}{\partial \xi^2}\right)\\
&+ \frac{\lambda}{Reh_1}\left(\frac{1}{h_1^2h_2h_3}\frac{\partial h_1}{\partial \xi} + \frac{1}{h_1h_2^2h_3}\frac{\partial h_2}{\partial \xi} + \frac{1}{h_1h_2h_3^2}\frac{\partial h_3}{\partial \xi}\right)\left(i\alpha h_2h_3 + h_2\frac{\partial h_3}{\partial \xi} + h_3\frac{\partial h_2}{\partial \xi}\right)\\
&- \frac{i2\alpha\mu}{Reh_1h_2h_3}\left(\frac{h_3}{h_1}\frac{\partial h_2}{\partial \xi} + \frac{h_2}{h_1}\frac{\partial h_3}{\partial \xi} - \frac{h_2h_3}{h_1^2}\frac{\partial h_1}{\partial \xi}\right) + \frac{2\alpha^2\mu}{Reh_1^2}\\
&+ \frac{1}{Reh_1^2h_2^2h_3}\frac{\partial h_1}{\partial \eta}\left(h_1h_3\frac{\partial \mu}{\partial T}\frac{\partial T}{\partial \eta} + h_1\mu\frac{\partial h_3}{\partial \eta} + h_3\mu\frac{\partial h_1}{\partial \eta}\right)\\
&- \frac{\mu}{Reh_1h_2^2}\left(\frac{1}{h_2}\frac{\partial h_2}{\partial \eta}\frac{\partial h_1}{\partial \eta} + \frac{1}{h_1}\frac{\partial h_1}{\partial \eta}\frac{\partial h_1}{\partial \eta} - \frac{\partial^2 h_1}{\partial \eta^2}\right)\\
&- \frac{\mu}{Reh_1h_2h_3}\left(\frac{i\beta}{h_3} - \frac{1}{h_1h_3}\frac{\partial h_1}{\partial \zeta}\right)\left(h_1\frac{\partial h_2}{\partial \zeta} + h_2\frac{\partial h_1}{\partial \zeta}\right)\\
&+ \frac{\mu}{Reh_3}\left(\frac{\beta^2}{h_3} + \frac{i\beta}{h_3^2}\frac{\partial h_3}{\partial \zeta} + \frac{i\beta}{h_1h_3}\frac{\partial h_1}{\partial \zeta} - \frac{1}{h_1^2h_3}\frac{\partial h_1}{\partial \zeta}\frac{\partial h_1}{\partial \zeta} - \frac{1}{h_1h_3^2}\frac{\partial h_3}{\partial \zeta}\frac{\partial h_1}{\partial \zeta} + \frac{1}{h_1h_3}\frac{\partial^2 h_1}{\partial \zeta^2}\right)\\
&+ \frac{\mu}{Reh_1^2h_2^2}\left[\left(\frac{\partial h_1}{\partial \eta}\right)^2 + 2\left(\frac{\partial h_2}{\partial \xi}\right)^2\right]\\
&+ \frac{\mu}{Reh_1h_3}\left[\frac{2}{h_1h_3}\left(\frac{\partial h_3}{\partial \xi}\right)^2 - \frac{\partial h_1}{\partial \zeta}\left(\frac{i\beta}{h_3} - \frac{1}{h_1h_3}\frac{\partial h_1}{\partial \zeta}\right)\right]\\
\mathcal{C}_{1,2} = &\rho\left(\frac{1}{h_2}\frac{\partial u}{\partial \eta} + \frac{u}{h_1h_2}\frac{\partial h_1}{\partial \eta}\right)\\
&- \frac{\lambda}{Reh_1^2h_2h_3}\left(i\alpha h_1\frac{\partial h_3}{\partial \eta} + \frac{\partial h_1}{\partial \xi}\frac{\partial h_3}{\partial \eta} + h_1\frac{\partial^2 h_3}{\partial \xi\partial \eta} + i\alpha h_3\frac{\partial h_1}{\partial \eta} + \frac{\partial h_3}{\partial \xi}\frac{\partial h_1}{\partial \eta} + h_3\frac{\partial^2 h_1}{\partial \xi\partial \eta}\right)\\
&+ \frac{\lambda}{Reh_1}\left(\frac{1}{h_1^2h_2h_3}\frac{\partial h_1}{\partial \xi} + \frac{1}{h_1h_2^2h_3}\frac{\partial h_2}{\partial \xi} + \frac{1}{h_1h_2h_3^2}\frac{\partial h_3}{\partial \xi}\right)\left(h_1\frac{\partial h_3}{\partial \eta} + h_3\frac{\partial h_1}{\partial \eta}\right)\\
&- \frac{2\mu}{Reh_1h_2h_3}\left(i\alpha\frac{h_3}{h_1}\frac{\partial h_1}{\partial \eta} + \frac{1}{h_1}\frac{\partial h_1}{\partial \eta}\frac{\partial h_3}{\partial \xi} - \frac{h_3}{h_1^2}\frac{\partial h_1}{\partial \eta}\frac{\partial h_1}{\partial \xi} + \frac{h_3}{h_1}\frac{\partial^2 h_1}{\partial \eta\partial \xi}\right)\\
&- \frac{1}{Reh_1^2h_2h_3}\left(h_1h_3\frac{\partial \mu}{\partial T}\frac{\partial T}{\partial \eta} + h_1\mu\frac{\partial h_3}{\partial \eta} + h_3\mu\frac{\partial h_1}{\partial \eta}\right)\left(i\alpha - \frac{1}{h_2}\frac{\partial h_2}{\partial \xi}\right)\\
&+ \frac{\mu}{Reh_2}\left(\frac{i\alpha}{h_1^2}\frac{\partial h_1}{\partial \eta} + \frac{1}{h_1h_2}\frac{\partial^2 h_2}{\partial \xi\partial \eta} - \frac{1}{h_1^2h_2}\frac{\partial h_2}{\partial \xi}\frac{\partial h_1}{\partial \eta} - \frac{1}{h_1h_2^2}\frac{\partial h_2}{\partial \xi}\frac{\partial h_2}{\partial \eta}\right)\\
&- \frac{\mu}{Reh_1^2h_2}\frac{\partial h_1}{\partial \eta}\left(i\alpha - \frac{1}{h_2}\frac{\partial h_2}{\partial \xi}\right) + \frac{2\mu}{Reh_1h_2h_3^2}\frac{\partial h_3}{\partial \xi}\frac{\partial h_3}{\partial \eta}\\
\mathcal{C}_{1,3} = &\frac{\rho}{h_1h_3}\left(u\frac{\partial h_1}{\partial \zeta} - 2w\frac{\partial h_3}{\partial \xi}\right) - \frac{\lambda}{Reh_1^2h_2h_3}\left(-\alpha\beta h_1h_2 + i\beta h_1\frac{\partial h_2}{\partial \xi} + i\beta h_2\frac{\partial h_1}{\partial \xi}\right.
\end{aligned}
$$

$$
\begin{aligned}
&+i\alpha h_1\frac{\partial h_2}{\partial\zeta}+\frac{\partial h_1}{\partial\xi}\frac{\partial h_2}{\partial\zeta}+h_1\frac{\partial^2 h_2}{\partial\xi\partial\zeta}+i\alpha h_2\frac{\partial h_1}{\partial\zeta}+\frac{\partial h_2}{\partial\xi}\frac{\partial h_1}{\partial\zeta}+h_2\frac{\partial^2 h_1}{\partial\xi\partial\zeta}\Bigg)\\
&+\frac{\lambda}{Reh_1}\left(\frac{1}{h_1^2h_2h_3}\frac{\partial h_1}{\partial\xi}+\frac{1}{h_1h_2^2h_3}\frac{\partial h_2}{\partial\xi}+\frac{1}{h_1h_2h_3^2}\frac{\partial h_3}{\partial\xi}\right)\left(i\beta h_1h_2+h_1\frac{\partial h_2}{\partial\zeta}+h_2\frac{\partial h_1}{\partial\zeta}\right)\\
&-\frac{2\mu}{Reh_1^2h_2h_3}\left(i\alpha h_2\frac{\partial h_1}{\partial\zeta}+\frac{\partial h_1}{\partial\zeta}\frac{\partial h_2}{\partial\xi}+h_2\frac{\partial^2 h_1}{\partial\xi\partial\zeta}-\frac{h_2}{h_1}\frac{\partial h_1}{\partial\zeta}\frac{\partial h_1}{\partial\xi}\right)\\
&-\frac{\mu}{Reh_1h_2h_3}\left(\frac{i\alpha}{h_1}-\frac{1}{h_1h_3}\frac{\partial h_3}{\partial\xi}\right)\left(h_1\frac{\partial h_2}{\partial\zeta}+h_2\frac{\partial h_1}{\partial\zeta}\right)\\
&+\frac{\mu}{Reh_3}\left(\frac{\alpha\beta}{h_1}+\frac{i\alpha}{h_1^2}\frac{\partial h_1}{\partial\zeta}+\frac{i\beta}{h_1h_3}\frac{\partial h_3}{\partial\xi}-\frac{1}{h_1^2h_3}\frac{\partial h_3}{\partial\xi}\frac{\partial h_1}{\partial\zeta}-\frac{1}{h_1h_3^2}\frac{\partial h_3}{\partial\xi}\frac{\partial h_3}{\partial\zeta}+\frac{1}{h_1h_3}\frac{\partial^2 h_3}{\partial\xi\partial\zeta}\right)\\
&-\frac{\mu}{Reh_1^2h_3}\frac{\partial h_1}{\partial\zeta}\left(i\alpha-\frac{1}{h_3}\frac{\partial h_3}{\partial\xi}\right)+\frac{2\mu}{Reh_1h_2^2h_3}\frac{\partial h_2}{\partial\xi}\frac{\partial h_2}{\partial\zeta}+\frac{i2\mu\beta}{Reh_1h_3^2}\frac{\partial h_3}{\partial\xi}\\
\mathcal{C}_{1,4}=&\frac{i\alpha\rho}{h_1\gamma M^2}-\frac{1}{Re}\frac{\lambda}{\mu}\frac{\partial\mu}{\partial T}\left\{\left(uh_2\frac{\partial h_3}{\partial\xi}+uh_3\frac{\partial h_2}{\partial\xi}+wh_1\frac{\partial h_2}{\partial\zeta}+wh_2\frac{\partial h_1}{\partial\zeta}\right)\right.\\
&\left.\left[\frac{i\alpha}{h_1^2h_2h_3}-\frac{1}{h_1}\left(\frac{1}{h_1^2h_2h_3}\frac{\partial h_1}{\partial\xi}+\frac{1}{h_1h_2^2h_3}\frac{\partial h_2}{\partial\xi}+\frac{1}{h_1h_2h_3^2}\frac{\partial h_3}{\partial\xi}\right)\right]\right\}\\
&-\frac{1}{Reh_1^2h_2h_3}\frac{\lambda}{\mu}\frac{\partial\mu}{\partial T}\left(2u\frac{\partial h_2}{\partial\xi}\frac{\partial h_3}{\partial\xi}+uh_2\frac{\partial^2 h_3}{\partial\xi^2}+uh_3\frac{\partial^2 h_2}{\partial\xi^2}\right.\\
&\left.+w\frac{\partial h_1}{\partial\xi}\frac{\partial h_2}{\partial\zeta}+wh_1\frac{\partial^2 h_2}{\partial\xi\partial\zeta}+w\frac{\partial h_2}{\partial\xi}\frac{\partial h_1}{\partial\zeta}+wh_2\frac{\partial^2 h_1}{\partial\xi\partial\zeta}\right)\\
&-\frac{2w}{Reh_1^2h_2h_3}\frac{\partial\mu}{\partial T}\left(i\alpha h_2\frac{\partial h_1}{\partial\zeta}+\frac{\partial h_1}{\partial\zeta}\frac{\partial h_2}{\partial\xi}-\frac{h_2}{h_1}\frac{\partial h_1}{\partial\zeta}\frac{\partial h_1}{\partial\xi}+h_2\frac{\partial^2 h_1}{\partial\xi\partial\zeta}\right)\\
&-\frac{1}{Reh_1h_2h_3}\frac{\partial\mu}{\partial T}\left(\frac{1}{h_2}\frac{\partial u}{\partial\eta}-\frac{u}{h_1h_2}\frac{\partial h_1}{\partial\eta}\right)\left(h_1\frac{\partial h_3}{\partial\eta}+h_3\frac{\partial h_1}{\partial\eta}\right)\\
&-\frac{1}{Reh_2}\frac{\partial^2\mu}{\partial T^2}\frac{\partial T}{\partial\eta}\left(\frac{1}{h_2}\frac{\partial u}{\partial\eta}-\frac{u}{h_1h_2}\frac{\partial h_1}{\partial\eta}\right)\\
&-\frac{1}{Reh_2}\frac{\partial\mu}{\partial T}\left(\frac{1}{h_2}\frac{\partial^2 u}{\partial\eta^2}-\frac{1}{h_2^2}\frac{\partial u}{\partial\eta}\frac{\partial h_2}{\partial\eta}-\frac{1}{h_1h_2}\frac{\partial u}{\partial\eta}\frac{\partial h_1}{\partial\eta}\right.\\
&\left.-\frac{u}{h_1h_2}\frac{\partial^2 h_1}{\partial\eta^2}+\frac{u}{h_1^2h_2}\frac{\partial h_1}{\partial\eta}\frac{\partial h_1}{\partial\eta}+\frac{u}{h_1h_2^2}\frac{\partial h_2}{\partial\eta}\frac{\partial h_1}{\partial\eta}\right)\\
&+\frac{1}{Reh_1h_2h_3}\frac{\partial\mu}{\partial T}\left(\frac{u}{h_1h_3}\frac{\partial h_1}{\partial\zeta}+\frac{w}{h_1h_3}\frac{\partial h_3}{\partial\xi}\right)\left(i\beta h_1h_2+h_1\frac{\partial h_2}{\partial\zeta}+h_2\frac{\partial h_1}{\partial\zeta}\right)\\
&+\frac{1}{Reh_3}\frac{\partial\mu}{\partial T}\left(\frac{u}{h_1h_3}\frac{\partial^2 h_1}{\partial\zeta^2}-\frac{u}{h_1^2h_3}\frac{\partial h_1}{\partial\zeta}\frac{\partial h_1}{\partial\zeta}-\frac{u}{h_1h_3^2}\frac{\partial h_3}{\partial\zeta}\frac{\partial h_1}{\partial\zeta}+\frac{w}{h_1h_3}\frac{\partial^2 h_3}{\partial\xi\partial\zeta}\right.\\
&\left.-\frac{w}{h_1^2h_3}\frac{\partial h_1}{\partial\zeta}\frac{\partial h_3}{\partial\xi}-\frac{w}{h_1h_3^2}\frac{\partial h_3}{\partial\zeta}\frac{\partial h_3}{\partial\xi}\right)-\frac{1}{Reh_1h_2^2}\frac{\partial\mu}{\partial T}\frac{\partial h_1}{\partial\eta}\left(\frac{\partial u}{\partial\eta}-\frac{u}{h_1}\frac{\partial h_1}{\partial\eta}\right)\\
&+\frac{1}{Reh_1^2h_3^2}\frac{\partial\mu}{\partial T}\frac{\partial h_1}{\partial\zeta}\left(w\frac{\partial h_3}{\partial\xi}+u\frac{\partial h_1}{\partial\zeta}\right)+\frac{2}{Reh_1h_2^2}\frac{\partial\mu}{\partial T}\frac{\partial h_2}{\partial\xi}\left(\frac{w}{h_3}\frac{\partial h_2}{\partial\zeta}+\frac{u}{h_1}\frac{\partial h_2}{\partial\xi}\right)\\
&+\frac{2u}{Reh_1^2h_3^2}\frac{\partial\mu}{\partial T}\frac{\partial h_3}{\partial\xi}\frac{\partial h_3}{\partial\xi}
\end{aligned}
$$

$$\mathcal{C}_{1,5} = \frac{w}{h_1 h_3}\left(u\frac{\partial h_1}{\partial \zeta} - w\frac{\partial h_3}{\partial \xi}\right) + \frac{i\alpha T}{h_1 \gamma M^2}$$

$$\begin{aligned}
\mathcal{C}_{2,1} =& -\frac{2\rho u}{h_1 h_2}\frac{\partial h_1}{\partial \eta} + \left\{\left[\frac{\lambda}{Reh_2}\left(\frac{1}{h_1^2 h_2 h_3}\frac{\partial h_1}{\partial \eta} + \frac{1}{h_1 h_2^2 h_3}\frac{\partial h_2}{\partial \eta} + \frac{1}{h_1 h_2 h_3^2}\frac{\partial h_3}{\partial \eta}\right)\right.\right. \\
&\left.\left. -\frac{1}{Reh_1 h_2^2 h_3}\frac{\lambda}{\mu}\frac{\partial \mu}{\partial T}\frac{\partial T}{\partial \eta}\right]\left(i\alpha h_2 h_3 + h_2\frac{\partial h_3}{\partial \xi} + h_3\frac{\partial h_2}{\partial \xi}\right)\right\} \\
&- \frac{\lambda}{Reh_1 h_2^2 h_3}\left(i\alpha h_2\frac{\partial h_3}{\partial \eta} + i\alpha h_3\frac{\partial h_2}{\partial \eta} + \frac{\partial h_2}{\partial \eta}\frac{\partial h_3}{\partial \xi} + h_2\frac{\partial^2 h_3}{\partial \xi \partial \eta} + \frac{\partial h_3}{\partial \eta}\frac{\partial h_2}{\partial \xi} + h_3\frac{\partial^2 h_2}{\partial \xi \partial \eta}\right) \\
&+ \frac{\mu}{Reh_1^2 h_2 h_3}\left(i\alpha h_3\frac{\partial h_1}{\partial \eta} + \frac{\partial h_3}{\partial \xi}\frac{\partial h_1}{\partial \eta} + h_3\frac{\partial^2 h_1}{\partial \xi \partial \eta} - \frac{h_3}{h_1}\frac{\partial h_1}{\partial \xi}\frac{\partial h_1}{\partial \eta}\right) \\
&- \frac{2}{Reh_1 h_2^2}\frac{\partial h_2}{\partial \xi}\frac{\partial \mu}{\partial T}\frac{\partial T}{\partial \eta} - \frac{2\mu}{Reh_1 h_2^2 h_3}\left(\frac{\partial h_3}{\partial \eta}\frac{\partial h_2}{\partial \xi} + h_3\frac{\partial^2 h_2}{\partial \xi \partial \eta} - \frac{h_3}{h_2}\frac{\partial h_2}{\partial \eta}\frac{\partial h_2}{\partial \xi}\right) \\
&+ \frac{\mu}{Reh_1^2 h_2^2}\frac{\partial h_1}{\partial \eta}\frac{\partial h_2}{\partial \xi} + \frac{2\mu}{Reh_1 h_2 h_3^2}\frac{\partial h_3}{\partial \eta}\frac{\partial h_3}{\partial \xi} + \frac{i2\alpha\mu}{Reh_1^2 h_2}\frac{\partial h_1}{\partial \eta} \\
\mathcal{C}_{2,2} =& \rho\left[-i\omega + \frac{u}{h_1}i\alpha + \frac{w}{h_3}i\beta + \frac{\partial h_2}{\partial \zeta}\frac{w}{h_2 h_3} + \frac{\partial h_2}{\partial \xi}\frac{u}{h_1 h_2}\right] \\
&+ \left\{\left[\frac{\lambda}{Reh_2}\left(\frac{1}{h_1^2 h_2 h_3}\frac{\partial h_1}{\partial \eta} + \frac{1}{h_1 h_2^2 h_3}\frac{\partial h_2}{\partial \eta} + \frac{1}{h_1 h_2 h_3^2}\frac{\partial h_3}{\partial \eta}\right) - \frac{1}{Reh_1 h_2^2 h_3}\frac{\lambda}{\mu}\frac{\partial \mu}{\partial T}\frac{\partial T}{\partial \eta}\right]\right. \\
&\left.\left(h_1\frac{\partial h_3}{\partial \eta} + h_3\frac{\partial h_1}{\partial \eta}\right)\right\} - \frac{\lambda}{Reh_1 h_2^2 h_3}\left(2\frac{\partial h_1}{\partial \eta}\frac{\partial h_3}{\partial \eta} + h_1\frac{\partial^2 h_3}{\partial \eta^2} + h_3\frac{\partial^2 h_1}{\partial \eta^2}\right) \\
&- \frac{\mu}{Reh_1^2 h_2 h_3}\left(i\alpha h_2\frac{\partial h_3}{\partial \xi} - \alpha^2 h_2 h_3 - \frac{i\alpha h_2 h_3}{h_1}\frac{\partial h_1}{\partial \xi} - \frac{\partial h_3}{\partial \xi}\frac{\partial h_2}{\partial \xi}\right. \\
&\left. -h_3\frac{\partial^2 h_2}{\partial \xi^2} + \frac{h_3}{h_1}\frac{\partial h_2}{\partial \xi}\frac{\partial h_1}{\partial \xi}\right) \\
&- \frac{\mu}{Reh_1 h_2 h_3^2}\left(i\beta h_2\frac{\partial h_1}{\partial \zeta} - \beta^2 h_1 h_2 - \frac{i\beta h_1 h_2}{h_3}\frac{\partial h_3}{\partial \zeta} - \frac{\partial h_1}{\partial \zeta}\frac{\partial h_2}{\partial \zeta}\right. \\
&\left. -h_1\frac{\partial^2 h_2}{\partial \zeta^2} + \frac{h_1}{h_3}\frac{\partial h_3}{\partial \zeta}\frac{\partial h_2}{\partial \zeta}\right) \\
&- \frac{\mu}{Reh_2 h_3}\frac{\partial h_2}{\partial \zeta}\left(\frac{i\beta}{h_3} - \frac{1}{h_2 h_3}\frac{\partial h_2}{\partial \zeta}\right) - \frac{\mu}{Reh_1 h_2}\frac{\partial h_2}{\partial \xi}\left(\frac{i\alpha}{h_1} - \frac{1}{h_1 h_2}\frac{\partial h_2}{\partial \xi}\right) \\
&+ \frac{2\mu}{Reh_2^2 h_3^2}\frac{\partial h_3}{\partial \eta}\frac{\partial h_3}{\partial \eta} + \frac{2\mu}{Reh_1^2 h_2^2}\frac{\partial h_1}{\partial \eta}\frac{\partial h_1}{\partial \eta} \\
\mathcal{C}_{2,3} =& -2\frac{\rho w}{h_2 h_3}\frac{\partial h_3}{\partial \eta} + \left\{\left[\frac{\lambda}{Reh_2}\left(\frac{1}{h_1^2 h_2 h_3}\frac{\partial h_1}{\partial \eta} + \frac{1}{h_1 h_2^2 h_3}\frac{\partial h_2}{\partial \eta} + \frac{1}{h_1 h_2 h_3^2}\frac{\partial h_3}{\partial \eta}\right)\right.\right. \\
&\left.\left. -\frac{1}{Reh_1 h_2^2 h_3}\frac{\lambda}{\mu}\frac{\partial \mu}{\partial T}\frac{\partial T}{\partial \eta}\right]\left(i\beta h_1 h_2 + h_1\frac{\partial h_2}{\partial \zeta} + h_2\frac{\partial h_1}{\partial \zeta}\right)\right\}
\end{aligned}$$

$$
\begin{aligned}
&- \frac{\lambda}{Reh_1h_2^2h_3}\left(i\beta h_1\frac{\partial h_2}{\partial \eta}+i\beta h_2\frac{\partial h_1}{\partial \eta}+\frac{\partial h_1}{\partial \eta}\frac{\partial h_2}{\partial \zeta}\right.\\
&\left.+h_1\frac{\partial^2 h_2}{\partial \eta\partial \zeta}+\frac{\partial h_2}{\partial \eta}\frac{\partial h_1}{\partial \zeta}+h_2\frac{\partial^2 h_1}{\partial \eta\partial \zeta}\right)-\frac{2}{Reh_2^2h_3}\frac{\partial h_2}{\partial \zeta}\frac{\partial \mu}{\partial T}\frac{\partial T}{\partial \eta}\\
&- \frac{2\mu}{Reh_1h_2^2h_3}\left(\frac{\partial h_1}{\partial \eta}\frac{\partial h_2}{\partial \zeta}+h_1\frac{\partial^2 h_2}{\partial \eta\partial \zeta}-\frac{h_1}{h_2}\frac{\partial h_2}{\partial \eta}\frac{\partial h_2}{\partial \zeta}\right)\\
&+ \frac{\mu}{Reh_1h_2h_3^2}\left(i\beta h_1\frac{\partial h_3}{\partial \eta}+\frac{\partial h_1}{\partial \zeta}\frac{\partial h_3}{\partial \eta}+h_1\frac{\partial^2 h_3}{\partial \eta\partial \zeta}-\frac{h_1}{h_3}\frac{\partial h_3}{\partial \eta}\frac{\partial h_3}{\partial \zeta}\right)\\
&+ \frac{\mu}{Reh_2^2h_3^2}\frac{\partial h_2}{\partial \zeta}\frac{\partial h_3}{\partial \eta}+\frac{i2\beta\mu}{Reh_2h_3^2}\frac{\partial h_3}{\partial \eta}+\frac{2\mu}{Reh_1^2h_2h_3}\frac{\partial h_1}{\partial \eta}\frac{\partial h_1}{\partial \zeta}\\
\mathcal{C}_{2,4} =& \frac{1}{h_2\gamma M^2}\frac{\partial \rho}{\partial \eta}+\left\{\left[\frac{1}{Reh_2}\frac{\lambda}{\mu}\frac{\partial \mu}{\partial T}\left(\frac{1}{h_1^2h_2h_3}\frac{\partial h_1}{\partial \eta}+\frac{1}{h_1h_2^2h_3}\frac{\partial h_2}{\partial \eta}+\frac{1}{h_1h_2h_3^2}\frac{\partial h_3}{\partial \eta}\right)\right.\right.\\
&\left.\left.-\frac{1}{Reh_1h_2^2h_3}\frac{\lambda}{\mu}\frac{\partial^2 \mu}{\partial T^2}\frac{\partial T}{\partial \eta}\right]\left(uh_2\frac{\partial h_3}{\partial \xi}+uh_3\frac{\partial h_2}{\partial \xi}+wh_1\frac{\partial h_2}{\partial \zeta}+wh_2\frac{\partial h_1}{\partial \zeta}\right)\right\}\\
&- \frac{1}{Reh_1h_2^2h_3}\frac{\lambda}{\mu}\frac{\partial \mu}{\partial T}\left(h_2\frac{\partial h_3}{\partial \xi}\frac{\partial u}{\partial \eta}+u\frac{\partial h_2}{\partial \eta}\frac{\partial h_3}{\partial \xi}+uh_2\frac{\partial^2 h_3}{\partial \xi\partial \eta}+h_3\frac{\partial h_2}{\partial \xi}\frac{\partial u}{\partial \eta}\right.\\
&+u\frac{\partial h_3}{\partial \eta}\frac{\partial h_2}{\partial \xi}+uh_3\frac{\partial^2 h_2}{\partial \xi\partial \eta}+h_1\frac{\partial h_2}{\partial \zeta}\frac{\partial w}{\partial \eta}+w\frac{\partial h_1}{\partial \eta}\frac{\partial h_2}{\partial \zeta}+wh_1\frac{\partial^2 h_2}{\partial \eta\partial \zeta}\\
&\left.+h_2\frac{\partial h_1}{\partial \zeta}\frac{\partial w}{\partial \eta}+w\frac{\partial h_2}{\partial \eta}\frac{\partial h_1}{\partial \zeta}+wh_2\frac{\partial^2 h_1}{\partial \eta\partial \zeta}\right)-\frac{i\alpha}{Reh_1h_2h_3}\frac{\partial \mu}{\partial T}\left(h_3\frac{\partial u}{\partial \eta}-\frac{uh_3}{h_1}\frac{\partial h_1}{\partial \eta}\right)\\
&- \frac{1}{Reh_1h_2h_3}\frac{\partial \mu}{\partial T}\left(\frac{\partial u}{\partial \eta}\frac{\partial h_3}{\partial \xi}-\frac{u}{h_1}\frac{\partial h_3}{\partial \xi}\frac{\partial h_1}{\partial \eta}-\frac{uh_3}{h_1}\frac{\partial^2 h_1}{\partial \xi\partial \eta}+\frac{uh_3}{h_1^2}\frac{\partial h_1}{\partial \xi}\frac{\partial h_1}{\partial \eta}\right)\\
&- \frac{2}{Reh_1h_2h_3}\frac{\partial^2 \mu}{\partial T^2}\frac{\partial T}{\partial \eta}\left(\frac{wh_1}{h_2}\frac{\partial h_2}{\partial \zeta}+\frac{uh_3}{h_2}\frac{\partial h_2}{\partial \xi}\right)\\
&- \frac{2}{Reh_1h_2h_3}\frac{\partial \mu}{\partial T}\left(\frac{h_1}{h_2}\frac{\partial w}{\partial \eta}\frac{\partial h_2}{\partial \zeta}+\frac{w}{h_2}\frac{\partial h_1}{\partial \eta}\frac{\partial h_2}{\partial \zeta}+\frac{wh_1}{h_2}\frac{\partial^2 h_2}{\partial \eta\partial \zeta}-\frac{wh_1}{h_2^2}\frac{\partial h_2}{\partial \eta}\frac{\partial h_2}{\partial \zeta}\right.\\
&\left.+\frac{h_3}{h_2}\frac{\partial u}{\partial \eta}\frac{\partial h_2}{\partial \xi}+\frac{u}{h_2}\frac{\partial h_3}{\partial \eta}\frac{\partial h_2}{\partial \xi}+\frac{uh_3}{h_2}\frac{\partial^2 h_2}{\partial \xi\partial \eta}-\frac{uh_3}{h_2^2}\frac{\partial h_2}{\partial \eta}\frac{\partial h_2}{\partial \xi}\right)\\
&- \frac{i\beta}{Reh_1h_2h_3}\frac{\partial \mu}{\partial T}\left(h_1\frac{\partial w}{\partial \eta}-\frac{wh_1}{h_3}\frac{\partial h_3}{\partial \eta}\right)\\
&- \frac{1}{Reh_1h_2h_3}\frac{\partial \mu}{\partial T}\left(\frac{\partial h_1}{\partial \zeta}\frac{\partial w}{\partial \eta}-\frac{w}{h_3}\frac{\partial h_1}{\partial \zeta}\frac{\partial h_3}{\partial \eta}-\frac{wh_1}{h_3}\frac{\partial^2 h_3}{\partial \eta\partial \zeta}+\frac{wh_1}{h_3^2}\frac{\partial h_3}{\partial \eta}\frac{\partial h_3}{\partial \zeta}\right)\\
&- \frac{1}{Reh_2h_3}\frac{\partial \mu}{\partial T}\frac{\partial h_2}{\partial \zeta}\left(\frac{1}{h_2}\frac{\partial w}{\partial \eta}-\frac{w}{h_2h_3}\frac{\partial h_3}{\partial \eta}\right)-\frac{1}{Reh_1h_2}\frac{\partial \mu}{\partial T}\frac{\partial h_2}{\partial \xi}\left(\frac{1}{h_2}\frac{\partial u}{\partial \eta}-\frac{u}{h_1h_2}\frac{\partial h_1}{\partial \eta}\right)\\
&+ \frac{2u}{h_1h_2h_3^2}\frac{\partial \mu}{\partial T}\frac{\partial h_3}{\partial \eta}\frac{\partial h_3}{\partial \xi}+\frac{2w}{h_1^2h_2h_3}\frac{\partial \mu}{\partial T}\frac{\partial h_1}{\partial \eta}\frac{\partial h_1}{\partial \zeta}\\
\mathcal{C}_{2,5} =& -\left(\frac{w^2}{h_2h_3}\frac{\partial h_3}{\partial \eta}+\frac{u^2}{h_1h_2}\frac{\partial h_1}{\partial \eta}\right)+\frac{1}{h_2\gamma M^2}\frac{\partial T}{\partial \eta}
\end{aligned}
$$

$$
\begin{aligned}
\mathcal{C}_{3,1} = & \frac{\rho}{h_1 h_3}\left(w\frac{\partial h_3}{\partial \xi} - 2u\frac{\partial h_1}{\partial \zeta}\right) - \frac{\lambda}{Re h_1 h_2 h_3^2}\left(-\alpha\beta h_2 h_3 + i\alpha h_2\frac{\partial h_3}{\partial \zeta} + i\alpha h_3\frac{\partial h_2}{\partial \zeta}\right. \\
& \left. + i\beta h_2\frac{\partial h_3}{\partial \xi} + \frac{\partial h_2}{\partial \zeta}\frac{\partial h_3}{\partial \xi} + h_2\frac{\partial^2 h_3}{\partial \xi \partial \zeta} + i\beta h_3\frac{\partial h_2}{\partial \xi} + \frac{\partial h_3}{\partial \zeta}\frac{\partial h_2}{\partial \xi} + h_3\frac{\partial^2 h_2}{\partial \xi \partial \zeta}\right) \\
& + \frac{\lambda}{Re h_3}\left(i\alpha h_2 h_3 + h_2\frac{\partial h_3}{\partial \xi} + h_3\frac{\partial h_2}{\partial \xi}\right)\left(\frac{1}{h_1^2 h_2 h_3}\frac{\partial h_1}{\partial \zeta} + \frac{1}{h_1 h_2^2 h_3}\frac{\partial h_2}{\partial \zeta} + \frac{1}{h_1 h_2 h_3^2}\frac{\partial h_3}{\partial \zeta}\right) \\
& - \frac{\mu}{Re h_1 h_2 h_3}\left(-\alpha\beta h_2 + i\beta\frac{\partial h_2}{\partial \xi} - \frac{i\alpha h_2}{h_1}\frac{\partial h_1}{\partial \zeta} - \frac{1}{h_1}\frac{\partial h_2}{\partial \xi}\frac{\partial h_1}{\partial \zeta} - \frac{h_2}{h_1}\frac{\partial^2 h_1}{\partial \xi \partial \zeta} + \frac{h_2}{h_1^2}\frac{\partial h_1}{\partial \zeta}\frac{\partial h_1}{\partial \xi}\right) \\
& - \frac{2\mu}{Re h_1 h_2 h_3}\left(\frac{i\beta h_2}{h_3}\frac{\partial h_3}{\partial \xi} + \frac{1}{h_3}\frac{\partial h_2}{\partial \zeta}\frac{\partial h_3}{\partial \xi} + \frac{h_2}{h_3}\frac{\partial^2 h_3}{\partial \xi \partial \zeta} - \frac{h_2}{h_3^2}\frac{\partial h_3}{\partial \xi}\frac{\partial h_3}{\partial \zeta}\right) \\
& - \frac{\mu}{Re h_1 h_3^2}\frac{\partial h_3}{\partial \xi}\left(i\beta - \frac{1}{h_1}\frac{\partial h_1}{\partial \zeta}\right) + \frac{i2\mu\alpha}{Re h_1^2 h_3}\frac{\partial h_1}{\partial \zeta} + \frac{2\mu}{Re h_1 h_2^2 h_3}\frac{\partial h_2}{\partial \xi}\frac{\partial h_2}{\partial \zeta} \\
\mathcal{C}_{3,2} = & \frac{\rho}{h_2}\left(\frac{\partial w}{\partial \eta} + \frac{w}{h_3}\frac{\partial h_3}{\partial \eta}\right) - \frac{\lambda}{Re h_1 h_2 h_3^2}\left(i\beta h_1\frac{\partial h_3}{\partial \eta} + \frac{\partial h_1}{\partial \zeta}\frac{\partial h_3}{\partial \eta} + h_1\frac{\partial^2 h_3}{\partial \eta \partial \zeta}\right. \\
& \left. + i\beta h_3\frac{\partial h_1}{\partial \eta} + \frac{\partial h_3}{\partial \zeta}\frac{\partial h_1}{\partial \eta} + h_3\frac{\partial^2 h_1}{\partial \eta \partial \zeta}\right) \\
& + \frac{\lambda}{Re h_3}\left(h_1\frac{\partial h_3}{\partial \eta} + h_3\frac{\partial h_1}{\partial \eta}\right)\left(\frac{1}{h_1^2 h_2 h_3}\frac{\partial h_1}{\partial \zeta} + \frac{1}{h_1 h_2^2 h_3}\frac{\partial h_2}{\partial \zeta} + \frac{1}{h_1 h_2 h_3^2}\frac{\partial h_3}{\partial \zeta}\right) \\
& - \frac{1}{Re h_1 h_2 h_3}\frac{\partial \mu}{\partial T}\frac{\partial T}{\partial \eta}\left(i\beta h_1 - \frac{h_1}{h_2}\frac{\partial h_2}{\partial \zeta}\right) \\
& - \frac{\mu}{Re h_1 h_2 h_3}\left(i\beta\frac{\partial h_1}{\partial \eta} - \frac{1}{h_2}\frac{\partial h_1}{\partial \eta}\frac{\partial h_2}{\partial \zeta} - \frac{h_1}{h_2}\frac{\partial^2 h_2}{\partial \eta \partial \zeta} + \frac{h_1}{h_2^2}\frac{\partial h_2}{\partial \eta}\frac{\partial h_2}{\partial \zeta}\right) \\
& - \frac{2\mu}{Re h_1 h_2 h_3}\left(\frac{i\beta h_1}{h_3}\frac{\partial h_3}{\partial \eta} + \frac{1}{h_3}\frac{\partial h_1}{\partial \zeta}\frac{\partial h_3}{\partial \eta} + \frac{h_1}{h_3}\frac{\partial^2 h_3}{\partial \eta \partial \zeta} - \frac{h_1}{h_3^2}\frac{\partial h_3}{\partial \zeta}\frac{\partial h_3}{\partial \eta}\right) \\
& - \frac{\mu}{Re h_2 h_3^2}\frac{\partial h_3}{\partial \eta}\left(i\beta - \frac{1}{h_2}\frac{\partial h_2}{\partial \zeta}\right) + \frac{2\mu}{Re h_1^2 h_2 h_3}\frac{\partial h_1}{\partial \zeta}\frac{\partial h_1}{\partial \eta} \\
\mathcal{C}_{3,3} = & \rho\left(-i\omega + \frac{iu\alpha}{h_1} + \frac{iw\beta}{h_3} + \frac{u}{h_1 h_3}\frac{\partial h_3}{\partial \xi}\right) \\
& - \frac{\lambda}{Re h_1 h_2 h_3^2}\left(-\beta^2 h_1 h_2 + i2\beta h_1\frac{\partial h_2}{\partial \zeta} + i2\beta h_2\frac{\partial h_1}{\partial \zeta} + 2\frac{\partial h_1}{\partial \zeta}\frac{\partial h_2}{\partial \zeta} + h_1\frac{\partial^2 h_2}{\partial \zeta^2} + h_2\frac{\partial^2 h_1}{\partial \zeta^2}\right) \\
& + \frac{\lambda}{Re h_3}\left(i\beta h_1 h_2 + h_1\frac{\partial h_2}{\partial \zeta} + h_2\frac{\partial h_1}{\partial \zeta}\right)\left(\frac{1}{h_1^2 h_2 h_3}\frac{\partial h_1}{\partial \zeta} + \frac{1}{h_1 h_2^2 h_3}\frac{\partial h_2}{\partial \zeta} + \frac{1}{h_1 h_2 h_3^2}\frac{\partial h_3}{\partial \zeta}\right) \\
& + \frac{\mu}{Re h_1 h_2 h_3}\left(\frac{\alpha^2 h_2 h_3}{h_1} - \frac{i\alpha h_3}{h_1}\frac{\partial h_2}{\partial \xi} + \frac{i\alpha h_2 h_3}{h_1^2}\frac{\partial h_1}{\partial \xi}\right. \\
& \left. + \frac{1}{h_1}\frac{\partial h_2}{\partial \xi}\frac{\partial h_3}{\partial \xi} + \frac{h_2}{h_1}\frac{\partial^2 h_3}{\partial \xi^2} - \frac{h_2}{h_1^2}\frac{\partial h_1}{\partial \xi}\frac{\partial h_3}{\partial \xi}\right) \\
& + \frac{1}{Re h_2^2 h_3}\frac{\partial h_3}{\partial \eta}\frac{\partial \mu}{\partial T}\frac{\partial T}{\partial \eta} + \frac{\mu}{Re h_1 h_2 h_3}\left(\frac{1}{h_2}\frac{\partial h_1}{\partial \eta}\frac{\partial h_3}{\partial \eta} + \frac{h_1}{h_2}\frac{\partial^2 h_3}{\partial \eta^2} - \frac{h_1}{h_2^2}\frac{\partial h_2}{\partial \eta}\frac{\partial h_3}{\partial \eta}\right)
\end{aligned}
$$

$$
\begin{aligned}
&- \frac{2\mu}{Reh_1h_2h_3}\left(-\frac{\beta^2 h_1h_2}{h_3}+\frac{i\beta h_1}{h_3}\frac{\partial h_2}{\partial\zeta}+\frac{i\beta h_2}{h_3}\frac{\partial h_1}{\partial\zeta}-\frac{i\beta h_1h_2}{h_3^2}\frac{\partial h_3}{\partial\zeta}\right)\\
&- \frac{\mu}{Reh_1^2h_3}\frac{\partial h_3}{\partial\xi}\left(i\alpha-\frac{1}{h_3}\frac{\partial h_3}{\partial\xi}\right)+\frac{\mu}{Reh_2^2h_3^2}\left[\left(\frac{\partial h_3}{\partial\eta}\right)^2+2\left(\frac{\partial h_2}{\partial\zeta}\right)^2\right]\\
&+ \frac{2\mu}{Reh_1^2h_3^2}\left(\frac{\partial h_1}{\partial\zeta}\right)^2\\
\mathcal{C}_{3,4} =& \frac{i\beta\rho}{h_3\gamma M^2}-\left[\frac{1}{Reh_3}\frac{\lambda}{\mu}\frac{\partial\mu}{\partial T}\left(\frac{i\beta}{h_1h_2h_3}-\frac{1}{h_1^2h_2h_3}\frac{\partial h_1}{\partial\zeta}-\frac{1}{h_1h_2^2h_3}\frac{\partial h_2}{\partial\zeta}-\frac{1}{h_1h_2h_3^2}\frac{\partial h_3}{\partial\zeta}\right)\right.\\
&\left.\left(uh_2\frac{\partial h_3}{\partial\xi}+uh_3\frac{\partial h_2}{\partial\xi}+wh_1\frac{\partial h_2}{\partial\zeta}+wh_2\frac{\partial h_1}{\partial\zeta}\right)\right]\\
&- \frac{1}{Reh_1h_2h_3^2}\frac{\lambda}{\mu}\frac{\partial\mu}{\partial T}\left(u\frac{\partial h_2}{\partial\zeta}\frac{\partial h_3}{\partial\xi}+uh_2\frac{\partial^2 h_3}{\partial\xi\partial\zeta}+u\frac{\partial h_3}{\partial\zeta}\frac{\partial h_2}{\partial\xi}\right.\\
&\left.+uh_3\frac{\partial^2 h_2}{\partial\xi\partial\zeta}+2w\frac{\partial h_1}{\partial\zeta}\frac{\partial h_2}{\partial\zeta}+wh_1\frac{\partial^2 h_2}{\partial\zeta^2}+wh_2\frac{\partial^2 h_1}{\partial\zeta^2}\right)\\
&+ \frac{1}{Reh_1h_2h_3}\frac{\partial\mu}{\partial T}\left(\frac{i\alpha h_2}{h_1}+\frac{1}{h_1}\frac{\partial h_2}{\partial\xi}-\frac{h_2}{h_1^2}\frac{\partial h_1}{\partial\xi}\right)\left(u\frac{\partial h_1}{\partial\zeta}+w\frac{\partial h_3}{\partial\xi}\right)\\
&+ \frac{1}{Reh_1^2h_3}\frac{\partial\mu}{\partial T}\left(u\frac{\partial^2 h_1}{\partial\xi\partial\zeta}+w\frac{\partial^2 h_3}{\partial\xi^2}\right)-\frac{1}{Reh_2^2h_3}\frac{\partial\mu}{\partial T}\left(h_3\frac{\partial^2 w}{\partial\eta^2}-w\frac{\partial^2 h_3}{\partial\eta^2}\right)\\
&- \frac{1}{Reh_1h_2h_3}\left(\frac{\partial^2\mu}{\partial T^2}\frac{h_1}{h_2}\frac{\partial T}{\partial\eta}+\frac{1}{h_2}\frac{\partial h_1}{\partial\eta}\frac{\partial\mu}{\partial T}-\frac{h_1}{h_2^2}\frac{\partial h_2}{\partial\eta}\frac{\partial\mu}{\partial T}\right)\left(h_3\frac{\partial w}{\partial\eta}-w\frac{\partial h_3}{\partial\eta}\right)\\
&- \frac{2u}{Reh_1h_2h_3}\frac{\partial\mu}{\partial T}\left(\frac{i\beta h_2}{h_3}\frac{\partial h_3}{\partial\xi}+\frac{1}{h_3}\frac{\partial h_2}{\partial\zeta}\frac{\partial h_3}{\partial\xi}+\frac{h_2}{h_3}\frac{\partial^2 h_3}{\partial\xi\partial\zeta}-\frac{h_2}{h_3^2}\frac{\partial h_3}{\partial\xi}\frac{\partial h_3}{\partial\zeta}\right)\\
&+ \frac{1}{Reh_1^2h_3^2}\frac{\partial\mu}{\partial T}\frac{\partial h_3}{\partial\xi}\left(u\frac{\partial h_1}{\partial\zeta}+w\frac{\partial h_3}{\partial\xi}\right)-\frac{1}{Reh_2^2h_3}\frac{\partial\mu}{\partial T}\frac{\partial h_3}{\partial\eta}\left(\frac{\partial w}{\partial\eta}-\frac{w}{h_3}\frac{\partial h_3}{\partial\eta}\right)\\
&+ \frac{2}{Re}\frac{\partial\mu}{\partial T}\left[\frac{w}{h_1^2h_3^2}\left(\frac{\partial h_1}{\partial\zeta}\right)^2+\frac{w}{h_2^2h_3^2}\left(\frac{\partial h_2}{\partial\zeta}\right)^2+\frac{u}{h_1h_2^2h_3}\frac{\partial h_2}{\partial\xi}\frac{\partial h_2}{\partial\zeta}\right]\\
\mathcal{C}_{3,5} =& -\frac{u}{h_1h_3}\left(u\frac{\partial h_1}{\partial\zeta}-w\frac{\partial h_3}{\partial\xi}\right)+\frac{i\beta T}{h_3\gamma M^2}
\end{aligned}
$$

$$
\begin{aligned}
\mathcal{C}_{4,1} =& -\frac{(\gamma-1)M^2}{Re}\left\{\frac{i2\alpha w}{h_1^2h_3}\frac{\partial h_1}{\partial\zeta}(2\mu+\lambda)+\frac{2}{h_1h_2}\frac{\partial h_2}{\partial\xi}(2\mu+\lambda)\left(\frac{w}{h_2h_3}\frac{\partial h_2}{\partial\zeta}+\frac{u}{h_1h_2}\frac{\partial h_2}{\partial\xi}\right)\right.\\
&-2\mu\left(\frac{w}{h_1h_3}\frac{\partial h_3}{\partial\xi}+\frac{u}{h_1h_3}\frac{\partial h_1}{\partial\zeta}\right)\left(\frac{i\beta}{h_3}-\frac{1}{h_1h_3}\frac{\partial h_1}{\partial\zeta}\right)+(2\mu+\lambda)\frac{2u}{h_1^2h_3^2}\frac{\partial h_3}{\partial\xi}\frac{\partial h_3}{\partial\xi}\\
&\left.-\frac{2\mu}{h_1h_2}\frac{\partial h_1}{\partial\eta}\left(\frac{1}{h_2}\frac{\partial u}{\partial\eta}-\frac{u}{h_1h_2}\frac{\partial h_1}{\partial\eta}\right)+\frac{i2\lambda\alpha}{h_1}\left(\frac{w}{h_2h_3}\frac{\partial h_2}{\partial\zeta}+\frac{u}{h_1h_2}\frac{\partial h_2}{\partial\xi}\right)\right.
\end{aligned}
$$

$$
\begin{aligned}
&+\frac{2\lambda w}{h_1^2 h_2 h_3}\frac{\partial h_2}{\partial \xi}\frac{\partial h_1}{\partial \zeta}+\frac{i2\lambda\alpha u}{h_1^2 h_3}\frac{\partial h_3}{\partial \xi}+\frac{2\lambda w}{h_1^2 h_3^2}\frac{\partial h_1}{\partial \zeta}\frac{\partial h_3}{\partial \xi}\\
&+\frac{2\lambda u}{h_1^2 h_2 h_3}\frac{\partial h_2}{\partial \xi}\frac{\partial h_3}{\partial \xi}+\frac{2\lambda}{h_1 h_3}\frac{\partial h_3}{\partial \xi}\left(\frac{w}{h_2 h_3}\frac{\partial h_2}{\partial \zeta}+\frac{u}{h_1 h_2}\frac{\partial h_2}{\partial \xi}\right)\Bigg\}\\
\mathcal{C}_{4,2}=&\frac{\rho}{h_2}\frac{\partial T}{\partial \eta}-\frac{(\gamma-1)}{\gamma h_2}\left(T\frac{\partial \rho}{\partial \eta}+\rho\frac{\partial T}{\partial \eta}\right)-\frac{(\gamma-1)M^2}{Re}\Bigg\{(2\mu+\lambda)\frac{2w}{h_1^2 h_2 h_3}\frac{\partial h_1}{\partial \eta}\frac{\partial h_1}{\partial \zeta}\\
&+2\mu\left(\frac{1}{h_2}\frac{\partial w}{\partial \eta}-\frac{w}{h_2 h_3}\frac{\partial h_3}{\partial \eta}\right)\left(\frac{i\beta}{h_3}-\frac{1}{h_2 h_3}\frac{\partial h_2}{\partial \zeta}\right)+(2\mu+\lambda)\frac{2u}{h_1 h_2 h_3^2}\frac{\partial h_3}{\partial \xi}\frac{\partial h_3}{\partial \eta}\\
&+2\mu\left(\frac{1}{h_2}\frac{\partial u}{\partial \eta}-\frac{u}{h_1 h_2}\frac{\partial h_1}{\partial \eta}\right)\left(\frac{i\alpha}{h_1}-\frac{1}{h_1 h_2}\frac{\partial h_2}{\partial \xi}\right)+\frac{2\lambda}{h_1 h_2}\frac{\partial h_1}{\partial \eta}\left(\frac{w}{h_2 h_3}\frac{\partial h_2}{\partial \zeta}+\frac{u}{h_1 h_2}\frac{\partial h_2}{\partial \xi}\right)\\
&\frac{2\lambda u}{h_1^2 h_2 h_3}\frac{\partial h_3}{\partial \xi}\frac{\partial h_1}{\partial \eta}+\frac{2\lambda w}{h_1 h_2 h_3^2}\frac{\partial h_1}{\partial \zeta}\frac{\partial h_3}{\partial \eta}+\frac{2\lambda}{h_2 h_3}\frac{\partial h_3}{\partial \eta}\left(\frac{w}{h_2 h_3}\frac{\partial h_2}{\partial \zeta}+\frac{u}{h_1 h_2}\frac{\partial h_2}{\partial \xi}\right)\Bigg\}\\
\mathcal{C}_{4,3}=&-\frac{(\gamma-1)M^2}{Re}\Bigg\{(2\mu+\lambda)\frac{2w}{h_1^2 h_3^2}\frac{\partial h_1}{\partial \zeta}\frac{\partial h_1}{\partial \zeta}-\frac{2\mu}{h_2 h_3}\frac{\partial h_3}{\partial \eta}\left(\frac{1}{h_2}\frac{\partial w}{\partial \eta}-\frac{w}{h_2 h_3}\frac{\partial h_3}{\partial \eta}\right)\\
&+(2\mu+\lambda)\frac{2}{h_2 h_3}\frac{\partial h_2}{\partial \zeta}\left(\frac{w}{h_2 h_3}\frac{\partial h_2}{\partial \zeta}+\frac{u}{h_1 h_2}\frac{\partial h_2}{\partial \xi}\right)\\
&-2\mu\left(\frac{w}{h_1 h_3}\frac{\partial h_3}{\partial \xi}+\frac{u}{h_1 h_3}\frac{\partial h_1}{\partial \zeta}\right)\left(\frac{i\alpha}{h_1}-\frac{1}{h_1 h_3}\frac{\partial h_3}{\partial \xi}\right)\\
&+(2\mu+\lambda)\frac{i2\beta u}{h_1 h_3^2}\frac{\partial h_3}{\partial \xi}+\frac{2\lambda}{h_1 h_3}\frac{\partial h_1}{\partial \zeta}\left(\frac{w}{h_2 h_3}\frac{\partial h_2}{\partial \zeta}+\frac{u}{h_1 h_2}\frac{\partial h_2}{\partial \xi}\right)+\frac{2\lambda w}{h_1 h_2 h_3^2}\frac{\partial h_1}{\partial \zeta}\frac{\partial h_2}{\partial \zeta}\\
&+\frac{2\lambda u}{h_1^2 h_3^2}\frac{\partial h_3}{\partial \xi}\frac{\partial h_1}{\partial \zeta}+\frac{i2\lambda\beta w}{h_1 h_3^2}\frac{\partial h_1}{\partial \zeta}+\frac{2\lambda u}{h_1 h_2 h_3^2}\frac{\partial h_3}{\partial \xi}\frac{\partial h_2}{\partial \zeta}+\frac{i2\lambda\beta}{h_3}\left(\frac{w}{h_2 h_3}\frac{\partial h_2}{\partial \zeta}+\frac{u}{h_1 h_2}\frac{\partial h_2}{\partial \xi}\right)\Bigg\}\\
\mathcal{C}_{4,4}=&\rho\left(-i\omega+\frac{iu\alpha}{h_1}+\frac{iw\beta}{h_3}\right)-\frac{(\gamma-1)\rho}{\gamma}\left(-i\omega+\frac{iu\alpha}{h_1}+\frac{iw\beta}{h_3}\right)\\
&-\frac{1}{PrRe h_1 h_2 h_3}\Bigg[\kappa\left(\frac{i\alpha h_2}{h_1}\frac{\partial h_3}{\partial \xi}+\frac{i\alpha h_3}{h_1}\frac{\partial h_2}{\partial \xi}-\frac{\alpha^2 h_2 h_3}{h_1}-\frac{i\alpha h_2 h_3}{h_1^2}\frac{\partial h_1}{\partial \xi}\right.\\
&\left.+\frac{i\beta h_2}{h_3}\frac{\partial h_1}{\partial \zeta}+\frac{i\beta h_1}{h_3}\frac{\partial h_2}{\partial \zeta}-\frac{\beta^2 h_1 h_2}{h_3}-\frac{i\beta h_1 h_2}{h_3^2}\frac{\partial h_3}{\partial \zeta}\right)\\
&+\frac{\partial \kappa}{\partial T}\left(\frac{h_1}{h_2}\frac{\partial T}{\partial \eta}\frac{\partial h_3}{\partial \eta}+\frac{h_3}{h_2}\frac{\partial T}{\partial \eta}\frac{\partial h_1}{\partial \eta}-\frac{h_1 h_3\frac{\partial T}{\partial \eta}}{h_2^2}\frac{\partial h_2}{\partial \eta}+\frac{h_1 h_3\frac{\partial^2 T}{\partial \eta^2}}{h_2}\right)+\frac{\partial^2 \kappa}{\partial T^2}\left(\frac{\partial T}{\partial \eta}\right)^2\frac{h_1 h_3}{h_2}\Bigg]\\
&-\frac{(\gamma-1)M^2}{Re}\frac{\partial \mu}{\partial T}\Bigg\{\left(2+\frac{\lambda}{\mu}\right)\left(\frac{w}{h_1 h_3}\frac{\partial h_1}{\partial \zeta}\right)^2+\left(\frac{1}{h_2}\frac{\partial w}{\partial \eta}-\frac{w}{h_2 h_3}\frac{\partial h_3}{\partial \eta}\right)^2\\
&+\left(2+\frac{\lambda}{\mu}\right)\left(\frac{w}{h_2 h_3}\frac{\partial h_2}{\partial \zeta}+\frac{u}{h_1 h_2}\frac{\partial h_2}{\partial \xi}\right)^2+\left(\frac{w}{h_1 h_3}\frac{\partial h_3}{\partial \xi}+\frac{u}{h_1 h_3}\frac{\partial h_1}{\partial \zeta}\right)^2\\
&+\left(2+\frac{\lambda}{\mu}\right)\left(\frac{u}{h_1 h_3}\frac{\partial h_3}{\partial \xi}\right)^2+\left(\frac{1}{h_2}\frac{\partial u}{\partial \eta}-\frac{u}{h_1 h_2}\frac{\partial h_1}{\partial \eta}\right)^2\\
&+2\frac{\lambda}{\mu}\frac{w}{h_1 h_3}\frac{\partial h_1}{\partial \zeta}\left(\frac{w}{h_2 h_3}\frac{\partial h_2}{\partial \zeta}+\frac{u}{h_1 h_2}\frac{\partial h_2}{\partial \xi}\right)+2\frac{\lambda}{\mu}\frac{uw}{h_1^2 h_3^2}\frac{\partial h_1}{\partial \zeta}\frac{\partial h_3}{\partial \xi}
\end{aligned}
$$

$$+2\frac{\lambda}{\mu}\frac{u}{h_1 h_3}\frac{\partial h_3}{\partial \xi}\left(\frac{w}{h_2 h_3}\frac{\partial h_2}{\partial \zeta}+\frac{u}{h_1 h_2}\frac{\partial h_2}{\partial \xi}\right)\Bigg\}$$

$$\mathcal{C}_{4,5} = -\frac{(\gamma-1)\,T}{\gamma}\left(-i\omega+\frac{i\alpha u}{h_1}+\frac{i\beta w}{h_3}\right)$$

$$\mathcal{C}_{5,1} = \frac{\rho}{h_1}\left(i\alpha+\frac{1}{h_2}\frac{\partial h_2}{\partial \xi}+\frac{1}{h_3}\frac{\partial h_3}{\partial \xi}\right)$$

$$\mathcal{C}_{5,2} = \frac{1}{h_2}\left[\frac{\partial \rho}{\partial \eta}+\rho\left(\frac{1}{h_3}\frac{\partial h_3}{\partial \eta}+\frac{1}{h_1}\frac{\partial h_1}{\partial \eta}\right)\right]$$

$$\mathcal{C}_{5,3} = \frac{\rho}{h_3}\left(i\beta+\frac{1}{h_2}\frac{\partial h_2}{\partial \zeta}+\frac{1}{h_1}\frac{\partial h_1}{\partial \zeta}\right)$$

$$\mathcal{C}_{5,4} = 0$$

$$\mathcal{C}_{5,5} = -i\omega+\frac{u}{h_1}\left(i\alpha+\frac{1}{h_2}\frac{\partial h_2}{\partial \xi}+\frac{1}{h_3}\frac{\partial h_3}{\partial \xi}\right)+\frac{w}{h_3}\left(i\beta+\frac{1}{h_2}\frac{\partial h_2}{\partial \zeta}+\frac{1}{h_1}\frac{\partial h_1}{\partial \zeta}\right)$$

APPENDIX C

LPSE MATRIX FORMULATION

Details of the LPSE stability problem are now provided for the five linear matrices shown in equation C.1.

$$\mathcal{A}\frac{\partial^2\hat{\phi}}{\partial\eta^2} + \mathcal{B}\frac{\partial^2\hat{\phi}}{\partial\xi\partial\eta} + \mathcal{C}\frac{\partial\hat{\phi}}{\partial\eta} + \mathcal{D}\frac{\partial\hat{\phi}}{\partial\xi} + \mathcal{E}\hat{\phi} = 0 \tag{C.1}$$

Similar to LST, matrices $\mathcal{A}$ through $\mathcal{E}$ are (5×5) matrices containing linear terms. However, these matrices now exist for each wall-normal and streamwise point. Terms within each matrix are basic-state values and the solution vector takes the form $\hat{\phi} = \left[\hat{u},\ \hat{v},\ \hat{w},\ \hat{T},\ \hat{\rho}\right]$. Columns $1-5$ represent terms associated with $\hat{u}$, $\hat{v}$, $\hat{w}$, $\hat{T}$, and $\hat{\rho}$, respectively. Similarly, the first through last rows correspond to ξ-momentum, η-momentum, ζ-momentum, energy, and continuity.

C.1 A-Matrix

$$\mathcal{A} = \begin{bmatrix} -\frac{\mu}{Reh_2^2} & 0 & 0 & 0 & 0 \\ 0 & -\frac{1}{Reh_2^2}\left(\lambda+2\mu\right) & 0 & 0 & 0 \\ 0 & 0 & -\frac{\mu}{Reh_2^2} & 0 & 0 \\ 0 & 0 & 0 & -\frac{\kappa}{PrReh_2^2} & 0 \\ 0 & 0 & 0 & 0 & 0 \end{bmatrix}$$

C.2 B-Matrix

$$\mathcal{B} = \begin{bmatrix} 0 & -\frac{1}{Reh_1h_2}(\lambda+\mu) & 0 & 0 & 0 \\ -\frac{1}{Reh_1h_2}(\lambda+\mu) & 0 & 0 & 0 & 0 \\ 0 & 0 & 0 & 0 & 0 \\ 0 & 0 & 0 & 0 & 0 \\ 0 & 0 & 0 & 0 & 0 \end{bmatrix}$$

C.3 C-Matrix

$$\mathcal{C}_{1,1} = -\frac{1}{Reh_2^2}\frac{\partial\mu}{\partial T}\frac{\partial T}{\partial\eta} - \frac{\mu}{Reh_2^2h_3}\left(\frac{\partial h_3}{\partial\eta} - \frac{h_3}{h_2}\frac{\partial h_2}{\partial\eta} + \frac{h_3}{h_1}\frac{\partial h_1}{\partial\eta}\right) + \frac{\rho v}{h_2}$$

$$\mathcal{C}_{1,2} = \frac{\lambda h_3}{Re}\left(\frac{1}{h_1^2h_2h_3}\frac{\partial h_1}{\partial\xi} + \frac{1}{h_1h_2^2h_3}\frac{\partial h_2}{\partial\xi} + \frac{1}{h_1h_2h_3^2}\frac{\partial h_3}{\partial\xi}\right) - \frac{1}{Reh_1h_2}\frac{\lambda}{\mu}\frac{\partial\mu}{\partial T}\frac{\partial T}{\partial\xi}$$
$$- \frac{\lambda}{Reh_1^2h_2h_3}\left(h_1\frac{\partial h_3}{\partial\xi} + h_3\frac{\partial h_1}{\partial\xi} + i\alpha h_1h_3\right) + \frac{3\mu}{Reh_1h_2^2}\frac{\partial h_2}{\partial\xi} - \frac{i\alpha\mu}{Reh_1h_2}$$

$$\mathcal{C}_{1,3} = 0$$

$$\mathcal{C}_{1,4} = -\frac{1}{Reh_1h_2}\frac{\partial\mu}{\partial T}\left(\frac{\partial v}{\partial\xi} - \frac{v}{h_2}\frac{\partial h_2}{\partial\xi} + \frac{h_1}{h_2}\frac{\partial u}{\partial\eta} - \frac{u}{h_2}\frac{\partial h_1}{\partial\eta}\right)$$

$$\mathcal{C}_{1,5} = 0$$

$$
\begin{aligned}
\mathcal{C}_{2,1} =& -\frac{\lambda}{Reh_1h_2^2h_3}\left(i\alpha h_2h_3 + h_2\frac{\partial h_3}{\partial \xi} + h_3\frac{\partial h_2}{\partial \xi}\right) - \frac{1}{Reh_1h_2}\frac{\partial \mu}{\partial T}\frac{\partial T}{\partial \xi} \\
& -\frac{\mu}{Reh_1h_2h_3}\left(\frac{\partial h_3}{\partial \xi} + h_3 i\alpha\right) - \frac{3\mu}{Reh_1h_2^2}\frac{\partial h_2}{\partial \xi} \\
\mathcal{C}_{2,2} =& \frac{\rho v}{h_2} - \frac{h_1h_3}{Re}\left[\frac{1}{h_1h_2^2h_3}\frac{\lambda}{\mu}\frac{\partial \mu}{\partial T}\frac{\partial T}{\partial \eta} - \frac{\lambda}{h_2}\left(\frac{1}{h_1^2h_2h_3}\frac{\partial h_1}{\partial \eta} + \frac{1}{h_1h_2^2h_3}\frac{\partial h_2}{\partial \eta} + \frac{1}{h_1h_2h_3^2}\frac{\partial h_3}{\partial \eta}\right)\right] \\
& -\frac{2\lambda}{Reh_1h_2^2h_3}\left(h_3\frac{\partial h_1}{\partial \eta} + h_1\frac{\partial h_3}{\partial \eta}\right) - \frac{2}{Reh_2^2}\frac{\partial \mu}{\partial T}\frac{\partial T}{\partial \eta} \\
& -\frac{2\mu}{Reh_1h_2^2h_3}\left(h_3\frac{\partial h_1}{\partial \eta} + h_1\frac{\partial h_3}{\partial \eta} - \frac{h_1h_3}{h_2}\frac{\partial h_2}{\partial \eta}\right) \\
\mathcal{C}_{2,3} =& -\frac{\lambda}{Reh_1h_2^2h_3}\left(i\beta h_1h_2 + h_1\frac{\partial h_2}{\partial \zeta} + h_2\frac{\partial h_1}{\partial \zeta}\right) \\
& -\frac{\mu}{Reh_1h_2h_3}\left(\frac{\partial h_1}{\partial \zeta} + h_1 i\beta\right) - \frac{3\mu}{Reh_2^2h_3}\frac{\partial h_2}{\partial \zeta} \\
\mathcal{C}_{2,4} =& \frac{\rho}{h_2\gamma M^2} - \frac{1}{Reh_1h_2^2h_3}\frac{\lambda}{\mu}\frac{\partial \mu}{\partial T}\left(h_2h_3\frac{\partial u}{\partial \xi} + uh_2\frac{\partial h_3}{\partial \xi} + uh_3\frac{\partial h_2}{\partial \xi} + h_1h_3\frac{\partial v}{\partial \eta} + vh_3\frac{\partial h_1}{\partial \eta}\right. \\
& \left. + vh_1\frac{\partial h_3}{\partial \eta} + wh_1\frac{\partial h_2}{\partial \zeta} + wh_2\frac{\partial h_1}{\partial \zeta}\right) - \frac{2}{Reh_1h_2^2h_3}\frac{\partial \mu}{\partial T}\left(h_1h_3\frac{\partial v}{\partial \eta} + wh_1\frac{\partial h_2}{\partial \zeta} + uh_3\frac{\partial h_2}{\partial \xi}\right) \\
\mathcal{C}_{2,5} =& \frac{T}{h_2\gamma M^2}
\end{aligned}
$$

$$
\begin{aligned}
\mathcal{C}_{3,1} =& 0 \\
\mathcal{C}_{3,2} =& \frac{\lambda h_1}{Re}\left(\frac{1}{h_1^2h_2h_3}\frac{\partial h_1}{\partial \zeta} + \frac{1}{h_1h_2^2h_3}\frac{\partial h_2}{\partial \zeta} + \frac{1}{h_1h_2h_3^2}\frac{\partial h_3}{\partial \zeta}\right) \\
& -\frac{\lambda}{Reh_1h_2h_3^2}\left(i\beta h_1h_3 + h_1\frac{\partial h_3}{\partial \zeta} + h_3\frac{\partial h_1}{\partial \zeta}\right) + \frac{3\mu}{Reh_2^2h_3}\frac{\partial h_2}{\partial \zeta} - \frac{i\beta\mu}{Reh_2h_3} \\
\mathcal{C}_{3,3} =& \frac{\rho v}{h_2} - \frac{1}{Reh_2^2}\frac{\partial \mu}{\partial T}\frac{\partial T}{\partial \eta} - \frac{\mu}{Reh_1h_2^2}\left(\frac{\partial h_1}{\partial \eta} - \frac{h_1}{h_2}\frac{\partial h_2}{\partial \eta} + \frac{h_1}{h_3}\frac{\partial h_3}{\partial \eta}\right) \\
\mathcal{C}_{3,4} =& -\frac{1}{Reh_2^2h_3}\frac{\partial \mu}{\partial T}\left(h_3\frac{\partial w}{\partial \eta} - w\frac{\partial h_3}{\partial \eta} - v\frac{\partial h_2}{\partial \eta}\right) \\
\mathcal{C}_{3,5} =& 0
\end{aligned}
$$

$$\mathcal{C}_{4,1} = -\frac{2(\gamma-1)M^2\mu}{Reh_2}\left(\frac{1}{h_1}\frac{\partial v}{\partial \xi} - \frac{v}{h_1h_2}\frac{\partial h_2}{\partial \xi} + \frac{1}{h_2}\frac{\partial u}{\partial \eta} - \frac{u}{h_1h_2}\frac{\partial h_1}{\partial \eta}\right)$$

$$\mathcal{C}_{4,2} = -\frac{-2(\gamma-1)M^2}{Reh_2}\left[(2\mu+\lambda)\left(\frac{1}{h_2}\frac{\partial v}{\partial \eta} + \frac{w}{h_2h_3}\frac{\partial h_2}{\partial \zeta} + \frac{u}{h_1h_2}\frac{\partial h_2}{\partial \xi}\right)\right.$$
$$\left. + \frac{\lambda}{h_3}\left(\frac{u}{h_1}\frac{\partial h_3}{\partial \xi} + \frac{v}{h_2}\frac{\partial h_3}{\partial \eta}\right) + \frac{\lambda}{h_1}\left(\frac{\partial u}{\partial \xi} + \frac{v}{h_2}\frac{\partial h_1}{\partial \eta} + \frac{w}{h_3}\frac{\partial h_1}{\partial \zeta}\right)\right]$$

$$\mathcal{C}_{4,3} = -\frac{2(\gamma-1)M^2\mu}{Reh_2}\left(\frac{1}{h_2}\frac{\partial w}{\partial \eta} - \frac{w}{h_2h_3}\frac{\partial h_3}{\partial \eta} - \frac{v}{h_2h_3}\frac{\partial h_2}{\partial \zeta}\right)$$

$$\mathcal{C}_{4,4} = \frac{\rho v}{h_2} - \frac{(\gamma-1)}{\gamma}\frac{v\rho}{h_2} - \frac{1}{PrReh_1h_2^2h_3}\left(2\frac{\partial \kappa}{\partial T}\frac{\partial T}{\partial \eta}h_1h_3 + \kappa h_1\frac{\partial h_3}{\partial \eta} + \kappa h_3\frac{\partial h_1}{\partial \eta} - \frac{\kappa h_1h_3}{h_2}\frac{\partial h_2}{\partial \eta}\right)$$

$$\mathcal{C}_{4,5} = -\frac{(\gamma-1)}{\gamma}\frac{vT}{h_2}$$

$$\mathcal{C}_{5,1} = 0$$

$$\mathcal{C}_{5,2} = \frac{\rho}{h_2}$$

$$\mathcal{C}_{5,3} = 0$$

$$\mathcal{C}_{5,4} = 0$$

$$\mathcal{C}_{5,5} = \frac{v}{h_2}$$

C.4 D-Matrix

$$
\begin{aligned}
\mathcal{D}_{1,1} =& \frac{\rho u}{h_1} - \frac{2\lambda}{Re h_1^2 h_2 h_3}\left(i\alpha h_2 h_3 + h_2\frac{\partial h_3}{\partial \xi} + h_3\frac{\partial h_2}{\partial \xi}\right) \\
&+ \frac{\lambda h_2 h_3}{Re h_1}\left(\frac{1}{h_1^2 h_2 h_3}\frac{\partial h_1}{\partial \xi} + \frac{1}{h_1 h_2^2 h_3}\frac{\partial h_2}{\partial \xi} + \frac{1}{h_1 h_2 h_3^2}\frac{\partial h_3}{\partial \xi}\right) \\
&- \frac{2\mu}{Re h_1^2 h_2 h_3}\left(h_2\frac{\partial h_3}{\partial \xi} + h_3\frac{\partial h_2}{\partial \xi} - \frac{h_2 h_3}{h_1}\frac{\partial h_1}{\partial \xi} + i2\alpha h_2 h_3\right) \\
\mathcal{D}_{1,2} =& -\frac{\lambda}{Re h_1^2 h_2 h_3}\left(h_1\frac{\partial h_3}{\partial \eta} + h_3\frac{\partial h_1}{\partial \eta}\right) - \frac{3\mu}{Re h_1^2 h_2}\frac{\partial h_1}{\partial \eta} - \frac{1}{Re h_1 h_2}\frac{\partial \mu}{\partial T}\frac{\partial T}{\partial \eta} - \frac{\mu}{Re h_1 h_2 h_3}\frac{\partial h_3}{\partial \eta} \\
\mathcal{D}_{1,3} =& -\frac{\lambda}{Re h_1^2 h_2 h_3}\left(i\beta h_1 h_2 + h_1\frac{\partial h_2}{\partial \zeta} + h_2\frac{\partial h_1}{\partial \zeta}\right) - \frac{3\mu}{Re h_1^2 h_3}\frac{\partial h_1}{\partial \zeta} \\
&- \frac{i\beta\mu}{Re h_1 h_3} - \frac{\mu}{Re h_1 h_2 h_3}\frac{\partial h_2}{\partial \zeta} \\
\mathcal{D}_{1,4} =& \Omega\frac{\rho}{h_1\gamma M^2} - \frac{1}{Re h_1^2 h_2 h_3}\frac{\lambda}{\mu}\frac{\partial \mu}{\partial T}\left(u h_2\frac{\partial h_3}{\partial \xi} + u h_3\frac{\partial h_2}{\partial \xi} + v h_1\frac{\partial h_3}{\partial \eta} + v h_3\frac{\partial h_1}{\partial \eta} + h_1 h_3\frac{\partial v}{\partial \eta}\right. \\
&\left. + w h_1\frac{\partial h_2}{\partial \zeta} + w h_2\frac{\partial h_1}{\partial \zeta}\right) - \frac{2}{Re h_1 h_2 h_3}\frac{\partial \mu}{\partial T}\left(\frac{v h_3}{h_1}\frac{\partial h_1}{\partial \eta} + \frac{w h_2}{h_1}\frac{\partial h_1}{\partial \zeta}\right) \\
\mathcal{D}_{1,5} =& \Omega\frac{T}{h_1\gamma M^2}
\end{aligned}
$$

$$
\begin{aligned}
\mathcal{D}_{2,1} =& -\frac{h_2 h_3}{Re}\left[\frac{1}{h_1 h_2^2 h_3}\frac{\lambda}{\mu}\frac{\partial \mu}{\partial T}\frac{\partial T}{\partial \eta} - \frac{\lambda}{h_2}\left(\frac{1}{h_1^2 h_2 h_3}\frac{\partial h_1}{\partial \eta} + \frac{1}{h_1 h_2^2 h_3}\frac{\partial h_2}{\partial \eta} + \frac{1}{h_1 h_2 h_3^2}\frac{\partial h_3}{\partial \eta}\right)\right] \\
&- \frac{\lambda}{Re h_1 h_2^2 h_3}\left(h_3\frac{\partial h_2}{\partial \eta} + h_2\frac{\partial h_3}{\partial \eta}\right) + \frac{3\mu}{Re h_1^2 h_2}\frac{\partial h_1}{\partial \eta} \\
\mathcal{D}_{2,2} =& \frac{\rho u}{h_1} - \frac{\mu}{Re h_1^2 h_2 h_3}\left(i2\alpha h_2 h_3 + h_2\frac{\partial h_3}{\partial \xi} + h_3\frac{\partial h_2}{\partial \xi} - \frac{h_2 h_3}{h_1}\frac{\partial h_1}{\partial \xi}\right) \\
\mathcal{D}_{2,3} =& 0 \\
\mathcal{D}_{2,4} =& -\frac{1}{Re h_1^2 h_2 h_3}\frac{\partial \mu}{\partial T}\left(-v h_3\frac{\partial h_2}{\partial \xi} + \frac{h_3}{h_1}\frac{\partial u}{\partial \eta} - u h_3\frac{\partial h_1}{\partial \eta}\right) \\
\mathcal{D}_{2,5} =& 0
\end{aligned}
$$

$$\mathcal{D}_{3,1} = \frac{\lambda h_2}{Re}\left(\frac{1}{h_1^2 h_2 h_3}\frac{\partial h_1}{\partial \zeta} + \frac{1}{h_1 h_2^2 h_3}\frac{\partial h_2}{\partial \zeta} + \frac{1}{h_1 h_2 h_3^2}\frac{\partial h_3}{\partial \zeta}\right)$$
$$- \frac{\lambda}{Re h_1 h_2 h_3^2}\left(i\beta h_2 h_3 + h_2\frac{\partial h_3}{\partial \zeta} + h_3\frac{\partial h_2}{\partial \zeta}\right) + \frac{3\mu}{Re h_1^2 h_3}\frac{\partial h_1}{\partial \zeta} - \frac{i\beta\mu}{Re h_1 h_3}$$

$$\mathcal{D}_{3,2} = 0$$

$$\mathcal{D}_{3,3} = \frac{\rho u}{h_1} - \frac{\mu}{Re h_1^2 h_2 h_3}\left(i2\alpha h_2 h_3 - \frac{h_2 h_3}{h_1}\frac{\partial h_1}{\partial \xi} + h_3\frac{\partial h_2}{\partial \xi} + h_2\frac{\partial h_3}{\partial \xi}\right)$$

$$\mathcal{D}_{3,4} = - \frac{1}{Re h_1^2 h_2 h_3}\frac{\partial \mu}{\partial T}\left(-u h_2\frac{\partial h_1}{\partial \zeta} - w h_2\frac{\partial h_3}{\partial \xi}\right)$$

$$\mathcal{D}_{3,5} = 0$$

$$\mathcal{D}_{4,1} = - \frac{2(\gamma-1)M^2}{Re h_1}\left[(2\mu+\lambda)\left(\frac{v}{h_1 h_2}\frac{\partial h_1}{\partial \eta} + \frac{w}{h_1 h_3}\frac{\partial h_1}{\partial \zeta}\right) + \frac{\lambda}{h_2}\left(\frac{\partial v}{\partial \eta} + \frac{w}{h_3}\frac{\partial h_2}{\partial \zeta} + \frac{u}{h_1}\frac{\partial h_2}{\partial \xi}\right)\right.$$
$$\left. + \frac{\lambda}{h_3}\left(\frac{u}{h_1}\frac{\partial h_3}{\partial \xi} + \frac{v}{h_2}\frac{\partial h_3}{\partial \eta}\right)\right]$$

$$\mathcal{D}_{4,2} = - \frac{2\mu(\gamma-1)M^2}{Re h_1}\left(-\frac{v}{h_1 h_2}\frac{\partial h_2}{\partial \xi} + \frac{1}{h_2}\frac{\partial u}{\partial \eta} - \frac{u}{h_1 h_2}\frac{\partial h_1}{\partial \eta}\right)$$

$$\mathcal{D}_{4,3} = - \frac{2\mu(\gamma-1)M^2}{Re h_1}\left(-\frac{w}{h_1 h_3}\frac{\partial h_3}{\partial \xi} - \frac{u}{h_1 h_3}\frac{\partial h_1}{\partial \zeta}\right)$$

$$\mathcal{D}_{4,4} = \frac{u\rho}{h_1} - \Omega\frac{(\gamma-1)u\rho}{\gamma h_1} - \frac{1}{Pr Re h_1^2 h_2 h_3}\left(\kappa h_2\frac{\partial h_3}{\partial \xi} + \kappa h_3\frac{\partial h_2}{\partial \xi} - \frac{\kappa h_2 h_3}{h_1}\frac{\partial h_1}{\partial \xi} + i2\alpha\kappa h_2 h_3\right)$$

$$\mathcal{D}_{4,5} = - \Omega\frac{(\gamma-1)uT}{\gamma h_1}$$

$$\mathcal{D}_{5,1} = \frac{\rho}{h_1}$$

$$\mathcal{D}_{5,2} = 0$$

$$\mathcal{D}_{5,3} = 0$$

$$\mathcal{D}_{5,4} = 0$$

$$\mathcal{D}_{5,5} = \frac{u}{h_1}$$

C.5 E-Matrix

$$\begin{aligned}
\mathcal{E}_{1,1} = &\rho\left(-i\omega + \frac{1}{h_1}\frac{\partial u}{\partial \xi} + \frac{iu\alpha}{h_1} + \frac{iw\beta}{h_3} + \frac{v}{h_1 h_2}\frac{\partial h_1}{\partial \eta} + \frac{w}{h_1 h_3}\frac{\partial h_1}{\partial \zeta}\right) \\
&- \frac{\lambda}{Re h_1^2 h_2 h_3}\left(i2\alpha h_2\frac{\partial h_3}{\partial \xi} + i2\alpha h_3\frac{\partial h_2}{\partial \xi} - \alpha^2 h_2 h_3 + ih_2 h_3\frac{\partial \alpha}{\partial \xi}\right. \\
&\left.+2\frac{\partial h_2}{\partial \xi}\frac{\partial h_3}{\partial \xi} + h_2\frac{\partial^2 h_3}{\partial \xi^2} + h_3\frac{\partial^2 h_2}{\partial \xi^2}\right) \\
&- \frac{1}{Re}\left\{\left[\frac{1}{h_1^2 h_2 h_3}\frac{\lambda}{\mu}\frac{\partial \mu}{\partial T}\frac{\partial T}{\partial \xi} - \frac{\lambda}{h_1}\left(\frac{1}{h_1^2 h_2 h_3}\frac{\partial h_1}{\partial \xi} + \frac{1}{h_1 h_2^2 h_3}\frac{\partial h_2}{\partial \xi} + \frac{1}{h_1 h_2 h_3^2}\frac{\partial h_3}{\partial \xi}\right)\right]\right. \\
&\left.\left(i\alpha h_2 h_3 + h_2\frac{\partial h_3}{\partial \xi} + h_3\frac{\partial h_2}{\partial \xi}\right)\right\} - \frac{i2\alpha}{Re h_1^2}\frac{\partial \mu}{\partial T}\frac{\partial T}{\partial \xi} \\
&- \frac{2\mu}{Re h_1 h_2 h_3}\left[i\alpha\left(\frac{h_3}{h_1}\frac{\partial h_2}{\partial \xi} + \frac{h_2}{h_1}\frac{\partial h_3}{\partial \xi} - \frac{h_2 h_3}{h_1^2}\frac{\partial h_1}{\partial \xi}\right) + i\frac{h_2 h_3}{h_1}\frac{\partial \alpha}{\partial \xi} - \alpha^2\frac{h_2 h_3}{h_1}\right] \\
&+ \frac{1}{Re h_1 h_2^2}\frac{\partial \mu}{\partial T}\frac{\partial h_1}{\partial \eta}\frac{\partial T}{\partial \eta} + \frac{\mu}{Re h_1 h_2 h_3}\left(\frac{h_3}{h_2}\frac{\partial^2 h_1}{\partial \eta^2} + \frac{1}{h_2}\frac{\partial h_3}{\partial \eta}\frac{\partial h_1}{\partial \eta} - \frac{h_3}{h_2^2}\frac{\partial h_2}{\partial \eta}\frac{\partial h_1}{\partial \eta}\right) \\
&- \frac{\mu}{Re h_1 h_2 h_3}\left(i\beta\frac{h_1}{h_3}\frac{\partial h_2}{\partial \zeta} - i\beta\frac{h_1 h_2}{h_3^2}\frac{\partial h_3}{\partial \zeta} - \beta^2\frac{h_1 h_2}{h_3}\right. \\
&\left.-\frac{1}{h_3}\frac{\partial h_2}{\partial \zeta}\frac{\partial h_1}{\partial \zeta} - \frac{h_2}{h_3}\frac{\partial^2 h_1}{\partial \zeta^2} + \frac{h_2}{h_3^2}\frac{\partial h_3}{\partial \zeta}\frac{\partial h_1}{\partial \zeta}\right) + \frac{\mu}{Re h_1^2 h_2^2}\left(\left(\frac{\partial h_1}{\partial \eta}\right)^2 + 2\left(\frac{\partial h_2}{\partial \xi}\right)^2\right) \\
&- \frac{\mu}{Re h_1 h_3^2}\frac{\partial h_1}{\partial \zeta}\left(i\beta - \frac{1}{h_1}\frac{\partial h_1}{\partial \zeta}\right) + \frac{2\mu}{Re h_1^2 h_3^2}\left(\frac{\partial h_3}{\partial \xi}\right)^2 \\
\mathcal{E}_{1,2} = &\rho\left[\frac{1}{h_2}\frac{\partial u}{\partial \eta} - \frac{1}{h_1 h_2}\left(2v\frac{\partial h_2}{\partial \xi} - u\frac{\partial h_1}{\partial \eta}\right)\right] \\
&- \frac{\lambda}{Re h_1^2 h_2 h_3}\left(i\alpha h_1\frac{\partial h_3}{\partial \eta} + \frac{\partial h_1}{\partial \xi}\frac{\partial h_3}{\partial \eta} + h_1\frac{\partial^2 h_3}{\partial \xi \partial \eta} + i\alpha h_3\frac{\partial h_1}{\partial \eta} + \frac{\partial h_3}{\partial \xi}\frac{\partial h_1}{\partial \eta} + h_3\frac{\partial^2 h_1}{\partial \xi \partial \eta}\right)
\end{aligned}$$

$$
\begin{aligned}
&- \frac{1}{Re}\left\{\left[\frac{1}{h_1^2h_2h_3}\frac{\lambda}{\mu}\frac{\partial\mu}{\partial T}\frac{\partial T}{\partial\xi} - \frac{\lambda}{h_1}\left(\frac{1}{h_1^2h_2h_3}\frac{\partial h_1}{\partial\xi} + \frac{1}{h_1h_2^2h_3}\frac{\partial h_2}{\partial\xi} + \frac{1}{h_1h_2h_3^2}\frac{\partial h_3}{\partial\xi}\right)\right]\right.\\
&\left.\left(h_1\frac{\partial h_3}{\partial\eta} + h_3\frac{\partial h_1}{\partial\eta}\right)\right\} - \frac{2}{Reh_1^2h_2}\frac{\partial\mu}{\partial T}\frac{\partial T}{\partial\xi}\frac{\partial h_1}{\partial\eta}\\
&- \frac{2\mu}{Reh_1h_2h_3}\left(i\alpha\frac{h_3}{h_1}\frac{\partial h_1}{\partial\eta} + \frac{1}{h_1}\frac{\partial h_3}{\partial\xi}\frac{\partial h_1}{\partial\eta} + \frac{h_3}{h_1}\frac{\partial^2 h_1}{\partial\xi\partial\eta} - \frac{h_3}{h_1^2}\frac{\partial h_1}{\partial\xi}\frac{\partial h_1}{\partial\eta}\right)\\
&- \frac{1}{Reh_1h_2}\frac{\partial\mu}{\partial T}\frac{\partial T}{\partial\eta}\left(i\alpha - \frac{1}{h_2}\frac{\partial h_2}{\partial\xi}\right)\\
&- \frac{\mu}{Reh_1h_2h_3}\left(i\alpha\frac{\partial h_3}{\partial\eta} - \frac{1}{h_2}\frac{\partial h_3}{\partial\eta}\frac{\partial h_2}{\partial\xi} - \frac{h_3}{h_2}\frac{\partial^2 h_2}{\partial\xi\partial\eta} + \frac{h_3}{h_2^2}\frac{\partial h_2}{\partial\eta}\frac{\partial h_2}{\partial\xi}\right)\\
&- \frac{\mu}{Reh_1^2h_2}\frac{\partial h_1}{\partial\eta}\left(i\alpha - \frac{1}{h_2}\frac{\partial h_2}{\partial\xi}\right) + \frac{2\mu}{Reh_1h_2h_3^2}\frac{\partial h_3}{\partial\xi}\frac{\partial h_3}{\partial\eta}
\end{aligned}
$$

$$
\begin{aligned}
\mathcal{E}_{1,3} =& \rho\left(\frac{u}{h_1h_3}\frac{\partial h_1}{\partial\zeta} - \frac{2w}{h_1h_3}\frac{\partial h_3}{\partial\xi}\right) - \frac{\lambda}{Reh_1^2h_2h_3}\left(i\beta h_1\frac{\partial h_2}{\partial\xi} + i\beta h_2\frac{\partial h_1}{\partial\xi} - \alpha\beta h_1h_2 + i\alpha h_1\frac{\partial h_2}{\partial\zeta}\right.\\
&\left.+\frac{\partial h_1}{\partial\xi}\frac{\partial h_2}{\partial\zeta} + h_1\frac{\partial^2 h_2}{\partial\xi\partial\zeta} + i\alpha h_2\frac{\partial h_1}{\partial\zeta} + \frac{\partial h_2}{\partial\xi}\frac{\partial h_1}{\partial\zeta} + h_2\frac{\partial^2 h_1}{\partial\xi\partial\zeta}\right) - \frac{1}{Re}\left\{\left[\frac{1}{h_1^2h_2h_3}\frac{\lambda}{\mu}\frac{\partial\mu}{\partial T}\frac{\partial T}{\partial\xi}\right.\right.\\
&\left.\left.-\frac{\lambda}{h_1}\left(\frac{1}{h_1^2h_2h_3}\frac{\partial h_1}{\partial\xi} + \frac{1}{h_1h_2^2h_3}\frac{\partial h_2}{\partial\xi} + \frac{1}{h_1h_2h_3^2}\frac{\partial h_3}{\partial\xi}\right)\right]\left(i\beta h_1h_2 + h_1\frac{\partial h_2}{\partial\zeta} + h_2\frac{\partial h_1}{\partial\zeta}\right)\right\}\\
&- \frac{2}{Reh_1^2h_3}\frac{\partial\mu}{\partial T}\frac{\partial T}{\partial\xi}\frac{\partial h_1}{\partial\zeta} - \frac{2\mu}{Reh_1^2h_2h_3}\left(\frac{\partial h_2}{\partial\xi}\frac{\partial h_1}{\partial\zeta} + h_2\frac{\partial^2 h_1}{\partial\xi\partial\zeta} - \frac{h_2}{h_1}\frac{\partial h_1}{\partial\xi}\frac{\partial h_1}{\partial\zeta} + i\alpha h_2\frac{\partial h_1}{\partial\zeta}\right)\\
&- \frac{\mu}{Reh_1h_2h_3}\left(i\alpha\frac{\partial h_2}{\partial\zeta} - h_2\alpha\beta - \frac{i\beta h_2}{h_3}\frac{\partial h_3}{\partial\xi} - \frac{1}{h_3}\frac{\partial h_2}{\partial\zeta}\frac{\partial h_3}{\partial\xi} - \frac{h_2}{h_3}\frac{\partial^2 h_3}{\partial\xi\partial\zeta} + \frac{h_2}{h_3^2}\frac{\partial h_3}{\partial\xi}\frac{\partial h_3}{\partial\zeta}\right)\\
&- \frac{\mu}{Reh_1^2h_3}\frac{\partial h_1}{\partial\zeta}\left(i\alpha - \frac{1}{h_3}\frac{\partial h_3}{\partial\xi}\right) + \frac{2\mu}{Reh_1h_2^2h_3}\frac{\partial h_2}{\partial\xi}\frac{\partial h_2}{\partial\zeta} + \frac{i2\mu\beta}{Reh_1h_3^2}\frac{\partial h_3}{\partial\xi}
\end{aligned}
$$

$$
\begin{aligned}
\mathcal{E}_{1,4} =& \frac{1}{h_1\gamma M^2}\left(i\alpha\rho + \Omega\frac{\partial\rho}{\partial\xi}\right) - \frac{1}{Re}\left\{\left[\frac{1}{h_1^2h_2h_3}\frac{\lambda}{\mu}\left(\frac{\partial^2\mu}{\partial T^2}\frac{\partial T}{\partial\xi} + i\alpha\frac{\partial\mu}{\partial T}\right)\right.\right.\\
&\left.\left.-\frac{1}{h_1}\frac{\lambda}{\mu}\frac{\partial\mu}{\partial T}\left(\frac{1}{h_1^2h_2h_3}\frac{\partial h_1}{\partial\xi} + \frac{1}{h_1h_2^2h_3}\frac{\partial h_2}{\partial\xi} + \frac{1}{h_1h_2h_3^2}\frac{\partial h_3}{\partial\xi}\right)\right]\left(uh_2\frac{\partial h_3}{\partial\xi} + uh_3\frac{\partial h_2}{\partial\xi}\right.\right.\\
&\left.\left.+h_2h_3\frac{\partial u}{\partial\xi} + vh_1\frac{\partial h_3}{\partial\eta} + vh_3\frac{\partial h_1}{\partial\eta} + h_1h_3\frac{\partial v}{\partial\eta} + wh_1\frac{\partial h_2}{\partial\zeta} + wh_2\frac{\partial h_1}{\partial\zeta}\right)\right\}\\
&- \frac{1}{Reh_1^2h_2h_3}\frac{\lambda}{\mu}\frac{\partial\mu}{\partial T}\left(2h_2\frac{\partial u}{\partial\xi}\frac{\partial h_3}{\partial\xi} + 2u\frac{\partial h_2}{\partial\xi}\frac{\partial h_3}{\partial\xi} + uh_2\frac{\partial^2 h_3}{\partial\xi^2} + 2h_3\frac{\partial u}{\partial\xi}\frac{\partial h_2}{\partial\xi}\right.\\
&+uh_3\frac{\partial^2 h_2}{\partial\xi^2} + h_1\frac{\partial v}{\partial\xi}\frac{\partial h_3}{\partial\eta} + v\frac{\partial h_1}{\partial\xi}\frac{\partial h_3}{\partial\eta} + vh_1\frac{\partial^2 h_3}{\partial\xi\partial\eta} + h_3\frac{\partial v}{\partial\xi}\frac{\partial h_1}{\partial\eta} + v\frac{\partial h_3}{\partial\xi}\frac{\partial h_1}{\partial\eta}\\
&+vh_3\frac{\partial^2 h_1}{\partial\xi\partial\eta} + h_3\frac{\partial h_1}{\partial\xi}\frac{\partial v}{\partial\eta} + h_1\frac{\partial h_3}{\partial\xi}\frac{\partial v}{\partial\eta} + h_1h_3\frac{\partial^2 v}{\partial\xi\partial\eta} + h_1\frac{\partial w}{\partial\xi}\frac{\partial h_2}{\partial\zeta} + w\frac{\partial h_1}{\partial\xi}\frac{\partial h_2}{\partial\zeta}\\
&\left.+wh_1\frac{\partial^2 h_2}{\partial\xi\partial\zeta} + h_2\frac{\partial w}{\partial\xi}\frac{\partial h_1}{\partial\zeta} + w\frac{\partial h_2}{\partial\xi}\frac{\partial h_1}{\partial\zeta} + wh_2\frac{\partial^2 h_1}{\partial\xi\partial\zeta}\right)\\
&- \frac{2}{Reh_1h_2h_3}\left(i\alpha\frac{\partial\mu}{\partial T} + \frac{\partial^2\mu}{\partial T^2}\frac{\partial T}{\partial\xi}\right)\left(\frac{h_2h_3}{h_1}\frac{\partial u}{\partial\xi} + \frac{vh_3}{h_1}\frac{\partial h_1}{\partial\eta} + \frac{wh_2}{h_1}\frac{\partial h_1}{\partial\zeta}\right)
\end{aligned}
$$

$$
\begin{aligned}
&- \frac{2}{Reh_1h_2h_3}\frac{\partial\mu}{\partial T}\left(\frac{h_3}{h_1}\frac{\partial h_2}{\partial\xi}\frac{\partial u}{\partial\xi} + \frac{h_2}{h_1}\frac{\partial h_3}{\partial\xi}\frac{\partial u}{\partial\xi} - \frac{h_2h_3}{h_1^2}\frac{\partial h_1}{\partial\xi}\frac{\partial u}{\partial\xi} + \frac{v}{h_1}\frac{\partial h_3}{\partial\xi}\frac{\partial h_1}{\partial\eta}\right.\\
&+\frac{h_3}{h_1}\frac{\partial v}{\partial\xi}\frac{\partial h_1}{\partial\eta} + \frac{vh_3}{h_1}\frac{\partial^2 h_1}{\partial\xi\partial\eta} - \frac{vh_3}{h_1^2}\frac{\partial h_1}{\partial\xi}\frac{\partial h_1}{\partial\eta} + \frac{w}{h_1}\frac{\partial h_2}{\partial\xi}\frac{\partial h_1}{\partial\zeta} + \frac{h_2}{h_1}\frac{\partial w}{\partial\xi}\frac{\partial h_1}{\partial\zeta}\\
&\left.+\frac{wh_2}{h_1}\frac{\partial^2 h_1}{\partial\xi\partial\zeta} - \frac{wh_2}{h_1^2}\frac{\partial h_1}{\partial\xi}\frac{\partial h_1}{\partial\zeta}\right)\\
&- \frac{1}{Reh_1h_2h_3}\frac{\partial^2\mu}{\partial T^2}\frac{\partial T}{\partial\eta}\left(h_3\frac{\partial v}{\partial\xi} - \frac{vh_3}{h_2}\frac{\partial h_2}{\partial\xi} + \frac{h_1h_3}{h_2}\frac{\partial u}{\partial\eta} - \frac{uh_3}{h_2}\frac{\partial h_1}{\partial\eta}\right)\\
&- \frac{1}{Reh_1h_2h_3}\frac{\partial\mu}{\partial T}\left(\frac{\partial h_3}{\partial\eta}\frac{\partial v}{\partial\xi} + h_3\frac{\partial^2 v}{\partial\xi\partial\eta} - \frac{h_3}{h_2}\frac{\partial v}{\partial\eta}\frac{\partial h_2}{\partial\xi} - \frac{v}{h_2}\frac{\partial h_3}{\partial\eta}\frac{\partial h_2}{\partial\xi} - \frac{vh_3}{h_2}\frac{\partial^2 h_2}{\partial\xi\partial\eta}\right.\\
&+\frac{vh_3}{h_2^2}\frac{\partial h_2}{\partial\eta}\frac{\partial h_2}{\partial\xi} + \frac{h_1}{h_2}\frac{\partial h_3}{\partial\eta}\frac{\partial u}{\partial\eta} + \frac{h_1h_3}{h_2}\frac{\partial^2 u}{\partial\eta^2}\\
&\left.-\frac{h_1h_3}{h_2^2}\frac{\partial h_2}{\partial\eta}\frac{\partial u}{\partial\eta} - \frac{u}{h_2}\frac{\partial h_3}{\partial\eta}\frac{\partial h_1}{\partial\eta} - \frac{uh_3}{h_2}\frac{\partial^2 h_1}{\partial\eta^2} + \frac{uh_3}{h_2^2}\frac{\partial h_2}{\partial\eta}\frac{\partial h_1}{\partial\eta}\right)\\
&- \frac{i\beta}{Reh_1h_2h_3}\frac{\partial\mu}{\partial T}\left(h_2\frac{\partial w}{\partial\xi} - \frac{uh_2}{h_3}\frac{\partial h_1}{\partial\zeta} - \frac{wh_2}{h_3}\frac{\partial h_3}{\partial\xi}\right)\\
&- \frac{1}{Reh_1h_2}\frac{\partial\mu}{\partial T}\frac{\partial h_1}{\partial\eta}\left(\frac{1}{h_1}\frac{\partial v}{\partial\xi} - \frac{v}{h_1h_2}\frac{\partial h_2}{\partial\xi} + \frac{1}{h_2}\frac{\partial u}{\partial\eta} - \frac{u}{h_1h_2}\frac{\partial h_1}{\partial\eta}\right)\\
&- \frac{1}{Reh_1h_3}\frac{\partial\mu}{\partial T}\frac{\partial h_1}{\partial\zeta}\left(\frac{1}{h_1}\frac{\partial w}{\partial\xi} - \frac{w}{h_1h_3}\frac{\partial h_3}{\partial\xi} - \frac{u}{h_1h_3}\frac{\partial h_1}{\partial\zeta}\right)\\
&+ \frac{2}{Reh_1h_2}\frac{\partial\mu}{\partial T}\frac{\partial h_2}{\partial\xi}\left(\frac{1}{h_2}\frac{\partial v}{\partial\eta} + \frac{w}{h_2h_3}\frac{\partial h_2}{\partial\zeta} + \frac{u}{h_1h_2}\frac{\partial h_2}{\partial\xi}\right)\\
&+ \frac{2}{Reh_1h_3}\frac{\partial\mu}{\partial T}\frac{\partial h_3}{\partial\xi}\left(\frac{u}{h_1h_3}\frac{\partial h_3}{\partial\xi} + \frac{v}{h_2h_3}\frac{\partial h_3}{\partial\eta}\right)\\
&+ \frac{1}{Reh_1^2}\frac{\lambda}{\mu}\frac{\partial^2\mu}{\partial T^2}\frac{\partial T}{\partial\xi}\frac{\partial u}{\partial\xi} + \frac{2}{Reh_1^2}\frac{\partial^2\mu}{\partial T^2}\frac{\partial T}{\partial\xi}\frac{\partial u}{\partial\xi}\\
\mathcal{E}_{1,5} =& \frac{u}{h_1}\frac{\partial u}{\partial\xi} + \frac{v}{h_2}\frac{\partial u}{\partial\eta} - \frac{v^2}{h_1h_2}\frac{\partial h_2}{\partial\xi} - \frac{w^2}{h_1h_3}\frac{\partial h_3}{\partial\xi} + \frac{vu}{h_1h_2}\frac{\partial h_1}{\partial\eta} + \frac{wu}{h_1h_3}\frac{\partial h_1}{\partial\zeta}\\
&+ \frac{1}{h_1\gamma M^2}\left(i\alpha T + \Omega\frac{\partial T}{\partial\xi}\right)
\end{aligned}
$$

$$
\begin{aligned}
\mathcal{E}_{2,1} =& \rho\left(\frac{1}{h_1}\frac{\partial v}{\partial\xi} - \frac{2u}{h_1h_2}\frac{\partial h_1}{\partial\eta} + \frac{v}{h_1h_2}\frac{\partial h_2}{\partial\xi}\right) - \frac{1}{Re}\left\{\left[\frac{1}{h_1h_2^2h_3}\frac{\lambda}{\mu}\frac{\partial\mu}{\partial T}\frac{\partial T}{\partial\eta}\right.\right.\\
&\left.\left.-\frac{\lambda}{h_2}\left(\frac{1}{h_1^2h_2h_3}\frac{\partial h_1}{\partial\eta} + \frac{1}{h_1h_2^2h_3}\frac{\partial h_2}{\partial\eta} + \frac{1}{h_1h_2h_3^2}\frac{\partial h_3}{\partial\eta}\right)\right]\left(i\alpha h_2h_3 + h_2\frac{\partial h_3}{\partial\xi} + h_3\frac{\partial h_2}{\partial\xi}\right)\right\}
\end{aligned}
$$

$$
\begin{aligned}
&- \frac{\lambda}{Reh_1h_2^2h_3}\left(i\alpha h_2\frac{\partial h_3}{\partial \eta} + i\alpha h_3\frac{\partial h_2}{\partial \eta} + \frac{\partial h_2}{\partial \eta}\frac{\partial h_3}{\partial \xi} + h_2\frac{\partial^2 h_3}{\partial \xi \partial \eta} + \frac{\partial h_3}{\partial \eta}\frac{\partial h_2}{\partial \xi} + h_3\frac{\partial^2 h_2}{\partial \xi \partial \eta}\right)\\
&+ \frac{1}{Reh_1^2h_2}\frac{\partial \mu}{\partial T}\frac{\partial T}{\partial \xi}\frac{\partial h_1}{\partial \eta} + \frac{\mu}{Reh_1^2h_2h_3}\left(i\alpha h_3\frac{\partial h_1}{\partial \eta} + \frac{\partial h_3}{\partial \xi}\frac{\partial h_1}{\partial \eta} + h_3\frac{\partial^2 h_1}{\partial \xi \partial \eta} - \frac{h_3}{h_1}\frac{\partial h_1}{\partial \xi}\frac{\partial h_1}{\partial \eta}\right)\\
&- \frac{2}{Reh_1h_2^2}\frac{\partial \mu}{\partial T}\frac{\partial h_2}{\partial \xi}\frac{\partial T}{\partial \eta} - \frac{2\mu}{Reh_1h_2^2h_3}\left(\frac{\partial h_2}{\partial \xi}\frac{\partial h_3}{\partial \eta} + h_3\frac{\partial^2 h_2}{\partial \xi \partial \eta} - \frac{h_3}{h_2}\frac{\partial h_2}{\partial \xi}\frac{\partial h_2}{\partial \eta}\right)\\
&+ \frac{\mu}{Reh_1^2h_2^2}\frac{\partial h_2}{\partial \xi}\frac{\partial h_1}{\partial \eta} + \frac{2\mu}{Reh_1h_2h_3^2}\frac{\partial h_3}{\partial \eta}\frac{\partial h_3}{\partial \xi} + \frac{i2\mu\alpha}{Reh_1^2h_2}\frac{\partial h_1}{\partial \eta}\\
\mathcal{E}_{2,2} =& \rho\left(-i\omega + \frac{iu\alpha}{h_1} + \frac{1}{h_2}\frac{\partial v}{\partial \eta} + \frac{iw\beta}{h_3} + \frac{w}{h_2h_3}\frac{\partial h_2}{\partial \zeta} + \frac{u}{h_1h_2}\frac{\partial h_2}{\partial \xi}\right) - \frac{1}{Re}\left\{\left[\frac{1}{h_1h_2^2h_3}\frac{\lambda}{\mu}\frac{\partial \mu}{\partial T}\frac{\partial T}{\partial \eta}\right.\right.\\
&\left.\left.-\frac{\lambda}{h_2}\left(\frac{1}{h_1^2h_2h_3}\frac{\partial h_1}{\partial \eta} + \frac{1}{h_1h_2^2h_3}\frac{\partial h_2}{\partial \eta} + \frac{1}{h_1h_2h_3^2}\frac{\partial h_3}{\partial \eta}\right)\right]\left(h_1\frac{\partial h_3}{\partial \eta} + h_3\frac{\partial h_1}{\partial \eta}\right)\right\}\\
&- \frac{\lambda}{Reh_1h_2^2h_3}\left(2\frac{\partial h_1}{\partial \eta}\frac{\partial h_3}{\partial \eta} + h_1\frac{\partial^2 h_3}{\partial \eta^2} + h_3\frac{\partial^2 h_1}{\partial \eta^2}\right) - \frac{1}{Reh_1^2h_2}\frac{\partial \mu}{\partial T}\frac{\partial T}{\partial \xi}\left(i\alpha h_2 - \frac{\partial h_2}{\partial \xi}\right)\\
&- \frac{\mu}{Reh_1^2h_2h_3}\left(i\alpha h_2\frac{\partial h_3}{\partial \xi} - \frac{i\alpha h_2h_3}{h_1}\frac{\partial h_1}{\partial \xi} + ih_2h_3\frac{\partial \alpha}{\partial \xi} - \alpha^2 h_2h_3\right.\\
&\left.-\frac{\partial h_3}{\partial \xi}\frac{\partial h_2}{\partial \xi} - h_3\frac{\partial^2 h_2}{\partial \xi^2} + \frac{h_3}{h_1}\frac{\partial h_1}{\partial \xi}\frac{\partial h_2}{\partial \xi}\right) - \frac{\mu}{Reh_1h_2h_3^2}\left(i\beta h_2\frac{\partial h_1}{\partial \zeta} - \beta^2 h_1h_2\right.\\
&\left.-\frac{i\beta h_1h_2}{h_3}\frac{\partial h_3}{\partial \zeta} - \frac{\partial h_1}{\partial \zeta}\frac{\partial h_2}{\partial \zeta} - h_1\frac{\partial^2 h_2}{\partial \zeta^2} + \frac{h_1}{h_3}\frac{\partial h_3}{\partial \zeta}\frac{\partial h_2}{\partial \zeta}\right) - \frac{\mu}{Reh_2h_3^2}\frac{\partial h_2}{\partial \zeta}\left(i\beta - \frac{1}{h_2}\frac{\partial h_2}{\partial \zeta}\right)\\
&- \frac{\mu}{Reh_1^2h_2}\frac{\partial h_2}{\partial \xi}\left(i\alpha - \frac{1}{h_2}\frac{\partial h_2}{\partial \xi}\right) + \frac{2\mu}{Reh_2^2h_3^2}\left(\frac{\partial h_3}{\partial \eta}\right)^2 + \frac{2\mu}{Reh_1^2h_2^2}\left(\frac{\partial h_1}{\partial \eta}\right)^2\\
\mathcal{E}_{2,3} =& \rho\left(\frac{v}{h_2h_3}\frac{\partial h_2}{\partial \zeta} - \frac{2w}{h_2h_3}\frac{\partial h_3}{\partial \eta}\right) - \frac{1}{Re}\left\{\left[\frac{1}{h_1h_2^2h_3}\frac{\lambda}{\mu}\frac{\partial \mu}{\partial T}\frac{\partial T}{\partial \eta}\right.\right.\\
&\left.\left.-\frac{\lambda}{h_2}\left(\frac{1}{h_1^2h_2h_3}\frac{\partial h_1}{\partial \eta} + \frac{1}{h_1h_2^2h_3}\frac{\partial h_2}{\partial \eta} + \frac{1}{h_1h_2h_3^2}\frac{\partial h_3}{\partial \eta}\right)\right]\left(i\beta h_1h_2 + h_1\frac{\partial h_2}{\partial \zeta} + h_2\frac{\partial h_1}{\partial \zeta}\right)\right\}\\
&- \frac{\lambda}{Reh_1h_2^2h_3}\left(i\beta h_1\frac{\partial h_2}{\partial \eta} + i\beta h_2\frac{\partial h_1}{\partial \eta} + \frac{\partial h_1}{\partial \eta}\frac{\partial h_2}{\partial \zeta} + h_1\frac{\partial^2 h_2}{\partial \eta \partial \zeta} + \frac{\partial h_2}{\partial \eta}\frac{\partial h_1}{\partial \zeta} + h_2\frac{\partial^2 h_1}{\partial \eta \partial \zeta}\right)\\
&- \frac{2}{Reh_2^2h_3}\frac{\partial \mu}{\partial T}\frac{\partial h_2}{\partial \zeta}\frac{\partial T}{\partial \eta} - \frac{2\mu}{Reh_1h_2^2h_3}\left(\frac{\partial h_1}{\partial \eta}\frac{\partial h_2}{\partial \zeta} + h_1\frac{\partial^2 h_2}{\partial \eta \partial \zeta} - \frac{h_1}{h_2}\frac{\partial h_2}{\partial \eta}\frac{\partial h_2}{\partial \zeta}\right)\\
&+ \frac{\mu}{Reh_1h_2h_3^2}\left(3i\beta h_1\frac{\partial h_3}{\partial \eta} + \frac{\partial h_1}{\partial \zeta}\frac{\partial h_3}{\partial \eta} + h_1\frac{\partial^2 h_3}{\partial \eta \partial \zeta} - \frac{h_1}{h_3}\frac{\partial h_3}{\partial \eta}\frac{\partial h_3}{\partial \zeta}\right) + \frac{\mu}{Reh_2^2h_3^2}\frac{\partial h_2}{\partial \zeta}\frac{\partial h_3}{\partial \eta}\\
&+ \frac{2\mu}{Reh_1^2h_2h_3}\frac{\partial h_1}{\partial \eta}\frac{\partial h_1}{\partial \zeta}\\
\mathcal{E}_{2,4} =& \frac{1}{h_2\gamma M^2}\frac{\partial \rho}{\partial \eta} - \frac{1}{Re}\left\{\left[\frac{1}{h_1h_2^2h_3}\frac{\lambda}{\mu}\frac{\partial^2 \mu}{\partial T^2}\frac{\partial T}{\partial \eta}\right.\right.\\
&\left.\left.-\frac{1}{h_2}\frac{\lambda}{\mu}\frac{\partial \mu}{\partial T}\left(\frac{1}{h_1^2h_2h_3}\frac{\partial h_1}{\partial \eta} + \frac{1}{h_1h_2^2h_3}\frac{\partial h_2}{\partial \eta} + \frac{1}{h_1h_2h_3^2}\frac{\partial h_3}{\partial \eta}\right)\right]\left(h_2h_3\frac{\partial u}{\partial \xi}\right.\right.\\
&\left.\left.+uh_2\frac{\partial h_3}{\partial \xi} + uh_3\frac{\partial h_2}{\partial \xi} + h_1h_3\frac{\partial v}{\partial \eta} + vh_3\frac{\partial h_1}{\partial \eta} + vh_1\frac{\partial h_3}{\partial \eta} + wh_1\frac{\partial h_2}{\partial \zeta} + wh_2\frac{\partial h_1}{\partial \zeta}\right)\right\}
\end{aligned}
$$

$$
\begin{aligned}
&- \frac{1}{Reh_1h_2^2h_3}\frac{\lambda}{\mu}\frac{\partial\mu}{\partial T}\left(h_2h_3\frac{\partial^2 u}{\partial\xi\partial\eta}+h_2\frac{\partial h_3}{\partial\eta}\frac{\partial u}{\partial\xi}+h_3\frac{\partial h_2}{\partial\eta}\frac{\partial u}{\partial\xi}+h_2\frac{\partial u}{\partial\eta}\frac{\partial h_3}{\partial\xi}+u\frac{\partial h_2}{\partial\eta}\frac{\partial h_3}{\partial\xi}\right.\\
&+uh_2\frac{\partial^2 h_3}{\partial\xi\partial\eta}+h_3\frac{\partial u}{\partial\eta}\frac{\partial h_2}{\partial\xi}+u\frac{\partial h_3}{\partial\eta}\frac{\partial h_2}{\partial\xi}+uh_3\frac{\partial^2 h_2}{\partial\xi\partial\eta}\\
&+h_1h_3\frac{\partial^2 v}{\partial\eta^2}+2h_1\frac{\partial h_3}{\partial\eta}\frac{\partial v}{\partial\eta}+2h_3\frac{\partial h_1}{\partial\eta}\frac{\partial v}{\partial\eta}+2v\frac{\partial h_1}{\partial\eta}\frac{\partial h_3}{\partial\eta}+vh_3\frac{\partial^2 h_1}{\partial\eta^2}+vh_1\frac{\partial^2 h_3}{\partial\eta^2}\\
&\left.+h_1\frac{\partial w}{\partial\eta}\frac{\partial h_2}{\partial\zeta}+w\frac{\partial h_1}{\partial\eta}\frac{\partial h_2}{\partial\zeta}+wh_1\frac{\partial^2 h_2}{\partial\eta\partial\zeta}+h_2\frac{\partial w}{\partial\eta}\frac{\partial h_1}{\partial\zeta}+w\frac{\partial h_2}{\partial\eta}\frac{\partial h_1}{\partial\zeta}+wh_2\frac{\partial^2 h_1}{\partial\eta\partial\zeta}\right)\\
&- \frac{1}{Reh_1h_2h_3}\left(\frac{\partial^2\mu}{\partial T^2}\frac{\partial T}{\partial\xi}+i\alpha\frac{\partial\mu}{\partial T}\right)\left(\frac{h_2h_3}{h_1}\frac{\partial v}{\partial\xi}-\frac{vh_3}{h_1}\frac{\partial h_2}{\partial\xi}+h_3\frac{\partial u}{\partial\eta}-\frac{uh_3}{h_1}\frac{\partial h_1}{\partial\eta}\right)\\
&- \frac{1}{Reh_1h_2h_3}\frac{\partial\mu}{\partial T}\left(\frac{h_2}{h_1}\frac{\partial h_3}{\partial\xi}\frac{\partial v}{\partial\xi}-\frac{h_2h_3}{h_1^2}\frac{\partial h_1}{\partial\xi}\frac{\partial v}{\partial\xi}-\frac{v}{h_1}\frac{\partial h_2}{\partial\xi}\frac{\partial h_3}{\partial\xi}-\frac{vh_3}{h_1}\frac{\partial^2 h_2}{\partial\xi^2}\right.\\
&+\frac{vh_3}{h_1^2}\frac{\partial h_1}{\partial\xi}\frac{\partial h_2}{\partial\xi}+\frac{\partial h_3}{\partial\xi}\frac{\partial u}{\partial\eta}+h_3\frac{\partial^2 u}{\partial\xi\partial\eta}-\frac{h_3}{h_1}\frac{\partial h_1}{\partial\eta}\frac{\partial u}{\partial\xi}-\frac{u}{h_1}\frac{\partial h_3}{\partial\xi}\frac{\partial h_1}{\partial\eta}-\frac{uh_3}{h_1}\frac{\partial^2 h_1}{\partial\xi\partial\eta}\\
&\left.+\frac{uh_3}{h_1^2}\frac{\partial h_1}{\partial\xi}\frac{\partial h_1}{\partial\eta}\right)-\frac{2}{Reh_1h_2h_3}\frac{\partial^2\mu}{\partial T^2}\frac{\partial T}{\partial\eta}\left(\frac{h_1h_3}{h_2}\frac{\partial v}{\partial\eta}+\frac{wh_1}{h_2}\frac{\partial h_2}{\partial\zeta}+\frac{uh_3}{h_2}\frac{\partial h_2}{\partial\xi}\right)\\
&- \frac{2}{Reh_1h_2h_3}\frac{\partial\mu}{\partial T}\left(\frac{h_1h_3}{h_2}\frac{\partial^2 v}{\partial\eta^2}+\frac{h_1}{h_2}\frac{\partial h_3}{\partial\eta}\frac{\partial v}{\partial\eta}+\frac{h_3}{h_2}\frac{\partial h_1}{\partial\eta}\frac{\partial v}{\partial\eta}-\frac{h_1h_3}{h_2^2}\frac{\partial h_2}{\partial\eta}\frac{\partial v}{\partial\eta}+\frac{h_1}{h_2}\frac{\partial h_2}{\partial\zeta}\frac{\partial w}{\partial\eta}\right.\\
&+\frac{w}{h_2}\frac{\partial h_1}{\partial\eta}\frac{\partial h_2}{\partial\zeta}+\frac{wh_1}{h_2}\frac{\partial^2 h_2}{\partial\eta\partial\zeta}-\frac{wh_1}{h_2^2}\frac{\partial h_2}{\partial\eta}\frac{\partial h_2}{\partial\zeta}+\frac{h_3}{h_2}\frac{\partial h_2}{\partial\xi}\frac{\partial u}{\partial\eta}+\frac{u}{h_2}\frac{\partial h_3}{\partial\eta}\frac{\partial h_2}{\partial\xi}\\
&\left.+\frac{uh_3}{h_2}\frac{\partial^2 h_2}{\partial\xi\partial\eta}-\frac{uh_3}{h_2^2}\frac{\partial h_2}{\partial\xi}\frac{\partial h_2}{\partial\eta}\right)-\frac{i\beta}{Reh_1h_2h_3}\frac{\partial\mu}{\partial T}\left(h_1\frac{\partial w}{\partial\eta}-\frac{wh_1}{h_3}\frac{\partial h_3}{\partial\eta}-\frac{vh_1}{h_3}\frac{\partial h_2}{\partial\zeta}\right)\\
&- \frac{1}{Reh_1h_2h_3}\frac{\partial\mu}{\partial T}\left(\frac{\partial h_1}{\partial\zeta}\frac{\partial w}{\partial\eta}-\frac{w}{h_3}\frac{\partial h_1}{\partial\zeta}\frac{\partial h_3}{\partial\eta}-\frac{wh_1}{h_3}\frac{\partial^2 h_3}{\partial\eta\partial\zeta}+\frac{wh_1}{h_3^2}\frac{\partial h_3}{\partial\eta}\frac{\partial h_3}{\partial\zeta}\right.\\
&\left.-\frac{v}{h_3}\frac{\partial h_1}{\partial\zeta}\frac{\partial h_2}{\partial\zeta}-\frac{vh_1}{h_3}\frac{\partial^2 h_2}{\partial\zeta^2}+\frac{vh_1}{h_3^2}\frac{\partial h_3}{\partial\zeta}\frac{\partial h_2}{\partial\zeta}\right)\\
&- \frac{1}{Reh_2^2h_3}\frac{\partial\mu}{\partial T}\frac{\partial h_2}{\partial\zeta}\left(\frac{\partial w}{\partial\eta}-\frac{w}{h_3}\frac{\partial h_3}{\partial\eta}-\frac{v}{h_3}\frac{\partial h_2}{\partial\zeta}\right)\\
&- \frac{1}{Reh_1h_2}\frac{\partial\mu}{\partial T}\frac{\partial h_2}{\partial\xi}\left(\frac{1}{h_1}\frac{\partial v}{\partial\xi}-\frac{v}{h_1h_2}\frac{\partial h_2}{\partial\xi}+\frac{1}{h_2}\frac{\partial u}{\partial\eta}-\frac{u}{h_1h_2}\frac{\partial h_1}{\partial\eta}\right)\\
&+ \frac{2}{Reh_2h_3^2}\frac{\partial\mu}{\partial T}\frac{\partial h_3}{\partial\eta}\left(\frac{u}{h_1}\frac{\partial h_3}{\partial\xi}+\frac{v}{h_2}\frac{\partial h_3}{\partial\eta}\right)+\frac{2}{Reh_1^2h_2}\frac{\partial\mu}{\partial T}\frac{\partial h_1}{\partial\eta}\left(\frac{\partial u}{\partial\xi}+\frac{v}{h_2}\frac{\partial h_1}{\partial\eta}+\frac{w}{h_3}\frac{\partial h_1}{\partial\zeta}\right)\\
&+ \frac{1}{Reh_1^2}\frac{\partial^2\mu}{\partial T^2}\frac{\partial T}{\partial\xi}\frac{\partial v}{\partial\xi}\\
\mathcal{E}_{2,5} =& \frac{u}{h_1}\frac{\partial v}{\partial\xi}+\frac{v}{h_2}\frac{\partial v}{\partial\eta}-w\left(\frac{w}{h_2h_3}\frac{\partial h_3}{\partial\eta}-\frac{v}{h_2h_3}\frac{\partial h_2}{\partial\zeta}\right)+u\left(\frac{v}{h_1h_2}\frac{\partial h_2}{\partial\xi}-\frac{u}{h_1h_2}\frac{\partial h_1}{\partial\eta}\right)\\
&+ \frac{1}{h_2\gamma M^2}\frac{\partial T}{\partial\eta}
\end{aligned}
$$

$$
\begin{aligned}
\mathcal{E}_{3,1} =& \rho\left(\frac{1}{h_1}\frac{\partial w}{\partial \xi} - \frac{2u}{h_1 h_3}\frac{\partial h_1}{\partial \zeta} + \frac{w}{h_1 h_3}\frac{\partial h_3}{\partial \xi}\right) - \frac{\lambda}{Re h_1 h_2 h_3^2}\left(i\alpha h_2\frac{\partial h_3}{\partial \zeta} + i\alpha h_3\frac{\partial h_2}{\partial \zeta} - \alpha\beta h_2 h_3\right.\\
&\left.+i\beta h_2\frac{\partial h_3}{\partial \xi} + \frac{\partial h_2}{\partial \zeta}\frac{\partial h_3}{\partial \xi} + h_2\frac{\partial^2 h_3}{\partial \xi \partial \zeta} + i\beta h_3\frac{\partial h_2}{\partial \xi} + \frac{\partial h_3}{\partial \zeta}\frac{\partial h_2}{\partial \xi} + h_3\frac{\partial^2 h_2}{\partial \xi \partial \zeta}\right)\\
&+ \frac{\lambda}{Re h_3}\left(\frac{1}{h_1^2 h_2 h_3}\frac{\partial h_1}{\partial \zeta} + \frac{1}{h_1 h_2^2 h_3}\frac{\partial h_2}{\partial \zeta} + \frac{1}{h_1 h_2 h_3^2}\frac{\partial h_3}{\partial \zeta}\right)\left(i\alpha h_2 h_3 + h_2\frac{\partial h_3}{\partial \xi} + h_3\frac{\partial h_2}{\partial \xi}\right)\\
&- \frac{1}{Re h_1 h_3}\frac{\partial \mu}{\partial T}\frac{\partial T}{\partial \xi}\left(i\beta - \frac{1}{h_1}\frac{\partial h_1}{\partial \zeta}\right)\\
&- \frac{\mu}{Re h_1 h_2 h_3}\left(i\beta\frac{\partial h_2}{\partial \xi} - \alpha\beta h_2 - \frac{i\alpha h_2}{h_1}\frac{\partial h_1}{\partial \zeta} - \frac{1}{h_1}\frac{\partial h_2}{\partial \xi}\frac{\partial h_1}{\partial \zeta} - \frac{h_2}{h_1}\frac{\partial^2 h_1}{\partial \xi \partial \zeta} + \frac{h_2}{h_1^2}\frac{\partial h_1}{\partial \xi}\frac{\partial h_1}{\partial \zeta}\right)\\
&- \frac{2\mu}{Re h_1 h_2 h_3^2}\left(i\beta h_2\frac{\partial h_3}{\partial \xi} + \frac{\partial h_2}{\partial \zeta}\frac{\partial h_3}{\partial \xi} + h_2\frac{\partial^2 h_3}{\partial \xi \partial \zeta} - \frac{h_2}{h_3}\frac{\partial h_3}{\partial \zeta}\frac{\partial h_3}{\partial \xi}\right)\\
&- \frac{\mu}{Re h_1 h_3^2}\frac{\partial h_3}{\partial \xi}\left(i\beta - \frac{1}{h_1}\frac{\partial h_1}{\partial \zeta}\right) + \frac{i2\mu\alpha}{Re h_1^2 h_3}\frac{\partial h_1}{\partial \zeta} + \frac{2\mu}{Re h_1 h_2^2 h_3}\frac{\partial h_2}{\partial \zeta}\frac{\partial h_2}{\partial \xi}\\
\mathcal{E}_{3,2} =& \rho\left(\frac{1}{h_2}\frac{\partial w}{\partial \eta} - \frac{2v}{h_2 h_3}\frac{\partial h_2}{\partial \zeta} + \frac{w}{h_2 h_3}\frac{\partial h_3}{\partial \eta}\right)\\
&- \frac{\lambda}{Re h_1 h_2 h_3^2}\left(i\beta h_1\frac{\partial h_3}{\partial \eta} + \frac{\partial h_1}{\partial \zeta}\frac{\partial h_3}{\partial \eta} + h_1\frac{\partial^2 h_3}{\partial \eta \partial \zeta} + i\beta h_3\frac{\partial h_1}{\partial \eta} + \frac{\partial h_3}{\partial \zeta}\frac{\partial h_1}{\partial \eta} + h_3\frac{\partial^2 h_1}{\partial \eta \partial \zeta}\right)\\
&+ \frac{\lambda}{Re h_3}\left(\frac{1}{h_1^2 h_2 h_3}\frac{\partial h_1}{\partial \zeta} + \frac{1}{h_1 h_2^2 h_3}\frac{\partial h_2}{\partial \zeta} + \frac{1}{h_1 h_2 h_3^2}\frac{\partial h_3}{\partial \zeta}\right)\left(h_1\frac{\partial h_3}{\partial \eta} + h_3\frac{\partial h_1}{\partial \eta}\right)\\
&- \frac{1}{Re h_2 h_3}\frac{\partial \mu}{\partial T}\frac{\partial T}{\partial \eta}\left(i\beta - \frac{1}{h_2}\frac{\partial h_2}{\partial \zeta}\right)\\
&- \frac{\mu}{Re h_1 h_2 h_3}\left(i\beta\frac{\partial h_1}{\partial \eta} - \frac{1}{h_2}\frac{\partial h_1}{\partial \eta}\frac{\partial h_2}{\partial \zeta} - \frac{h_1}{h_2}\frac{\partial^2 h_2}{\partial \eta \partial \zeta} + \frac{h_1}{h_2^2}\frac{\partial h_2}{\partial \eta}\frac{\partial h_2}{\partial \zeta}\right)\\
&- \frac{2\mu}{Re h_1 h_2 h_3^2}\left(i\beta h_1\frac{\partial h_3}{\partial \eta} + \frac{\partial h_1}{\partial \zeta}\frac{\partial h_3}{\partial \eta} + h_1\frac{\partial^2 h_3}{\partial \eta \partial \zeta} - \frac{h_1}{h_3}\frac{\partial h_3}{\partial \zeta}\frac{\partial h_3}{\partial \eta}\right)\\
&- \frac{\mu}{Re h_2 h_3^2}\frac{\partial h_3}{\partial \eta}\left(i\beta - \frac{1}{h_2}\frac{\partial h_2}{\partial \zeta}\right) + \frac{2\mu}{Re h_1^2 h_2 h_3}\frac{\partial h_1}{\partial \eta}\frac{\partial h_1}{\partial \zeta}\\
\mathcal{E}_{3,3} =& \rho\left(-i\omega + \frac{iu\alpha}{h_1} + \frac{iw\beta}{h_3} + \frac{v}{h_2 h_3}\frac{\partial h_3}{\partial \eta} + \frac{u}{h_1 h_3}\frac{\partial h_3}{\partial \xi}\right)\\
&- \frac{\lambda}{Re h_1 h_2 h_3^2}\left(i2\beta h_1\frac{\partial h_2}{\partial \zeta} + i2\beta h_2\frac{\partial h_1}{\partial \zeta} - \beta^2 h_1 h_2 + 2\frac{\partial h_1}{\partial \zeta}\frac{\partial h_2}{\partial \zeta} + h_1\frac{\partial^2 h_2}{\partial \zeta^2} + h_2\frac{\partial^2 h_1}{\partial \zeta^2}\right)\\
&+ \frac{\lambda}{Re h_3}\left(\frac{1}{h_1^2 h_2 h_3}\frac{\partial h_1}{\partial \zeta} + \frac{1}{h_1 h_2^2 h_3}\frac{\partial h_2}{\partial \zeta} + \frac{1}{h_1 h_2 h_3^2}\frac{\partial h_3}{\partial \zeta}\right)\left(i\beta h_1 h_2 + h_1\frac{\partial h_2}{\partial \zeta} + h_2\frac{\partial h_1}{\partial \zeta}\right)\\
&- \frac{1}{Re h_1^2 h_3}\frac{\partial \mu}{\partial T}\frac{\partial T}{\partial \xi}\left(ih_3\alpha - \frac{\partial h_3}{\partial \xi}\right) - \frac{\mu}{Re h_1^2 h_2 h_3}\left(i\frac{\partial \alpha}{\partial \xi}h_2 h_3 - \alpha^2 h_2 h_3 + i\alpha h_3\frac{\partial h_2}{\partial \xi}\right.\\
&\left.-\frac{i\alpha h_2 h_3}{h_1}\frac{\partial h_1}{\partial \xi} - \frac{\partial h_2}{\partial \xi}\frac{\partial h_3}{\partial \xi} - h_2\frac{\partial^2 h_3}{\partial \xi^2} + \frac{h_2}{h_1}\frac{\partial h_1}{\partial \xi}\frac{\partial h_3}{\partial \xi}\right)
\end{aligned}
$$

$$
\begin{aligned}
&+\frac{1}{Reh_2^2h_3}\frac{\partial\mu}{\partial T}\frac{\partial h_3}{\partial\eta}\frac{\partial T}{\partial\eta}+\frac{\mu}{Reh_1h_2^2h_3}\left(\frac{\partial h_1}{\partial\eta}\frac{\partial h_3}{\partial\eta}+h_1\frac{\partial^2h_3}{\partial\eta^2}-\frac{h_1}{h_2}\frac{\partial h_2}{\partial\eta}\frac{\partial h_3}{\partial\eta}\right)\\
&-\frac{2\mu}{Reh_1h_2h_3^2}\left(i\beta h_1\frac{\partial h_2}{\partial\zeta}+i\beta h_2\frac{\partial h_1}{\partial\zeta}-\beta^2h_1h_2-\frac{i\beta h_1h_2}{h_3}\frac{\partial h_3}{\partial\zeta}\right)-\frac{i\alpha\mu}{Reh_1^2h_3}\frac{\partial h_3}{\partial\xi}\\
&+\frac{\mu}{Reh_1^2h_3^2}\left(\frac{\partial h_3}{\partial\xi}\right)^2+\frac{\mu}{Reh_2^2h_3^2}\left(\frac{\partial h_3}{\partial\eta}\right)^2+\frac{2\mu}{Reh_1^2h_3^2}\left(\frac{\partial h_1}{\partial\zeta}\right)^2+\frac{2\mu}{Reh_2^2h_3^2}\left(\frac{\partial h_2}{\partial\zeta}\right)^2\\
\mathcal{E}_{3,4}=&\frac{i\beta\rho}{h_3\gamma M^2}-\left[\frac{1}{Reh_3}\frac{\lambda}{\mu}\frac{\partial\mu}{\partial T}\left(\frac{i\beta}{h_1h_2h_3}-\frac{1}{h_1^2h_2h_3}\frac{\partial h_1}{\partial\zeta}-\frac{1}{h_1h_2^2h_3}\frac{\partial h_2}{\partial\zeta}-\frac{1}{h_1h_2h_3^2}\frac{\partial h_3}{\partial\zeta}\right)\right.\\
&\left(h_2h_3\frac{\partial u}{\partial\xi}+uh_2\frac{\partial h_3}{\partial\xi}+uh_3\frac{\partial h_2}{\partial\xi}+h_1h_3\frac{\partial v}{\partial\eta}+vh_1\frac{\partial h_3}{\partial\eta}+vh_3\frac{\partial h_1}{\partial\eta}\right.\\
&\left.\left.+wh_1\frac{\partial h_2}{\partial\zeta}+wh_2\frac{\partial h_1}{\partial\zeta}\right)\right]-\frac{1}{Reh_1h_2h_3^2}\frac{\lambda}{\mu}\frac{\partial\mu}{\partial T}\left(h_2\frac{\partial h_3}{\partial\zeta}\frac{\partial u}{\partial\xi}+h_3\frac{\partial h_2}{\partial\zeta}\frac{\partial u}{\partial\xi}+u\frac{\partial h_2}{\partial\zeta}\frac{\partial h_3}{\partial\xi}\right.\\
&+uh_2\frac{\partial^2h_3}{\partial\xi\partial\zeta}+u\frac{\partial h_3}{\partial\zeta}\frac{\partial h_2}{\partial\xi}+uh_3\frac{\partial^2h_2}{\partial\xi\partial\zeta}+h_1\frac{\partial h_3}{\partial\zeta}\frac{\partial v}{\partial\eta}+h_3\frac{\partial h_1}{\partial\zeta}\frac{\partial v}{\partial\eta}+v\frac{\partial h_1}{\partial\zeta}\frac{\partial h_3}{\partial\eta}\\
&\left.+vh_1\frac{\partial^2h_3}{\partial\eta\partial\zeta}+v\frac{\partial h_3}{\partial\zeta}\frac{\partial h_1}{\partial\eta}+vh_3\frac{\partial^2h_1}{\partial\eta\partial\zeta}+2w\frac{\partial h_1}{\partial\zeta}\frac{\partial h_2}{\partial\zeta}+wh_1\frac{\partial^2h_2}{\partial\zeta^2}+wh_2\frac{\partial^2h_1}{\partial\zeta^2}\right)\\
&-\frac{1}{Reh_1h_2h_3}\left(\frac{\partial^2\mu}{\partial T^2}\frac{\partial T}{\partial\xi}+i\alpha\frac{\partial\mu}{\partial T}\right)\left(\frac{h_2h_3}{h_1}\frac{\partial w}{\partial\xi}-\frac{uh_2}{h_1}\frac{\partial h_1}{\partial\zeta}-\frac{wh_2}{h_1}\frac{\partial h_3}{\partial\xi}\right)\\
&-\frac{1}{Reh_1h_2h_3}\frac{\partial\mu}{\partial T}\left(\frac{h_3}{h_1}\frac{\partial h_2}{\partial\xi}\frac{\partial w}{\partial\xi}-\frac{h_2h_3}{h_1^2}\frac{\partial h_1}{\partial\xi}\frac{\partial w}{\partial\xi}-\frac{h_2}{h_1}\frac{\partial h_1}{\partial\zeta}\frac{\partial u}{\partial\xi}-\frac{u}{h_1}\frac{\partial h_2}{\partial\xi}\frac{\partial h_1}{\partial\zeta}\right.\\
&\left.-\frac{uh_2}{h_1}\frac{\partial^2h_1}{\partial\xi\partial\zeta}+\frac{uh_2}{h_1^2}\frac{\partial h_1}{\partial\xi}\frac{\partial h_1}{\partial\zeta}-\frac{wh_2}{h_1}\frac{\partial^2h_3}{\partial\xi^2}-\frac{w}{h_1}\frac{\partial h_2}{\partial\xi}\frac{\partial h_3}{\partial\xi}+\frac{wh_2}{h_1^2}\frac{\partial h_1}{\partial\xi}\frac{\partial h_3}{\partial\xi}\right)\\
&-\frac{1}{Reh_1h_2^2h_3}\frac{\partial^2\mu}{\partial T^2}\frac{\partial T}{\partial\eta}\left(h_1h_3\frac{\partial w}{\partial\eta}-wh_1\frac{\partial h_3}{\partial\eta}-vh_1\frac{\partial h_2}{\partial\zeta}\right)\\
&-\frac{1}{Reh_1h_2h_3}\frac{\partial\mu}{\partial T}\left(\frac{h_1h_3}{h_2}\frac{\partial^2w}{\partial\eta^2}+\frac{h_3}{h_2}\frac{\partial h_1}{\partial\eta}\frac{\partial w}{\partial\eta}-\frac{h_1h_3}{h_2^2}\frac{\partial h_2}{\partial\eta}\frac{\partial w}{\partial\eta}-\frac{w}{h_2}\frac{\partial h_1}{\partial\eta}\frac{\partial h_3}{\partial\eta}\right.\\
&\left.-\frac{wh_1}{h_2}\frac{\partial^2h_3}{\partial\eta^2}+\frac{wh_1}{h_2^2}\frac{\partial h_2}{\partial\eta}\frac{\partial h_3}{\partial\eta}-\frac{h_1}{h_2}\frac{\partial h_2}{\partial\zeta}\frac{\partial v}{\partial\eta}-\frac{v}{h_2}\frac{\partial h_1}{\partial\eta}\frac{\partial h_2}{\partial\zeta}-\frac{vh_1}{h_2}\frac{\partial^2h_2}{\partial\eta\partial\zeta}+\frac{vh_1}{h_2^2}\frac{\partial h_2}{\partial\eta}\frac{\partial h_2}{\partial\zeta}\right)\\
&-\frac{i2\beta}{Reh_1h_2h_3^2}\frac{\partial\mu}{\partial T}\left(uh_2\frac{\partial h_3}{\partial\xi}+vh_1\frac{\partial h_3}{\partial\eta}\right)-\frac{2}{Reh_1h_2h_3}\frac{\partial\mu}{\partial T}\left(\frac{uh_2}{h_3}\frac{\partial^2h_3}{\partial\xi\partial\zeta}+\frac{u}{h_3}\frac{\partial h_2}{\partial\zeta}\frac{\partial h_3}{\partial\xi}\right.\\
&\left.-\frac{uh_2}{h_3^2}\frac{\partial h_3}{\partial\zeta}\frac{\partial h_3}{\partial\xi}+\frac{vh_1}{h_3}\frac{\partial^2h_3}{\partial\eta\partial\zeta}+\frac{v}{h_3}\frac{\partial h_1}{\partial\zeta}\frac{\partial h_3}{\partial\eta}-\frac{vh_1}{h_3^2}\frac{\partial h_3}{\partial\zeta}\frac{\partial h_3}{\partial\eta}\right)\\
&-\frac{1}{Reh_1^2h_3}\frac{\partial\mu}{\partial T}\frac{\partial h_3}{\partial\xi}\left(\frac{\partial w}{\partial\xi}-\frac{u}{h_3}\frac{\partial h_1}{\partial\zeta}-\frac{w}{h_3}\frac{\partial h_3}{\partial\xi}\right)\\
&-\frac{1}{Reh_2^2h_3}\frac{\partial\mu}{\partial T}\frac{\partial h_3}{\partial\eta}\left(\frac{\partial w}{\partial\eta}-\frac{w}{h_3}\frac{\partial h_3}{\partial\eta}-\frac{v}{h_3}\frac{\partial h_2}{\partial\zeta}\right)\\
&+\frac{2}{Reh_1^2h_3}\frac{\partial\mu}{\partial T}\frac{\partial h_1}{\partial\zeta}\left(\frac{\partial u}{\partial\xi}+\frac{v}{h_2}\frac{\partial h_1}{\partial\eta}+\frac{w}{h_3}\frac{\partial h_1}{\partial\zeta}\right)\\
&+\frac{2}{Reh_2^2h_3}\frac{\partial\mu}{\partial T}\frac{\partial h_2}{\partial\zeta}\left(\frac{\partial v}{\partial\eta}+\frac{w}{h_3}\frac{\partial h_2}{\partial\zeta}+\frac{u}{h_1}\frac{\partial h_2}{\partial\xi}\right)+\frac{1}{Reh_1^2}\frac{\partial^2\mu}{\partial T^2}\frac{\partial T}{\partial\xi}\frac{\partial w}{\partial\xi}
\end{aligned}
$$

$$\mathcal{E}_{3,5} = \frac{u}{h_1}\frac{\partial w}{\partial \xi} + \frac{v}{h_2}\frac{\partial w}{\partial \eta} - u\left(\frac{u}{h_1 h_3}\frac{\partial h_1}{\partial \zeta} - \frac{w}{h_1 h_3}\frac{\partial h_3}{\partial \xi}\right) + v\left(\frac{w}{h_2 h_3}\frac{\partial h_3}{\partial \eta} - \frac{v}{h_2 h_3}\frac{\partial h_2}{\partial \zeta}\right) + \frac{i\beta T}{h_3 \gamma M^2}$$

$$\begin{aligned}
\mathcal{E}_{4,1} = {} & \frac{\rho}{h_1}\frac{\partial T}{\partial \xi} - \frac{(\gamma-1)}{\gamma h_1}\left(T\frac{\partial \rho}{\partial \xi} + \rho\frac{\partial T}{\partial \xi}\right) \\
& - \frac{(\gamma-1)M^2}{Re}\left\{\frac{i2\alpha}{h_1}(2\mu+\lambda)\left(\frac{1}{h_1}\frac{\partial u}{\partial \xi} + \frac{v}{h_1 h_2}\frac{\partial h_1}{\partial \eta} + \frac{w}{h_1 h_3}\frac{\partial h_1}{\partial \zeta}\right)\right. \\
& + \frac{2}{h_1 h_2}\frac{\partial h_2}{\partial \xi}(2\mu+\lambda)\left(\frac{1}{h_2}\frac{\partial v}{\partial \eta} + \frac{w}{h_2 h_3}\frac{\partial h_2}{\partial \zeta} + \frac{u}{h_1 h_2}\frac{\partial h_2}{\partial \xi}\right) \\
& + 2\mu\left(\frac{i\beta}{h_3} - \frac{1}{h_1 h_3}\frac{\partial h_1}{\partial \zeta}\right)\left(\frac{1}{h_1}\frac{\partial w}{\partial \xi} - \frac{w}{h_1 h_3}\frac{\partial h_3}{\partial \xi} - \frac{u}{h_1 h_3}\frac{\partial h_1}{\partial \zeta}\right) \\
& + \frac{2}{h_1 h_3}\frac{\partial h_3}{\partial \xi}\left[(2\mu+\lambda)\left(\frac{u}{h_1 h_3}\frac{\partial h_3}{\partial \xi} + \frac{v}{h_2 h_3}\frac{\partial h_3}{\partial \eta}\right)\right. \\
& \left. + \lambda\left(\frac{1}{h_1}\frac{\partial u}{\partial \xi} + \frac{v}{h_1 h_2}\frac{\partial h_1}{\partial \eta} + \frac{w}{h_1 h_3}\frac{\partial h_1}{\partial \zeta} + \frac{1}{h_2}\frac{\partial v}{\partial \eta} + \frac{w}{h_2 h_3}\frac{\partial h_2}{\partial \zeta} + \frac{u}{h_1 h_2}\frac{\partial h_2}{\partial \xi}\right)\right] \\
& + \frac{i2\lambda\alpha}{h_1}\left(\frac{1}{h_2}\frac{\partial v}{\partial \eta} + \frac{w}{h_2 h_3}\frac{\partial h_2}{\partial \zeta} + \frac{u}{h_1 h_2}\frac{\partial h_2}{\partial \xi} + \frac{u}{h_1 h_3}\frac{\partial h_3}{\partial \xi} + \frac{v}{h_2 h_3}\frac{\partial h_3}{\partial \eta}\right) \\
& + \frac{2\lambda}{h_1 h_2}\frac{\partial h_2}{\partial \xi}\left(\frac{1}{h_1}\frac{\partial u}{\partial \xi} + \frac{v}{h_1 h_2}\frac{\partial h_1}{\partial \eta} + \frac{w}{h_1 h_3}\frac{\partial h_1}{\partial \zeta} + \frac{u}{h_1 h_3}\frac{\partial h_3}{\partial \xi} + \frac{v}{h_2 h_3}\frac{\partial h_3}{\partial \eta}\right) \\
& \left. - \frac{2\mu}{h_1 h_2}\frac{\partial h_1}{\partial \eta}\left(\frac{1}{h_1}\frac{\partial v}{\partial \xi} - \frac{v}{h_1 h_2}\frac{\partial h_2}{\partial \xi} + \frac{1}{h_2}\frac{\partial u}{\partial \eta} - \frac{u}{h_1 h_2}\frac{\partial h_1}{\partial \eta}\right)\right\}
\end{aligned}$$

$$\begin{aligned}
\mathcal{E}_{4,2} = {} & \frac{\rho}{h_2}\frac{\partial T}{\partial \eta} - \frac{(\gamma-1)}{h_2 \gamma}\left(T\frac{\partial \rho}{\partial \eta} + \rho\frac{\partial T}{\partial \eta}\right) \\
& - \frac{(\gamma-1)M^2}{Re}\left\{\frac{2}{h_1 h_2}\frac{\partial h_1}{\partial \eta}\left[(2\mu+\lambda)\left(\frac{1}{h_1}\frac{\partial u}{\partial \xi} + \frac{v}{h_1 h_2}\frac{\partial h_1}{\partial \eta} + \frac{w}{h_1 h_3}\frac{\partial h_1}{\partial \zeta}\right)\right.\right. \\
& \left. + \lambda\left(\frac{1}{h_2}\frac{\partial v}{\partial \eta} + \frac{w}{h_2 h_3}\frac{\partial h_2}{\partial \zeta} + \frac{u}{h_1 h_2}\frac{\partial h_2}{\partial \xi} + \frac{u}{h_1 h_3}\frac{\partial h_3}{\partial \xi} + \frac{v}{h_2 h_3}\frac{\partial h_3}{\partial \eta}\right)\right] \\
& + 2\mu\left[\left(\frac{1}{h_2}\frac{\partial w}{\partial \eta} - \frac{w}{h_2 h_3}\frac{\partial h_3}{\partial \eta} - \frac{v}{h_2 h_3}\frac{\partial h_2}{\partial \zeta}\right)\left(\frac{i\beta}{h_3} - \frac{1}{h_2 h_3}\frac{\partial h_2}{\partial \zeta}\right)\right. \\
& \left. + \left(\frac{1}{h_1}\frac{\partial v}{\partial \xi} - \frac{v}{h_1 h_2}\frac{\partial h_2}{\partial \xi} + \frac{1}{h_2}\frac{\partial u}{\partial \eta} - \frac{u}{h_1 h_2}\frac{\partial h_1}{\partial \eta}\right)\left(\frac{i\alpha}{h_1} - \frac{1}{h_1 h_2}\frac{\partial h_2}{\partial \xi}\right)\right] \\
& + \frac{2}{h_2 h_3}\frac{\partial h_3}{\partial \eta}\left[(2\mu+\lambda)\left(\frac{u}{h_1 h_3}\frac{\partial h_3}{\partial \xi} + \frac{v}{h_2 h_3}\frac{\partial h_3}{\partial \eta}\right)\right.
\end{aligned}$$

$$
\begin{aligned}
&+\lambda\left(\frac{1}{h_1}\frac{\partial u}{\partial \xi}+\frac{v}{h_1h_2}\frac{\partial h_1}{\partial \eta}+\frac{w}{h_1h_3}\frac{\partial h_1}{\partial \zeta}+\frac{1}{h_2}\frac{\partial v}{\partial \eta}+\frac{w}{h_2h_3}\frac{\partial h_2}{\partial \zeta}+\frac{u}{h_1h_2}\frac{\partial h_2}{\partial \xi}\right)\Bigg]\Bigg\}\\
\mathcal{E}_{4,3}=&-\frac{(\gamma-1)\,M^2}{Re}\left\{\frac{2}{h_1h_3}\frac{\partial h_1}{\partial \zeta}\left[(2\mu+\lambda)\left(\frac{1}{h_1}\frac{\partial u}{\partial \xi}+\frac{v}{h_1h_2}\frac{\partial h_1}{\partial \eta}+\frac{w}{h_1h_3}\frac{\partial h_1}{\partial \zeta}\right)\right.\right.\\
&\left.+\lambda\left(\frac{1}{h_2}\frac{\partial v}{\partial \eta}+\frac{w}{h_2h_3}\frac{\partial h_2}{\partial \zeta}+\frac{u}{h_1h_2}\frac{\partial h_2}{\partial \xi}+\frac{u}{h_1h_3}\frac{\partial h_3}{\partial \xi}+\frac{v}{h_2h_3}\frac{\partial h_3}{\partial \eta}\right)\right]\\
&-\frac{2\mu}{h_2h_3}\frac{\partial h_3}{\partial \eta}\left(\frac{1}{h_2}\frac{\partial w}{\partial \eta}-\frac{w}{h_2h_3}\frac{\partial h_3}{\partial \eta}-\frac{v}{h_2h_3}\frac{\partial h_2}{\partial \zeta}\right)\\
&+\frac{2}{h_2h_3}\frac{\partial h_2}{\partial \zeta}\left[(2\mu+\lambda)\left(\frac{1}{h_2}\frac{\partial v}{\partial \eta}+\frac{w}{h_2h_3}\frac{\partial h_2}{\partial \zeta}+\frac{u}{h_1h_2}\frac{\partial h_2}{\partial \xi}\right)\right.\\
&\left.+\lambda\left(\frac{1}{h_1}\frac{\partial u}{\partial \xi}+\frac{v}{h_1h_2}\frac{\partial h_1}{\partial \eta}+\frac{w}{h_1h_3}\frac{\partial h_1}{\partial \zeta}+\frac{u}{h_1h_3}\frac{\partial h_3}{\partial \xi}+\frac{v}{h_2h_3}\frac{\partial h_3}{\partial \eta}\right)\right]\\
&+2\mu\left(\frac{1}{h_1}\frac{\partial w}{\partial \xi}-\frac{w}{h_1h_3}\frac{\partial h_3}{\partial \xi}-\frac{u}{h_1h_3}\frac{\partial h_1}{\partial \zeta}\right)\left(\frac{i\alpha}{h_1}-\frac{1}{h_1h_3}\frac{\partial h_3}{\partial \xi}\right)\\
&+\frac{i2\lambda\beta}{h_3}\left(\frac{1}{h_1}\frac{\partial u}{\partial \xi}+\frac{v}{h_1h_2}\frac{\partial h_1}{\partial \eta}+\frac{w}{h_1h_3}\frac{\partial h_1}{\partial \zeta}+\frac{1}{h_2}\frac{\partial v}{\partial \eta}+\frac{w}{h_2h_3}\frac{\partial h_2}{\partial \zeta}+\frac{u}{h_1h_2}\frac{\partial h_2}{\partial \xi}\right)\\
&\left.+\frac{i2\beta}{h_3}\left(2\mu+\lambda\right)\left(\frac{u}{h_1h_3}\frac{\partial h_3}{\partial \xi}+\frac{v}{h_2h_3}\frac{\partial h_3}{\partial \eta}\right)\right\}\\
\mathcal{E}_{4,4}=&\frac{i\rho}{\gamma}\left(-\omega+\frac{u\alpha}{h_1}+\frac{w\beta}{h_3}\right)-\frac{(\gamma-1)}{\gamma}\left(\Omega\frac{u}{h_1}\frac{\partial \rho}{\partial \xi}+\frac{v}{h_2}\frac{\partial \rho}{\partial \eta}\right)\\
&-\frac{1}{PrReh_1h_2h_3}\left\{\frac{i\alpha}{h_1}\left(h_2h_3\frac{\partial \kappa}{\partial T}\frac{\partial T}{\partial \xi}+\kappa h_2\frac{\partial h_3}{\partial \xi}+\kappa h_3\frac{\partial h_2}{\partial \xi}-\frac{\kappa h_2h_3}{h_1}\frac{\partial h_1}{\partial \xi}\right)\right.\\
&+i\frac{\partial \alpha}{\partial \xi}\frac{\kappa h_2h_3}{h_1}-\frac{\alpha^2\kappa h_2h_3}{h_1}+\frac{i\beta}{h_3}\left(\kappa h_1\frac{\partial h_2}{\partial \zeta}+\kappa h_2\frac{\partial h_1}{\partial \zeta}-\frac{\kappa h_1h_2}{h_3}\frac{\partial h_3}{\partial \zeta}\right)-\frac{\beta^2\kappa h_1h_2}{h_3}\\
&+\left(\frac{\partial^2\kappa}{\partial T^2}\frac{\partial T}{\partial \xi}+i\alpha\frac{\partial \kappa}{\partial T}\right)\frac{h_2h_3}{h_1}\frac{\partial T}{\partial \xi}+\frac{\partial^2\kappa}{\partial T^2}\frac{h_1h_3}{h_2}\left(\frac{\partial T}{\partial \eta}\right)^2\\
&+\frac{\partial \kappa}{\partial T}\left(\frac{h_2}{h_1}\frac{\partial h_3}{\partial \xi}\frac{\partial T}{\partial \xi}+\frac{h_3}{h_1}\frac{\partial h_2}{\partial \xi}\frac{\partial T}{\partial \xi}-\frac{h_2h_3}{h_1^2}\frac{\partial h_1}{\partial \xi}\frac{\partial T}{\partial \xi}+\frac{h_1h_3}{h_2}\frac{\partial^2 T}{\partial \eta^2}\right.\\
&\left.\left.+\frac{h_1}{h_2}\frac{\partial h_3}{\partial \eta}\frac{\partial T}{\partial \eta}+\frac{h_3}{h_2}\frac{\partial h_1}{\partial \eta}\frac{\partial T}{\partial \eta}-\frac{h_1h_3}{h_2^2}\frac{\partial h_2}{\partial \eta}\frac{\partial T}{\partial \eta}\right)\right\}\\
&-\frac{(\gamma-1)\,M^2}{Re}\frac{\partial \mu}{\partial T}\left\{\left(2+\frac{\lambda}{\mu}\right)\left[\left(\frac{1}{h_1}\frac{\partial u}{\partial \xi}+\frac{v}{h_1h_2}\frac{\partial h_1}{\partial \eta}+\frac{w}{h_1h_3}\frac{\partial h_1}{\partial \zeta}\right)^2\right.\right.\\
&\left.+\left(\frac{1}{h_2}\frac{\partial v}{\partial \eta}+\frac{w}{h_2h_3}\frac{\partial h_2}{\partial \zeta}+\frac{u}{h_1h_2}\frac{\partial h_2}{\partial \xi}\right)^2+\left(\frac{u}{h_1h_3}\frac{\partial h_3}{\partial \xi}+\frac{v}{h_2h_3}\frac{\partial h_3}{\partial \eta}\right)^2\right]\\
&+\left(\frac{1}{h_2}\frac{\partial w}{\partial \eta}-\frac{w}{h_2h_3}\frac{\partial h_3}{\partial \eta}-\frac{v}{h_2h_3}\frac{\partial h_2}{\partial \zeta}\right)^2+\left(\frac{1}{h_1}\frac{\partial w}{\partial \xi}-\frac{w}{h_1h_3}\frac{\partial h_3}{\partial \xi}-\frac{u}{h_1h_3}\frac{\partial h_1}{\partial \zeta}\right)^2\\
&+\left(\frac{1}{h_1}\frac{\partial v}{\partial \xi}-\frac{v}{h_1h_2}\frac{\partial h_2}{\partial \xi}+\frac{1}{h_2}\frac{\partial u}{\partial \eta}-\frac{u}{h_1h_2}\frac{\partial h_1}{\partial \eta}\right)^2
\end{aligned}
$$

$$
\begin{aligned}
&+2\frac{\lambda}{\mu}\left[\left(\frac{1}{h_1}\frac{\partial u}{\partial \xi}+\frac{v}{h_1h_2}\frac{\partial h_1}{\partial \eta}+\frac{w}{h_1h_3}\frac{\partial h_1}{\partial \zeta}\right)\left(\frac{1}{h_2}\frac{\partial v}{\partial \eta}+\frac{w}{h_2h_3}\frac{\partial h_2}{\partial \zeta}+\frac{u}{h_1h_2}\frac{\partial h_2}{\partial \xi}\right)\right.\\
&+\left(\frac{1}{h_1}\frac{\partial u}{\partial \xi}+\frac{v}{h_1h_2}\frac{\partial h_1}{\partial \eta}+\frac{w}{h_1h_3}\frac{\partial h_1}{\partial \zeta}\right)\left(\frac{u}{h_1h_3}\frac{\partial h_3}{\partial \xi}+\frac{v}{h_2h_3}\frac{\partial h_3}{\partial \eta}\right)\\
&\left.+\left(\frac{1}{h_2}\frac{\partial v}{\partial \eta}+\frac{w}{h_2h_3}\frac{\partial h_2}{\partial \zeta}+\frac{u}{h_1h_2}\frac{\partial h_2}{\partial \xi}\right)\left(\frac{u}{h_1h_3}\frac{\partial h_3}{\partial \xi}+\frac{v}{h_2h_3}\frac{\partial h_3}{\partial \eta}\right)\right]\Bigg\}\\
&+\frac{1}{PrRe h_1^2}\frac{\partial^2\kappa}{\partial T^2}\frac{\partial T}{\partial \xi}\frac{\partial T}{\partial \xi}\\
&+\frac{(\gamma-1)M^2}{Re}\frac{\partial \mu}{\partial T}\left[\left(2+\frac{\lambda}{\mu}\right)\left(\frac{1}{h_1}\frac{\partial u}{\partial \xi}\right)^2+\left(\frac{1}{h_1}\frac{\partial v}{\partial \xi}\right)^2+\left(\frac{1}{h_1}\frac{\partial w}{\partial \xi}\right)^2\right]\\
\mathcal{E}_{4,5}=&\frac{u}{h_1}\frac{\partial T}{\partial \xi}+\frac{v}{h_2}\frac{\partial T}{\partial \eta}-\frac{(\gamma-1)}{\gamma}\left[iT\left(-\omega+\frac{\alpha u}{h_1}+\frac{\beta w}{h_3}\right)+\Omega\frac{u}{h_1}\frac{\partial T}{\partial \xi}+\frac{v}{h_2}\frac{\partial T}{\partial \eta}\right]
\end{aligned}
$$

$$
\begin{aligned}
\mathcal{E}_{5,1}=&\frac{1}{h_1}\frac{\partial \rho}{\partial \xi}+\frac{\rho}{h_1}\left(i\alpha+\frac{1}{h_2}\frac{\partial h_2}{\partial \xi}+\frac{1}{h_3}\frac{\partial h_3}{\partial \xi}\right)\\
\mathcal{E}_{5,2}=&\frac{1}{h_2}\frac{\partial \rho}{\partial \eta}+\frac{\rho}{h_2}\left(\frac{1}{h_3}\frac{\partial h_3}{\partial \eta}+\frac{1}{h_1}\frac{\partial h_1}{\partial \eta}\right)\\
\mathcal{E}_{5,3}=&\frac{\rho}{h_3}\left(i\beta+\frac{1}{h_2}\frac{\partial h_2}{\partial \zeta}+\frac{1}{h_1}\frac{\partial h_1}{\partial \zeta}\right)\\
\mathcal{E}_{5,4}=&0\\
\mathcal{E}_{5,5}=&-i\omega+\frac{1}{h_1}\frac{\partial u}{\partial \xi}+\frac{u}{h_1}\left(i\alpha+\frac{1}{h_2}\frac{\partial h_2}{\partial \xi}+\frac{1}{h_3}\frac{\partial h_3}{\partial \xi}\right)+\frac{1}{h_2}\frac{\partial v}{\partial \eta}+\frac{v}{h_2}\left(\frac{1}{h_3}\frac{\partial h_3}{\partial \eta}+\frac{1}{h_1}\frac{\partial h_1}{\partial \eta}\right)\\
&+\frac{w}{h_3}\left(i\beta+\frac{1}{h_2}\frac{\partial h_2}{\partial \zeta}+\frac{1}{h_1}\frac{\partial h_1}{\partial \zeta}\right)
\end{aligned}
$$